Thermophysical properties from experimental speed of sound measurements for working fluids in organic Rankine cycles

Der Fakultät für Maschinenbau
der Universität Paderborn
zur Erlangung des akademischen Grades

Doktor-Ingenieur (Dr.-Ing.)
vorgelegte
Dissertation

von

Herrn

Dipl.-Wirt.-Ing. Frithjof H. Dubberke

aus Bad Segeberg

2017

Betreuer der Dissertation: Prof. Dr.-Ing. habil. Jadran Vrabec

Danksagung

Die vorliegende Arbeit entstand in den Jahren 2009-2017 am Lehrstuhl für Thermodynamik und Energietechnik der Fakultät Maschinenbau an der Universität Paderborn unter Anleitung von Herrn Prof. Dr. Jadran Vrabec, der mir in fachlicher aber auch in persönlicher Hinsicht ein wertvoller Mentor war und die Qualität meiner Arbeit deutlich verbessert hat.

Die vorliegende Ausarbeitung, welche zwei experimentelle Themengebiete umfasst, wäre ohne die Unterstützung von einer Vielzahl von Personen so nicht möglich gewesen.

Hier ist in allererster Linie Elmar Baumhögger zu danken, der nicht nur ein guter Freund geworden ist, sondern mich mit seinem umfangreichen Fachwissen in der Messtechnik, sowie seiner Erfahrung in der Planung und technischen Auslegung von wissentschaftlichen Experimenten, ausnahmslos erstklassig beraten hat. Beim experimentalen Aufbau wurde ich maßgeblich und kompetent von Rüdiger Pflock, Alexander Reimann, Norbert Temborius und Ilona Stasny unterstützt. Die Hilfe der studentischen Hilfskräfte Sebastian Pflock, David Rasche, Carlos Guillermo La Rubia García, Markus Riepold und Simon Schönborn war ebenfalls sehr förderlich und motivierend. Bedanken möchte ich mich auch für die beratende Unterstützung durch Dr. Jens Rautenberg, Dr. Fabian Bause und Dr. Andreas Quellmalz vom Fachgebiet Elektrische Messtechnik.

Für die Ideen hinsichtlich der Entwicklung und die tatkräftige Mithilfe beim Aufbau der ORC-Versuchsanlage möchte ich besonders Klaus-Peter Priebe danken. Des Weiteren haben hier hilfreich mitgewirkt Matthias Linnemann, Steffen Greve, Stefan Rode, Hanke Bohlen, Wameedh Khider Abbas und Martin Mader. Bester Dank gilt em. Prof. Dr. Johann Fischer für seine stetige Hilfsbereitschaft und die hochgeschätzten Diskussionen zum Thema ORC.

Für die Unterstützung theoretischer Natur gilt mein besonderer Dank Dr. Gerhard Herres. Er ist in fachlichen Themen, aber auch in nahezu allen weiteren skurrilen Sachthemen interdisziplinärer Natur profund sattelfest und hat mir nachhaltig durch seine freundliche und hilfsbereite Art viel Freude und Erheiterung bereitet.

Genauso kann die durchgehend gute Stimmung am Lehrstuhl gar nicht genug hervorgehoben werden. Hauptverantwortlich waren hierfür meine beiden Kolleginnen Jutta Jäger und Dr. Svetlana Miroshnichenko, letztere auch meine langjährige und hochgeschätzte Bürokollegin. Das Zusammenspiel eines bunten Potpourris weiterer KollegINNEN, (neben schon benannten) hier namentlich Dr. Marc Schlüter, Dr. Thorsten Windmann, Dr. Andreas Köster, Gerrit Sonnenrein, Andreas Elsner, Dr. Gabor Rutkai, Matthias Heinen, Andreas Paul, Marco Greve, Dr. Gabriela F. Guevara

Carrion und Tatjana Janzen lassen mich auf eine unvergesslich muntere Zeit zurückblicken. Diese wurde durch eine Prise großväterlicher Zuwendung von em. Prof. Dr. Dieter Gorenflo stets selbstlos und herzlich bereichert. In lebhafter Erinnerung bleiben mir ebenso eine Vielzahl an kuriosen Erlebnissen mit JProf. Dr. Martin Horsch sowie lehrreiche und interessante Diskussionen mit René S. Chatwell.

Spezieller Dank gilt Stefan Eckelsbach für die langen Nächte der geduldigen und umfangreichen Hilfe bei der finalen Formatierung des Manuskripts.

Mein Dank gilt auch der freundlichen und kompetenten Verwaltung der Universität Paderborn für zügige und unkomplizierte Sachbearbeitungen.

Einen ausdrücklichen Gruß möchte ich an dieser Stelle an die KollegINNEN nach Bochum richten, besonders an Prof. Dr. Roland Span, der in mir das Interesse an der Thermodynamik geweckt hat, und an Frau Dr. Monika Thol für die produktive Zusammenarbeit im Rahmen unserer gemeinsamen Publikationen.

Ebenfalls erinnere ich mich nur allzu gern an die lehrreiche und intensive Studentenzeit, bei der ein umfangreiches, versatil brauchbares Fundament aufgebaut wurde und die maßgeblich von meinen ehemaligen Kommilitonen Dr. Stefan Theis, Mark Berger, Andreas Rapp aus Wedel sowie Dr. Markus Durchardt und René Behrmann aus Paderborn und Benjamin Flick, Stefan Gent, Nikolaus Sigrist und Cornelius Maurer aus Caracas geprägt wurde. Einen heiteren Gruß möchte ich an Frau Dr. Judith Probst richten für die abwechslungsreichen Diskussionen in lockerer Atmosphäre zur ambivalenten Rollenambiguität.

Danken möchte ich auch meiner Familie, speziell meinen Eltern für durchgehend stärkende emotionale Unterstützung und meinem Onkel Wolf für die stets geduldige Bereitschaft mir die Grundlagen der Mathematik und der Physik näher zu bringen.

Abschließender Dank richtet sich an meine Frau Yvonne, die mir den Rücken über einen so langen Zeitraum freigehalten hat sowie an meine Mühlsteine, die mich auch in motivationsschwachen Zeiten unermüdlich mit Lebensenergie gestärkt haben.

Paderborn, 13.08.2018
Fiete H. Dubberke

Abstract / Zusammenfassung

In the first part of the present work the setup of a cascaded organic Rankine cycle (CORC) process is presented. Two organic Rankine cycles (ORC) are coupled as a cascade to reach a higher exergetic performance than conventional single ORC by reducing thermal dissipation losses. The test-rig was designed to offer a maximum of flexibility, operating the ORC with different working fluids over a wide range of temperature and pressure. Moreover, the test-rig may help to assess the performance and adaptability of individual components such as heat exchangers, pumps, condensers or turbines at low cost and little complexity. To evaluate potential working fluids accurate equations of state (EOS) are required, which are typically based on thermodynamic properties from experiments. The second part of this work discusses an apparatus for the speed of sound measurement based on the pulse-echo method. An advanced routine for determining the propagation time, applying signal enhancement and pulse design, is introduced and speed of sound measurement results for various fluids in a temperature and pressure range up to 500 K and 120 MPa are provided.

Im ersten Abschnitt dieser Arbeit wird der Aufbau eines kaskardierten organic Rankine cycle (CORC) Prozesses vorgestellt. Die zweistufige Kaskade kombiniert zwei organic Rankine cycles (ORC), von denen der zweite Kreislauf über einen Wärmeübertrager durch die Abwärme des ersten Kreislaufs angetrieben wird. Dadurch können thermische Verluste verringert und höhere exergetische Wirkungsgrade erreicht werden, als es bei herkömmlichen einstufigen ORC üblich ist. Der Fokus der Auslegung des Versuchsaufbaus liegt auf der Flexibilität beim Einsatz von potentiellen Arbeitsmedien für einen weiten Temperatur- und Druckbereich. Zudem soll das Design einen unkomplizierten Austausch sowie die technische Adaption verschiedener Komponenten, wie Wärmeübertrager, Pumpen, Kondensatoren und Turbine zulassen. Die Bewertung und Auswahl von potentiellen Arbeitsmedien kann mittels Zustandsgleichungen (EOS) erfolgen, die typischerweise auf der Basis experimenteller thermodynamischer Zustandsgrößen aufgestellt werden. Der zweite Teil dieser Arbeit beschreibt die Auslegung und den Aufbau einer Apparatur zur Messung der Schallgeschwindigkeit in Fluiden, deren Messprinzip auf der Puls-Echo-Methode aufbaut. In diesem Rahmen wird eine neue Routine zur Laufzeitbestimmung vorgestellt, die auf der digitalen Signalaufbereitung und einer verbesserten Pulsmodulation des Anregesignals des Emitters beruht. Zudem werden für verschiedene Fluide Ergebnisse aus Schallgeschwindigkeitsmessungen in einem Temperatur- und Druckbereich von bis zu 500 K und bis zu 120 MPa präsentiert.

Contents

1 Introduction

It is a fundamental fact that life depends on energy. In human history the rise and fall of societies always depended on the availability of energy, whether in form of nutrition or for technical applications. Energy demand continuously increased along with population size and the rising utilization of energy made population growth possible. Profound technical developments, beginning with the industrial revolution in England in the 18th century, boosted global primary energy needs to about 550 EJ per year in 2015 and are steadily increasing by about 1.9 % per year.[1] Along with mobility and heating, today the electrical supply is predominantly based on fossil-fired power plants using traditional steam cycles. Even though overall efficiencies of modern plants are brought nearly to the physical limitations, the urgent need to reduce carbon dioxide release into the atmosphere to alleviate climate change is one of the greatest challenges. Heat recovery systems, such as organic Rankine cycles (ORC), which represent a viable technical approach for the conversion of low temperature heat sources, can help for the efficient use of fossil fuels, utilizing waste heat from generators (CHP), industrial applications or renewable heat sources, such as from geothermal or solar reservoirs [1–3]. Performance improvements of ORC processes are based on the technological development of hardware and the selection of suitable working fluids, which is made on the basis of thermophysical properties and safety requirements, considering the characteristics of the heat source. Thus, efficiency increases for technically well advanced ORC plants require reliable and accurate thermophysical property data on working fluids.

One group of suitable ORC working fluids are the siloxanes, which belong to the wider class of organosilicone compounds. In particular, hexamethyldisiloxane (MM) appears to be a good candidate for becoming a widely used working fluid for high temperature processes. However, the current lack of accurate thermophysical property data of siloxanes may lead to sub-optimally designed cycles and processes. Information on the thermophysical behavior affects all aspects of the chemical and power engineering industry in traditional and nontraditional applications with respect to pure component as well as mixture properties [4]. Thermal properties in the homogeneous fluid region, together with the speed of sound and the vapor pressure, are used to develop accurate equations of state (EOS) that describe the entire range of fluid states. "Prop-

---

[1] Primary consumption and consumption growth over a ten year average up to 2015 according to the BP Statistical Review of World Energy, June 2016.

erly designed multi-parameter equations of state are able to represent thermodynamic properties of a certain substance within the accuracy of the most accurate experimental data" [5]. While dimensioning and constructing ORC plants, accurate speed of sound data are also directly relevant for the fluid expansion in turbo machines. Some types of turbines operate with supersonic expansion to transform the enthalpy of the compressed and superheated working fluid steam into kinetic energy before the turbine wheel. In applications of supersonic flow phenomena, like Laval nozzles, the mass flow rate is directly related to the speed of sound. Small errors in the knowledge of the speed of sound may decrease the performance of such turbo machines tremendously.

The present work is divided into two parts, the layout design and construction of a cascaded ORC (CORC) and an apparatus for determining the speed of sound. Conventional ORC may dissipate thermal energy at a high temperature level after expansion and during condensation. Coupling a second low temperature cycle to the first one may increase the utilization of the exergy and therefore increase the overall cycle efficiency. A big challenge is to determine the combination of working fluids according to their thermodynamic properties as well as their applicability to the hardware.

The apparatus for measuring the speed of sound is based on the pulse-echo technique and operates up to 150 MPa in the temperature range between 250 and 550 K [6]. It was designed in particular for the generation of data for potential ORC working fluids that were insufficiently studied. The most common measuring principle for determining the speed of sound of liquids is the pulse-echo technique, which was introduced by Kortbeek et al. [7] in 1985. Among others, this technique was used by Gedanitz et al. [8], Ye et al. [9], Wang and Nur [10], Zak et al. [11], Benedetto et al. [12] and Meier and Kabelac [13]. In this method, a burst of sound waves, emitted by an excited quartz crystal, propagates through the fluid over a known distance, is reflected and propagates back to the quartz crystal that also acts as a receiver for the echoes. This standard measurement procedure was further developed in the present work by burst design and signal enhancement for the determination of the propagation time, which not only optimizes the measurement accuracy, and thus the determination of the speed of sound, but also enlarges the measurement range for fluids in the supercritical region. In combination with numerical analysis, it may also simplify the measurement process [14].

2 Working fluids for organic Rankine cycles

(I) Heat sources for organic Rankine cycle applications

Water, being nearly a perfect working fluid in classic steam cycles, looses its benefits towards lower temperatures to other fluids, such as organic ones, due to its thermodynamic properties. Depending on the considered parameters, this turning point can be specified to a temperature level between 700 and 800 K[1]. Therefore, working processes powered by heat sources below that temperature should utilize other fluids. Since the temperature of the heat source is technically matched for steam cycles in conventional power plants, the temperature levels of waste heat or other natural reservoirs are diverse and often given. Natural heat sources may result from geothermal or solar thermal energy. The virtually inexhaustible geothermal heat energy potential can be found world wide and has an average temperature gradient of about 3.1 K / 100 m of depth into the earth's ground, in some areas even many times higher. The total installed capacity world wide reached about 10 GW_e in 2010 with an average annual growth rate of about 3 % since 1985. Even though the majority of the installed geothermal power plants is based on direct cycles, which means that sputtering water steam from a dwell is directly converted in an expansion device, so called binary power plants using separate organic working fluids are most widely installed today [15]. Also solar thermal energy offers a huge potential with a solar constant of about 1.3 kW per square meter [16] and a radiation of about 1 kW per square meter impacting earth's ground at sea level on average for Europe. However, due to ongoing exponential decline of photovoltaic cell production prices and the fact that modern large scale solar thermal power plants operate at very high temperatures of up to 1300 K and therefore use conventional water steam cycles, the ORC technology plays only a minor role for small scale purposes today.

Due to increasing energy prices and governmental requirements for conservation of energy world wide, waste heat as an energy source has become more attractive. Beside residual heat from industrial processes, other sources for waste heat may be power

---

[1] First International Seminar on ORC Power Systems, Delft 2011, lecture by Mario Gaia (TURBODEN): “30 Years of ORC development”

stations, micro gas turbines [17] and combined heat and power plants (CHP) operating on biogas. Along with the temperature level, the size of the steam based power plant can also be favorable for ORC technology. In case of high temperature heat sources, such as of biomass fired power plants [18] or vehicle engines [19], the use of water as a working fluid could be thermodynamically efficient, but not economically [20]. Components, such as expansion devices and heat exchangers, would have to cope with high volume flow rates and therefore a small plant design is not possible.

(II) ORC types

Since the difference between a classic Rankine cycle (RC) and an ORC is the working fluid, the basics types of construction and layout design are the same. In the following section, a brief overview of the fundamental ORC types is given. Fig. 2.1 shows the hydraulic flow diagram and the thermodynamic states in a temperature-entropy diagram for the most basic layout. The cycle consists out of a feed pump, an evaporator, an expansion device and a condenser (cf. Fig. 2.1 (left)). The four different corresponding thermodynamic states of the fluid, here for a sub- and a supercritical process with hexamethyldisiloxane (MM) as an exemplary dry fluid[1], are indicated in the diagram (cf. Fig. 2.1 (right)): pressurization by feed pump (1-2, 2'), subcritical isobaric heating (2, 2'-3'), evaporation and superheating (2-3') or supercritical isobaric heating (2-3), expansion in turbine (3-4) and isobaric condensation (4-1). Fig. 2.2

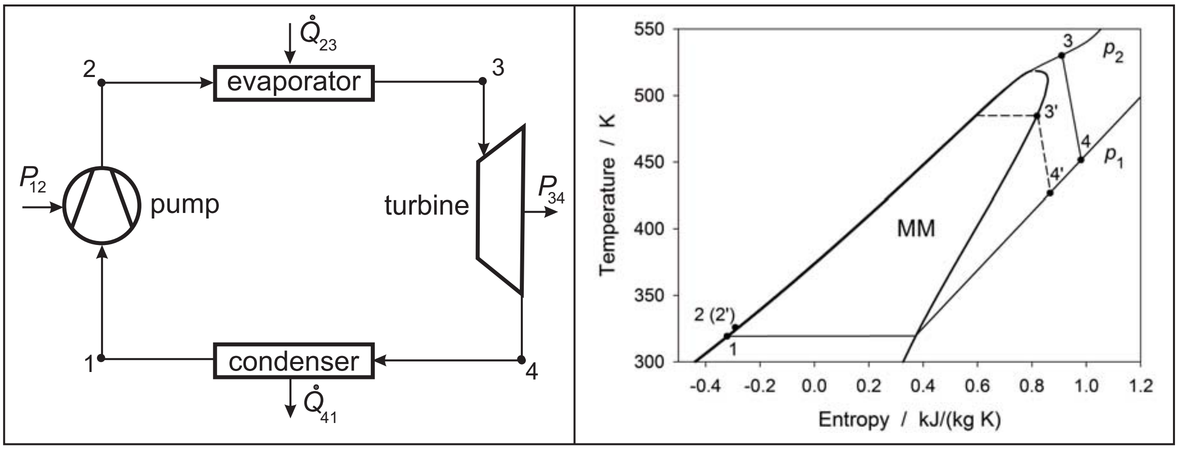

Figure 2.1: Classic Rankine cycle: (left) hydraulic flow diagram, (right) thermodynamic states for a sub- (– – –) and supercritical (——) operation mode with MM as an example for a typical dry fluid.

---

[1] The expression "dry fluid" refers to the positive slope of the saturated vapor line in the temperature-entropy diagram, cf. section (IV).

displays a cycle variation utilizing an internal heat exchanger (IHE) as a regenerator, which is a common ORC application recovering waste heat from exhaust gas with a high content of sulfur, such as a CHP fed by biogas and using a dry working fluid to reach a superheated vapor state after expansion. The IHE recuperates heat between state points 5 and 6 for the supercritical process, respectively 5' and 6 for the subcritical process and transfers it between state points 2, 2' and 3. Thereby, the exhaust gas is not cooled below the condensation point and the formation of aggressive sulfuric acid in the condenser is prevented. The use of an IHE leads to an increase of the thermal cycle efficiency η_{th} because the average temperature of the supplied heat is raised, but this does not lead to a higher power output. Supercritical Rankine cycles may have advantages to classic subcritical ones. The main thermodynamic advantage is the minimization of exergetic dissipation due to a high average temperature during the heat transfer along a supercritical isobar as depicted for MM in Fig. 2.7, cf. section (IV). Moreover, evaporation and superheating is avoided by supercritical process operation and leads, due to the more constant temperature difference minimizing the negative influence of pinch point effects during heat transfer, to smaller heat exchangers [21]. Various case studies of supercritical ORC have been described by several authors [22–24].

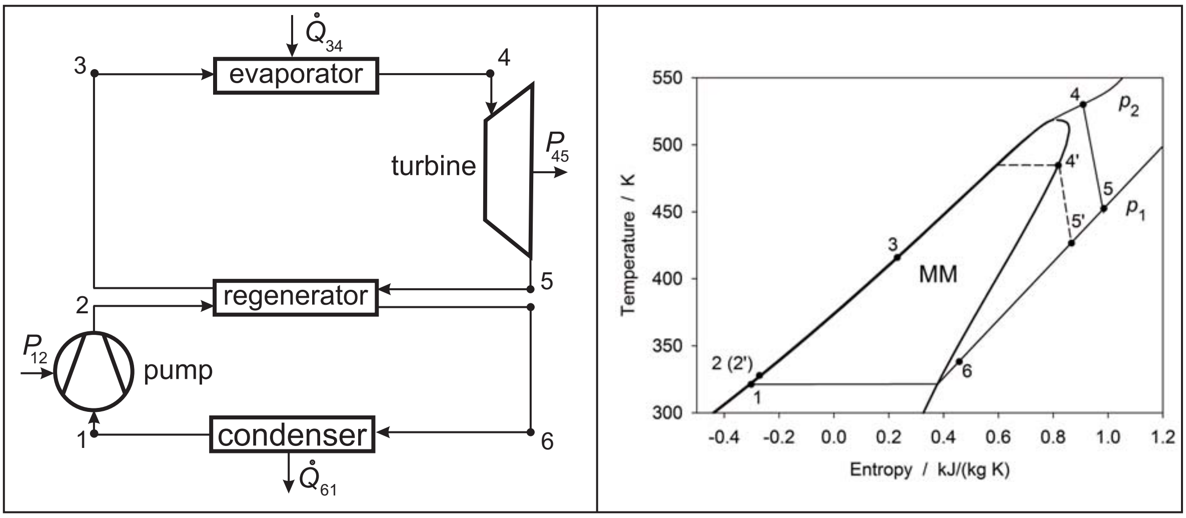

Figure 2.2: Classic Rankine cycle with regenerator: (left) hydraulic flow diagram, (right) thermodynamic states for a sub- (– – –) and supercritical (——) operation mode with MM as an example for a typical dry fluid.

Numerous technical variations or combinations of ORC can be applied to maximize the exploitation of a heat source. Common arrangements are the dual level and the two stage cycle. The dual level cycle is a serial connection of an ORC to a heat source [25], i.e. after transferring heat to drive cycle 1, residual heat of the heating source is transferred directly to cycle 2, cf. Fig. 2.3 (left). Two stage cycles combine two ORC, where the residual heat from the high temperature cycle is transferred to a low temperature cycle by an IHE (cf. Fig. 2.3 (right)), reaching an higher overall efficiency [26]. The challenge is to harmonize the design of the IHE as a link of both cycles in accordance with the fluid selection. This question is one of the topics of the present work and will be discussed later. Other developments of the ORC are the power flash cycles (PFC) which are a generalization of trilateral cycles (TLC). The compressed liquid is heated up to its boiling point and then a flash expansion through the two phase region is performed, ending either in the wet vapor region or in the dry region, cf. Fig. 2.4. Due to the significant improvement of temperature matching, and therefore the reduction of exergy losses during heat transfer, the efficiency of power utilization can be increased in comparison to conventional ORC, cf. Lai and Fischer [27], Ho et al. [28] and Löffler [29]. Löffler found that due to the exergetic advantages during heat transfer in the evaporator, TLC systems may have a significantly higher efficiency (between 50 and 100%) than conventional ORC, whereas Ho et al. [28] discussed the disadvantages due to irreversibilities of flash evaporation during expansion. Lai and Fischer [27] recommended water for high temperature and cyclopentane for low temperature heat sources as suitable working fluids, whereas Smith and da Silva [30] also suggested mixtures.

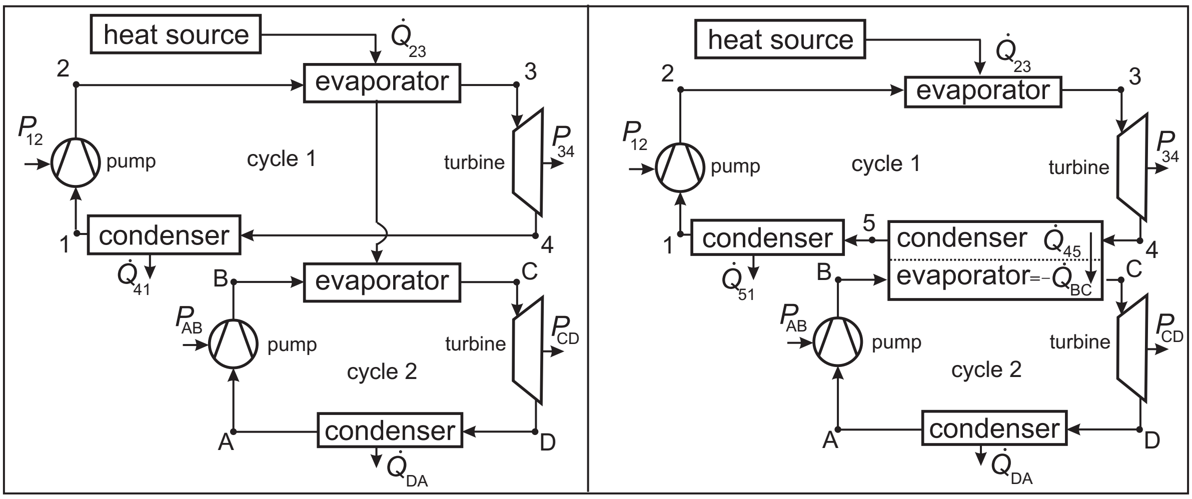

Figure 2.3: (left) Dual level cycle: residual heat after evaporation in cycle 1 is transferred directly to cycle 2. (right) Two staged ORC: cycles are coupled by an internal heat exchanger (IHE), the residual heat of cycle 1 is driving cycle 2.

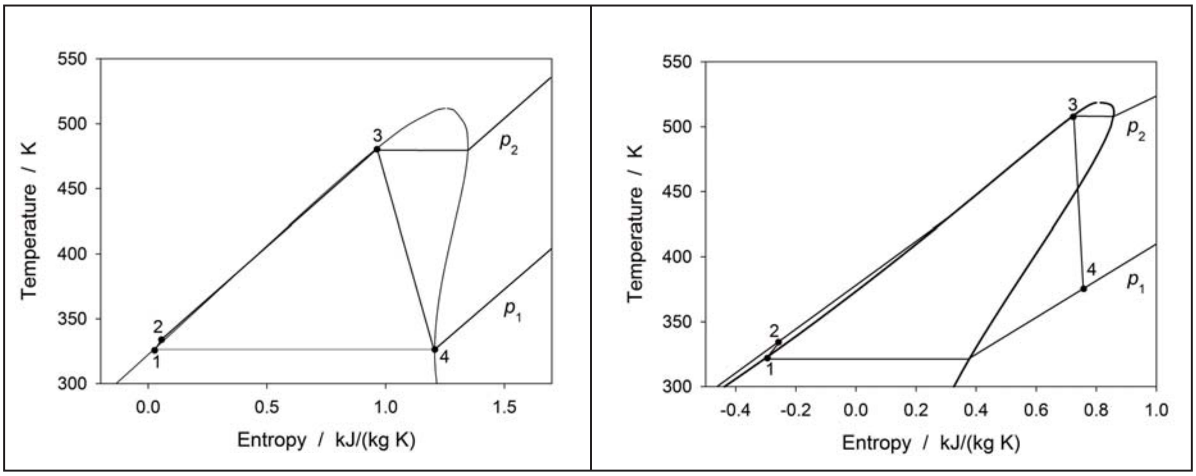

Figure 2.4: Power flash cycles (PFC) perform a flash expansion through the two phase region either to the saturated vapor region (left for cyclopentane) or to the superheated vapor region (right for MM).

In contrast to ORC processes, which are already successfully applied in several technical applications, PFC are still in a state of technical development, especially due to the technically challenging two-phase expander, which makes fluid selection even more crucial.

(III) Power cycle efficiencies and second law analysis

Various suggestions of efficiencies and benchmarks for evaluating cycle performance have been proposed. The energy flow $\dot{Q}$ from a heat source leads to a difference of the incoming and outgoing enthalpy flow $\Delta\dot{H}$ that can be expressed for an isobaric heat exchanger as

$$\dot{Q} = \Delta\dot{H} = \dot{H}_{\text{out}} - \dot{H}_{\text{in}} = \int_{T_{\text{out}}}^{T_{\text{in}}} T d\dot{S}, \tag{1}$$

with $\dot{S}$ as entropy flow. $\dot{Q}$ is thus the integral below the temperature profile of the heat source in the temperature-entropy diagram in Fig. 2.5 (left). The thermal efficiency

$$\eta = \frac{|-P|}{\dot{Q}}, \tag{2}$$

is the ratio of the effective power output $|-P|$ to the amount of driving heat flow $\dot{Q}$. Since $\dot{Q}$ consists out of exergy[1] ($\dot{E}$) flow and anergy flow ($\dot{A}$), where anergy is defined as the non-reversible heat below the ambient temperature level (depicted as a rectangle below T_{a} in Fig. 2.5 (left)), the thermal efficiency can reach, even for ideal reversible

---

[1] In 1956, Rant introduced the term exergy as the reversible energy in the context of heat [31].

heat cycles, at its maximum the Carnot factor $\eta_\mathrm{C} = (1 - T_\mathrm{a}/T) < 1$. This deviation to the unity does not only rate the efficiency of the heat cycle, but also the quality of the heat source [32].

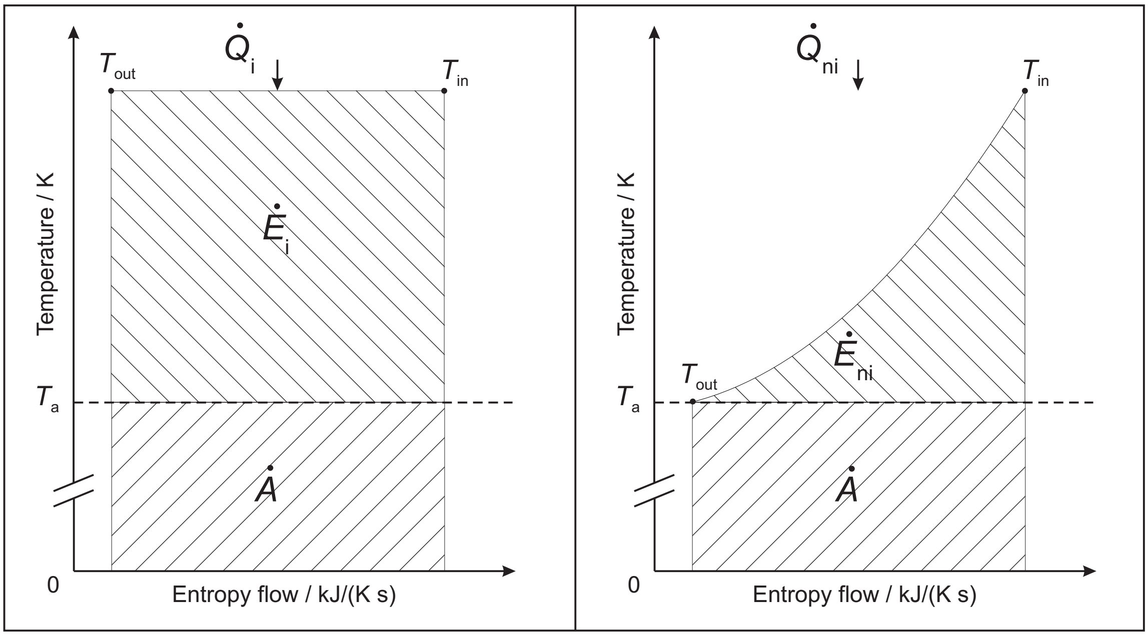

Figure 2.5: Isothermal $\dot{Q}_\mathrm{i}$ (left) and non-isothermal $\dot{Q}_\mathrm{ni}$ (right) heat flow, separated into exergy $\dot{E}$ and anergy flow $\dot{A}$ according to the ambient temperature T_a in the temperature-entropy diagram.

The exergy flow $\dot{E}$ is the heat flow content of $\dot{Q}$ related to the Carnot efficiency η_C according to

$$\dot{E}_i = \eta_\mathrm{C} \cdot \dot{Q} = (1 - \frac{T_\mathrm{a}}{T_\mathrm{in}}) \cdot \dot{Q}. \tag{3}$$

Because only the exergy of a heat source can be converted into mechanical power, a more stringent evaluation of the cycle efficiency is done by the exergetic efficiency

$$\xi = \frac{|-P|}{\dot{E}_\mathrm{r}}, \tag{4}$$

with $\dot{E}_\mathrm{r}$ as exergy flow which is received from the cycle between state points 2 to 3 and for which the maximum value $\xi = 1$ is reached for an ideal reversible heat cycle.
Both efficiency types focus on the heat cycle performance regarding the received heat, but do not evaluate the utilization of a given heat source supply. Since the general

focus is on the efficient use of energy sources, a reasonable comparison of heat cycles has to link cycle performance to the related properties of the given heat source. With an explicit description of the heat source, the result would be easily interpretable because the ORC type generating the maximum power output, based on the same exergy contribution to $\dot{Q}_{in}$, would be preferable.

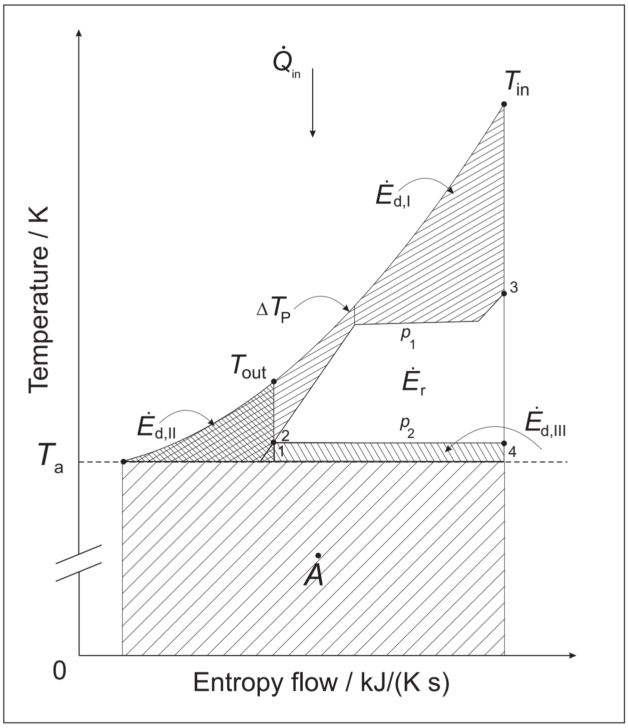

Figure 2.6: Exergy flow reception and dissipation of a heat cycle limited by the pinch point ΔT_p for a non-isothermal heat source in a temperature-entropy diagram.

The simple Carnot approach is valid for isothermal heat sources, which practically do not exist. For a non-isothermal heat source $\dot{Q}_{\mathrm{ni}}$ the integral is valid in the limits of T_{in} and T_{out}, where T_{out} converges to the ambient temperature T_{a}, cf. Fig. 2.5 (right), and therefore

$$\dot{E}_{\mathrm{ni}} = \dot{Q}_{\mathrm{ni}} - T_a \cdot \Delta\dot{S} = \int_{T_{\mathrm{a}}}^{T_{\mathrm{in}}} T d\dot{S} - T_a \cdot \Delta\dot{S}, \qquad (5)$$

cf. Bošnjaković [33]. Setting the outgoing temperature $T_{\mathrm{out}} = T_a$ is crucial for considering the full amount of the exergy flow $\dot{E}_{\mathrm{ni}}$ of a non-isothermal heat source and therefore the exergetic efficiency is

$$\xi' = \frac{|-P|}{\dot{E}_{\mathrm{ni}}}. \tag{6}$$

Since the cycle cannot absorb the full amount of $\dot{E}_{\mathrm{ni}}$ supplied by $\dot{Q}_{\mathrm{ni}}$, the difference between $\dot{E}_{\mathrm{r}}$, the received exergy by the cycle, and $\dot{E}_{\mathrm{ni}}$ is due to the exergy losses

$$\dot{E}_{\mathrm{r}} = \dot{E}_{\mathrm{ni}} - \dot{E}_{\mathrm{d,I}} - \dot{E}_{\mathrm{d,II}} - \dot{E}_{\mathrm{d,III}}. \tag{7}$$

The three latter contributions result from dissipation during heat transfer for preheating, evaporation and superheating ($\dot{E}_{\mathrm{d,I}}$: state points 2 to 3) and as well as from condensation ($\dot{E}_{\mathrm{d,III}}$: state points 4 to 1). In addition to the temperature difference ΔT as the driving force, a variety of process parameters influences dissipation during heat transfer, cf. Bejan [34].

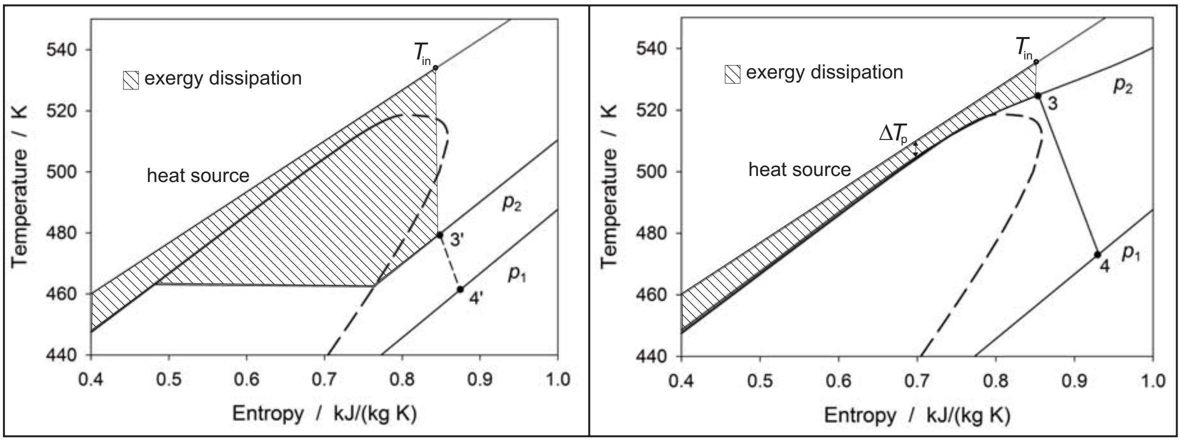

Figure 2.7: Examples for the exergy loss during heat transfer for a sub- (left) and a supercritical organic Rankine cycle (right) with the same ΔT_{P} and the same heat source based on MM as working fluid. (right) The supercritical cycle is advantageous because the temperature profiles of heat source and working fluid match.

The exergy loss $\dot{E}_{\mathrm{d,II}}$ is due to the fact that the heat source is just cooled down to the temperature T_{out} because heat transfer into the cycle starts at state point 2 and therefore the residual exergy from state point T_{out} to the ambient temperature T_{a} is not utilized, cf. Fig. 2.6. Such a thermodynamic evaluation is also known as second law analysis [15].

Fig. 2.6 depicts a close-up of a potential ORC and its thermodynamic states for a given exergetic supply from a non-isothermal heat source in a temperature-entropy diagram. The heat transfer is limited by the minimum temperature difference ΔT_{P} between the isobar p_2 of the working fluid and the temperature profile of the heat source. The so-called pinch point temperature ΔT_{P} is due to technical and economical reasons and limited by the size of the heat exchanger surface.

Fig. 2.7 shows an example for the exergetic dissipation during heat transfer for a sub- and a supercritical cycle. Since the average temperature difference, which is almost constant in case of the heat transfer into a supercritical cycle, is smaller than in case of an subcritical one. It matches better with the temperature profile of the heat source and therefore exergetic dissipation is smaller [22]. The ability for the exploitation of a heat source is always related to ΔT_{P}, however, for subcritical processes the isobar proceeds horizontally in the temperature-entropy diagram during evaporation and increases the average ΔT.

(IV) Classification of working fluids

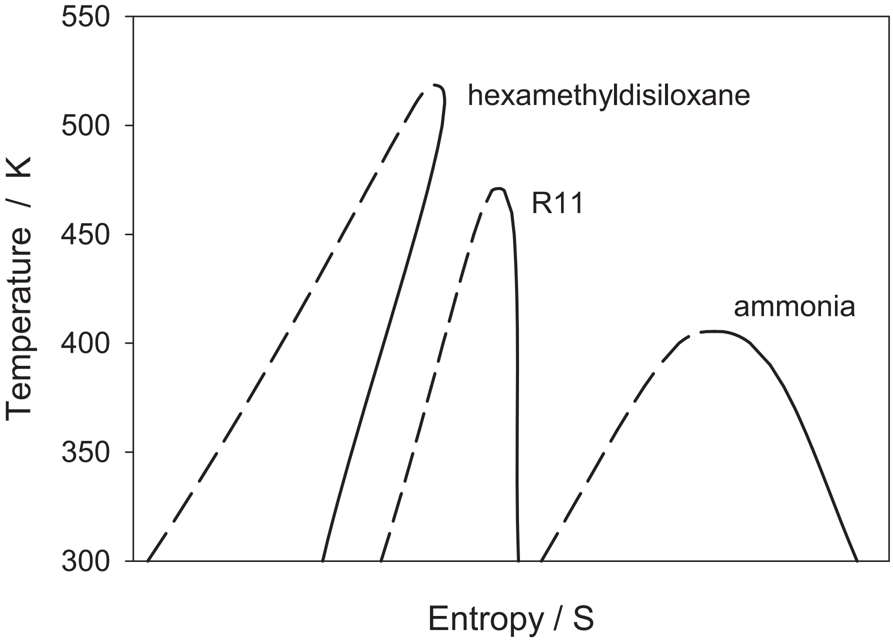

Figure 2.8: Example for the classification of working fluids according to the slope of the saturated vapor line in the temperature-entropy diagram: dry (hexamethyldisiloxane), isentropic (R11) and wet (ammonia); saturated liquid line (– – –), saturated vapor line (——).

The fluid classification according to the thermodynamic properties can be carried out according to the slope dT/ds of the saturated vapor line, which affects applicability of fluids to the thermodynamic design, the constructional layout and thus cycle efficiency.

Fig. 2.8 depicts three classical fluids as examples, whereas dry fluids show a positive slope, isentropic ones have an almost infinite slope and wet fluids a negative slope of the saturated vapor line.

Unlike wet fluids, such as water or ammonia, dry and isentropic fluids are common types for ORC applications for several reasons [35, 36]. The negative slope of a wet fluid, which is due to the large vaporization enthalpy (typically because strong hydrogen bonding among molecules), would lead to a high liquid fraction in the steam, entering the two phase region during an isentropic expansion, which leads to damages in the expansion device due to condensated droplets. Therefore, in most cases the use of wet fluids requires superheating [37]. Further subclassification leads to two groups of working fluids according to their thermal applicability for low and high temperature heat sources, whereas the transition temperature is about 500 K. Approximately above 650 K advantages of organic fluids in comparison to water vanish. The critical temperature of fluids for low temperature applications usually does not exceed $T_{\mathrm{c}} = 300$ K. Extensive studies for low temperature fluid selection were done by Saleh et al. [38] or Chen et al. [3] and for refrigerants by Borsukiewicz-Gozdur and Nowak [39]. Lai et al. [40] found for high temperature applications a maximum critical temperature of the working fluid of $T_{\mathrm{c}} = 500$ K and stated that cyclopentane is optimal for a variety of process parameters.

(V) Siloxanes

With an assumed annual worldwide production of several million tons, siloxanes are used in a wide range of applications, like in the textile and electrical industry, as an agrochemical, in industrial and household cleaning and also in personal care products [41]. They belong to the wider class of organosilicon compounds and are composed out of an alternating (linear or cyclic) backbone chain of silicon and oxygen atoms and two or tree methyl groups bound to the silicon atoms, according to their chemical bonding potential. With the shortest chain (Si-O-Si) for the linear siloxanes, hexamethyldisiloxane (MM) consists out of two M-units ($(CH_3)_3SiO_{0.5}$), whereas chain extension leading to other compounds consequently contains an additional D-unit ($(CH_3)_3SiO$). This is indicated in the nomenclature to the relation to the number of Si-O bonds, as octamethyltrisiloxane (MDM), decamethyltetrasiloxane (MD_2M) and dodecamethylpentasiloxane (MD_3M). Cyclic siloxanes consists only out of D-units. Fig. 2.9 (left) depicts four linear (MM, MDM, MD_2M, MD_3M) and three cyclic siloxanes (D_4, D_5, D_6) in a temperature-entropy diagram, whereas for both cases the critical temperature increases along with the number of units per molecule, starting for MM as linear and D_2 as a cyclic siloxane with critical temperatures of T_c = 518.75 K and T_c = 586.5 K, respectively. Siloxanes were recommended as working fluids for high

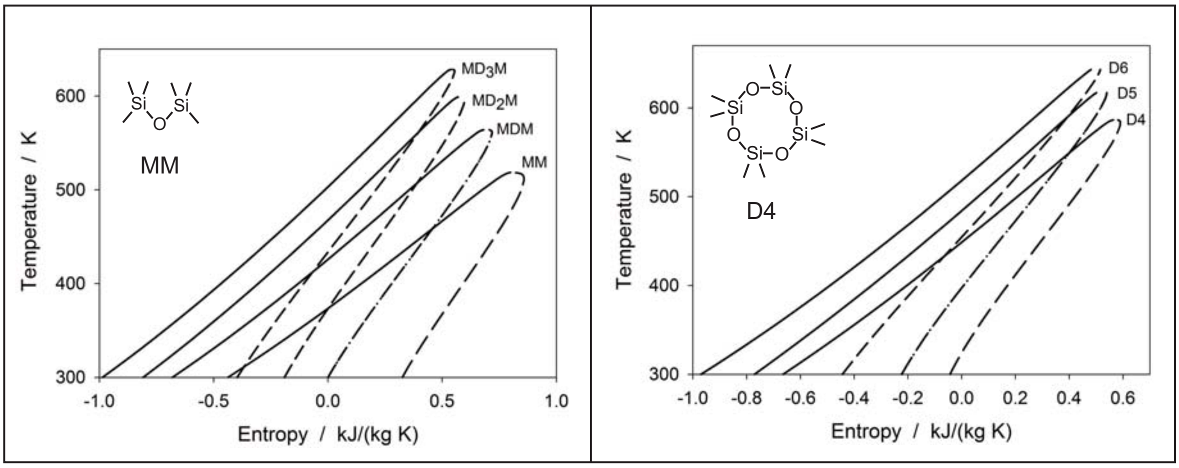

Figure 2.9: (Left) Linear siloxanes: hexamethyldisiloxane (MM), octamethyltrisiloxane (MDM), decamethyltetrasiloxane (MD_2M), dodecamethylpentasiloxane (MD_3M); (right) cyclic siloxanes: octamethylcyclotetrasiloxane (D_4), decamethylcyclopentasiloxane (D_5), dodecamethylcyclohexasiloxane (D_6); saturation lines for liquid (– – –) and vapor (——), according to the EOS by Thol et al. [42, 43] and Colonna et al. [44, 45]

temperature applications due to their thermodynamic, safety and environmental properties for pure fluids by Uusitalo et al. [46] and for mixtures by Kaczmarek et al. [47]. Due to their pronounced dry fluid behavior, cycle applications using siloxanes as working fluids are usually equipped with an internal regenerator for thermal efficiency enhancement. Several EOS where published based on experimental data (cf. Colonna et al. and Nannana et al. [44, 48]), on hybrid data sets from experiment and molecular modeling and simulation (cf. Thol et al. [42, 43]) and the PC-SAFT model (cf. Lai et al. [49]).

(VI) Thermal stability and environmental safety

To achieve a long time maintenance-free operation along with low maintenance costs, the working fluid and the material of the components, which are in continuous contact, should be compatible. Therefore, the working fluid should be non-corrosive and maintain its chemical and thermal stability at the highest operation temperature, besides being non-flammable and non-toxic to keep costs for essential safeguarding down. Furthermore, the fact that a change in the thermophysical properties of a fluid may affect the overall power cycle efficiency, exceeding the fluids thermal stability temperature might decompose to corrosive or toxic agents that jeopardize process operation and reduce equipment availability. Investigations for MM were performed by Preißinger and Brüggemann [50], who identified a temperature of 573 K with annual degradation rates of less than 3.5%. In the course of this work the working fluid SES 36, a potential candidate for low temperature ORC applications, a refrigerant mixture of 1,1,1,3,3-pentafluorobutane (R365mfc) and perfluoropolyether [51], was cracked at a temperature of 473 K within less than 20 hours, while performing speed of sound measurements, causing a severe reaction with the stainless steel measuring cell, cf. chapter 5.1.

Siloxanes show no or only weak toxicity to aquatic organisms [41] and up to now, investigations do not indicate significant atmospheric effects, such as Global Warming Potential (GWP) of anthropogenic silicon [52]. Because they have no Ozone Depletion Potential (ODP) and a low flammability, siloxanes appear to be preferable working fluids according to technical manageability and governmental regulations.

(VII) Cascaded organic Rankine cycle test-rig

In the context of this work, a test-rig was designed and assembled which couples two ORC as a cascade. Subsequently, the intention was to identify combinations of working fluids that exploit a maximum of the incoming exergy from a waste heat source and therefore determine the maximum achievable utilization efficiency. Fig. 2.10 shows the hydraulic scheme of the cascaded ORC process (CORC) and the heat exchanger as their connection, transferring heat from the high temperature cycle to the low temperature cycle, with the aim to reach a higher exergetic performance than conventional single

ORC by reducing thermal dissipation losses. Due to safety reasons the CORC was

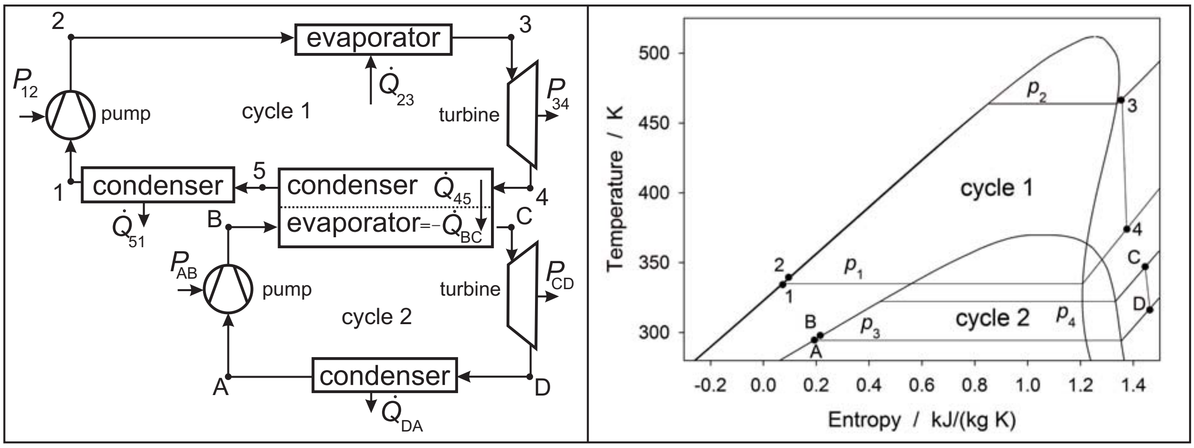

Figure 2.10: (Left) Cascaded organic Rankine cycle design in a hydraulic flow diagram which displays the coupling between cycle 1 (C1) and cycle 2 (C2) via a heat exchanger. (Right) Potential thermodynamic states of C1 for cyclopentane and C2 for propane as working fluids depicted in temperature-entropy-Diagram.

placed outside the laboratory in a separate container. Both the high temperature cycle (C1) and low temperature cycle (C2) were designed according to AD 2000-Regelwerk B7 (C1 / C2 in PN 100 / PN 60). All flanges were sealed with meshed metal (chrome-nickel-molybdenum alloy, Material-NR: 1.4404) strengthened graphite gaskets novaphit SSTCTA-L, provided by Frenzelit [53], limiting the leakage rate to a tolerable amount according to a pressure test.

The heating cycle is driven by a pump (Allweiler NTWH 25 200/01; 0.3 kW) which is capable of feeding a mass rate of up to 450 g/s of therminol 66 [54] and is heated by four 50 kW electrical heating rods (HR) which can variably be adjusted from 0-200 kW up to a temperature of 550 K. The overall waste heat is dissipated via an air-cooled heat exchanger outside of the container by a cooling cycle, which is connected by plate heat exchangers (GEA WTT PL 150) to cycles C1 and C2, that works on the basis of an ethylene-glycol/water mixture (1 : 1.125) and a pump (Grundfos TP 50-120/2) with a volume flow rate of about 17.6 m^3/h. To ensure that the maximum working temperature of the pressure sensors (6.4 MPa) does not exceed 353 K, a flexible metal tube was used as an extension which was sealed with a copper gasket to the piping system. Progressive cavity pumps (type Netzsch Nemo® NM031SY12S72B) were applied in both cycles which work with a helical rotor rotating inside a helical stator. The emerging cavities between rotor and stator move along the axis and transport the fluid. These cavities do not change their size and are sealed among each other by

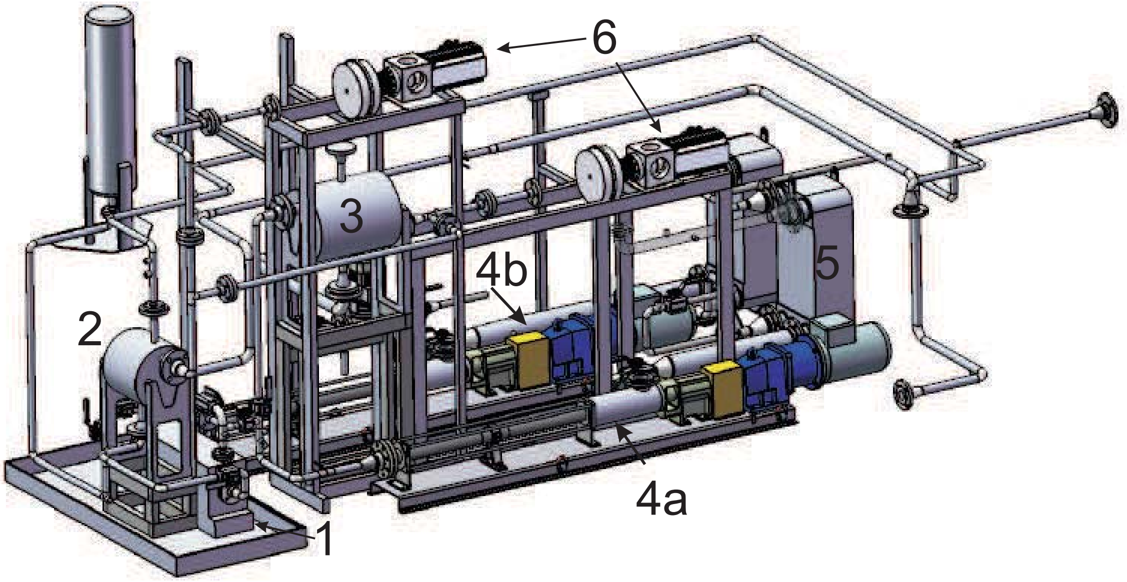

Figure 2.11: CORC construction layout: 1. pump of heating cycle; 2. heat exchanger of C1; 3. heat exchanger of C2; 4.(a,b) feed pumps of C1 and C2; 5. condensers C1 and C2 and 6. expansion devices of C1 and C2.

rotor and stator. This layout depends on the material properties of the stator and the operation temperature. Incompatibility of material resistance and working fluid may lead to swelling of the stator so that the resistance between stator and rotor increases and the operation stagnates. Therefore, before changing the working fluid, a swelling tests of mass and volume increments are obligatory.

The mass flow rate $\dot{m}$ measurement is based on a differential pressure aperture according to DIN EN ISO 5167, whereas for lower pressures up to approximately 0.5 MPa, $\dot{m}$ correlates to the revolution speed of the pump due to the constant volume and the low flow back of the cavities. Pumps and generators are controlled by a variable frequency drive (VFD).

For both cycles (C1 and C2) plate heat exchangers (PHE) were applied, operating up to a maximum pressure of nearly 6 MPa at temperatures of up to 550 K. In C1, an additional demister was installed between the PHE and the inlet of the turbine to remove potential fluid droplets. For testing reasons a variable nozzle was installed for C2, allowing an operation for diverse mass flow rates $\dot{m}$.

The design of the CORC turbine was based on an axial centrifugal pump that expands the superheated vapor through its curved Laval nozzles that were embedded in a blade wheel (1.4305 / X8CrNiS) outwards to the radial expansion tube in the turbine casing (1.4006+QT / X12Cr13). Due to the impulse principle, the torque was mainly generated by the acceleration of the high velocity flow in the blades. The connection between turbine and generator, which was a six pole synchronous servomotor working at 50 Hz (type SK-190-1-30-560 T1), was done by a non-contacting magnetic coupling. To minimize gap losses in the CORC turbine, the gap was designed as a labyrinth seal with 12 steps and a width of 0.25 mm and an additional rotary shaft seal. Two angular ball bearings in o-arrangement and one deep groove ball bearing form the fixed bearing at the turbine side which lead to a minimum slackness of the blade wheel. For cooling and lubrication of the ball bearings, the casing was flodded with hydraulic oil (Mobil DTE 10 EXCEL 15). The focus of this turbine lied on its applicability for testing very different working fluids over a wide range of thermodynamic conditions and therefore mechanical efficiency was subordinate.

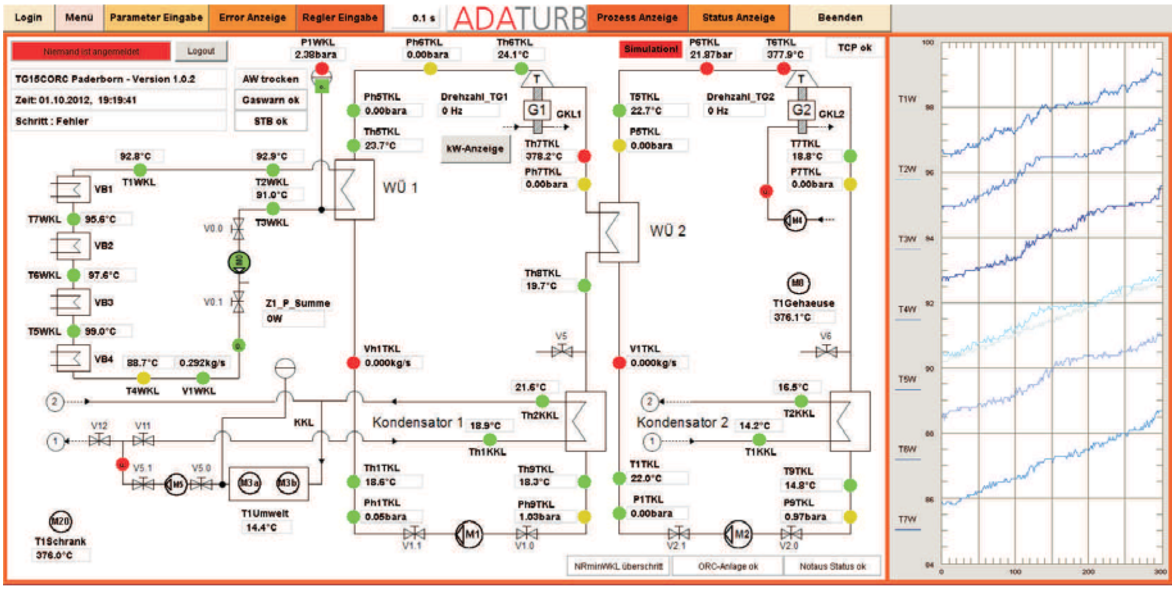

TG15CORC Paderborn - Version 1.0.2
Zeit: 01.10.2012, 19:19:41
Schritt : Fehler

Figure 2.12: CORC master display visualizing the hydraulic schematic and the main components of the HC, the HT and LT cycles as well as the CC with their essential operation parameters, such as temperatures and pressures. It enabled for an operation of the actors and allowed to set different thermodynamic states within the cycles.

The CORC software framework is based on two systems: the graphical user interface (GUI), which was programmed in Agilent VEE and a C program which provided functions for the GUI to access the programmable logic controller (PLC). The PLC works for digital in- and output (DI/DO) and analog in- and output (AI/AO) which expect either a voltage from 0 to 10 V, a current from 4 - 20 mA or a resistance, such as given by temperature (Pt1000) and pressure sensors. AO connectors were used for setting the motor speed of the pumps by sending a signal from 0 to 10 V to the device. The DI can only detect an activated (24 V) or deactivated current (0 V) and were used for receiving error status from the devices. With the DO variable frequency drives or non-controllable actors are switched on or off by sending a current to the device or their dedicated contactor. All these in- and output data were monitored or accessed via the GUI. The alternative to a PLC is a hard-wired programmed logic controller (HPC), which was used for important security functions.

For start up and testing reasons of the CORC and its components cyclopentane (about 30 kg) was used in C1 and propane (about 20 kg) for C2.

3 Thermodynamic properties from speed of sound measurements

Thermodynamic properties of fluids play an important role in many chemical and industrial applications. Information can be taken directly from databases, such as DDB [55] or DIPPR [56], or can be derived from equations of state (EOS) by computer programs, such as REFPROP [57]. Nowadays, modern industrial processes require a fast and accurate access to thermodynamic properties which can be provided by EOS and which therefore progressively play an important role. With an EOS, thermodynamic properties, such as temperature, pressure, speed of sound, volume, entropy or internal energy, are mathematically related and describe the state of matter under a given set of physical conditions. They are useful in describing the properties of fluids over a wide range of states [5]. As a fully fledged thermodynamic property, precise experimental speed of sound data are crucial for developing EOS [58].

(I) Measuring method

The most common measuring principle for determining the speed of sound of liquids is the pulse-echo technique, which was introduced by Kortbeek et al. [7] and nearly simultaneously by Muringer et al. [59] in 1985. In this method, a burst of sound waves, emitted by an excited quartz crystal, propagates through the fluid over a known distance, is reflected and propagates back to the quartz crystal that also acts as a receiver for the echoes, cf. Fig. 3.1. The speed of sound, neglecting dispersion and diffraction effects, is given by the following ratio of propagation distance and time

$$c = \frac{2(l_2 - l_1)}{\Delta t} = \frac{\Delta l}{\Delta t}. \tag{1}$$

In recent years, further modifications of this method have been made, whereas the construction of the measuring cell, such as quartz crystal and the proportion of propagation lengths and cell diameter as well as thermostat, stayed basically the same. Important technical upgrades took place for the method to determine the propagation time of the wave burst, where generally two approaches are applied: a) The propagation time of a single wave burst is determined directly [60]. b) The propagation time is determined through cancelation by interference, which takes place at the quartz crystal after emis-

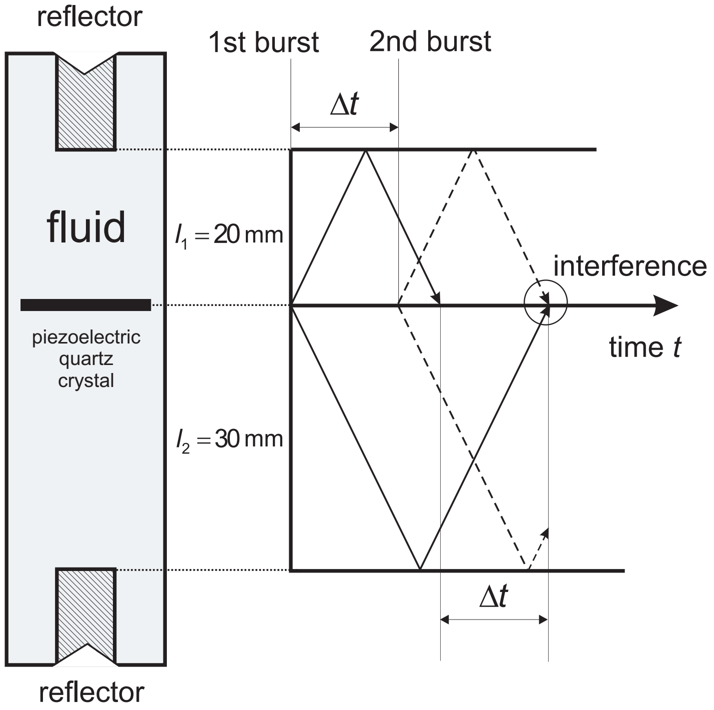

Figure 3.1: Principle of the pulse-echo technique for the single wave approach (Δt is the time difference between the received echoes of the wave burst) and interference approach (Δt is the time difference between first and second wave burst which cancel out at the quartz due to total interference).

sion and reflection of a second wave burst [58, 61]. Usually, interference of the echoes is achieved manually by visualizing the resulting wave signals by means of an oscilloscope [62]. Both approaches heavily depend on the oscilloscope's sampling resolution of the received wave signals, which limits the accuracy of the time measurement. To increase this accuracy, Ball and Trusler [60] introduced in 2001 a signal analysis that is based on a cross-correlation of the two echoes, which was optimized by a parabolic fit. Another numerical route for signal enhancement is to apply a Fast Fourier Transformation (FFT) based digital filter to the reflected wave signal. FFT filtering increases the signal-to-noise ratio and reduces offset effects due to hardware and other unwanted side effects [63]. FFT filtering not only enhances the accuracy of the propagation time measurement, and thus the determination of the speed of sound, in combination with numerical analysis it may also simplify the measurement process. One achievement of the present work was the significant improvement of the signal sampling by applying a combination of burst design and signal processing such that a wider range of thermodynamic states can be investigated. Moreover, the actual measurement process of the propagation time was completely (digitally) automated and takes thus less time. Applying a Fourier transformation based digital filter on acoustic wave signals increases their signal-to-noise ratio and enhances their time and amplitude resolutions, improving the overall measurement accuracy. In addition, burst design leads to technical advantages for determining the propagation time due to the associated conditioning of the echo, cf. Dubberke et al. [14]. Further details of the pulse-echo method and the construction of the apparatus used in this work are discussed in the following.

(II) Apparatus design

The pulse-echo technique, as a suitable method for speed of sound measurements in liquids and liquid-like fluids, determines the speed of sound directly by the ratio of the known propagation distance and propagation time. In the present work, a classical double path length type sensor with the identical dimension of the acoustic sensor as in Ref. [61] was applied, which allows speed of sound measurements up to about 2500 m/s. The use of such a double path sensor has significant advantages over other possibilities, as described by Meier [58]. Both signals take the same way through the circuitry and the mechanical branch of the system, except for the difference between the reflectors and the crystal. The distortion and delay times in electronic devices and cables cancel each other out due to parity in both signals which simplifies the measurement to a great extent. Similar acoustic cells were used by several other authors [58, 60, 63]. The applied propagation time measurement was based on the direct time measurement, which was also used by Ball and Trusler [60], in this work extended by signal processing and burst design, cf. Dubberke et al. [14]. A wave burst emitted by a quartz crystal in two directions propagates along $l_1 = 20$ mm and $l_2 = 30$ mm, both are reflected and propagate back to the quartz crystal, which acts now as a receiver. The propagation time difference Δt is that between the echoes arriving at the crystal due to the different propagation lengths, cf. Fig. 3.2.

The components of the measurement cell were made of stainless steel 1.4571 and were subjected to a heat treatment to remove self-stress from the manufacturing process. The piezoelectric quartz crystal was the main piece and was positioned between two polished reflectors, cf. Fig. 3.3. Both rear faces of the reflectors contained a conical cavity. Its advantage is that the part of the absorbed sound wave which would be reflected on the rear side of the reflectors does not return back to the quartz crystal, but is dissipated into other directions. Thus, the received signal is not affected by unintentional reflections. Other impairments of the speed of sound measurement can appear by reflections from the cavity walls. In order to avoid these, the diameter of the cavity wall was significantly larger than that of the quartz crystal.

A x-cut crystal quartz was taken as a transducer which operated at a resonance frequency of 8 MHz. It was shaped as a circular disk with a diameter of 15 mm, having gold coated electrodes on both sides which measured 10 mm in diameter. Two clamps

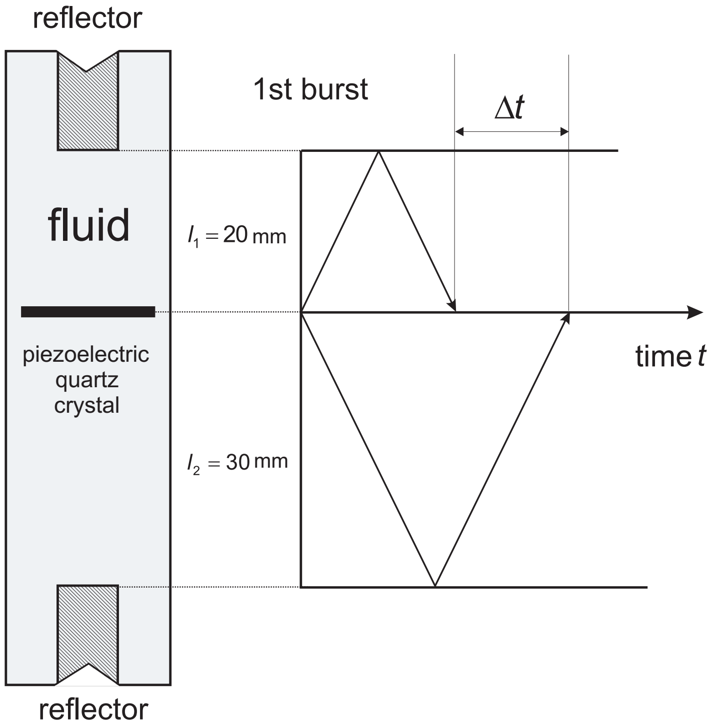

Figure 3.2: Principle of the pulse-echo technique for the single wave approach where the propagation time difference Δt is the time difference between the received echoes of the first wave burst.

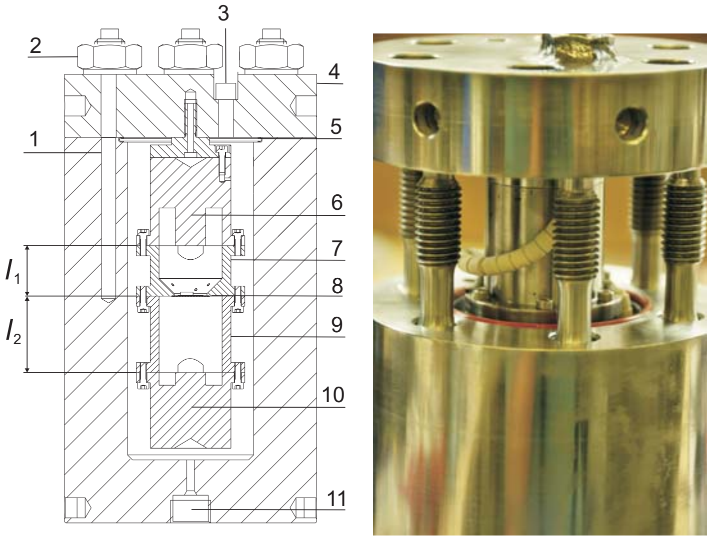

Figure 3.3: Measuring cell in the pressure vessel: (left) 1. thermometer seating, 2. fastening nuts, 3. safety outlet, 4. cell closure, 5. sealing ring, 6. reflector top, 7. path length l_1, 8. quartz, 9. path length l_2, 10. reflector bottom, 11. liquid sample inlet and outlet. (right) dissembled measuring cell.

were connecting the electrodes (cf. Fig. 3.4), one to ground potential and the other one through a teflon coated wire to the control unit outside of the pressure vessel.

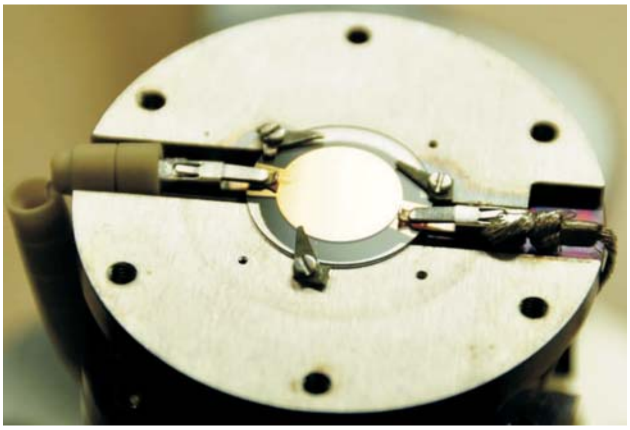

Figure 3.4: X-cut piezoelectric quartz crystal of 8 MHz with gold electrodes on both sides mounted to the measuring cell with three clamps. The connection clamps were surrounded by ceramic interlocking insulation beads to avoid a short circuit.

Fig. 3.5 shows the setup of the apparatus. In the center of the apparatus was the cell with the quartz crystal mounted in the pressure vessel. The pressure vessel had a cylindrical shape with an internal diameter of 50 mm and a wall thickness of 25 mm. It was made of highly tensile steel of type 1.4462 and locked by eight bolts M12. The sealing was done by a copper seal, supported by a rib profile which was milled into the surface of the sealing settings of the tap and the pressure cylinder. (Note that dry ammonia with a water content of less than 400 ppm does not react with copper [64].) The pressure vessel itself was girded and fixed by a copper jacket to yield a uniform temperature distribution. This copper jacket was surrounded by two larger copper shieldings, each equipped with a heating unit of 150 W electrical power for thermostating. Four layers of aluminum foil around the outer copper shielding reduced heat loss due to thermal radiation. Finally, the whole device was placed into a vacuum tank to reduce heat loss due to convection. Above the outer copper shielding, an aluminum plate was mounted to shield the cables and the electronic devices outside of the vacuum tank from thermal stress. The entire apparatus was mounted below an aluminum plate that was attached to the base frame of the test rig. The hanging construction was advantageous because of the good accessibility of the cell in case of maintenance, cf. Fig. 3.6. Heat loss through thermal conduction was minimized by contacting the acoustic sensor with the environment only by three distance holders

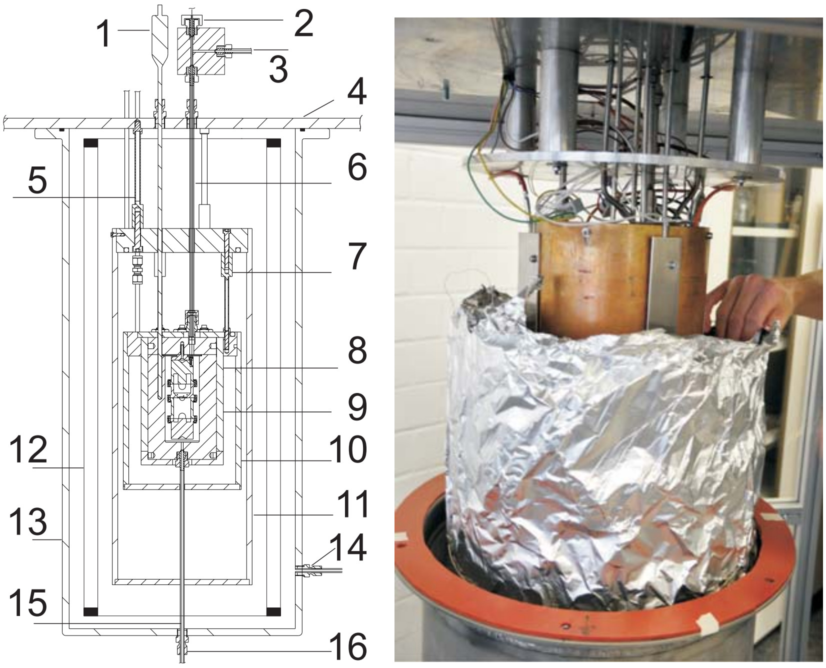

Figure 3.5: Setup of the apparatus: 1. PT-100 thermometer, 2. electrical feed through, 3. safety outlet / burst disc, 4. base plate, 5. distance holder, 6. safety outlet / cable passage, 7. distance holder, 8. pressure vessel, 9. inner copper shielding, 10. central copper shielding, 11. outer copper shielding, 12. aluminum foils, 13. vacuum tank, 14. vacuum tank outlet, 15. liquid sample inlet and outlet, 16. vacuum sealing.

Figure 3.6: (Left) Thermostat consisting of two copper shieldings, each including taps and three distance holders. (Center) Pressure vessel with copper jacket. (Right) Mounted pressure vessel in copper shielding with distance holders and tap for second distance copper shielding.

of stainless steel that were attached to the central copper shielding, which was again contacted to the base plate by three other distance holders. The vacuum tank was about 420 mm in diameter and 1100 mm in height and was sealed with rubber. It had an inlet / outlet at the bottom for liquid samples, leading straight to the measuring cell, and another opening on the side for a connection to a vacuum pump. Three additional openings were at the retaining plate for the safety outlet, for the thermometers as well as an electrical feed trough for the cables of the heating elements.

One of the neuralgic parts was the electrical feed through, which routes the electrical signal between the function generator and the quartz crystal, while withstanding high temperature and pressure in the vessel. It is based on a glass insulated wire contact surrounded by aluminum (cf. Fig. 3.7 (a)) which was also used by Wegge et al. [65]. The electrical feed through was placed at the end of the inlet above the acoustic sensor outside of the heated area of the apparatus (cf. Fig. 3.5 left (2)). Although the temperature resistant advantage of the feed through was not utilized, it proved high and stable pressure resistance and the possibility of a simple joint by soldering the connection to a teflon coated cable. The cable was led through the inlet above the acoustic sensor, which ends at a three-way valve (cf. Fig. 3.7 (right)). The valve separated the gas sample inlet and the electrical feed through. The teflon-coated cable

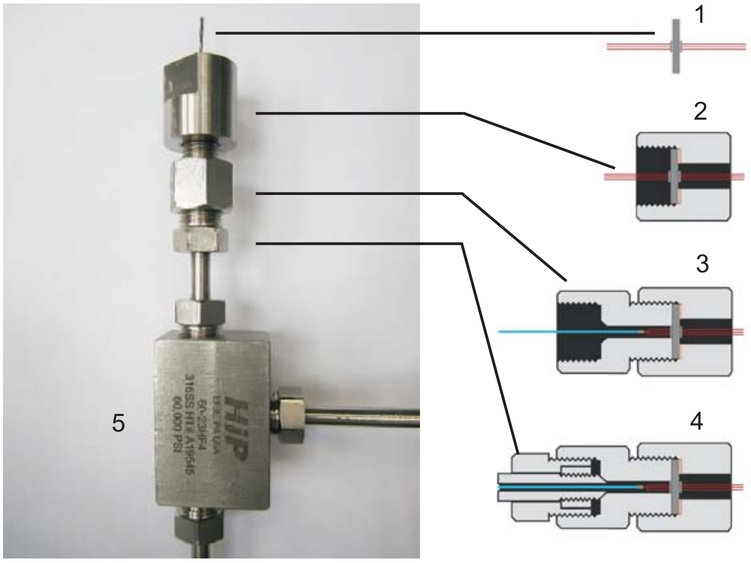

Figure 3.7: Design of electrical feed through: 1. Electrical glass insulated wire, 2. coupling half flange with copper sealing, 3. HIP collar, 4. HIP gland coupling for 1/4 inch tube, 5. three-way valve with mounted electrical feed through and tube connection to the gas sample inlet.

lead through the upper connection to the electrical feed through. The side connection of the valve was connected to the gas sample container. The disadvantage of the extended wiring of almost 0.65 m through the tube was the high capacitive impedance damping the quartz crystal. This was equalized with an inductive math box of variable inductive reactance.

4 Publications

In this section the publications that were generated within this work are presented. Overall seven publications, where four publications are main author contributions (*) and three publications are second author contributions (**), are relevant for present thesis and are presented in a chronological context in the following.

Publication I(*) describes the design, construction and operation of an apparatus for measuring the speed of sound of fluids based on the pulse-echo method. Here, speed of sound data of ammonia were determined for six isotherms in a temperature range from 230 K to 410 K from somewhat above the vapor pressure up to a pressure of 124 MPa.

Publication II(*), a technical development of the measurement of propagation time is presented. It was shown that burst design in combination with signal enhancement significantly enlarges the measuring range of the pulse-echo technique for supercritical argon and nitrogen.

Speed of sound measurements of hexamethyldisiloxane (MM), octamethylcyclotetrasiloxane (D_4), octamethyltrisiloxane (MDM) and decamethyltetrasiloxane (MD_2M) enlarged the experimental data basis for the development of equations of state (EOS) in publications III(**) and for new hybrid EOS in IV(**) and VI(**). Since the amount of thermodynamic property data for siloxanes is rather limited, data from experiments and in the present cases also from molecular simulation helped to enlarge the range of validity and also to enhance overall accuracy of EOS.

The results from publication II(*) have been applied in publication V(*), which presents speed of sound measurements of supercritcal oxygen in a temperature range of up to 500 K and a pressure of up to 100 MPa. Safety requirements while handling pure oxygen are discussed due to its severe oxidizing character and explosive reactivity with many materials. These results may be of interest for the development of a new EOS for oxygen or air, since the overall experimental data range was enlarged in temperature and pressure compared to measurements in the literature.

The coupling of two ORC as cascade is described in publication VII(*), focussing on the transfer of residual heat from a high temperature cycle to a low temperature cycle. This apparatus and the performed experiments may offer an interesting basis for future work.

4.1 Apparatus for the measurement of the speed of sound of ammonia up to high temperatures and pressures

Frithjof H. Dubberke, David B. Rasche, Elmar Baumhögger, and Jadran Vrabec, Review of Scientific Instruments, 85, 084901 (2014); doi: 10.1063/1.4891795

Reprinted from Journal of Applied Physics, Review of Scientific Instruments, Volume 85, Authors: Frithjof H. Dubberke, David B. Rasche, Elmar Baumhögger, and Jadran Vrabec, 084901, Copyright (2014), with permission from AIP Publishing.

The scientific work and discussion was coordinated and consolidated by Frithjof H. Dubberke under supervision of Jadran Vrabec.
Construction design was supported by Holger Gedanitz.
Mechanical construction was carried out by Frithjof H. Dubberke, Rüdiger Pflock and Alex Reimann.
Electrical design and wiring was carried out by Elmar Baumhögger.
Speed of sound measurements and data evaluation were performed by Frithjof H. Dubberke, Carlos Guillermo la Rubia García and Elmar Baumhögger.
The manuscript was revised by Elmar Baumhögger and Jadran Vrabec.

This publication is in the context of the master thesis of Carlos Guillermo la Rubia García (Speed of Sound Measurements in Ammonia and Ionic Liquids, 2012) under supervision of Frithjof H. Dubberke at the chair of Thermodynamics and Energy Technology headed by Prof. Dr.-Ing. habil. Jadran Vrabec.

REVIEW OF SCIENTIFIC INSTRUMENTS **85**, 084901 (2014)

Apparatus for the measurement of the speed of sound of ammonia up to high temperatures and pressures

Frithjof H. Dubberke, David B. Rasche, Elmar Baumhögger, and Jadran Vrabec[a)]
Lehrstuhl für Thermodynamik und Energietechnik, Universität Paderborn, Warburger Straße 100, 33098 Paderborn, Germany

(Received 19 May 2014; accepted 20 July 2014; published online 5 August 2014)

An apparatus for the measurement of the speed of sound based on the pulse-echo technique is presented. It operates up to a temperature of 480 K and a pressure of 125 MPa. After referencing and validating the apparatus with water, it is applied to liquid ammonia between 230 and 410 K up to a pressure of 124 MPa. Speed of sound data are presented with an uncertainty between 0.02% and 0.1%. © *2014 AIP Publishing LLC*. [http://dx.doi.org/10.1063/1.4891795]

I. INTRODUCTION

Ammonia is a ubiquitous compound due to its presence in many industrial processes and cleaning products. In addition to its classical applications in fermentation or fertilization, ammonia's properties allow for a good performance as a refrigerant or fuel. Due to the importance of ammonia, it is of great interest to have a very reliable model for its thermodynamic properties. Thermal pvT properties as well as heat capacity and speed of sound data in the homogenous fluid region, together with the vapor pressure and the saturated liquid density, form the basis of fundamental equations of state (EOS) that accurately describe the entire range of fluid states.

This work presents an apparatus for measuring the speed of sound at high temperatures and pressures to generate data for fluids that were insufficiently studied. The speed of sound of fluids can be measured in different ways. For gases, the spherical resonator is a suitable technique with a high accuracy that has been used, e.g., by Beckermann and Kohler,[1] Trusler and Zarari,[2] Benedetto *et al.*,[3] Mehl and Moldover,[4,5] or Ewing *et al.*[6] Another measurement principle for the speed of sound of liquids is based on the pulse-echo technique which was introduced in 1985 by Kortbeek *et al.*[7] Among others, it was used by Gedanitz *et al.*,[8] Ye *et al.*,[9] Wang and Nur,[10] Zak *et al.*,[11] Benedetto *et al.*,[12] or Meier and Kabelac.[13]

Speed of sound measurements for ammonia have been carried out since the late 1960s, however, leaving a wide range of fluid states without data. In 1968, Blagoi *et al.*[14] published the first experimental results for the speed of sound of ammonia. These measurements were made for the liquid along the saturation line up to 270 K and 0.4 MPa. In the same year, Bowen and Thompson[15] published values for the adiabatic compressibility of liquid ammonia, derived from speed of sound measurements between the freezing point and the normal boiling point (from 196 to 240 K). It was not until 2007 that the speed of sound of ammonia was measured again. Estrada-Alexanders and Hurly[16] used an acoustic Greenspan viscometer to measure the kinematic viscosity and the speed of sound of several fluids, including ammonia. The covered temperature and pressure ranges were 0.22–3.38 MPa and 300–375 K, respectively. Finally, Abramson[17] published in 2008 results for the very high pressure regime of liquid ammonia. Using the impulsive stimulated scattering technique, speed of sound measurements up to 680 K and 3.75 GPa were made. In the present work, measurements were made in the temperature range from 230 to 410 K from somewhat above the saturation line up to 124 MPa, cf. Fig. 1.

II. APPARATUS

A. Construction

The measurement principle of the present apparatus is based on the pulse-echo technique with a double path length.[8] After emitting a high frequency modulated burst signal by a piezoelectric quartz crystal, which was positioned between two reflectors in the fluid, the speed of sound was determined by the time measurement of the signal propagation through the fluid. The ultrasonic sensor was identical with the one used by Gedanitz *et al.*[8]

The components of the measurement cell were made of stainless steel 1.4571 and were subjected to a heat treatment to remove self-stress from the manufacturing process. The piezoelectric quartz crystal was the main piece and was positioned between two polished reflectors. These reflectors were mounted with stainless steel screws $L_1 = 20$ mm above and $L_2 = 30$ mm below the quartz crystal, cf. Fig. 2. A X-cut crystal quartz was taken as a transducer which operated at a resonance frequency of 8 MHz. It was shaped as a circular disk with a diameter of 15 mm, having gold coated electrodes on both sides which measured 10 mm in diameter. Two clamps were connecting the electrodes, one to ground potential and the other one through a teflon coated wire to the control unit outside of the pressure vessel. The electrical feed through was realized by a glass insulation which was placed outside of the thermostat at the end of the inlet. This had the advantage that it was shielded against high temperatures and only had to withstand high pressures.

Fig. 3 shows the setup of the apparatus. In the center of the apparatus was the cell with the quartz crystal mounted in the pressure vessel. The pressure vessel had a cylindrical shape with an internal diameter of 50 mm and a wall thickness of 25 mm. It was made of highly tensile steel of type 1.4462.

[a)] Author to whom correspondence should be addressed. Electronic mail: jadran.vrabec@upb.de. Tel.: +49-5251/60-2421. Fax: +49-5251/60-3522.

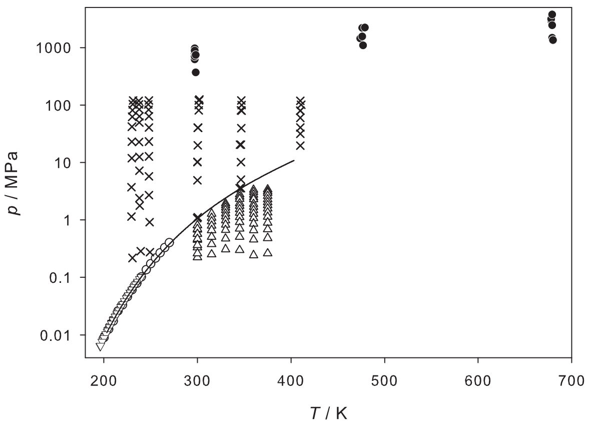

FIG. 1. Experimental speed of sound data for ammonia; ○ Blagoi *et al.*;[14] ▽ Bowen and Thompson;[15] △ Estrado-Alexanders and Hurly;[16] ● Abramson;[17] × this work; —— saturation line.

The sealing was done by a copper seal, supported by a rib profile which was milled into the surface of the sealing setting (note that dry ammonia with a water content of less than 400 ppm does not react with copper[18]). The pressure vessel itself was girded and fixed by a copper jacket to yield a uniform temperature distribution. This copper jacket was surrounded by two larger copper shieldings, each equipped with a heating unit of 150 W electrical power for thermostating. Four layers of aluminum foil around the outer copper shielding reduced heat loss due to thermal radiation. Finally, the whole device was placed into a vacuum tank to reduce heat loss due to convection. Above the outer copper shielding, an aluminum plate was mounted to shield the cables and the electronic devices outside of the vacuum tank from thermal stress. The entire apparatus was mounted below an aluminum plate that was attached to the base frame of the test rig. The hanging construction was advantageous because of the good accessibility of the cell in case of maintenance. Heat loss through thermal conduction was minimized by contacting the acoustic sensor with the environment only by three distance holders of stainless steel that were attached to the central copper shielding, which was again contacted to the base plate by three other distance holders. The vacuum tank was about 420 mm in diameter and 1100 mm in height and was sealed with rubber. It had an inlet/outlet at the bottom for liquid samples, leading straight to the measuring cell, and another opening on the side for a connection to a vacuum pump. Three additional openings were at the retaining plate for the safety outlet, for the thermometers, as well as an electrical feed through for the cables of the heating elements and the temperature sensors.

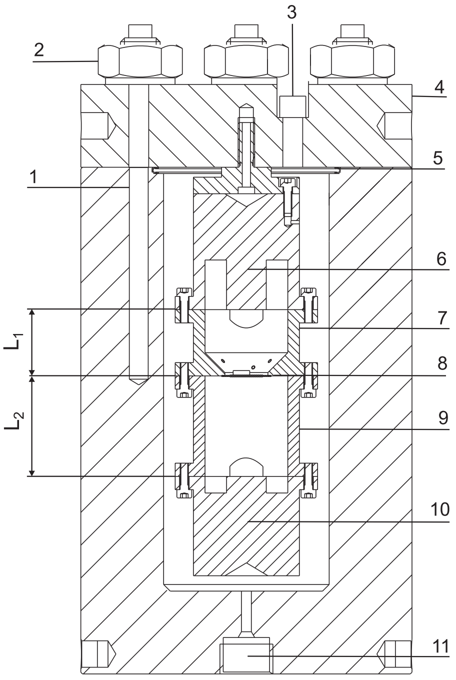

FIG. 2. Measuring cell in the pressure vessel: 1. thermometer seating, 2. fastening nuts, 3. safety outlet, 4. cell closure, 5. sealing ring, 6. reflector A, 7. path length L_1, 8. quartz, 9. path length L_2, 10. reflector B, 11. liquid sample inlet and outlet.

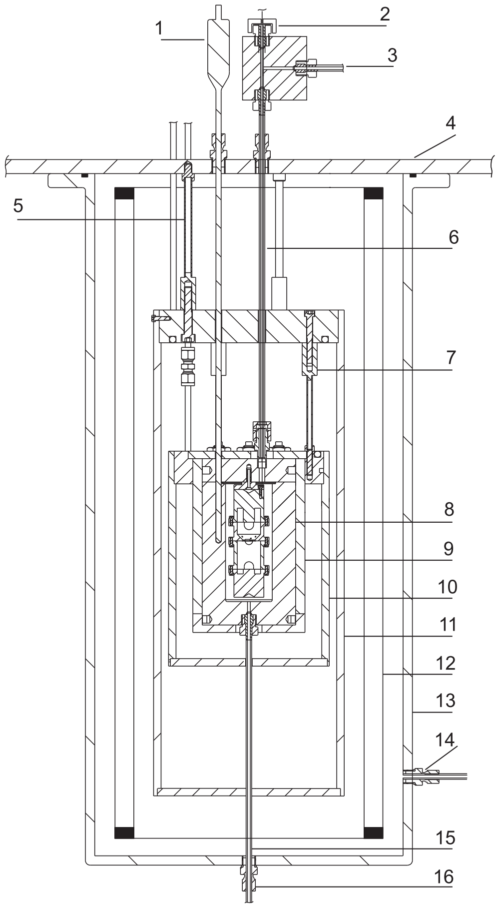

FIG. 3. Setup of the apparatus: 1. PT-100 thermometer, 2. electrical feed through, 3. safety outlet/burst disc, 4. base plate, 5. distance holder, 6. safety outlet/cable passage, 7. distance holder, 8. pressure vessel, 9. inner copper shielding, 10. central copper shielding, 11. outer copper shielding, 12. aluminum foils, 13. vacuum tank, 14. vacuum tank outlet, 15. liquid sample inlet and outlet, 16. vacuum sealing.

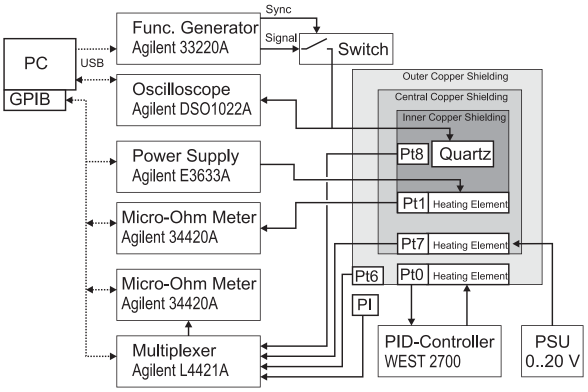

FIG. 4. Arrangement of electronic devices for temperature control, pressure measurement, as well as signal generation and detection.

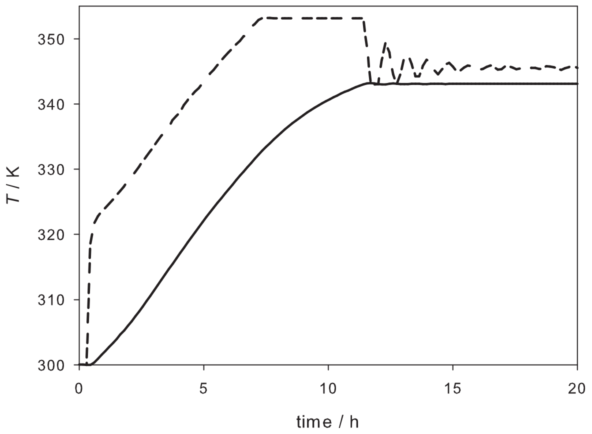

FIG. 5. Temperature control of the heating element. Solid line: cell temperature; dashed line: heating element temperature.

B. Temperature

For controlling the cell with a high accuracy over a wide range of temperature, the thermostat was constructed with three copper shields. Each was monitored with respect to the temperature and equipped with one independently adjustable heater, cf. Fig. 4. The temperature of the liquid was measured with a PT-100 thermometer (Rössel Messtechnik RM-type) mounted in the wall of the pressure cylinder next to the quartz, i.e., Pt8 in Fig. 4. The inner copper shielding was heated with a Thermocoax heating element and monitored with Pt1, cf. Fig. 4.

The control mode of the inner heating element is shown in Fig. 5. To quickly specify a constant temperature at the quartz without overshooting, a combination of a proportional integral differential (PID) controller and an additional proportional (P) controller was used. Both were implemented in the control computer software. The PID controller provided the temperature control at the inner heater with its sensor Pt1 that was very close to the heating element. To reach the specified temperature at the quartz, the set point of the PID controller was calculated from the difference of the temperature measured by Pt8 and its set point. To prevent overshooting, the set point of the PID controller was limited to an adjustable range around the set point of Pt8. This proportional control algorithm leads to a small deviation which can be minimized by adding it to the set point to accurately reach the specified temperature. The outer copper shielding had another heating element which was adjusted manually with the help of a PID controller to 2 K below the desired fluid temperature. A supporting heating element, with the only purpose to boost heating, was attached to the second shielding and was regulated by a manual adjustment of a 12 V power supply. To monitor and control the cell temperature, a multiplexer (Agilent L4421A), two $\mu\Omega$-meters (Agilent 34420A) and a programmable power supply (Agilent E3633A) were connected to the computer via a GPIB interface. The heating loop had an accuracy of ± 3 mK around the specified fluid temperature, cf. Fig. 6.

The calibration of the Pt8 (PT 100/0) thermometer was done with a standardized 25 Ω platinum thermometer (Rosemount 162 CE) which was calibrated from 84 to 693 K at the Physikalisch-Technische Bundesanstalt in Braunschweig with an given uncertainty of 2.5 mK.[19] Calibration of Pt8 took place from 290 to 650 K. The uncertainty of the temperature measurement consisted of the uncertainty of the thermometer calibration (10 mK), the uncertainty of the measurement of the resistance ratio (2 mK), the stability of the temperature in the thermostat (4 mK, operating experience), and the inhomogeneity of the temperature field inside the pressure vessel. For resistance measurement, a $\mu\Omega$-meter (Agilent 34420A) was used, which was validated against a standard 100 Ω resistor (H. Tinsley & Co 5685 A) with a given uncertainty of 27 mK drift per year. Hence, the overall uncertainty of the temperature measurement results according to the error propagation due the individual uncertainty contributions to $u_{\Delta T} = 30$ mK.

C. Pressure

The piping system is shown in Fig. 7. It was used to fill the cell with the liquid sample and to specify the pressure. Important components of the pressure system were an upper

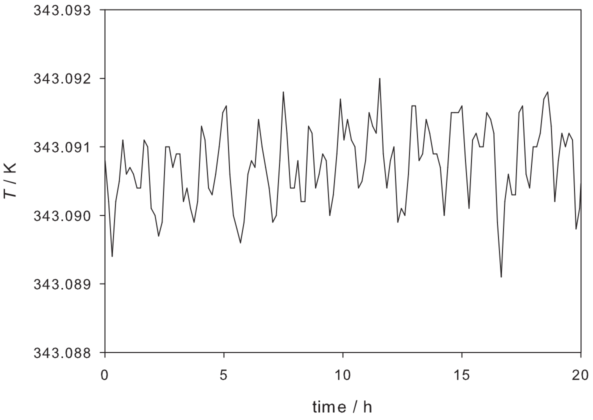

FIG. 6. Cell temperature reading via Pt8.

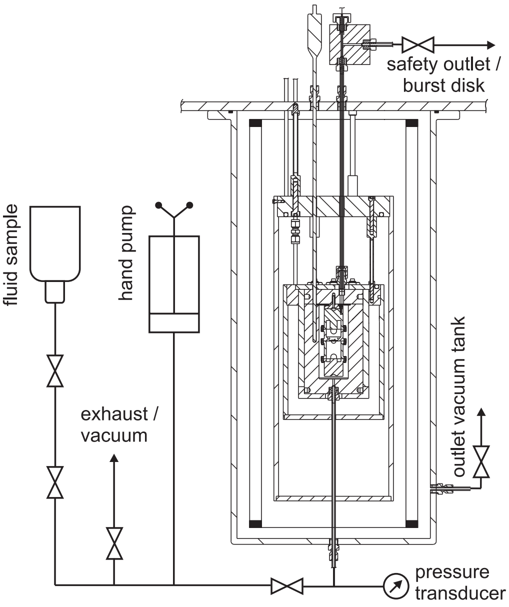

FIG. 7. Schematic of the pressure system.

safety outlet of the pressure vessel, giving the possibility to create a vacuum inside the pressure vessel, a liquid sample container at the end of the inlet, and a hand pump to adjust the pressure. Before filling the cell with a liquid, a vacuum was created. Subsequently, the liquid sample was imbibed into the cell. For an accurate pressure adjustment, a hand pump (HIP 50-5.75-30) was used. To achieve higher pressure levels, it was necessary to add more liquid into the cell. To this end, two valves were used to refill the hand pump without pressure loss in the cell.

The pressure was measured with a transducer (Honeywell TJE with a measuring range from 0 to 200 MPa and an accuracy of ±0.1% with respect to the full scale), which was protected by a blowout disc in case of overpressure. A $\mu\Omega$-meter (Agilent 34420A) was employed to measure the signal to supply voltage ratio. All pressurized components were connected via high pressure stainless steel tubes. The pressure transducer was calibrated with a dead weight tester (DH-Budenberg 580 EHX) for measurements up to 260 MPa with a specified uncertainty of 0.04% of its full scale. All valves (HIP 30.000 psi) were chosen to withstand operating pressures of up to 206 MPa. The maximum shear stress test of the pressure vessel was at about 190 MPa.

D. Signal

An arbitrary function generator (Agilent 33220A) was used to generate the burst signal and an oscilloscope (Agilent DSO1022A) was used as a detecting device, cf. Fig. 4. Both were connected to the control computer via a USB interface. The switch, which was triggered via the function generator sync output, transmitted the burst signal to the quartz crystal and its subsequent echoes to the oscilloscope. Coaxial cables with an impedance of 50 Ω were employed to connect the signal components. To compensate the capacitance of the quartz crystal, a variable inductance was placed into the circuit.

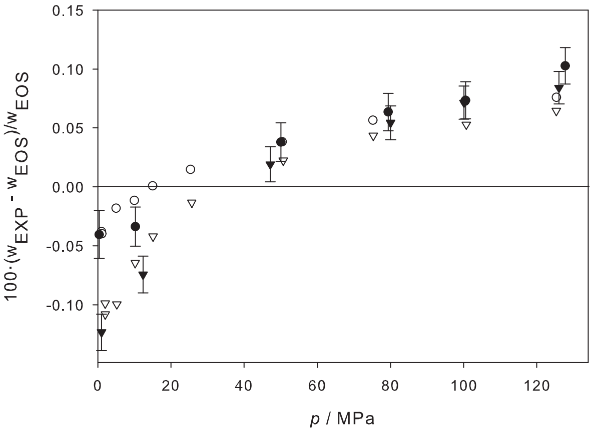

FIG. 8. Deviation of experimental speed of sound data from the EOS for water by Wagner and Pruss:[21] ○ 413 K, Lin and Trusler;[20] ● 413 K, this work; ▽ 473 K, Lin and Trusler;[20] ▼ 473 K, this work.

III. VALIDATION AND REFERENCING

Water is available at high purity and highly accurate speed of sound measurements have been done for this substance over a wide range of states. The referencing of the path length distance $\Delta L = L_2 - L_1$ was thus carried out with water following Gedanitz *et al.*[8] Furthermore, a comparison of the speed of sound measurements at high temperatures and high pressures was done with recently published data by Lin and Trusler,[20] because the uncertainty of the EOS by Wagner and Pruss[21] increases significantly for $T \geq 300$ K and $p \geq 100$ MPa to approximately 1%. Fig. 8 illustrates speed of sound measurements for two isotherms for water from this work and from Lin and Trusler[20] (with a given relative uncertainty of less than 0.04%) in comparison to the EOS[21] that is recommended by the International Association for the Properties of Water and Steam (IAPWS). These data show that the present apparatus operated reliably also at high temperatures and pressures.

IV. OPERATION PROCEDURE

After filling the liquid into the pressure vessel, an equilibration time of around 60 min to reach a constant pressure level was required. Subsequently, the quartz crystal was excited with a burst signal of 20 cycles, typically with a voltage of 10 V peak-to-peak, using the function generator. The two echoes, due to the reflections on both sides of the measuring cell, were loaded and stored into the computer via the oscilloscope and then identified via thresholds with an adjustable magnitude. To obtain an undistorted signal, a Fast Fourier Transform (FFT) algorithm was used.[22] Band path filtering with zero padding led to a high resolution in time and voltage amplitude as well as to a low random noise level. The time difference Δt, resulting from the path length difference $\Delta L = L_2 - L_1$, was calculated. Straightforwardly, the speed of sound is then given by

$$w = \frac{2\Delta L}{\Delta t}. \tag{1}$$

This equation does not consider diffraction, due to the phase shift of the signal relative to a planar propagation through the fluid, and dispersion effects leading to an uncertainty of the time difference Δt. The experimental speed of sound data were corrected by the diffraction correction by Harris,[23] whereas significant dispersion effects did not occur for a resonance frequency of 8 MHz.[24] Furthermore, there was an uncertainty of the path length difference $\Delta L(T, p)$ from the referencing procedure with pure water and the measurement itself. The correction of the path length variation due to temperature and pressure was done with the following equation, where $\Delta L(T_0, p_0)$ is the path length difference at $T_0 = 293.15$ K and $p_0 = 0.1$ MPa

$$\Delta L(T, p) = \Delta L(T_0, p_0) \cdot \left[1 + \alpha(T - T_0) + \frac{1}{E}(1 - 2\nu)(p - p_0)\right]. \tag{2}$$

Parameters of the steel material 1.4571 are the linear thermal expansion coefficient α, the elastic modulus E, and the poisson number ν, which were provided by steel supplier ThyssenKrupp Materials International (Werkstoffblatt 1.4571). Since two of these parameters (α and E) are temperature dependent, the thermal expansion is given by a fourth-order polynomial and the mechanical expansion by a first-order polynomial. The resulting speed of sound uncertainty due to the steel parameters was estimated to be negligible with 6×10^{-5}%.

V. RESULTS AND DISCUSSION

Measurements were made for ammonia as provided by Air Liquide (*N*50) with a given impurity of less than 8 ppm for a set of six isotherms, cf. Fig. 9. Starting somewhat above the vapor pressure, several measurements were made along each isotherm for different pressures up to 124 MPa. After each isotherm, the pressure was released and the measuring cell was refilled and pressurized with fresh ammonia.

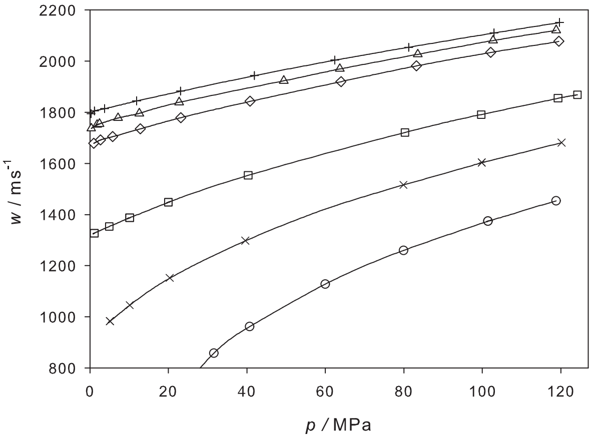

FIG. 9. Absolute values of the present speed of sound measurements along six isotherms: + 230 K; △ 237 K; ◊ 248 K; □ 300 K; × 346 K; ○ 410 K.

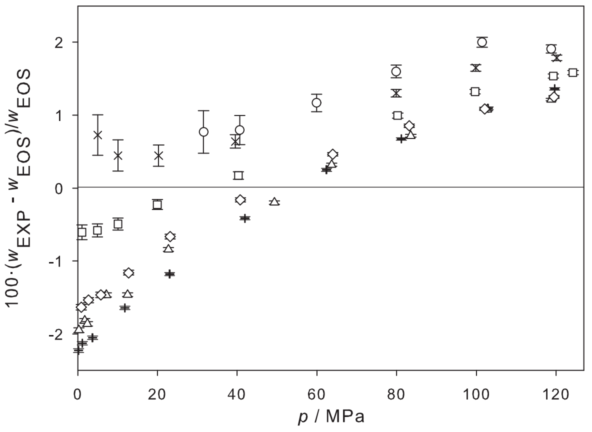

FIG. 10. Deviation of the present speed of sound measurements from the EOS by Tillner-Roth *et al.*:[25] + 230 K; △ 237 K; ◊ 248 K; □ 300 K; × 346 K; ○ 410 K.

The uncertainty of the present measurements is larger for lower pressures mainly due to the uncertainty of the pressure sensor. The measuring range of the pressure sensor was up to 200 MPa with an accuracy of ±0.1% of the full scale and therefore had an absolute uncertainty of 0.2 MPa. This uncertainty had the largest impact at high temperatures and low pressures, cf. Figs. 9 and 10. The overall speed of sound measurement uncertainty (u_w) is composed of the relevant contributions due to uncertainties of temperature ($u_{w,\Delta T}$) and pressure measurements ($u_{w,\Delta p}$), as well as the uncertainty of the referencing procedure (u_{Ref}) and the uncertainty of the path length difference ($u_{\Delta L}$)

$$u_w = \sqrt{{u_{w,\Delta T}}^2 + {u_{w,\Delta p}}^2 + {u_{Ref}}^2 + {u_{\Delta L}}^2}. \tag{3}$$

The uncertainty of the operation procedure was limited by the internal time reference of the function generator and was thus neglected. According to the error propagation law, the uncertainty due to the referencing process and path length difference was 0.012%. However, the total uncertainty increased up to 0.3% for measurements at 346 and 410 K below 60 MPa. This increase is due to the fact that the relative uncertainty of the pressure measurement was significantly higher at low pressures combined with the high isothermal compressibility of the fluid at such thermodynamic states. For the remaining state points the total uncertainty varied between 0.02% and 0.1%. Table I provides the present data together with their uncertainties.

The obtained speed of sound values were compared with the EOS by Tillner-Roth *et al.*[25] Observing the deviation from the experimental data, the accuracy of the EOS was assessed in the liquid state over a wide range of temperature and pressure, cf. Fig. 10. The uncertainty of the EOS for the speed of sound was specified by Tillner-Roth *et al.*[25] to be 2%, except for the critical region where it was not further defined. This 2% claim was confirmed here.

TABLE I. Experimental speed of sound data for ammonia, this work. The uncertainty of the pressure was throughout $\Delta p = 0.2$ MPa, the uncertainty of the speed of sound Δw is given for each state point individually.

T [K]	p [MPa]	w [m/s]	Δw [m/s]
230.61	0.2	1794.3	0.62
229.64	1.2	1805.8	0.61
229.64	3.7	1814.5	0.60
229.71	11.8	1844.3	0.58
229.8	23.1	1882.5	0.55
229.99	41.9	1943.9	0.51
230.37	62.4	2004.1	0.49
230.65	81.2	2054.9	0.47
230.99	103	2110.7	0.46
231.35	119.7	2151.2	0.45
239.44	0.3	1737	0.71
238.37	1.8	1751.8	0.69
238.1	2.4	1755	0.68
237.98	7.2	1778.3	0.66
237.83	12.5	1796	0.64
237.65	22.7	1839	0.60
237.8	49.4	1923.4	0.54
237.84	63.7	1970	0.52
237.75	83.6	2027.2	0.49
237.48	102.8	2081	0.48
237.37	118.8	2120.8	0.46
248.91	0.9	1678.4	0.79
248.1	2.7	1692.5	0.77
248.08	5.8	1705.2	0.75
248.05	12.8	1735.7	0.72
248.06	23.2	1779.2	0.67
248.13	40.8	1842.9	0.61
248.19	64	1920.4	0.56
247.65	83.2	1981.7	0.53
247.56	102.1	2034.4	0.50
248.07	119.5	2077.6	0.49
299.72	1.1	1327	1.48
299.89	4.9	1354	1.38
300.02	10.1	1388	1.27
300.2	20	1448	1.11
300.5	40.3	1553.6	0.91
301.21	80.3	1721.1	0.70
301.34	99.7	1791.4	0.64
301.55	119.3	1855	0.60
302.03	124.3	1868.5	0.59
345.08	3.6	979	2.88
346.56	5	983	2.37
346.63	10.1	1046	1.79
346.47	20.3	1152	1.28
346.75	39.6	1298	0.87
347.07	79.9	1516.4	0.86
347.12	99.8	1603.5	0.77
346.85	120.2	1681.5	0.69
409.89	31.6	858	1.99
409.85	40.7	962	1.42
409.88	59.9	1128	1.13
409.89	79.9	1260	1.13
410.89	101.4	1374	0.94
409.92	118.8	1454.1	0.84

VI. CONCLUSION

An apparatus for the measurement of the speed of sound of liquids using the pulse-echo technique was built and validated with water by comparing the results with an accurate EOS for water and recently published experimental data by Lin and Trusler.[20] The speed of sound of ammonia was measured here for six isotherms from 273.15 to 410 K from somewhat above the vapor pressure up to 124 MPa. The measured speed of sound data for ammonia were compared with the EOS by Tillner-Roth *et al.*[25] and it was confirmed that the maximum deviation of the EOS is about 2%.

This work covered a wide range of temperature and pressure in the liquid state for which no experimental data were available for ammonia. The present results show that the pulse-echo technique is a reliable and accurate method for the measurement of the speed of sound of liquid ammonia.

ACKNOWLEDGMENTS

The authors gratefully acknowledge the support of Holger Gedanitz and the assistance of Carlos Guillermo la Rubia García during the measurements.

[1] W. Bekermann and F. Kohler, Int. J. Thermophys. **16**, 455 (1995).

[2] J. P. M. Trusler and M. Zarari, J. Chem. Thermodyn. **24**, 973 (1992).

[3] G. Benedetto, R. M. Gavioso, and R. Spagnolo, Rivista del Nuovo Cimento **22**, 1 (1999).

[4] J. B. Mehl and M. R. Moldover, J. Chem. Phys. **74**, 4062 (1981).

[5] J. B. Mehl and M. R. Moldover, J. Chem. Phys. **77**, 455 (1982).

[6] M. B. Ewing, A. R. H. Goodwin, M. L. McGlashan, and J. P. M. Trusler, J. Chem. Thermodyn. **19**, 721 (1987).

[7] P. J. Kortbeek, M. J. P. Muringer, N. J. Trappeniers, and S. N. Biswas, Rev. Sci. Instrum. **56**, 1269 (1985).

[8] H. Gedanitz, M. Davila, E. Baumhögger, and R. Span, J. Chem. Thermodyn. **42**, 478 (2010).

[9] S. Ye, J. Alliez, B. Lagourette, H. Saint-Guirons, J. Arman, and P. Xans, Rev. Phys. Appl. **25**, 555 (1990).

[10] Z. Wang and A. Nur, J. Acoust. Soc. Am. **89**, 2725 (1991).

[11] A. Zak, M. Dzida, M. Zorebski, and A. Ernst, Rev. Sci. Instrum. **71**, 1756 (2000).

[12] G. Benedetto, R. M. Gavioso, P. A. G. Albo, S. Lago, D. M. Ripa, and R. Spagnolo, Int. J. Thermophys. **26**, 1651 (2005).

[13] K. Meier and S. Kabelac, Rev. Sci. Instrum. **77**, 123903 (2006).

[14] Y. P. Blagoi, A. E. Butko, S. Mikhailenko, and V. V. Yakuba, Russ. J. Phys. Chem. (USSR) **42**, 564 (1968).

[15] D. E. Bowen and J. C. Thompson, J. Chem. Eng. Data **13**, 206 (1968).

[16] A. Estrada-Alexanders and J. Hurly, J. Chem. Thermodyn. **40**, 193 (2008).

[17] E. Abramson, J. Chem. Eng. Data **53**, 1986 (2008).

[18] "Refrigerants - Requirements and symbols," Ref. No. DIN 8960:1998-11 (Normenausschuss Kältetechnik (FNKä) 1998).

[19] Physikalisch-Technische Bundesanstalt, see http://www.ptb.de/.

[20] C.-W. Lin and J. P. M. Trusler, J. Chem. Phys. **136**, 094511 (2012).

[21] W. Wagner and A. Pruss, J. Phys. Chem. Ref. Data **31**, 387 (2002).

[22] G. Benedetto, R. M. Gavioso, P. A. G. Albo, S. Lago, D. M. Ripa, and R. Spagnolo, Int. J. Thermophys. **26**, 1667 (2005).

[23] G. R. Harris, J. Acoust. Soc. Am. **70**, 10 (1981).

[24] K. Meier, *The Pulse-echo Method for High Precision Measurements of the Speed of Sound in Fluids* (University of the Federal Armed Forces, Hamburg, 2006).

[25] R. Tillner-Roth, F. Harms-Watzenberg, and H. D. Baehr, DKV-Tagungsbericht **20**, 167 (1993).

4.2 Burst design and signal processing for the speed of sound measurement of fluids with the pulse-echo technique

Frithjof H. Dubberke, Elmar Baumhögger, and Jadran Vrabec
Review of Scientific Instruments, 86, 054903 (2015); doi: 10.1063/1.4921478

Reprinted from Journal of Applied Physics, Review of Scientific Instruments with permission from AIP Publishing.

The scientific work and discussion was coordinated and consolidated by Frithjof H. Dubberke under supervision of Jadran Vrabec.
The manuscript was prepared by Frithjof H. Dubberke.
Electrical design and wiring was carried out by Elmar Baumhögger.
Speed of sound measurements and data evaluation were performed by Frithjof H. Dubberke and Elmar Baumhögger.
The manuscript was revised by Elmar Baumhögger and Jadran Vrabec.

This publication is in context of the speed of sound research under supervision of Frithjof H. Dubberke at the chair of Thermodynamics and Energy Technology headed by Prof. Dr.-Ing. habil. Jadran Vrabec.

REVIEW OF SCIENTIFIC INSTRUMENTS **86**, 054903 (2015)

Burst design and signal processing for the speed of sound measurement of fluids with the pulse-echo technique

Frithjof H. Dubberke, Elmar Baumhögger, and Jadran Vrabec[a)]
Lehrstuhl für Thermodynamik und Energietechnik, Universität Paderborn, Warburger Straße 100, 33098 Paderborn, Germany

(Received 26 January 2015; accepted 10 May 2015; published online 21 May 2015)

The pulse-echo technique determines the propagation time of acoustic wave bursts in a fluid over a known propagation distance. It is limited by the signal quality of the received echoes of the acoustic wave bursts, which degrades with decreasing density of the fluid due to acoustic impedance and attenuation effects. Signal sampling is significantly improved in this work by burst design and signal processing such that a wider range of thermodynamic states can be investigated. Applying a Fourier transformation based digital filter on acoustic wave signals increases their signal-to-noise ratio and enhances their time and amplitude resolutions, improving the overall measurement accuracy. In addition, burst design leads to technical advantages for determining the propagation time due to the associated conditioning of the echo. It is shown that the according operation procedure enlarges the measuring range of the pulse-echo technique for supercritical argon and nitrogen at 300 K down to 5 MPa, where it was limited to around 20 MPa before. © *2015 AIP Publishing LLC*. [http://dx.doi.org/10.1063/1.4921478]

I. INTRODUCTION

Acoustic measurements allow for a fast and convenient access to the speed of sound, which is a full-fledged thermodynamic property. Such measurements contribute substantially to the development and parameterization of fundamental Helmholtz equations of state (FEOS) for fluids[1] because accurate speed of sound data can efficiently be obtained over a large range of temperature and pressure. The most common measuring principle for determining the speed of sound of liquids is the pulse-echo technique, which was introduced by Kortbeek *et al.*[2] in 1985. In this method, a burst of sound waves, emitted by an excited quartz crystal, propagates through the fluid over a known distance, is reflected and propagates back to the quartz crystal that also acts as a receiver for the echoes. Two approaches for measuring the propagation time of the wave burst are applied: (a) The propagation time of a single wave burst is determined directly.[3] (b) The propagation time is determined through cancelation by interference, which takes place at the quartz crystal after emission and reflection of a second wave burst.[4,5] Usually, interference of the echoes is achieved manually by visualizing the resulting wave signals by means of an oscilloscope.[4,6]

Both approaches heavily depend on the oscilloscope's sampling resolution of the received wave signals, which limits the accuracy of the time measurement. To increase this accuracy, Ball and Trusler[3] introduced in 2001 a signal analysis that is based on a cross-correlation of the two echoes, which was optimized by a parabolic fit.

Another numerical route for signal enhancement is to apply a Fast Fourier Transformation (FFT) based digital filter to the reflected wave signal. FFT filtering increases the signal-to-noise ratio and reduces offset effects due to hardware and other unwanted side effects.[7] FFT filtering not only enhances the accuracy of the propagation time measurement, and thus the determination of the speed of sound, in combination with numerical analysis it may also simplify the measurement process.

II. MEASUREMENT APPROACHES

The measurement principle of the pulse-echo technique[8,9] is based on a sample cell that has two known propagation path lengths l_1 and l_2, where $l_2 > l_1$. By emitting a modulated high frequency wave burst with a piezoelectric quartz crystal, which is positioned between two reflectors in the fluid, the speed of sound c is determined by the time measurement of the wave propagation through the fluid, cf. Fig. 1. The speed of sound, neglecting dispersion and diffraction effects, is given by the following ratio of propagation distance and time:

$$c = \frac{2(l_2 - l_1)}{\Delta t}. \tag{1}$$

Two approaches are used: The single wave burst approach determines the propagation time difference Δt between the two echoes, which is caused by the different propagation path lengths l_1 and l_2, by measuring it directly with a correlation method.[3,7] With the interference approach, as introduced by Kortbeek *et al.*[2] and later modified by Meier,[5] the propagation time difference Δt is measured with the help of an additional second inverse wave burst. Interference occurs between the second echo of the first wave burst and the first echo of the second inverse wave burst if the second wave burst is emitted with a delay of Δt, cf. Fig. 1. By manually adjusting Δt, the maximum interference can be visually located with an oscilloscope.[4,6]

[a)] Author to whom correspondence should be addressed. Electronic mail: jadran.vrabec@upb.de. Tel.: +49-5251/60-2421. Fax: +49-5251/60-3522.

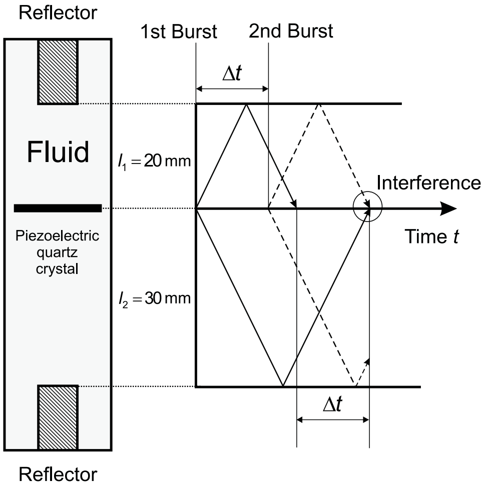

FIG. 1. Principle of the pulse-echo technique for the single wave approach (Δt is the time difference between the received echoes of the wave burst) and interference approach (Δt is the time difference between first and second inverse wave bursts, which cancel out at the quartz due to total interference).

III. SIGNAL ENHANCEMENT

Independent on the measurement approach, determining the speed of sound with a high accuracy requires an undistorted echo signal with a high resolution in time and amplitude as well as low random noise level. To exemplify the associated challenges, the resolution of the oscilloscope employed in the present work (Agilent DSO1022A) in terms of the voltage amplitude was seemingly rather poor at 256 samples (8 bit) compared to its time resolution of 10 200 samples (separated by 8 ns). However, at a typical resonance frequency of 8 MHz, this time resolution yields only 15.6 samples per oscillation period and thus affects the uncertainty of the time measurement by about 8 ns. This quantization at low resolution causes a strong distortion of the signal, which is also influenced by random noise.

Applying a FFT based band-pass filter algorithm for signal enhancement is a reliable routine in the present context as shown by Benedetto *et al.*[7] It helps to eliminate ambient noise as well as signal distortion and it concurrently increases the resolution of the echo signal. The width of the band-pass filter should be narrow enough to eliminate most of the noise and wide enough to preserve the original signal shape. In this work, a band-pass filter of ±20% around 8 MHz (6.4–9.6 MHz) was chosen, and all other frequency terms were set to zero.

The resolution in time was increased by zero padding in the frequency domain. This was done by appending zero values to the negative and positive ends of the Fourier transformed signal data. This did not affect the shape of the signal, but it quadrupled the number of data points by increasing the number of terms in the frequency domain accordingly.[10] Both algorithms were implemented into a data acquisition system and are efficient for interpolating large numbers of data points, increasing the amplitude resolution from 8 bit as provided by the oscilloscope to 64 bit (double) floating-point format with a fourfold resolution in time.

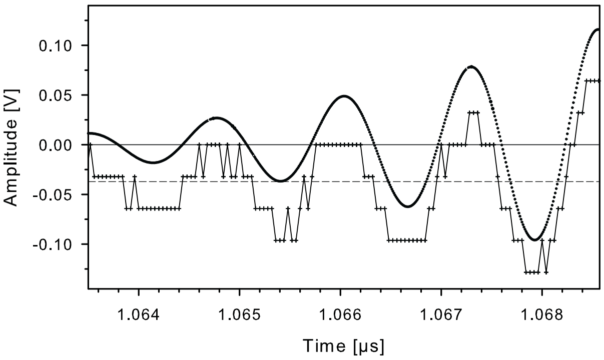

FIG. 2. Detailed view on an echo signal and its FFT reconstructed form. Raw signal (+), reconstructed signal (●), and offset voltage (- - -).

Fig. 2 depicts a section of an increasing echo at low voltage amplitude from the oscilloscope and the same echo reconstructed via FFT with a 6.4–9.6 MHz band-pass filter. The quantization of the raw echo signal, noise that randomly causes peaks, and the voltage offset are visible. The reconstructed signal has a considerably higher resolution both in terms of amplitude and time, while noise, offset voltage, and distortion were significantly reduced.

Fig. 3(a) displays a raw signal with a high noise ratio as recorded by the oscilloscope. Fig. 3(b) shows that the absolute value of the frequency spectrum of the signal lies in the range from about 7.6 to 8.3 MHz, which was not affected by the band-pass filter. (Note that a too narrow band-pass filter might cut off crucial properties of the signal.) After transforming the signal back to the time domain, noise and offset voltage were strongly reduced, cf. Fig. 3(c). FFT, band-pass filtering, and reconstruction lead to signal data that are much

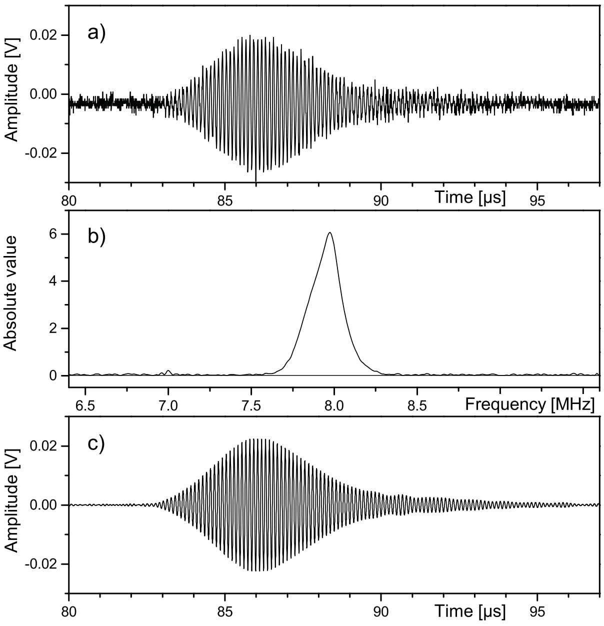

FIG. 3. (a) Raw echo signal with offset voltage, noise, and resolution defects due to sampling limits of the oscilloscope; (b) absolute value of the frequency spectrum of the echo signal; (c) echo signal reconstructed by FFT.

better suited for subsequent numerical operations as discussed in the following.

IV. TIME MEASUREMENT WITH PEAK-TO-PEAK METHOD AND HILBERT TRANSFORM

For determining the propagation time difference Δt with the single burst approach, different methods can be applied, cf. Ball and Trusler.[3] In case of short excitation bursts in dense liquids, which lead to short echoes because of negligible acoustic impedance and attenuation effects, Δt may well be identified as the time between the maximum amplitudes of both echoes, cf. Fig. 4 (top). The maximum amplitudes occur at the equivalent time interval in both echoes[11] and therefore Δt can be derived directly from the timing of the maximum amplitudes. This method was applied here to the minimum and maximum peaks and is termed peak-to-peak measurement (PPM) in the following. Fig. 4 (bottom) indicates Δt between the maximum peaks of both echoes with a high resolution. Note that noise inhibits measuring Δt by localizing the start or the end of the two echo waves.

Another method for determining Δt is to evaluate the Hilbert transform (HT) of the echo signals, which may be obtained from basic Fourier analysis and is widely used to map raw periodic functions into analytical signals, which represents the envelope of their varying magnitude.[12] The HT envelope functions yield Δt via their maxima, cf. Fig. 4 (bottom).

Under ideal conditions, where the echoes are perfect, time measurement by single and double burst methods, PPM, and HT should yield throughout the same Δt. However, it was observed in this work that PPM and HT do not necessarily converge to the same Δt under challenging conditions where the fluid density is low, cf. Fig. 4 (bottom). The results from HT seemed to be less reliable, particularly in case of weak signals with a high noise level in combination with a narrow band-pass filter.

V. LIMITATIONS OF PULSE-ECHO APPROACHES

All pulse-echo approaches are limited by the quality of the echoes,[12,13] which is influenced by acoustic impedance and attenuation. These effects predominantly play a role in low density fluids, i.e., gases up to the critical region[14] and other highly attenuating liquids,[15,16] and impede the readability of the echoes.

The following problems may result: First, the interference approach requires echoes with a plateau shaped amplitude (cf. Fig. 5(a)), which do not develop in low density fluids. Second, the shape of the echoes becomes so distorted that the interference and correlation approaches do not converge (cf. Fig. 5(b)). Third, the echoes overlap and interfere due to their increased temporal extension so that they cannot be distinguished anymore (cf. Fig. 5(c)). Fourth, the echo signal amplitudes decline to zero so that they vanish in the noise.

Fig. 6 illustrates present results from different methods for the speed of sound measurement of gaseous and supercritical nitrogen at 300 K up to a pressure of about 52 MPa compared to the highly accurate FEOS by Span *et al.*[17] All experimental results show a decreasing negative trend with respect to the baseline of the FEOS towards low pressure. This is caused by echo distortion, which induces a temporal extension and a shift of the maximum of the echo periods. Uneven echo distortion leads to a larger temporal extension of the second echo, due to its larger propagation distance, than in case of the first echo. Therefore, the correlation method and the PPM sample larger Δt. Echo distortion has a stronger impact on PPM and HT, which depend on the maximum amplitude periods, than on the correlation method, which depends on the entire echo signal.

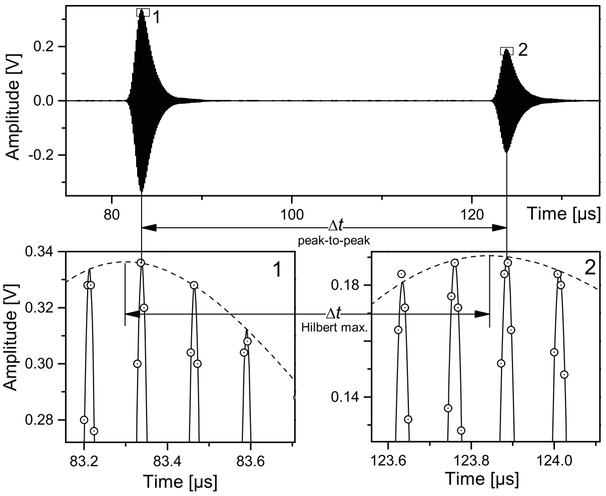

FIG. 4. Top: First (1) and second (2) echo signals as reconstructed by FFT; bottom: magnified view on both echo maxima indicating Δt via peak-to-peak measurement (time between periods with maximum amplitude) and Hilbert transform (time between the envelope maxima); raw echo signal from oscilloscope ⊙; echo signal reconstructed by FFT ——; and Hilbert transform - - -.

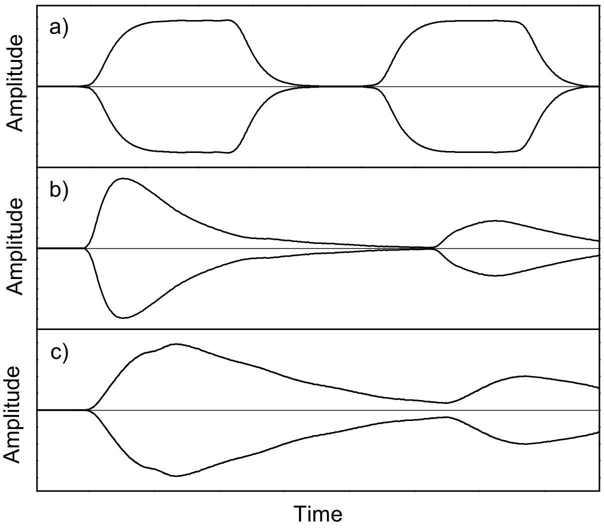

FIG. 5. Limitations of pulse-echo approaches due to acoustic impedance and attenuation illustrated via Hilbert transforms. (a) The interference approach requires echoes with a plateau shaped amplitude as shown here for liquid water at ambient conditions; (b) distorted echoes in nitrogen at 300 K and 10 MPa; (c) distorted and overlapping echoes in nitrogen at 300 K and 7 MPa.

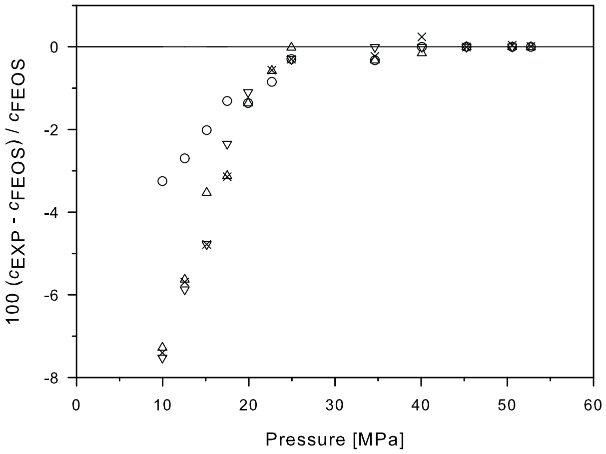

FIG. 6. Speed of sound measurements of nitrogen at 300 K up to a pressure of about 52 MPa for correlation method (○), peak-to-peak measurement for minimum (▽) and maximum (△) amplitudes, and Hilbert transform (×) compared to the FEOS by Span *et al.*[17]

Therefore, measurements below 25 MPa show progressive deviations of up to almost −4% in case of the correlation method and up to about −8% for PPM and HT at 10 MPa. Below 10 MPa, measurements were not feasible here with any pulse-echo method that has been described in the literature, whereas above 25 MPa, all methods converged.

VI. PULSE DESIGN

For obtaining echoes with a maximum that is better readable in case of the single burst approach, the burst should be created with only few periods that are modulated by increasing and decreasing the excitation. Thus, the quartz crystal excitation was modulated here by a sinus burst to which a narrow bandwidth window function (sinus squared) was applied. This has the additional advantage that its narrow-band signal is damping the frequency spectrum such that the distortion of the signal was minimized.[18]

In gaseous fluids, the shape of the echoes is less similar to the crystal excitation than in liquid-like fluids. The lower the fluid density, the more burst and echo differ from each other. This is caused by the sustained oscillation of the quartz crystal due to the low acoustic impedance of the fluid, where the kinetic energy of the oscillating quartz crystal is not efficiently transmitted to the fluid. Compared to liquids, gases have a significantly lower acoustic impedance $I_0 = \rho \cdot c$, which quantifies the resistance of the fluid to the propagation of sound,[19] mainly due to their low density ρ. Exciting the quartz crystal with fewer periods does not alter the problem of a sustained echo.

Fig. 7 (top) depicts a sinus-modulated burst of 20 periods and the corresponding echo in nitrogen at 300 K and 10 MPa. For better visibility, the echo is plotted with a shifted time axis that matches with the start of the excitation burst. Note that the amplitude axis scales for excitation and echo were chosen according to their different magnitudes. This comparison shows that the echo is much longer than the excitation burst and that it reaches its maximum amplitude with a delay.

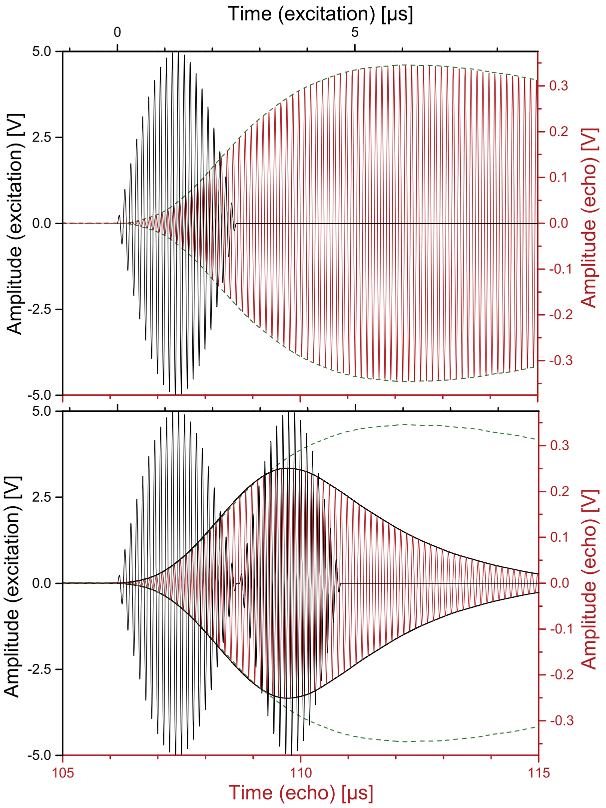

FIG. 7. Excitation burst and echo in nitrogen at 300 K and 10 MPa. Top: Sinusoidal excitation of 20 periods and its echo; bottom: sinusoidal excitation of 20 periods with a brake function of 17 periods and its restrained echo. Dashed lines indicate the Hilbert transform of the echo shown in the upper half of the figure.

In order to prevent a sustained oscillation of the quartz crystal, a brake function was introduced here. The braking was performed by a 180° phase shifted burst immediately following the regular initial burst (20 periods with a peak-to-peak amplitude of 10 V) to which the same sinus squared window function was applied and that was adjustable in its number of periods. Thereby, the oscillation of the quartz crystal was matched to the acoustic impedance that varies for different thermodynamic states of the fluid. To achieve an exact phase shift of the brake function, the excitation frequency was set to the actual resonance frequency of the quartz crystal, which was 7.98 MHz in the present case. Fig. 7 (bottom) shows the resulting echo of an excitation burst with an additional brake function of 17 periods as described above. The echo amplitude has a curved shape that is much better suited for subsequent analysis. It reaches its maximum amplitude approximately at the time of the maximum amplitude of the brake function and it decays much faster than without a brake function.

Fig. 8 shows the shape of both echoes of the excitation bursts illustrated in Fig. 7 with and without brake function. For better visibility, only the HT envelopes of the signals were plotted. In case of an excitation burst with 20 periods and a brake function of 17 periods, no peak shift occurred and the maxima were located at period number 30 of both echoes. Without a brake function, the maximum amplitude appears at

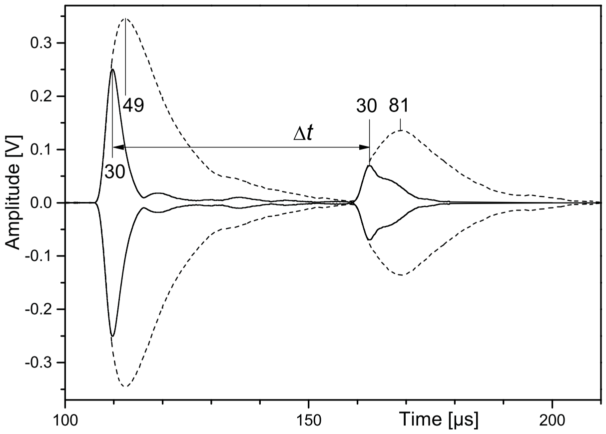

FIG. 8. Hilbert transform of first and second echoes in nitrogen at 300 K and 10 MPa. With a brake function (——), the position of the maximum amplitude is the same in both echoes; without, there is an uneven peak shift (- - -). The numbers indicate the maximum periods of the echoes.

period number 49 of the first echo and period number 81 of the second echo because of uneven echo distortion. Measuring Δt as the time interval between the peaks in the latter case would thus lead to wrong results.

The sinus-modulated burst with a brake function yields a very distinctive echo due to the narrow peak of its amplitude resulting from the fast decay, locating the period with the maximum amplitude in both echoes at the same position. For echoes from modulated excitations without a brake function, this is not the case, cf. Fig. 8.

VII. EXTENSION OF THE MEASUREMENT RANGE FOR GASES

Argon and nitrogen in their gaseous state are well suited as examples for assessing the present method that aims at extending the measurement range of the pulse-echo technique with burst design and signal processing. Due to their importance and availability at high purity (in this work with a given impurity for argon of ≤10 ppm and for nitrogen of ≤8 ppm, both purchased at Linde), these fluids have been measured by many authors.[20–23]

At around ambient temperature, a minimum pressure for argon of 15 MPa was determined by Meier and Kabelac[6] and of 100 MPa by Kortbeek *et al.*[2] and for nitrogen of 20 MPa by Meier[5] and Gedanitz[22] for measuring the speed of sound using the pulse-echo technique with the interference approach. These authors were not able to distinguish the echoes below these pressure limits, due to the challenges of the pulse-echo approaches discussed above. Fig. 9 (top) depicts the speed of sound of argon at 300 K up to 52 MPa measured with the correlation method, the PPM for minimum and maximum amplitude, and the HT using the brake function in comparison to the FEOS by Tegeler *et al.*[24] From 52 MPa down to about 25 MPa, all applied methods converge to the baseline of the FEOS. Below 25 MPa, the deviations for measurements carried out with the correlation method increase up to −3.4% at 5 MPa because of uneven echo distortion. PPM and HT lead to consistent results down to 5 MPa. Below that pressure, measurements were not possible here because of insufficient signal readability.

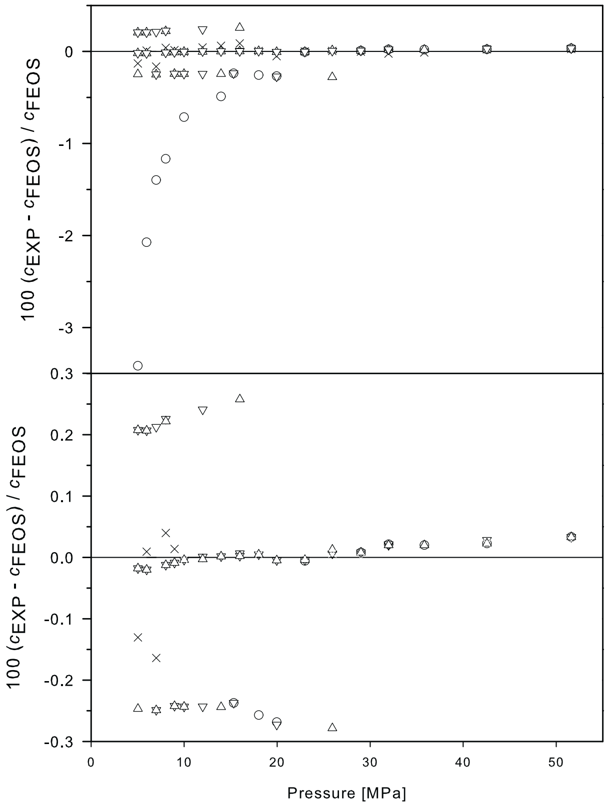

FIG. 9. Top: Speed of sound measurements of argon at 300 K up to a pressure of about 52 MPa with correlation method (○), PPM for minimum (▽) and maximum (△) amplitudes, and Hilbert transform (×) with applied brake function; bottom: magnified view of top. The error bars were omitted for better visibility.

For low pressures, the PPM leads to a number of measuring points with almost constant offsets. These discrete offsets result from misleading minimum and maximum peak amplitudes with a time difference of $1/(8\text{ MHz}) = 0.125\ \mu\text{s}$ due to signal noise and sampling rate of the oscilloscope. This offset increases towards higher pressure, starting at 5 MPa with ±0.2% to almost ±0.3% at 25 MPa due to the ratio of propagation distance and time, cf. Fig. 9 (bottom) and Eq. (1). In contrast to the PPM, the HT method does not depend on discrete periods for Δt measurements and responds to signal noise by scattering results for pressures below 30 MPa. Fig. 9 (bottom) is a magnified view on Fig. 9 (top) and depicts the results from PPM for minimum and maximum amplitudes and HT in a deviation range of ±0.1% over the pressure.

The present measurements were carried out with an apparatus based on the pulse-echo technique with double path length as presented recently.[9] The overall uncertainties of up to ±0.06% are mainly due to the uncertainty of the pressure (±100 Pa) and temperature (±15 mK) measurements. The uncertainty of pressure measurement alone is responsible for almost up to ±0.05% of the uncertainty, cf. Fig. 10. The overall uncertainty, however, is within the experimental error. With an increasing temporal extension of the echo due to

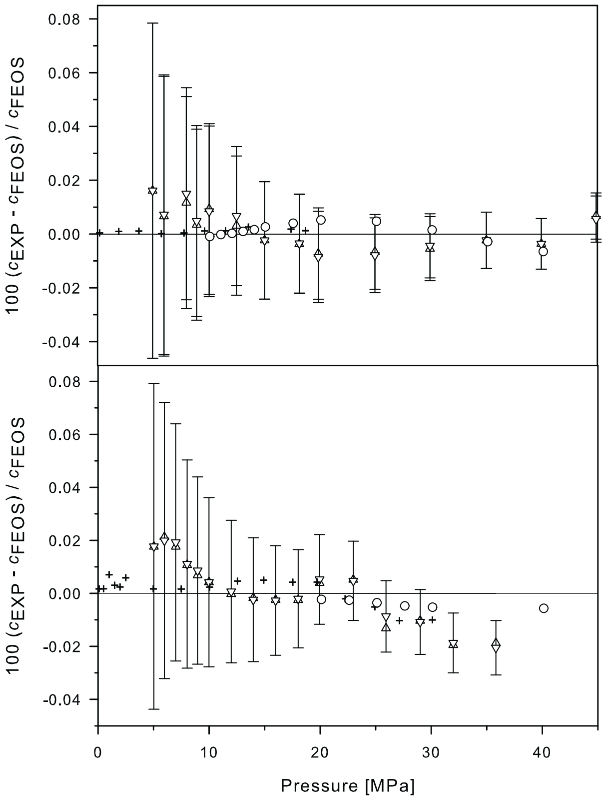

FIG. 10. Top: Speed of sound measurements of argon at 350 K up to a pressure of about 45 MPa with PPM for minimum (▽) and maximum (△) amplitudes, Estrada-Alexanders and Trusler[23] (+), and Meier and Kabelac[6] (○) compared to the FEOS by Tegeler *et al.*;[24] bottom: Speed of sound measurements of nitrogen at 300 K up to a pressure of about 36 MPa for PPM for minimum (▽) and maximum (△) amplitudes, Costa-Gomez *et al.*[20] (+), and Meier[5] (○) compared to the FEOS by Span *et al.*[17]

distortion, as seen for low density fluids, the determination of the speed of sound may be offset due to the ambiguity of the maximum period, cf. Fig. 9. This problem affects the interference approach and the correlation method as well. Therefore, measurements should be carried out starting from a high density, where results are unambiguous, going down to low density state points step by step.

VIII. CONCLUSION

It was shown that the direct time difference measurement approach with burst design and signal processing, either based on PPM or on the HT, has advantages over the traditional correlation method as well as the interference method for fluids in gaseous and supercritical states. The present results show that speed of sound measurements for argon and nitrogen are feasible with the pulse-echo technique down to a pressure of 5 MPa at ambient temperature. Hence, the new procedure extends the measurement range of the pulse-echo technique so that it better overlaps with that of other speed of sound measurement techniques. E.g., argon was measured by Estrada-Alexanders and Trusler[23] in a spherical resonator up to a pressure of 19 MPa.

ACKNOWLEDGMENTS

The authors thank Bernd Henning, Fabian Bause, Jens Rautenberg, and Andreas Schröder from the Chair of Measurement and Engineering at the University of Paderborn for fruitful discussions and their support.

[1] R. Span, *Multiparameter Equations of State: An Accurate Source of Thermodynamic Property Data* (Springer, Berlin, 2000).
[2] P. Kortbeek, M. Muringer, N. Trappeniers, and S. Biswas, Rev. Sci. Instrum. **56**, 1269 (1985).
[3] S. Ball and J. Trusler, Int. J. Thermophys. **22**, 427 (2001).
[4] H. Gedanitz, M. Davila, E. Baumhögger, and R. Span, J. Chem. Thermodyn. **42**, 478 (2010).
[5] K. Meier, "The pulse-echo method for high precision measurements of the speed of sound in fluids," Habilitation thesis (University of the Federal Armed Forces, Hamburg, 2006).
[6] K. Meier and S. Kabelac, Rev. Sci. Instrum. **77**, 123903 (2006).
[7] G. Benedetto, R. Gavioso, P. G. Albo, S. Lago, D. M. Ripa, and R. Spagnolo, Int. J. Thermophys. **26**, 1667 (2005).
[8] C. Lin and J. Trusler, J. Chem. Phys. **136**, 094511 (2012).
[9] F. H. Dubberke, D. B. Rasche, E. Baumhögger, and J. Vrabec, Rev. Sci. Instrum. **85**, 084901 (2014).
[10] J. Borkowski and J. Mroczka, Measurement **43**, 1595 (2010).
[11] S. J. Orfanidis, *Electromagnetic Waves and Antennas* (Rutgers University, Piscataway, NJ, 2014).
[12] S. Sugasawa, Jpn. J. Appl. Phys., Part 1 **41**, 3299 (2002).
[13] P. L. Edwards, J. Acoust. Soc. Am. **73**, 1608 (1983).
[14] R. Gordon, Physica **34**, 398 (1967).
[15] K. Matsuzawa, N. Inoue, and T. Hasegawa, J. Acoust. Soc. Am. **81**, 947 (1987).
[16] J. Champion, C. Langton, G. Meeten, and N. Sherman, Meas. Sci. Technol. **1**, 786 (1990).
[17] R. Span, E. W. Lemmon, R. T. Jacobsen, W. Wagner, and A. Yokozeki, J. Phys. Chem. Ref. Data **29**, 1361 (2000).
[18] F. J. Harris, Proc. IEEE **66**, 51 (1978).
[19] B. Henning and J. Rautenberg, Ultrasonics **44**, 1395 (2006).
[20] M. C. Gomez and J. Trusler, J. Chem. Thermodyn. **30**, 527 (1998).
[21] P. Kortbeek, N. Trappeniers, and S. Biswas, Int. J. Thermophys. **9**, 103 (1988).
[22] H. Gedanitz, "Schallgeschwindigkeits- und Dichtemessungen in Fluiden," Ph.D. thesis (Ruhr-University Bochum, 2010).
[23] A. F. Estrada-Alexanders and J. P. M. Trusler, J. Chem. Thermodyn. **27**, 1075 (1995).
[24] C. Tegeler, R. Span, and W. Wagner, J. Phys. Chem. Ref. Data **28**, 779 (1999).

4.3 Fundamental equation of state correlation for hexamethyldisiloxane based on experimental and molecular simulation data

Monika Thol, Frithjof H. Dubberke , Gabor Rutkai, Thorsten Windmann, Andreas Köster, Roland Span, Jadran Vrabec,
Fluid Phase Equilibria, 418, (2015) 133-155, http://dx.doi.org/10.1016/j.fluid.2015.09.047

Reprinted from Fluid Phase Equilibria (2015) with permission from Elsevier.

The scientific work and discussion was coordinated and consolidated by Monika Thol under supervision of Roland Span and Jadran Vrabec.
The manuscript was prepared by Monika Thol.
Molecular modeling and simulation was carried out by Thorsten Windmann and Gabor Rutkai.
Speed of sound measurements and data evaluation were performed by Frithjof H. Dubberke.
The manuscript was revised by Roland Span and Jadran Vrabec.

This publication is in the context of the precise modelling of thermophysical properties research under supervision of Monika Thol at the chair of Thermodynamic of the University of Bochum headed by Prof. Dr.-Ing. habil. Roland Span and the chair of Thermodynamic and Energy Technology headed by Prof. Dr.-Ing. habil. Jadran Vrabec.

Fluid Phase Equilibria 418 (2016) 133–151

Contents lists available at ScienceDirect

Fluid Phase Equilibria

journal homepage: www.elsevier.com/locate/fluid

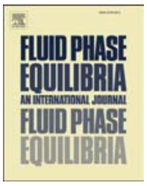

Fundamental equation of state correlation for hexamethyldisiloxane based on experimental and molecular simulation data

M. Thol [a], F.H. Dubberke [b], G. Rutkai [b], T. Windmann [b], A. Köster [b], R. Span [a], J. Vrabec [b, *]

[a] Lehrstuhl für Thermodynamik, Ruhr-Universität Bochum, 44801, Bochum, Germany
[b] Lehrstuhl für Thermodynamik und Energietechnik, Universität Paderborn, 33098, Paderborn, Germany

ARTICLE INFO

Article history:
Received 31 August 2015
Received in revised form
23 September 2015
Accepted 23 September 2015
Available online 23 October 2015

Keywords:
Thermodynamic properties
Fundamental equation of state
Molecular modeling and simulation
Hexamethyldisiloxane

ABSTRACT

An empirical fundamental equation of state correlation in terms of the Helmholtz energy is presented for hexamethyldisiloxane. The relatively small amount of thermodynamic data that is available in the literature for this substances is considerably extended by speed of sound measurements and numerical results for Helmholtz energy derivatives from molecular modeling and simulation. The speed of sound apparatus employed in this work is based on the pulse-echo technique and operates up to 150 MPa in the temperature range between 250 K and 600 K. The range of validity of the equation of state, based on laboratory data from literature and speed of sound data of this work, is from 270 K to 580 K and up to 130 MPa. Molecular simulation data are applied to extend the range of validity up to 1200 K and 600 MPa.

1. Introduction

In heat recovery systems, such as organic Rankine cycles (ORC), one important group of working fluids are siloxanes, which belong to the wider class of organo-silicone compounds. Among others, hexamethyldisiloxane (CAS No.: 107-46-0, $C_6H_{18}OSi_2$) appears to be a good candidate for becoming a widely employed working fluid for high temperature ORC processes. However, accurate thermodynamic data for siloxanes are a prerequisite for optimally designed processes.

Traditionally, thermodynamic properties obtained from experiments are summarized in different forms of empirical equations of state. Correlations of the fundamental equation of state (EOS) are particularly useful, because every thermodynamic equilibrium property can be expressed as a combination of derivatives of the thermodynamic potential in terms of which the EOS is explicit. However, a sufficient amount of thermodynamic data is a key factor when it comes to empirical EOS development.

For hexamethyldisiloxane a fundamental EOS was published by Colonna et al. [1] in 2006. Upon commission of our speed of sound measurement apparatus that is briefly described below, it was found that this model yields unreliable data for this property. In fact, with up to 15%, these deviations were so large that we decided to develop a molecular interaction model to independently corroborate our experimental findings.

Since 2006, the amount of experimental data that is available for hexamethyldisiloxane has expanded, particularly through the work of Abbas [2], but it is still rather poor; additional data sets were generated in the present work by means of speed of sound measurement and molecular modeling and simulation.

In principle, molecular simulation alone could provide any thermodynamic data at any state point and it is more cost and time efficient than laboratory measurements. However, its predictive capability is limited by the quality of the underlying molecular interaction model. Although molecular interaction models are usually adjusted only to a small amount of experimental data, it is generally accepted that they can provide reasonably good predictions for other state points and properties that were not considered during their optimization. However, consistently good inter- and extrapolation ability cannot be guaranteed. Our previous experience with several substances indicated that satisfactory performance still can be expected with respect to predicting various Helmholtz energy derivatives in the homogeneous fluid region, even if the molecular model was optimized exclusively to experimental vapor–liquid equilibrium data [3–7]. Nevertheless, due to the inherent uncertainty of molecular models, experimental data are still essential for EOS development.

Acoustic measurements allow for a fast and convenient access to

---

* Corresponding author. Warburger Str. 100, 33098, Paderborn, Germany.
E-mail address: jadran.vrabec@upb.de (J. Vrabec).

http://dx.doi.org/10.1016/j.fluid.2015.09.047
0378-3812/

the speed of sound. In case of fluids, such measurements contribute substantially to the development and parameterization of EOS [8] because accurate speed of sound data can efficiently be obtained over a large range of temperature and pressure. The common measuring principle for determining the speed of sound of liquids is the pulse-echo technique, which was introduced by Kortbeek et al. [9]. In this method, sound waves, emitted by an excited quartz crystal, propagate through a fluid over a known propagation distance, are reflected and travel back to the quartz crystal. The interference and correlation approaches are common for the pulse-echo technique for determining the propagation time of the wave signal. Here, the correlation approach was employed for the speed of sound measurement.

2. Speed of sound measurement

2.1. Measurement principle

Speed of sound measurements were carried out with the pulse-echo technique. By emitting a high frequency modulated burst signal with a piezoelectric quartz crystal, which was positioned in the fluid between two reflectors with different path lengths l_1 and l_2, where $l_1 < l_2$, the speed of sound was determined by the time measurement of the signal propagation through the fluid over a known distance [10,11]. The speed of sound, neglecting dispersion and diffraction effects, is given by the ratio of the propagation distance and the propagation time

$$w = \frac{2(l_2 - l_1)}{\Delta t}. \tag{1}$$

The measurement of the propagation time difference Δt was based on the correlation method, which was also used by Ball and Trusler [12], combined with a signal enhancement by applying Fast Fourier Transformation (FFT) to the original echo signals [13,14].

The quartz crystal was excited with a burst of 20 cycles, typically with a voltage of 10 V peak-to-peak. Both echoes were sampled, stored to a computer by an oscilloscope (Agilent, DSO1022A) and identified via a threshold. On the basis of the time intervals where the signals exceeded the specified threshold, a significantly extended number of data points in the time interval Δt_e was marked around both echo maxima, starting at t_1 for the first echo and at t_2 for the second echo, cf. Fig. 1 (top).

Because the second echo is affected by greater attenuation due to the longer propagation distance than the first echo, the ratio of the maximum amplitudes of the first echo and the second echo had be determined. The resulting amplitude factor r, which depends on the fluid and its thermodynamic state, is required in the correlation approach to consider attenuation [12]. This was done here by multiplying the second echo, i.e. the signal data within Δt_e after t_2, with the amplitude factor to achieve the same maximum peak magnitude for both echoes, cf. Fig. 1 (center).

The correlation z overlays the signals of both echoes by

$$z(\Delta t) = \sqrt{\sum_{t_1}^{t_1+\Delta t_e} [x(t)\cdot r x(t+\Delta t)]^2}, \tag{2}$$

where $x(t)$ refers to the echo amplitude at the time t. The time at the maximum of z is the measured propagation time difference Δt, cf. Fig. 1 (bottom).

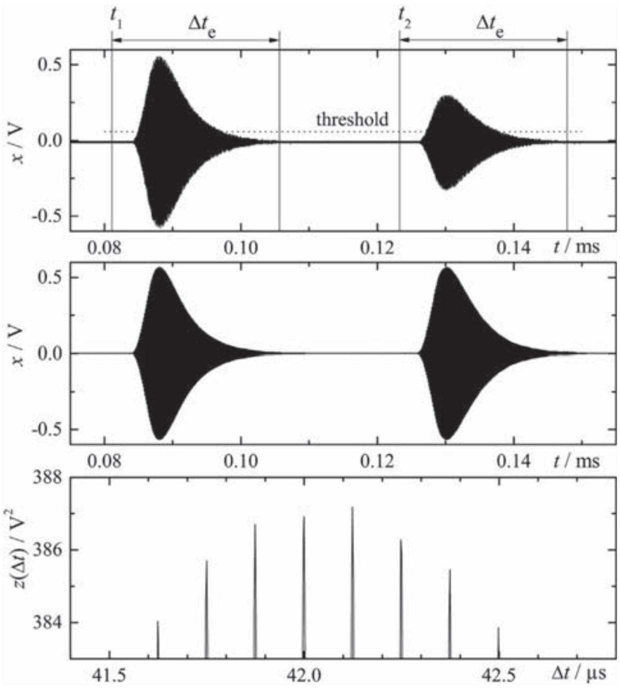

Fig. 1. Steps of the correlation method. Top: First and second echo signals identified via a threshold. Center: Signal reconstructed by Fast Fourier Transformation where the amplitude of the second echo is the same as the amplitude of the first echo. Bottom: Correlation function $z(\Delta t)$ according to Eq. (2).

2.2. Measurement procedure

After filling siloxane into the cell, it was compressed to about 20 MPa by a hand-pump and an equilibration time of around 1 h was given to reach a constant pressure level. Each isotherm was studied from high pressure to vapor pressure, where the pressure was measured with a transducer (Honeywell TJE with an operating range up to 70 MPa), which was calibrated with a dead weight tester (Degranges and Hout, 5201-S) and protected by a blowout disc.

The temperature was measured with a Pt100 thermometer (Rössel Messtechnik RM-type), which was mounted in the wall of the pressure cylinder next to the quartz and was calibrated with a standardized 25 Ω platinum thermometer (Rosemount 162 CE). Hence, the overall uncertainty of the temperature measurement results according to the error propagation law due the individual uncertainty contributions amounts to $u_T = \pm 15$ mK.

For controlling the cell with a high accuracy over a wide temperature range, the thermostat was constructed with three nested copper shields. Each was monitored with respect to the temperature and equipped with one independently adjustable heater, which was controlled with a combination of a PID controller and an additional proportional (P) controller to quickly specify a constant temperature without overshooting.

The referencing of the path length distance difference $\Delta l = l_2 - l_1$ was carried out with water, which is available at high purity and for which highly accurate speed of sound measurements are available over a wide range of states, see Ref. [15]. The experimental speed of sound data were corrected by the diffraction correction by Harris [16], where significant dispersion effects are not expected for a resonance frequency of 8 MHz [17].

2.3. Results

Speed of sound measurements were carried out for a set of 12 isotherms in the temperature range from 365 K to 573 K up to 20 MPa, cf. Fig. 2. The siloxane was obtained from WACKER with a given purity of ≥99% and was degassed before experimental measurements were carried out.

The uncertainty of the present measurements is larger for lower pressures mainly due to the uncertainty of the pressure sensor. The operating range of the pressure sensor was up to 70 MPa with an accuracy of ±0.035% of the full scale. Therefore, the absolute uncertainty was 0.025 MPa. This uncertainty had the largest impact at high temperatures and low pressures. The overall speed of sound measurement uncertainty u_w is composed of the relevant contributions due to uncertainties of temperature and pressure measurements as well as the uncertainty of the referencing procedure.

According to the error propagation law, the total uncertainty was between 0.03% and 0.3%. The higher end of this uncertainty range is mainly caused by the fact that the relative uncertainty of the pressure measurement was significantly higher at low pressures, combined with the high isothermal compressibility of the fluid at such thermodynamic states. Numerical measurement data together with their uncertainties can be found in the Supplementary Material.

3. Molecular modeling and simulation

3.1. Molecular model

A molecular interaction model for hexamethyldisiloxane was developed here. It was validated with respect to experimental data or respective correlations from the literature, including saturated liquid density, vapor pressure, enthalpy of vaporization, homogeneous liquid properties (density and speed of sound), second virial coefficient, and transport properties (thermal conductivity and shear viscosity).

The geometry of the model was determined by quantum chemical calculations using the software package GAMESS(US) [18] with the Hartree-Fock method and the 6-31G basis set. Three Lennard-Jones (LJ) sites and three point charges were placed on the silica (Si) and oxygen (O) atoms, while the six methyl groups (CH_3) were represented with LJ sites only, cf. Fig. 3. Its point charge magnitudes were specified such that they correspond to a dipole moment of $2.67 \cdot 10^{-30}$ Cm (a value taken from the DIPPR database [19]). The initial values of the LJ energy (ε) and size (σ) parameters of the CH_3 and O sites were adopted from Schnabel et al. [20] and Vrabec et al. [21], respectively. The LJ parameters of the Si sites were adjusted to experimental saturated liquid density and vapor pressure data. In a last step, all model parameters, including geometric structure and polarity, were fine-tuned with the reduced unit method [22]. The resulting model parameters are listed in Table 1.

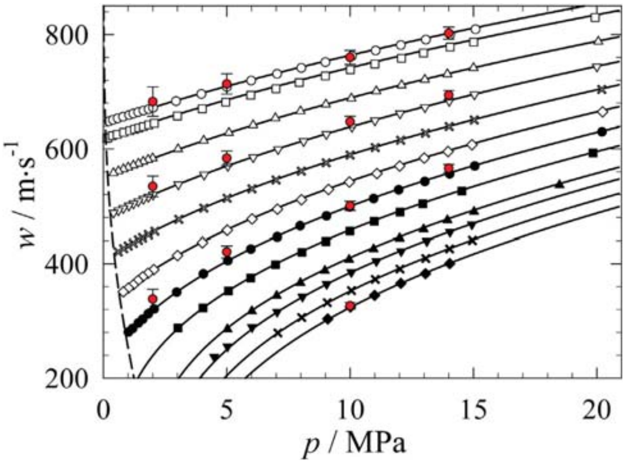

Fig. 2. Speed of sound of hexamethyldisiloxane. Present experimental data: ○ 365 K, □ 373 K, △ 393 K, ▽ 413 K, × 433 K, ◊ 453 K, ● 473 K, ■ 493 K, ▲ 518 K, ▼ 533 K, × 553 K, ◆ 573 K; ○ (red) present simulation data; — present equation of state; — — vapor pressure curve. (For interpretation of the references to color in this figure caption, the reader is referred to the web version of this article.)

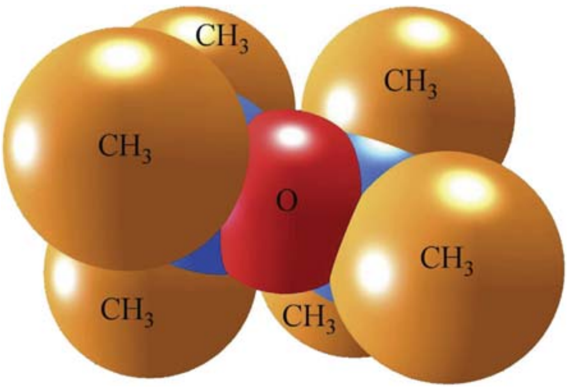

Fig. 3. Present molecular interaction model for hexamethyldisiloxane. CH_3: methyl site, O: oxygen site, not labeled: silica site. Note that the sphere diameters correspond to the Lennard-Jones size parameters, which are depicted according to the molecular geometry scale.

3.2. Validation of the molecular model

To validate the present molecular interaction model, simulation results for vapor–liquid equilibria, homogeneous liquid density, speed of sound, second virial coefficient, and transport properties were compared with experimental data from the literature and with correlations from the DIPPR database [19]. All simulation details and numerical data are given in the Supplementary Material. The simulation data for vapor pressure, saturated liquid density, saturated vapor density, and enthalpy of vaporization are presented in absolute plots in the Supplementary Material. As discussed in section 4.3 in detail, for the vapor pressure relative deviations between the molecular simulation data and the present EOS are less than 4% for all simulation points, except for the lowest temperature. Note that the experimental data scatter in this range, too. Experimental data for the saturated liquid density are available between 213 K and 358 K only. The simulation data in this region are well within the scatter of the experimental data and the uncertainty of the DIPPR correlation [19]. The simulation results for the enthalpy of

Table 1
Parameters of the present molecular interaction model for hexamethyldisiloxane. Lennard-Jones sites are denoted by the modeled atoms or atomic groups. Electrostatic sites are denoted by point charge magnitudes q. Coordinates are given with respect to the center of mass in a principal axes system.

Interaction site	x	y	z	σ	ε/k_B	q
	Å	Å	Å	Å	K	e
CH_3	−2.2796	−0.8698	−0.3545	3.8144	121.3515	
CH_3	−2.2150	1.2764	1.8825	3.8144	121.3515	
CH_3	0.5674	0.7717	−2.5502	3.8144	121.3515	
Si	−1.2334	−0.0730	1.0059	3.5133	15.1500	0.1458
O	0.1238	0.6680	0.3350	3.1180	43.6148	−0.2916
Si	1.2923	0.3890	−0.8475	3.5133	15.1500	0.1458
CH_3	−0.6830	−1.3930	2.2409	3.8144	121.3515	
CH_3	1.8613	−1.4145	−0.7878	3.8144	121.3515	
CH_3	2.7335	1.5447	−0.4734	3.8144	121.3515	

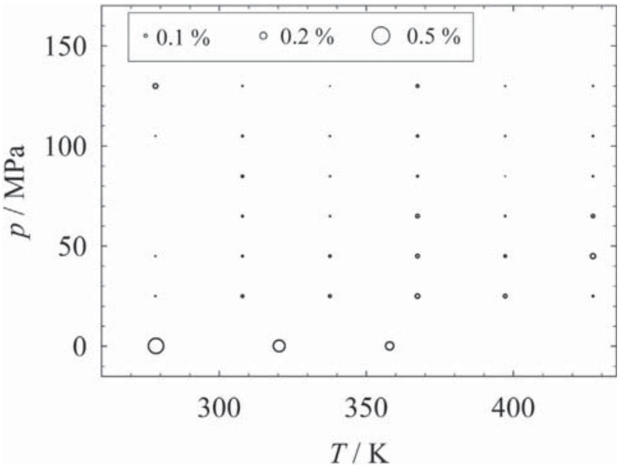

Fig. 4. Density in the homogeneous liquid region of hexamethyldisiloxane. Relative deviations between present simulation data and experimental data by Abbas [2] and McLure et al. [23]. ($\Delta z = (z_{\text{sim}} - z_{\text{exp}})/z_{\text{exp}}$). The size of the bubbles indicates the magnitude of the relative deviation.

vaporization agree well with the experimental data over the whole temperature range from 287 K to 500 K. The relative deviations are throughout less than about 1.5%, with the exception of the point at 495 K.

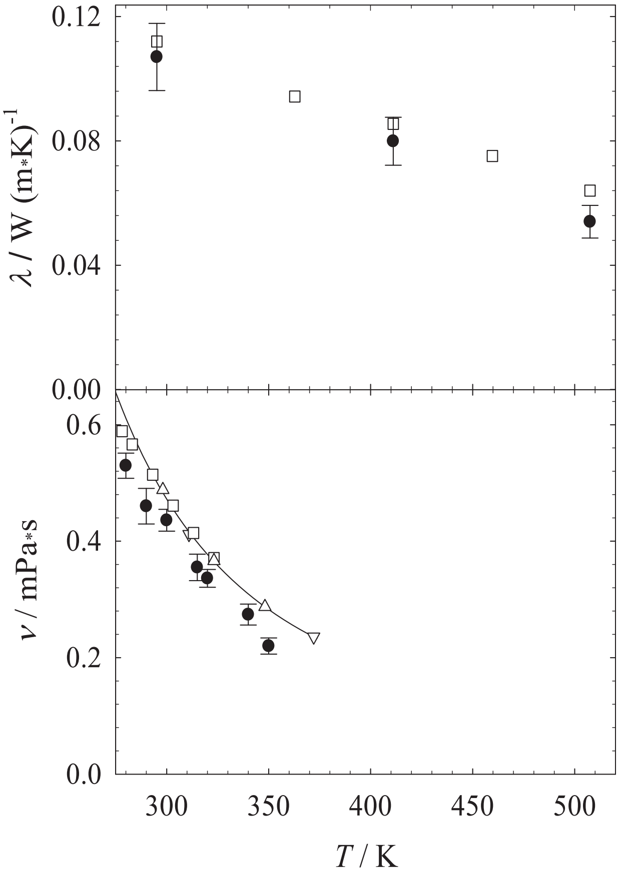

Fig. 5. Thermal conductivity at 10 MPa (top) and shear viscosity at 1 atm (bottom) of hexamethyldisiloxane: ● present simulation data; □ experimental data by Abbas [2], △ Hurd [26], and ▽ Wilcock [27]; — correlation of experimental data from the DIPPR database [19].

Table 2
Parameters of the ideal contribution of the present equation of state for hexamethyldisiloxane according to Eq. (10).

i	m_i	θ_i/K
1	18.59	20
2	29.58	1400
3	19.74	3600
4	4.87	6300
c_0	3.0	
c^{I}	−10.431499	
c^{II}	72.110754	

Simulation results for the homogeneous liquid density were compared to experimental data published by McLure et al. [23] and Abbas [2]. McLure et al. [23] provide data at 1 atm, Abbas [2] performed measurements over a wide temperature and pressure range. Fig. 4 shows the results of the comparison at temperatures from 303 K to 427 K up to a pressure of 130 MPa. It can be seen that the agreement between simulation and experimental data is very satisfying. In general, the relative deviation is less than 0.2%. For the three data points at 1 atm it is slightly higher.

The speed of sound in the liquid state was calculated by simulation, taking the ideal gas contribution of the present EOS into account (see section 4.1). These results were compared with the experimental data generated in the present work. As can be seen in Fig. 2, the simulation results are in line with the experimental data points at the four investigated isotherms 365 K, 413 K, 473 K and 573 K up to a pressure of 14 MPa. Nearly all simulation points agree with the experiment within their statistical uncertainties.

The second virial coefficient was predicted over a temperature range from 220 K to 1500 K by evaluating Mayer's *f*-function. This

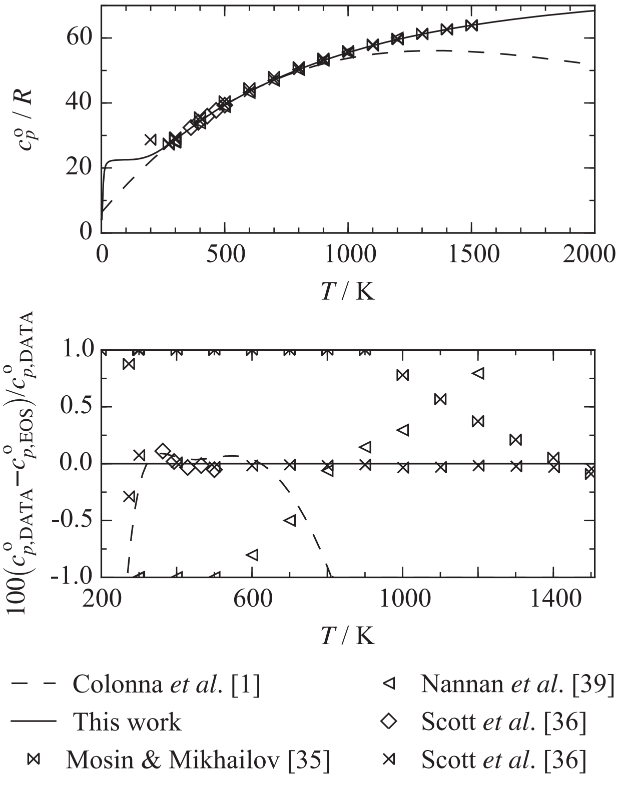

Fig. 6. Isobaric heat capacity of the ideal gas of hexamethyldisiloxane.

Table 3
Parameters of the residual contribution of the present equation of state for hexamethyldisiloxane according to Eq. (11), where $l_i = 1$.

i	n_i	t_i	d_i	p_i	η_i	β_i	γ_i	ε_i
1	$0.5063651 \cdot 10^{-1}$	1.000	4	–				
2	$0.8604724 \cdot 10^{+1}$	0.346	1	–				
3	$-0.9179684 \cdot 10^{+1}$	0.460	1	–				
4	$-0.1146325 \cdot 10^{+1}$	1.010	2	–				
5	$0.4878559 \cdot 10^{+0}$	0.590	3	–				
6	$-0.2434088 \cdot 10^{+1}$	2.600	1	2				
7	$-0.1621326 \cdot 10^{+1}$	3.330	3	2				
8	$0.6239872 \cdot 10^{+0}$	0.750	2	1				
9	$-0.2306057 \cdot 10^{+1}$	2.950	2	2				
10	$-0.5555096 \cdot 10^{-1}$	0.930	7	1				
11	$0.9385015 \cdot 10^{+1}$	1.330	1	–	1.0334	0.4707	1.7754	0.8927
12	$-0.2493508 \cdot 10^{+1}$	1.680	1	–	1.5440	0.3200	0.6920	0.5957
13	$-0.3308032 \cdot 10^{+1}$	1.700	3	–	1.1130	0.4040	1.2420	0.5590
14	$-0.1885803 \cdot 10^{+0}$	3.080	3	–	1.1130	0.5170	0.4210	1.0560
15	$-0.9883865 \cdot 10^{-1}$	5.410	1	–	1.1100	0.4320	0.4060	1.3000
16	$0.1111090 \cdot 10^{+0}$	1.400	2	–	7.2000	7.2000	0.1630	0.1060
17	$0.1061928 \cdot 10^{+0}$	1.100	3	–	1.4500	1.2000	0.7950	0.1810
18	$-0.1452454 \cdot 10^{-1}$	5.300	1	–	4.7300	35.8000	0.8800	0.5250

approach was described e.g. by Eckl et al. [24]. The present results are shown in section 4.5, where the mean absolute deviation over the whole considered temperature range is below 0.44 $\mathrm{dm}^3 \cdot \mathrm{mol}^{-1}$.

Thermal conductivity and shear viscosity of liquid hexamethyldisiloxane were obtained by equilibrium molecular dynamics simulations following the Green-Kubo formalism, cf. Guevara-Carrion et al. [25]. Fig. 5 shows the simulation results in comparison with experimental data from the literature and a correlation from the DIPPR database [19]. For the thermal conductivity, simulations were carried out at 10 MPa, cf. Fig. 5 (top). The simulations agree with the experimental data by Abbas [2] mostly within their statistical uncertainties. At 500 K, there is some deviation. The shear viscosity experimental data at 1 atm, published by Abbas [2], Hurd [26], and Wilcock [27], were used for comparison. The shear viscosity from simulation is about 0.1 mPa s below the experimental data in the entire temperature range from 280 K to 350 K, cf. Fig. 5 (bottom). The mean relative deviation of the simulation data with respect to the correlation from the DIPPR database [19] is about 12%.

3.3. Large scale thermodynamic data generation

In principle, once a molecular interaction model is available, any thermodynamic information can be obtained from molecular simulation. However, the generation of a data set that contains as much non-redundant thermodynamic information as possible may look cumbersome in practice, because standard textbook approaches in the molecular simulation literature imply that specific statistical mechanical ensembles are required for particular thermodynamic properties. It is true that certain properties have simpler statistical analogs in certain ensembles and may be difficult to derive in others, but it is nevertheless possible. The statistical mechanical formalism proposed by Lustig [28,29] was designed to provide an arbitrary number of Helmholtz energy derivatives

$$A^{\mathrm{r}}_{xy} = \tau^x \delta^y \frac{\partial^{x+y} \alpha^{\mathrm{r}}(\tau,\delta)}{\partial \tau^x \partial \delta^y} = (1/T)^x \rho^y \frac{\partial^{x+y} \alpha^{\mathrm{r}}(T,\rho)}{\partial (1/T)^x \partial \rho^y}, \tag{3}$$

from a single molecular simulation run for a given state point. In Eq. (3), α is the reduced Helmholtz energy, T the temperature, ρ the density, R the molar gas constant, $\tau = T_{\mathrm{c}}/T$ the inverse reduced temperature, and $\delta = \rho/\rho_{\mathrm{c}}$ the reduced density, in which T_{c} is the critical temperature and ρ_{c} the critical density. α is commonly divided into an ideal (superscript "o") and residual (superscript "r") contribution

$$\alpha(\tau,\delta) = \frac{a^{\mathrm{o}}(T,\rho) + a^{\mathrm{r}}(T,\rho)}{RT} = \alpha^{\mathrm{o}}(\tau,\delta) + \alpha^{\mathrm{r}}(\tau,\delta), \tag{4}$$

where a is the molar Helmholtz energy. The ideal contribution $\alpha^{\mathrm{o}}(T,\rho) = \alpha^{\mathrm{o}}(T) + \alpha^{\mathrm{o}}(\rho)$ corresponds to the value of $\alpha(T,\rho)$ when no intermolecular interactions are at work [8]. The density dependence of $\alpha^{\mathrm{o}}(T,\rho)$ is known from the ideal gas law and it is $\alpha^{\mathrm{o}}(\rho) = \ln(\rho/\rho_{\mathrm{ref}})$. The exclusively temperature dependent ideal part $\alpha^{\mathrm{o}}(T)$ has a non-trivial temperature dependence and it is often determined by spectroscopy or *ab initio* calculations. Although molecular interaction models with internal degrees of freedom may describe $\alpha^{\mathrm{o}}(T)$ accurately, the residual contribution $\alpha^{\mathrm{r}}(T,\rho) = \alpha(T,\rho) - \alpha^{\mathrm{o}}(T,\rho)$ is typically the target of molecular simulation.

The formalism proposed by Lustig is an implemented feature of our molecular simulation tool *ms*2 [30,31] that yields up to eight derivatives of the residual Helmholtz energy. With this method, the analytical derivatives of Eq. (3) can be directly fitted to A^{r}_{xy} simulation results, unlike usual thermodynamic properties, such as pressure p, isochoric heat capacity c_v, isobaric heat capacity c_p, and speed of sound w

$$\frac{p}{\rho RT} = 1 + A^{\mathrm{r}}_{01}, \tag{5}$$

$$\frac{c_v}{R} = -\left(A^{\mathrm{o}}_{20} + A^{\mathrm{r}}_{20}\right), \tag{6}$$

$$\frac{c_p}{R} = -\left(A^{\mathrm{o}}_{20} + A^{\mathrm{r}}_{20}\right) + \frac{\left(1 + A^{\mathrm{r}}_{01} - A^{\mathrm{r}}_{11}\right)^2}{1 + 2A^{\mathrm{r}}_{01} + A^{\mathrm{r}}_{02}}, \tag{7}$$

$$\frac{Mw^2}{RT} = 1 + 2A^{\mathrm{r}}_{01} + A^{\mathrm{r}}_{02} - \frac{\left(1 + A^{\mathrm{r}}_{01} - A^{\mathrm{r}}_{11}\right)^2}{A^{\mathrm{o}}_{20} + A^{\mathrm{r}}_{20}}, \tag{8}$$

that are linear or non-linear functions of A_{xy}. This approach is a convenient route to obtain an arbitrary number of independent thermodynamic properties, and its contribution to support EOS development was recently shown [3–7]. The large scale molecular simulation data set of the present work contains five derivatives A^{r}_{10}, A^{r}_{01}, A^{r}_{20}, A^{r}_{11}, and A^{r}_{02} as well as A^{r}_{00} at 194 state points that are well distributed in the homogeneous fluid region. At each state point 864 particles were sufficiently equilibrated and then sampled for 2 million production cycles with *NVT* Monte Carlo simulations [32]. Electrostatic long-range corrections were approximated by the reaction field method [33]. The reduced residual Helmholtz energy A^{r}_{00} was determined by Widom's test particle insertion [34]. A discussion of these data is given in section 4.6, their numerical values can be found in the Supplementary Material.

Table 4
Critical parameters from the literature, where the critical density was not measured, but estimated from theoretical models.

Authors	T_{c}	p_{c}	ρ_{c}
	K	MPa	$\mathrm{mol} \cdot \mathrm{dm}^{-3}$
Dickinson et al. [48]	518.8	1.91	1.715
McLure and Dickinson [45]	518.7	1.92	
McLure and Neville [49]			1.589
Nikitin et al. [50]	519	1.92	
Young [51]	516.6	1.91	1.745
Young [52]	516.6	1.91	1.744
This work	518.7	1.93	1.653

4. Fundamental equation of state correlation

In this section, an EOS for hexamethyldisiloxane is presented. Comparisons are made to experimental as well as molecular simulation data, and the physical and extrapolation behavior is analyzed. The present EOS for hexamethyldisiloxane is written in terms of the reduced Helmholtz energy as a function of temperature and density. Because this is a thermodynamic potential, every other equilibrium thermodynamic property can be obtained by differentiating Eqs. (10) and (11) analytically and combining the results. Examples, e.g. for the pressure, are given in Eqs. (5)–(8).

4.1. Ideal gas contribution

The exclusively temperature dependent ideal contribution $\alpha^o(\tau)$ of the reduced Helmholtz energy $\alpha(\tau,\delta)$ was derived from a c_p^o equation

$$\frac{c_p^o}{R} = n_0 + \sum_{i=1}^{I_{\mathrm{Pol}}} n_i \tau^{t_i} + \sum_{i=I_{\mathrm{Pol}}+1}^{I_{\mathrm{Pol}}+I_{\mathrm{PE}}} m_i \left(\frac{\theta_i}{T}\right)^2 \frac{\exp\left(\theta_i/T\right)}{\left(\exp\left(\theta_i/T\right)-1\right)^2}. \qquad (9)$$

For the application to a fundamental EOS in terms of the Helmholtz energy, this equation has to be integrated twice with respect to τ

$$\begin{aligned}\alpha^o(\tau,\delta) = {} & c^{\mathrm{II}} + c^{\mathrm{I}}\tau + c_0 \ln\left(\tau\right) + \sum_{i=1}^{I_{\mathrm{Pol}}} c_i \tau^{t_i} \\ & + \sum_{i=I_{\mathrm{Pol}}+1}^{I_{\mathrm{Pol}}+I_{\mathrm{PE}}} m_i \ln\left(1-\exp\left(-\theta_i/T_c\tau\right)\right) + \ln\left(\delta\right).\end{aligned} \qquad (10)$$

The integration constants c^{I} and c^{II} can be chosen arbitrarily. However, the most common reference state is the normal boiling point (NBP). Here, the temperature and density of the saturated liquid at the reference pressure $p_0 = 1$ atm have to be determined. At this state point, the default values of the corresponding reference entropy $s_0(T_{\mathrm{NBP}}, p_0 = 1\ \mathrm{atm})$ and enthalpy $h_0(T_{\mathrm{NBP}}, p_0 = 1\ \mathrm{atm})$ are set to be zero. Therefore, c^{I} and c^{II} depend on the residual part of the present equation of state.

In general, c_p^o equations are correlated to data for the isobaric heat capacity of the ideal gas. These data can be determined from spectroscopy, statistical mechanics, or extrapolation from gaseous speed of sound or isobaric heat capacity measurements. Spectroscopic data are very difficult to analyze for complex molecules. Therefore, they can rarely be used to set up equations of state. When extrapolating ideal gas heat capacities from experimental speed of sound or isobaric heat capacity data, highly accurate measurements are mandatory. Thus, such data are only available for well investigated fluids. Therefore, most data were determined by means of statistical mechanics. Depending on the complexity of the molecule, these data can be associated with high uncertainties so that they have to be treated carefully. When developing a c_p^o equation, some boundary conditions have to be kept in mind. The functional form of Eq. (9) is physically based and the contributions of molecular translation and rotation are combined in the temperature independent part n_0. For molecules like hexamethyldisiloxane, it can be assumed that the degrees of freedom of both contributions are fully excited also for very low temperatures. Therefore, $n_0 = 4$, corresponding to three degrees of freedom for translation and three degrees of freedom for rotation. The temperature dependent contribution of the molecular vibrations was modeled by

Table 5
Average absolute relative deviations of experimental vapor pressure and saturated liquid density data from the present equation of state for hexamethyldisiloxane. All temperatures were adapted to the ITS-90 scale. Datasets, which were applied to the fit, are marked with an asterisk.

Authors	No. of data	Temperature range	Average absolute relative deviations (AAD)/%			
			LT	MT	HT	Overall
Vapor pressure p_v						
Abbas [2]	18	284–375	1.894	2.214	–	2.072
Benkeser & Krysiak [54]	1	372.62	–	2.966	–	2.966
Bolotov et al. [55]	1	373.12	–	1.541	–	1.541
Dickinson et al. [48]	3	303–316	0.093	0.041	–	0.076
Flaningam & Williams [56]	1	373.65	–	0.023	–	0.023
Flaningam [57]	15	302–384	0.765	0.318	–	0.437
Guzman et al. [58]	6	333–374	–	0.589	–	0.589
Hunter et al. [59]	1	372.62	–	2.966	–	2.966
Kaczmarek & Radecki [60]	1	374.62	–	2.833	–	2.833
Kaczmarek & Radecki [61]	1	374.02	–	1.066	–	1.066
Kaczmarek & Radecki [62]	1	374.02	–	1.066	–	1.066
Kaczmarek [63]	1	373.62	–	0.099	–	0.099
Kaczmarek [64]	1	373.92	–	0.774	–	0.774
Kaczmarek [65]	1	374.65	–	2.912	–	2.912
Killgore et al. [66]	1	372.98	–	0.663	–	0.663
McLure & Dickinson [45]*	19	491–519	–	1.615	0.380	1.030
Pedersen et al. [67]	1	373.44	–	0.620	–	0.620
Radecki et al. [68]	2	293–375	0.860	1.359	–	1.110
Radecki & Kaczmarek [69]	2	373–374	–	1.541	–	1.541
Radecki & Kaczmarek [70]	1	373.12	–	1.541	–	1.541
Radecki & Kaczmarek [71]	1	373.37	–	0.822	–	0.822
Reuther & Reichel [72]	1	373.62	–	0.099	–	0.099
Sauer [73]	1	373.57	–	0.243	–	0.243
Scott et al. [36]*	21	309–412	0.044	0.030	–	0.031
Speier [74]	1	372.12	–	4.376	–	4.376
Stull [75]	10	244–373	18.34	4.428	–	12.78
Voronkov [76]	1	373.52	–	0.388	–	0.388
Waterman et al. [77]	1	373.82	–	0.043	–	0.043
Zhang et al. [78]	1	373.67	–	0.035	–	0.035
Saturated liquid density ρ'						
Gubareva [79]	10	273–354	0.249	0.085	–	0.167
Guzman et al. [58]	5	333–359	–	1.335	–	1.335
Mills & MacKenzie [80]	2	293–303	0.109	–	–	0.109

Planck–Einstein terms. For high temperatures, it has to be ensured that the ideal gas heat capacity approaches a maximum value related to fully excited degrees of freedom considering all contributions, i.e. translation, rotation, and vibration. Since it is too complex to express these contributions on a strictly physical basis, the Planck–Einstein terms were treated empirically. The ideal contribution of the present EOS for hexamethyldisiloxane thus consists of four Planck–Einstein terms and the corresponding parameters are given in Table 2. In Fig. 6, the representation of the isobaric heat capacity of the ideal hexamethyldisiloxane gas is illustrated. The upper part of that figure shows the absolute trend of c_p^o/T as a function of temperature. The present equation has a correct extrapolation behavior for low temperatures, i.e. $c_p^o(T \to 0\ \mathrm{K}) = 4R$. For high temperatures, an asymptotic behavior of the equation can be observed. Colonna et al. [1] have chosen a simple polynomial approach for fast calculations. This can be helpful when insufficient data are available for the correlation. However, these polynomial terms have to be used carefully because it is easily possible to compromize the extrapolation behavior. As a results of the chosen functional form, the transition of the equation of Colonna et al. [1] to very low temperatures yields a value of 6.3R and for increasing temperatures the ideal gas heat capacity decreases.

In Fig. 6 (bottom), relative deviations of literature data from the present EOS are shown. Only three different datasets are available. Mosin and Mikhailov [35] derived their data from statistical mechanics. Since no information is given on the accuracy of these data, they were not considered in the development of the present c_p^o equation. The data of Scott et al. [36] were gained from low temperature calometric measurements. Due to limitations of their apparatus, the temperature range was only 360 K to 500 K. Additionally, they used results from investigations on the barrier restricting internal rotation around the Si–O bond to determine the ideal gas heat capacity theoretically, which are in good agreement with their measurements. Therefore, the low temperature region ($T < 500$ K) of the present equation was correlated to the experimental results of Scott et al. [36], and higher temperatures were modeled with the help of their theoretical results. For $T > 300$ K, the ideal gas heat capacity is reproduced within 0.1%, which is also claimed to be the uncertainty of the present equation. For lower temperatures deviations increase.

Table 6

Average absolute relative deviations of the experimental data in the homogeneous region from the present equation of state for hexamethyldisiloxane. All temperatures were adapted to the ITS-90 scale. Datasets, which were applied to the fit, are marked with an asterisk.

Authors	No. of data	Temperature and pressure range		Average absolute relative deviation (AAD)/%						
				Gas	Liq	Crit. Reg.	Supercritical fluid			Overall
		T	p				LD	MD	HD	
$p\rho T$ data										
Abbas [2]*	459	278–438	0.9–130	–	0.071	–	–	–	–	0.071
Anderson et al. [88]	1	293.15	0.101325	–	0.120	–	–	–	–	0.120
Bolotov et al. [55]	1	293.15	0.101325	–	0.081	–	–	–	–	0.081
Dickinson [89] [b]	5	303–304	100–501	–	0.476	–	–	–	–	0.476
Fox et al. [90]	1	293.14	0.101325	–	0.174	–	–	–	–	0.174
Gaines [91]	1	297.14	0.101325	–	1.025	–	–	–	–	1.025
Golik and Cholpan [92]	1	303.13	0.101325	–	0.451	–	–	–	–	0.451
Good et al. [93]	1	298.14	0.101325	–	0.168	–	–	–	–	0.168
Hunter et al. [59]	1	298.14	0.101325	–	0.122	–	–	–	–	0.122
Hurd [26] [b]	3	273–314	0.1–1	–	0.275	–	–	–	–	0.275
Kaczmarek [63]	1	293.15	0.101325	–	0.199	–	–	–	–	0.199
Kaczmarek [94]	1	293.15	0.101325	–	0.173	–	–	–	–	0.173
Kaczmarek [64]	1	293.15	0.101325	–	0.199	–	–	–	–	0.199
Kaczmarek [65]	1	293.15	0.101325	–	0.199	–	–	–	–	0.199
Kaczmarek and Radecki [60]	1	293.15	0.101325	–	0.199	–	–	–	–	0.199
Kaczmarek and Radecki [61]	1	293.15	0.101325	–	0.199	–	–	–	–	0.199
Killgore et al. [66]	1	298.14	0.101325	–	0.234	–	–	–	–	0.234
Marcos et al. [95]	61	448–574	0.1–1	0.271	–	–	0.455	–	–	0.365
Matteoli et al. [96]	1	298.15	0.101325	–	0.089	–	–	–	–	0.089
McLure et al. [23]	13	278–358	0.1–1	–	0.328	–	–	–	–	0.328
Radecki et al. [68]	1	293.15	0.101325	–	0.383	–	–	–	–	0.383
Radecki and Kaczmarek [69]	1	293.15	0.101325	–	0.397	–	–	–	–	0.397
Reuther and Reichel [72]	1	293.14	0.101325	–	0.385	–	–	–	–	0.385
Sauer [73]	1	293.14	0.101325	–	0.398	–	–	–	–	0.398
Voronkov [76]	1	293.14	0.101325	–	0.174	–	–	–	–	0.174
Waterman et al. [77]	1	293.14	0.101325	–	0.214	–	–	–	–	0.214
Weast and Astle [97]	1	293.15	0.101325	–	0.147	–	–	–	–	0.147
Speed of sound w										
This work*	214	365–573	0.1–30	–	0.174	–	–	–	0.228	0.215
Isobaric heat capacity c_p										
Weast and Astle [97]	1	298.14	0.101325	–	0.921	–	–	–	–	0.921
Anderson et al. [88]	1	298.15	0.101325	–	1.310	–	–	–	–	1.310
Abbas [2]*	32	218–374	0.101325	–	0.303	–	–	–	–	0.303
Pedersen et al. [67]	8	301–346	0.101325	–	0.702	–	–	–	–	0.702
Good et al. [93]	1	298.14	0.101325	–	0.881	–	–	–	–	0.881
Scott et al. [36]*	11	363–501	0.0–1	0.042	–	–	–	–	–	0.042
Second virial coefficient B [a]										
Marcos et al. [95]	6	448–574	–	29.82	–	–	–	–	–	29.82
Scott et al. [36]*	3	332–374	–	35.51	–	–	–	–	–	35.51

[a] *AAD* of the second virial coefficient B in $\mathrm{cm^3\ mol^{-1}}$.

[b] Calculated values.

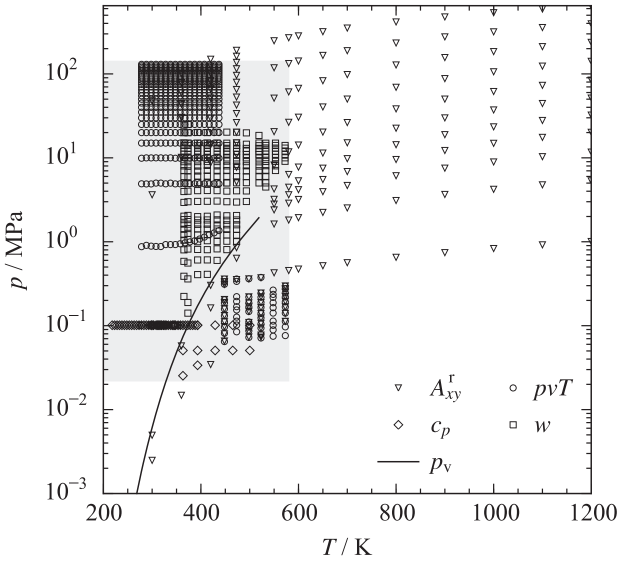

Fig. 7. Data in the homogeneous region of hexamethyldisiloxane. The gray area depicts the region where experimental data are available: $T_{max} = 580$ K and $p_{max} = 130$ MPa. Helmholtz energy derivatives from molecular simulation extend this region up to $T_{max} = 1200$ K and $p_{max} = 600$ MPa.

When Colonna et al. [1] developed their EOS in 2006, no information on the ideal gas heat capacity was available. Therefore, they applied the Harrison-Seaton zeroth order contribution method [37] to gain information on this property. Unfortunately, the method yields results with 25% uncertainty [19], which is too large for accurate EOS. However, this was the only group contribution method applicable to siloxanes because it is the only one providing information on Si—O bonds. Poling et al. [38] state the same findings, which led to further investigations on the ideal gas heat capacity of siloxanes by Nannan et al. [39]. They made *ab initio* calculations, which were based on information about hexamethyldisiloxane from the literature, and were then transferred to several other siloxanes. Unfortunately, these results were not compared to their experimental results for octamethylcyclotetrasiloxane so that it is not possible to assess the accuracy of their *ab initio* calculations. In a publication that reports a conclusion of their investigations on more accurate ideal gas heat capacities of siloxanes, they claim that the HF/6-31G(d) method is the most accurate one. This method yields an ideal gas isobaric heat capacity of $c_p^o = 503\ \mathrm{J\cdot mol^{-1}\cdot K^{-1}}$ at $T = 500$ K, which is the same value as their experiment at $T = 495$ K. Therefore, these data are assumed to be less accurate than the data of Scott et al. [36] and were only used for comparison here.

4.2. Residual contribution

The residual contribution consists of polynomial, exponential, and Gaussian bell-shaped terms

$$\begin{aligned}\alpha^r(\tau,\delta) &= \alpha^r_{\mathrm{Pol}}(\tau,\delta) + \alpha^r_{\mathrm{Exp}}(\tau,\delta) + \alpha^r_{\mathrm{GBS}}(\tau,\delta)\\ &= \sum_{i=1}^{I_{\mathrm{Pol}}} n_i\delta^{d_i}\tau^{t_i} + \sum_{i=I_{\mathrm{Pol}}+1}^{I_{\mathrm{Pol}}+I_{\mathrm{Exp}}} n_i\delta^{d_i}\tau^{t_i}\exp\left(-l_i\delta^{p_i}\right)\\ &\quad + \sum_{i=I_{\mathrm{Pol}}+I_{\mathrm{Exp}}+1}^{I_{\mathrm{Pol}}+I_{\mathrm{Exp}}+I_{\mathrm{GBS}}} n_i\delta^{d_i}\tau^{t_i}\exp\left(-\eta_i(\delta-\varepsilon_i)^2-\beta_i(\tau-\gamma_i)^2\right).\end{aligned} \tag{11}$$

Polynomial and exponential terms are generally sufficient to accurately describe the whole fluid region, except for critical states. The Gaussian bell-shaped terms [40], which were first applied to Helmholtz EOS by Setzmann and Wagner [41] in 1991, are used for a more accurate description of the critical region. Furthermore, they allow for the development of EOS, which can reproduce data within their experimental uncertainty with a much lower number of terms as before.

The residual contribution of the present EOS consists of five polynomial, five exponential, and eight Gaussian bell-shaped terms. The corresponding parameters are listed in Table 3. These parameters were determined by non-linear fitting techniques, which were also used to set up other modern EOS, e.g. R-125 [42], propane [43], or propylene [44]. Tables 5 and 6 list all data sources, indicating which data were considered in the present fitting routine. Their selection is discussed in detail below. The available dataset is presented in Fig. 7. The shaded area marks the region that is covered by experimental measurements ($T = 220$ K to 570 K, $p_{max} = 130$ MPa). Most are homogeneous liquid density and speed of sound data. The experimental dataset was supplemented here by Helmholtz energy derivatives from molecular simulation. In this way, the range of validity of the present equation of state was extended to a maximum temperature of $T_{max} = 1200$ K and a maximum pressure of $p_{max} = 600$ MPa. The critical temperature was constrained to the value of McLure and Dickinson [45] ($T_c = 518.7$ K), which is in close agreement with the other literature values, cf. Table 4. The critical density $\rho_c = 1.653\ \mathrm{mol\ dm^{-3}}$ and the critical pressure $p_c = 1.9311$ MPa were determined during the present fitting procedure. The critical pressure agrees well with the literature values, whereas the critical density differs by up to 5.5%. However, none of the critical density values given in the literature are measurements, they were rather estimated from theoretical models. The triple point temperature $T_{tp} = 204.93$ K was taken from Scott et al. [36]. The corresponding liquid triple point density $\rho_{tp,liq} = 5.266\ \mathrm{mol\ dm^{-3}}$ was determined by extrapolating the saturated liquid line to the triple point temperature. Furthermore, the gas constant $R = 8.3144621\ \mathrm{J\ mol^{-1}\ K^{-1}}$ [46] and the molecular weight $M = 162.3768\ \mathrm{g\ mol^{-1}}$ [47] were applied.

4.3. Assessment of vapor—liquid equilibrium properties

Relative deviations of experimental vapor pressure data from the present equation of state are shown in Fig. 8. Additionally, the corresponding average absolute relative deviations are listed in Table 5. Relative deviations were calculated by

$$\Delta X = 100\left(\frac{X_{\mathrm{DATA}} - X_{\mathrm{EOS}}}{X_{\mathrm{DATA}}}\right). \tag{12}$$

Based on this definition, the average absolute relative deviation is defined as

$$\mathrm{AAD} = \frac{1}{N}\sum_{i=1}^{N}|\Delta X_i|. \tag{13}$$

Vapor—liquid equilibrium data were separated into three temperature ranges: low temperature (LT: $T/T_c \le 0.6$), medium temperature (MT: $0.6 \le T/T_c \le 0.98$), and high temperature (HT: $T/T_c > 0.98$). All other properties were classified into gas, liquid, critical region ($0.98 \le T/T_c \le 1.1$ and $0.7 \le \rho/\rho_c \le 1.4$), and supercritical region. The latter was further divided into low density (LD: $\rho/\rho_c \le 0.6$), medium density (MD: $0.6 \le \rho/\rho_c \le 1.5$), and high density (HD: $\rho/\rho_c > 1.5$). In the figures, the equation of state of Colonna et al. [1] and the ancillary equations of the DIPPR [19] and TDE [53] databases are plotted for comparison.

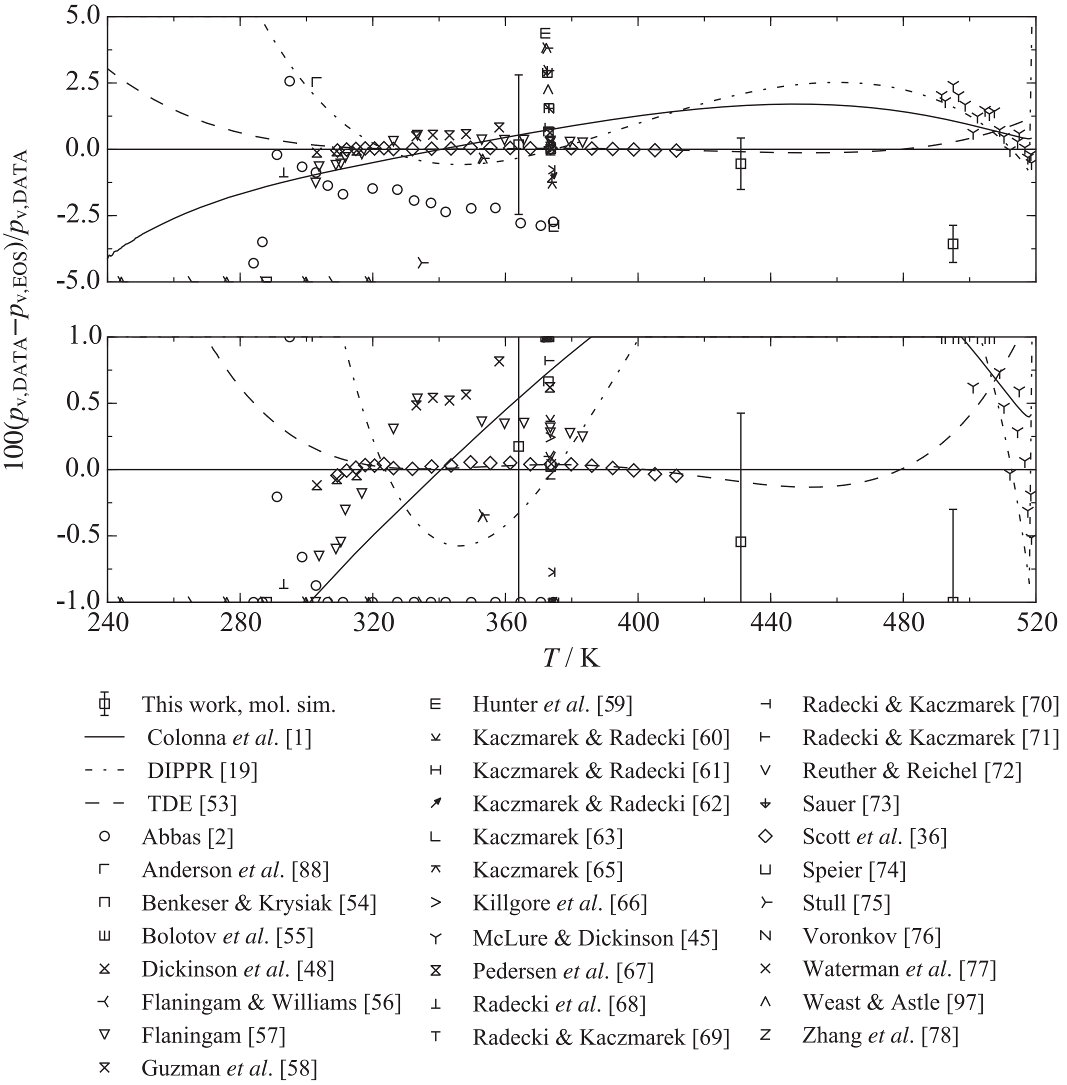

Fig. 8. Relative deviations of experimental vapor pressure data from the present equation of state for hexamethyldisiloxane.

The large number of authors in Table 5 may lead to the impression that the vapor pressure was very well investigated. However, in many references only a single data point is reported. Most of these publications focused on measurements of mixture properties with hexamethyldisiloxane as an involved component. For verification of the sample purity, the normal boiling point was reported. These values differ by more than 1% from each other so that they were not useful for the development of the present EOS. When excluding these data from the dataset, measurements by six different authors remain, which are mostly located between $T = 300$ K and 400 K.

Abbas [2] reports a comprehensive investigation on thermodynamic properties of hexamethyldisiloxane for a sample purity of 99.7%. The vapor pressure was measured with a comparative ebulliometer, which requires a very well known reference fluid with a high purification grade. No information is given on the reference fluid in her thesis. Since she is calling her apparatus a “Scott-ebulliometer”, it is assumed here that she was using water as a reference fluid as recommended in the original paper describing the apparatus [81]. This method is known to be very accurate, but Abbas' [2] data exhibit a systematic negative offset when comparing to the present EOS and other literature data, e.g. Scott et al. [36] or Flaningam [57]. For low temperatures the data by Abbas [2] scatter significantly, which could be due the choice of the reference fluid. Because water can easily be superheated for vapor pressures of $p < 0.003$ MPa, other reference fluids should be chosen for the low temperature region. The specified uncertainties of $\Delta_p = 0.0005 \cdot p_v + 10$ Pa and $\Delta_T = 0.05$ K yield a combined uncertainty of 0.4% to 1.5% for a coverage factor $k = 2$. No information is given how these uncertainties were ascertained and the sample purity was not considered.

The vapor pressure measurements of Scott et al. [36] and Flaningam [57] agree with each other within approximately 0.5%. Scott et al. [36] report a very detailed description of their sample preparation. The sample purity of 99.996% was verified by calorimetric studies of the melting point as a function of fraction melted. Similar to Abbas [2], Scott et al. [36] used a comparative ebulliometer for their measurements. As a reference, water was used for

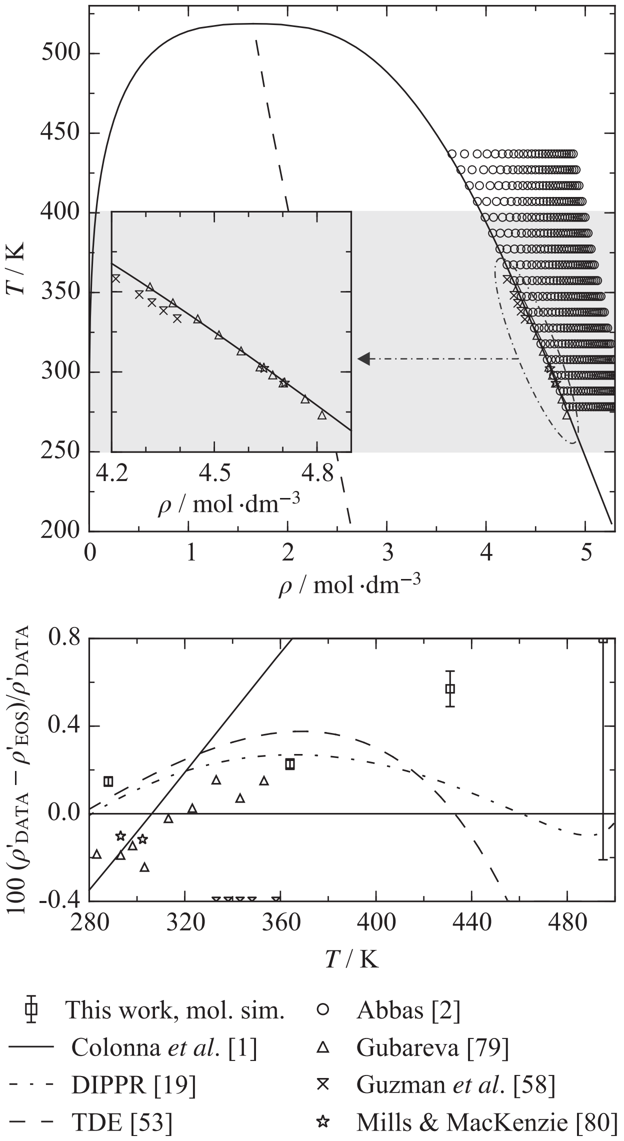

Fig. 9. Saturated liquid density of hexamethyldisiloxane. Top: T–ρ diagram including saturated liquid and homogeneous states near the saturated liquid line. Bottom: Relative deviations of experimental saturated liquid density data from the present equation of state.

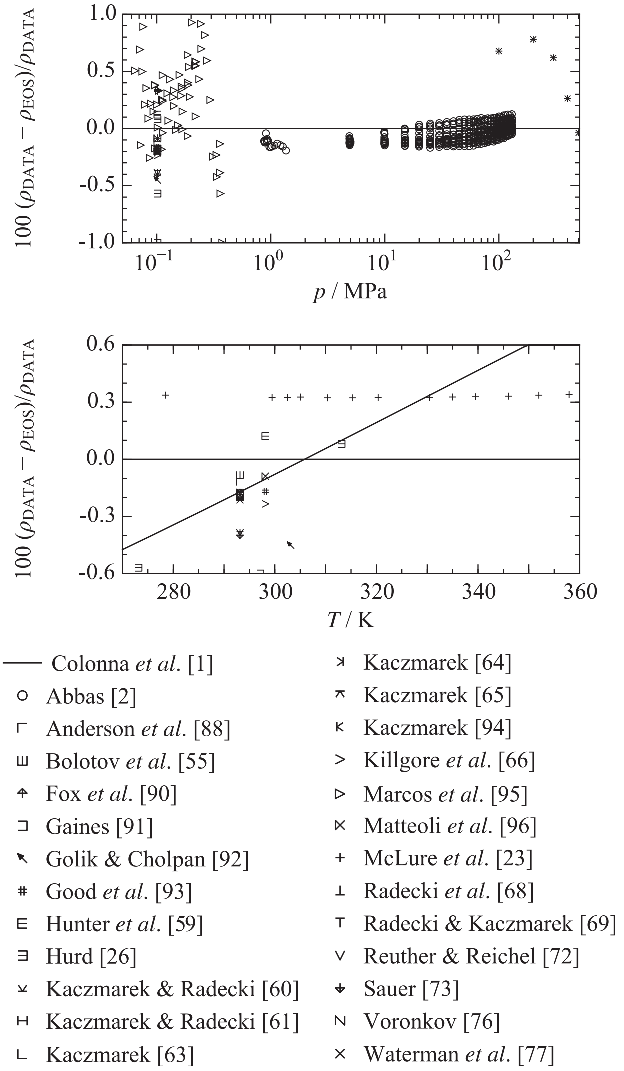

Fig. 10. Homogeneous density of hexamethyldisiloxane. Top: Relative deviations of experimental homogeneous density data from the present equation of state. Bottom: Relative deviations of the experimental homogeneous density data at atmospheric pressure from the present equation of state.

high temperatures only, benzene was applied in case of low temperatures. This procedure yields consistent vapor pressure data over the whole temperature range. The measurements of Dickinson et al. [48] confirm the data of Scott et al. [36] at low temperatures. The three state points between $T = 303$ K and 315 K are reproduced with an $AAD = 0.076\%$. At $T = 373$ K, the most recent measurement of the normal boiling point by Zhang et al. [78] from 2011 also agrees very well with the data by Scott et al. [36]. Therefore, the present equation was fitted to the data of Scott et al. [36]. These data are reproduced within 0.06% ($AAD = 0.031\%$), which is well within the expected uncertainty. Flaningam [57] carried out his measurements with a sample purity of 99.9% using an ebulliometer as proposed by Stull [82]. In comparison to the comparative ebulliometer, the usage of a capacitive pressure sensor enables for the investigation of the low temperature regime without any modification of the apparatus. In his publication, he verified his apparatus with test measurements on water, methylcyclohexane, and diphenyl ether. However, except for water, these fluids are not practical for test measurements because they are not well investigated. The average pressure error of 0.07% is not expressed in absolute values, which falsifies the results by opposite algebraic signs. Nonetheless, most of the data are reproduced within 0.5% ($AAD = 0.437\%$).

The data by Stull et al. [75] are presented in a paper together with several hundred additional fluids. Thus, they were not measured, but collected from the literature. Compared to the present EOS and other literature sources, these data show huge deviations ($AAD = 12.78\%$) and were thus not taken into account. The vapor pressure measurements of Guzman et al. [58] exhibit a systematic positive offset when comparing to the present EOS or the data of Scott et al. [36]. In their publication, the procedure of sample preparation is described in detail. However, they do not give the value of their sample purity. The only hint is a comparison of the

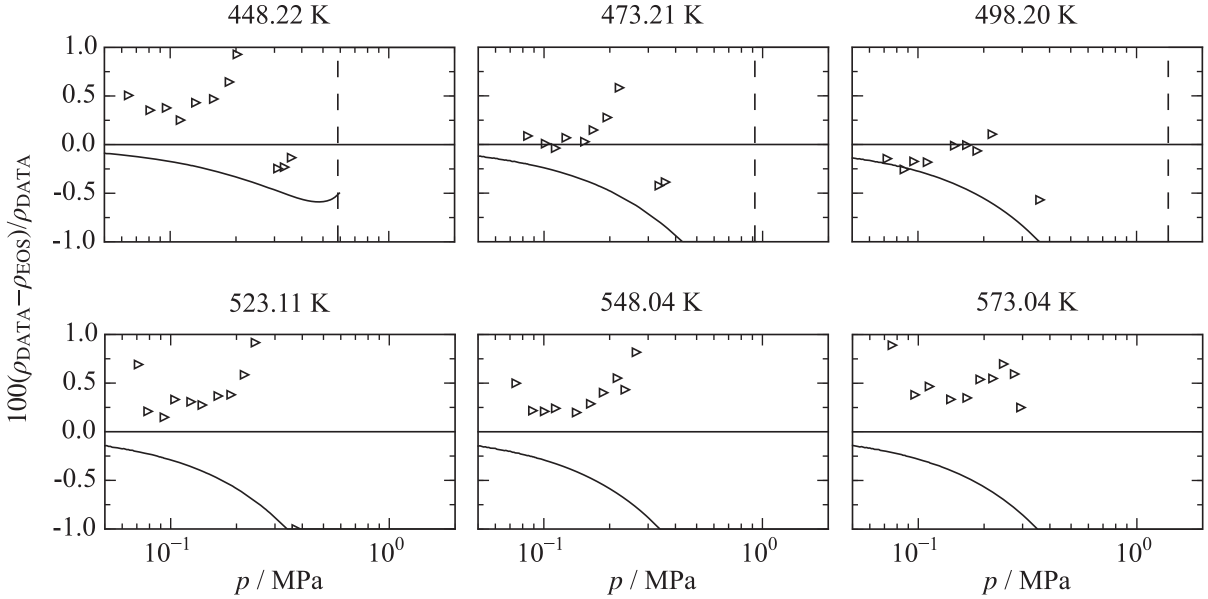

Fig. 11. Relative deviations of gaseous $p\rho T$ data of Marcos et al. [95] from the present equation of state for hexamethyldisiloxane. — equation of state, Colonna et al. [1]; – – phase boundary.

NBP to the value published by Radecki and Kaczmarek [71]. Because their value already differs by 0.82% from the present EOS, this confirmation is questionable and the positive deviation of the vapor pressure data of Guzman et al. [58] from the present EOS is reasonable.

Finally, there is one dataset of McLure and Dickinson [45] in the high temperature region (T = 491 K to 519 K). Because there are no other data available in this region, they cannot be compared to other measurements. Moreover, the lack of data between T = 412 K and 491 K prohibits a reliable transition from the low temperature region to the data of McLure and Dickinson [45]. Therefore, the accuracy of these data can only be evaluated with the information given in the corresponding publication and by comparison to the present EOS. They state a sample purity of 99.99%, which was determined with gas chromatography. The experiment was carried out with Pyrex tubes [83] and the temperature was monitored with a thermo couple (type K), which is a quite inaccurate device, if it is not calibrated very carefully. However, the choice of calibrating the thermo couple to the critical points of hexane, heptane, octane, and nonane is questionable. All of these hydrocarbons are not well investigated and are barely available with a sufficient purity from common manufacturers (e.g. Sigma–Aldrich Co. LLC [84], Merck Millipore Corporation [85], or Alfa Aesar GmbH & Co. KG [86]). This is affirmed by the quite low sample purities of heptane (99.5%) and octane (99%) [83], which were used for calibration. Furthermore, the critical temperatures of hexane (T_c = 507.4 K) and octane (T_c = 568.7 K) [45] differ from those of the EOS of Lemmon and Span [87], which are the most accurate models in the literature for these fluids (hexane: T_c = 507.82 K, octane: T_c = 569.32 K). Additionally, the influence of the sample purity on the critical temperature was investigated in the same paper. A difference of 2.6 K was observed when decreasing the sample purity from 99.99% to 99.7%. Although the hydrocarbons do not behave exactly like hexamethyldisiloxane, these findings show that the purification grade has a large impact on the critical temperature and, therefore, the vapor pressure in the critical region. Thus, the uncertainty of 0.1 MPa (corresponding to

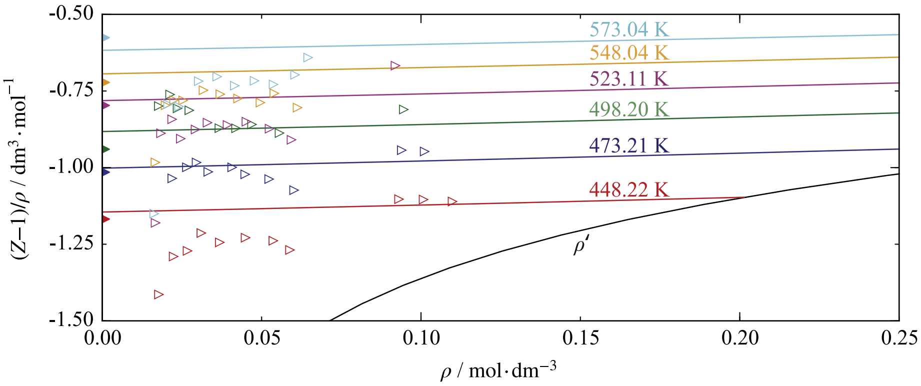

Fig. 12. $(Z-1)/\rho - \rho$ diagram of hexamethyldisiloxane. ▷ $p\rho T$ measurements of Marcos et al. [95]; ► second virial coefficient of Marcos et al. [95]; — present equation of state.

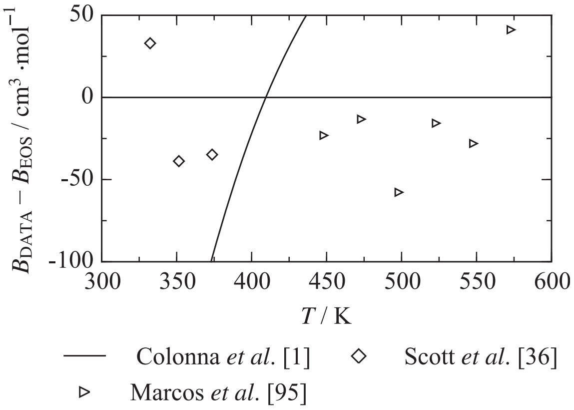

Fig. 13. Absolute deviations of the second virial coefficient of Marcos et al. [95] and Scott et al. [36] from the present equation of state for hexamethyldisiloxane.

0.5% to 0.8%) as specified by the authors [45] has to be questioned. In fact, during the fitting procedure it was not possible to achieve smaller deviations than 2% from the EOS without compromizing the representation of other properties. Based on these findings, the expected uncertainty of the present EOS regarding the vapor pressure is 0.2% for $T \leq 410$ K and 2% for higher temperatures.

Literature shows that the saturated liquid density has been investigated less than the vapor pressure. There are only three different datasets available, which are also very restricted in terms of the temperature range ($T = 270$ K to 360 K). This is insufficient to model the saturated liquid line of hexamethyldisiloxane. Alternatively, the homogeneous density data of Abbas [2] were used. Since no experimental measurements of the saturated vapor line were published, a straight rectilinear diameter ($RD = (\rho' + \rho'')/2$) was applied as a fitting constraint. In Fig. 9, an overview about the available saturated liquid density and homogeneous density data located near the saturated liquid line is given. The data of Abbas [2] were measured close enough to the phase boundary and cover a broader temperature range than the saturated liquid density data. When correlating the present EOS to the dataset of Abbas [2], the saturated liquid density of Gubareva [79] and Mills and MacKenzie [80], which agree well with each other, are reproduced within 0.2% ($AAD = 0.167$ % and $AAD = 0.109$ %, respectively). The data of Guzman et al. [58] show a systematic negative offset of about −1.3%. Unfortunately, no information on the sample purity or the measurement device is available in Ref. [58] so that it is not possible to discuss the reason for this offset.

For all three vapor–liquid equilibrium properties, ancillary equations were developed, which can be used for initial calculations of starting values of iterative phase equilibrium calculations. The equations and the corresponding parameters can be found in the Supplementary Material.

4.4. *Assessment of homogeneous state properties*

There are several different datasets available for the homogeneous density. Average absolute relative deviations are given in Table 6 and relative deviations from the present EOS are illustrated in Fig. 10. Similar to the vapor pressure, most of the authors reported only a single value to verify their sample purity.

When leaving out these sources, five datasets of Abbas [2], Dickinson [89], Hurd [26], Marcos et al. [95], and McLure et al. [23] were considered for the development of the present EOS. The data of Dickinson [89] were calculated from a correlation equation based on the available experimental data from the literature. Abbas [2] published the only pressure dependent dataset in the liquid phase. All other measurements were carried out at atmospheric pressure. Abbas [2] covered a temperature range of 270 K to 440 K with a maximum pressure of 130 MPa. A flexural resonator, which was used for the measurements, was calibrated to water ($p \leq 30$ MPa) and heptane ($p > 30$ MPa). For test purposes, liquid densities of water and heptane were compared to the IAPWS-95 [98] (0.04%) and the equation of Lemmon and Span [87] (0.08%). No experimental uncertainty was specified for hexamethyldisiloxane. However, Abbas [2] indicates the uncertainty by referring to the diploma thesis of Schedemann [99], who claimed an uncertainty of 0.7 mg*cm^{-3} to 0.8 mg*cm^{-3}.

For hexamethyldisiloxane, these values correspond to a relative deviation of 0.08% to 0.13%. When considering this statement as a combined uncertainty, including all relevant irritations during the measurement, the calibration has to be carried out extremely carefully. Keeping in mind the sample purity (99.7%) and the test measurements on water and heptane, the deviation of 0.2% from the present equation of state is most probably within the true experimental uncertainty. Therefore, this deviation is also claimed to be the uncertainty of the homogeneous liquid density of the present EOS. Fig. 10, (bottom) presents the deviations of the homogeneous density data measured at atmospheric pressure. The equation of state of Colonna et al. [1] was probably correlated to the data of Hurd [26], because his data point at $T = 293.15$ K agrees very well with many other data measured at the same temperature. However, these data are not based on real measurements, but were calculated from an equation. For the development of that equation, they measured liquid density data at $p = 1$ atm. During their measurements they observed a loss of sample, which could be the reason of the different trend in comparison to the dataset of McLure et al. [23]. However, in this work none of the data at $p = 1$ atm were applied to the fit, which leads to a better representation of the data of McLure et al. [23] at least in terms of the correct slope and curvature. Their measurements were carried out between $T = 278$ K and 358 K and a systematic offset of 0.33% with respect to the present EOS can be observed. In their publication only little information on the experiment is provided and no experimental uncertainty is given. During the fitting procedure, these data were also applied to the fit to reduce the offset. It turned out that it is not possible to improve the representation of these data without increasing deviations of the liquid density data of Abbas [2]. Since the data of Abbas [2] were chosen to be fitted primarily, the data of McLure et al. [23] were finally rejected from the fit. Therefore, it is assumed that the systematic offset is caused by the comparatively low purity of the sample (99%).

The homogeneous gas phase was exclusively investigated by Marcos et al. [95]. A bore-tube with a varied volume was used for the measurements. The pressure was obtained with a mercury manometer and the temperature was regulated by two thermopiles. The absence of a measurement device to weigh the sample raises the question how they determined the density of their sample. At least one reference value has to be known, which is commonly measured at atmospheric conditions as explained by Singh and Kudchadker [100].

This value can then be used to calculate the density during the experiment when varying the volume with a constant mass. Fig. 10 shows that these values differ by about 0.5% in the literature, but no value for hexamethyldisiloxane was cited by Marcos et al. [95]. Furthermore, they measured a density range of 2 kg*m^{-3} to 18 kg*m^{-3}, which are extremely small values even for state points in the gaseous phase. Therefore, these measurements had to be carried out extremely carefully. Fig. 11 shows that the density data of Marcos et al. [95] are reproduced within 1%, but they are not completely consistent. For a consistency test, the density was recalculated to the compressibility factor $Z = pv/(RT)$ and represented in terms of $(Z-1)/\rho$ as a function of the density in Fig. 12. Six isotherms ranging from 448 K to 573 K are illustrated. For a better assessment, the corresponding isotherms calculated with the present EOS are depicted for orientation. The "high density" data seem to be consistent, at least for the two lowest isotherms. With decreasing density the data start to scatter, which is becoming worse with increasing temperature. The isotherms T = 448.22 K and 473.21 K are slightly shifted to lower values with respect to the present EOS. The other isotherms exhibit a larger scatter and even merge. Therefore, the uncertainty specified by Marcos et al. [95] (0.33 kPa, corresponding to 0.1% to 0.5%) seems to be questionable. Furthermore, a sample purity of 99% is probably insufficient to carry out these sensitive measurements. Thus, the deviation of 1% is assumed to be the uncertainty of both the experimental data and the present EOS in the gaseous region.

Similar to the approach illustrated in Fig. 12, Marcos et al. [95] used their density measurements to extrapolate the second virial coefficient B of each isotherm. They fitted their data to a virial expansion and extrapolated it to $\rho \rightarrow 0$ mol dm^{-3}. The resulting virial coefficient is shown in Fig. 12. When comparing their results for the second virial coefficient with their density measurements, it is not clear how they determined it. Except for the two lowest isotherms the extrapolation does not agree with the underlying dataset. Therefore, these results should be treated carefully. In Fig. 13, absolute deviations of the second virial coefficient data from the present EOS are illustrated. Except for one outlier, the data of Marcos et al. [95] and Scott et al. [36] are represented within 50 cm^3 mol^{-1}, corresponding to 7%.

The reason for setting up a new EOS for hexamethyldisiloxane was the finding that the present measurements of the speed of sound deviate by up to 15% from the equation of Colonna et al. [1].

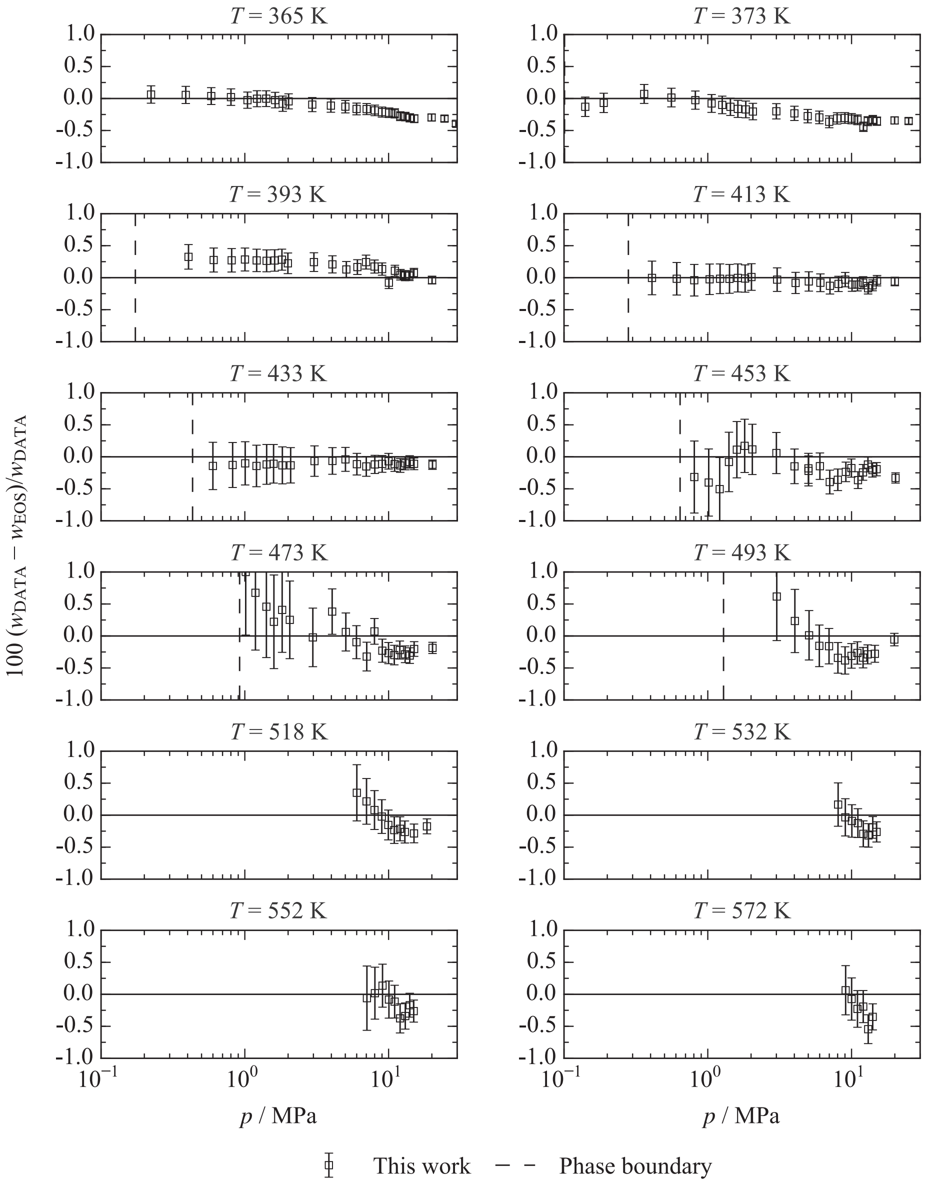

Fig. 14. Relative deviations of experimental speed of sound data of this work from the present equation of state for hexamethyldisiloxane.

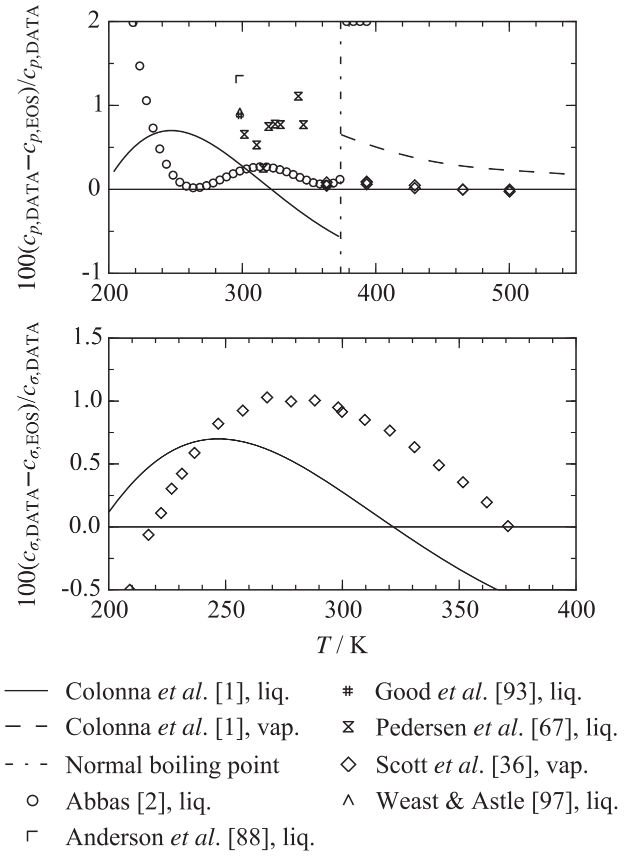

Fig. 15. Heat capacities of hexamethyldisiloxane. Top: Relative deviations of experimental isobaric heat capacity data from the present equation of state. — Liquid phase of Colonna et al. [1] at $p = 1$ atm; – – vapor phase of Colonna et al. [1] at $p = 1$ atm; – – normal boiling point temperature. Bottom: relative deviations of experimental saturated heat capacity data from the present equation of state.

This was caused by the fact the there was no information available on the speed of sound when Colonna et al. [1] developed their equation. In this work, new measurements are reported with a combined expanded uncertainty as indicated in Fig. 14. The sample purity of 99% was not considered for the determination of the experimental uncertainty. These data are reproduced with the present EOS within 0.5% and most of them are represented within the experimental uncertainty. Therefore, the deviation of 0.5% is expected to be the uncertainty of the EOS for liquid state speed of sound data.

The only available caloric data in the gaseous region are the heat capacity measurements of Scott et al. [36]. They were measured with a low temperature calorimeter as explained by Huffman [101] and no statement on the uncertainty was made. However, these data are reproduced here within 0.1%, which is most likely well within the expected experimental uncertainty. Further measurements on the isobaric heat capacity are listed in Table 6 and depicted in Fig. 15. There are four different datasets available in the liquid region at atmospheric pressure. Anderson et al. [88] and Good et al. [93] report only single data points and, therefore, they were only considered for comparison. Thus, the results of Abbas [2] and Pedersen et al. [67] remained for fitting the present EOS.

A nonsteady hot-wire method was used by Abbas [2], where platinum was employed to heat the sample. The pressure was measured by a diaphragm pressure sensor and the temperature was controlled with a Pt100 thermometer. In this way, results with an experimental uncertainty of 1% were achieved. The same measurement accuracy was stated by Pedersen et al. [67], however, their data are not as consistent as the ones from Abbas [2] and they are restricted to a narrow temperature range. Therefore, the data of Abbas [2] were chosen in the present fitting procedure. These data are represented within 0.5%, excluding four state points at low temperatures $T<240$ K. In this way, the data of Pedersen et al. [67] are represented within their experimental uncertainty. Finally, Scott et al. [36] published saturation heat capacity data c_σ (for the thermodynamic definition see Hoge [102]) measured with the same type of apparatus. They state an experimental uncertainty of 0.2%, which is probably too low. During the development of the EOS, it turned out that it was not possible to fit these data within the given uncertainty without compromizing the representation of the isobaric heat capacity. Since there are several different datasets available, which agree with each other within the given experimental uncertainty, the homogeneous isobaric heat capacity was chosen to be modeled primarily.

4.5. *Assessment of physical and extrapolation behavior*

In Fig. 16, typical plots are illustrated to verify the physical and extrapolation behavior of the present EOS. The top, left part of the figure shows the temperature as a function of density along selected isobars ($p_{\mathrm{min}} = 0.5$ MPa, $p_{\mathrm{max}} = 5$ MPa). Additionally, the saturated liquid and vapor curves as well as the rectilinear diameter are presented. It is important that there are no bumps in the course of the isobars, the saturation lines have to meet in a flat maximum, and the rectilinear diameter has to be a straight line up to the critical point. The top, right diagram shows the pressure as a function of density along selected isotherms with a maximum temperature of $T = 10^6$ K. Again, bumps have to be avoided and the isotherms have to approach each other at extremely high temperatures, densities, and pressures in this double logarithmic plot. In the center of Fig. 16, the residual isochoric heat capacity and the speed of sound are presented. For the isochoric heat capacity, the liquid phase has to exhibit a positive curvature over the whole temperature range for non-associating fluids. When extrapolating it to metastable temperatures below the triple point, the residual isochoric heat capacity has to have a negative slope on the hypothetical liquid side, whereas a positive slope has to be observed in the liquid region approaching the critical temperature. The isochoric heat capacity of the vapor phase has to increase monotonously with increasing temperature. Finally, both phases have to merge with a distinctive peak at the critical point. The speed of sound of the saturated liquid and vapor phase have to have a negative slope and curvature in the vicinity of the critical point. Similar to the maximum of the isochoric heat capacity, the saturation curves of the speed of sound have to merge in a minimum at the critical temperature. Furthermore, the extrapolated liquid phase has to exhibit a negative slope and no curvature, or rather a slightly positive curvature. At the bottom of Fig. 16, the second, third, and fourth thermal virial coefficients are shown as well as some characteristic ideal curves. Detailed information on the behavior of the virial coefficients can be taken from the publication of Thol et al. [7]. For the present equation of state, all of the three coefficients show a correct trend. For $T \rightarrow 0$ K the virial coefficients have to approach negative infinity. With increasing temperature the virial coefficients have to increase and finally vanish at high temperatures after passing a maximum. The maxima of the third and fourth virial coefficient have to be located in the vicinity of

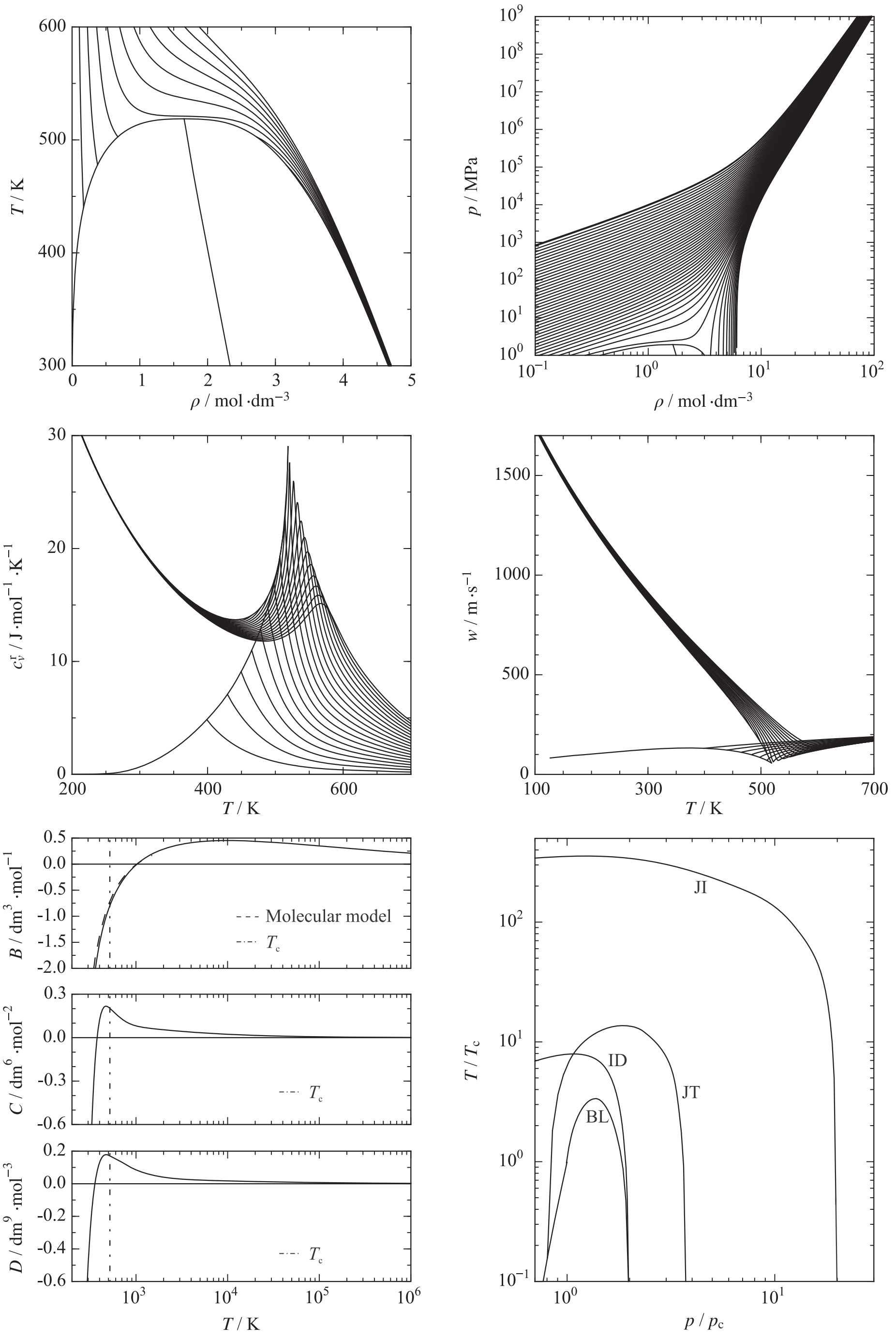

Fig. 16. Physical behavior of some thermodynamic properties of hexamethyldisiloxane. Top, left: Isobars and vapor–liquid equilibrium curves together with the rectilinear diameter. Top, right: Pressure as a function of density along isotherms at extreme conditions ($T_{\max} = 10^6$ K). Center, left: Residual isochoric heat capacity. Center, right: Speed of sound. Bottom, left: Second, third, and fourth virial coefficients, including B from the molecular interaction model. Bottom, right: Characteristic ideal curves.

the critical temperature. The characteristic ideal curves (for definition see Span and Wagner [103] or Span [8]) have to be smooth without any bumps. All of the plots presented in Fig. 16 exhibit a reasonable behavior with only small changes in the curvature of the Joule-Thomson inversion curve and the Joule inversion curve. Having in mind the restricted dataset available for hexamethyldisiloxane, the plot of the ideal curves still proves excellent extrapolation behavior.

4.6. *Assessment of molecular simulation data*

In Fig. 7, the shaded area indicates the region where experimental data are available for hexamethyldisiloxane. On this basis, the range of validity of the present EOS was defined to be

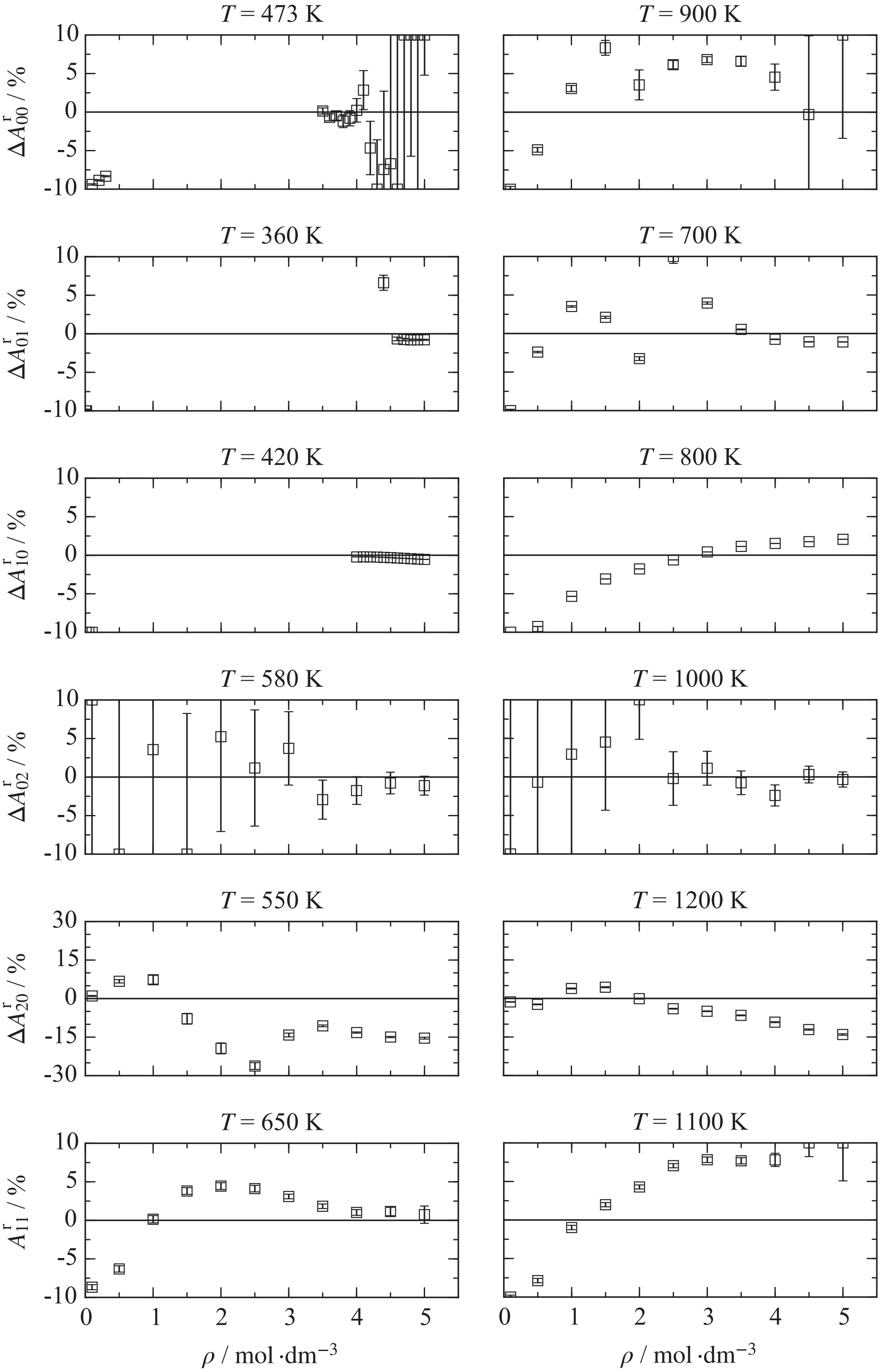

Fig. 17. Relative deviations of simulated residual Helmholtz energy derivative data along selected isotherms from the present equation of state for hexamethyldisiloxane. Relative deviations are calculated according to Eq. (12).

$T = 220$–570 K with a maximum pressure of $p_{\rm max} = 130$ MPa. The large scale molecular simulation data presented in this work were applied to the fit to extend the range of validity to a maximum temperature of $T_{\rm max} = 1200$ K and a maximum pressure of $p_{\rm max} = 600$ MPa. During these simulations the thermal stability of the fluid was not considered. Therefore, the extended range of validity has to be comprehended as an extrapolation from the real fluid behavior. The temperature of thermal decomposition, which could not be retrieved from the literature, was considered irrelevant for the development of the EOS and the fluid was treated as if it is stable throughout.

In Fig. 17, relative deviations of the simulated residual Helmholtz energy derivatives from the present EOS are shown along selected isotherms. A comprehensive overview including all simulation data is provided in the Supplementary Material. Generally, the uncertainties of the residual Helmholtz energy $A^{\rm r}_{00}$, the first derivative with respect to the temperature $A^{\rm r}_{10}$, the first derivative with respect to the density $A^{\rm r}_{01}$, the first mixed derivative with respect to the temperature and density $A^{\rm r}_{11}$, and the second derivative with respect to the density $A^{\rm r}_{02}$ are 10%. The deviations increase with decreasing density and increasing temperature. The second derivative with respect to the temperature $A^{\rm r}_{20}$ was reproduced within 20%. These values may lead to the assumption that it is not reasonable to apply these data to the fit. However, it has to be kept in mind that these data exclusively represent the residual contribution of the EOS. Common thermodynamic properties, which are usually used for the development of EOS, always include the ideal contribution. Therefore, the ideal contribution of the present EOS was used to recalculate the thermodynamic properties pressure, isochoric heat capacity, isobaric heat capacity, and speed of sound from the residual molecular simulation data according to Eqs. (6)–(8).

In Fig. 18, the resulting data are compared to the present EOS. Additionally, the involved residual Helmholtz energy derivatives are indicated in the gray boxes. Although the deviations of the involved derivatives amount to 10% or even 20%, the deviations of the common thermodynamic properties are much smaller. Density data deviate from the present equation of state by no more than 2%, the isochoric heat capacity is reproduced within 1%, the isobaric heat capacity is within 2.5%, and the speed of sound scatters within 4%. Therefore, residual Helmholtz energy derivatives with uncertainties of up to 20% are statistically useful values when an extension of validity ranges is aimed at. Keeping in mind that other simulations for validation predicted the available homogeneous liquid density data within their experimental uncertainties, and the speed of sound data within 4%, the deviations presented in Fig. 18 can be assumed to be a rough estimate of the uncertainty of the present EOS in the extended range of validity. Of course, for a reliable statement further experimental measurements are required in this region.

5. Conclusion

The present EOS is written in terms of the reduced Helmholtz energy and can be used to calculate all thermodynamic equilibrium properties. Reference values are given in the Supplementary Material to verify a computer implementation of the EOS. Moreover, an input file for the equation of state packages REFPROP [104] and Trend [105] as well as a C++ implementation is supplied there. The underlying set of experimental literature data was extended considerably by the speed of sound measurements that were carried out at 210 state points. In addition, five Helmholtz energy derivatives and the Helmholtz energy itself were predicted by molecular simulation at 194 state points, providing 1164 non-

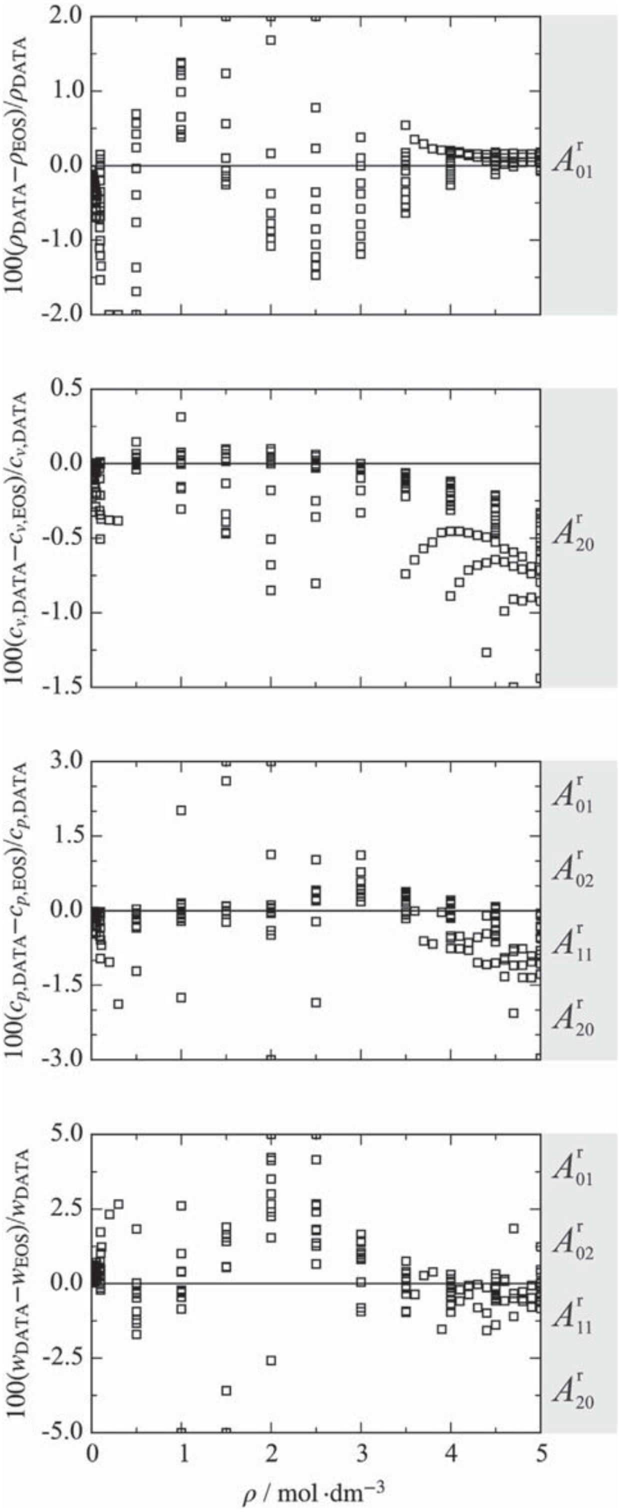

Fig. 18. Comparison of several thermodynamic properties obtained from molecular simulation data with the present equation of state for hexamethyldisiloxane. The involved residual Helmholtz energy derivatives are indicated in the gray boxes.

redundant thermodynamic data points for the EOS fit. The range of validity based on the experimental data covers $T = 220$ K to 570 K with a maximum pressure of $p_{\max} = 130$ MPa. By means of molecular simulation data, the temperature and pressure limits were extended to $T_{\max} = 1200$ K and $p_{\max} = 600$ MPa. The expected uncertainty in terms of vapor pressure amounts to 0.2% for $T \leq 410$ K and 2% for higher temperatures. Homogeneous density data can be calculated with an accuracy of 0.2% in the liquid phase and 1% in the gaseous phase. The specified uncertainty for speed of sound data in the liquid phase is 0.5%. The expected uncertainty of the isobaric heat capacity is 0.2% in the gaseous phase and 1% in the liquid phase. The extrapolation behavior was found to be reasonable. For the extended range of validity, only rough estimates on the uncertainty can be made.

Acknowlegdements

The authors gratefully acknowledge financial support by Deutsche Forschungsgemeinschaft under the grants VR6/4-1 and SP507/7-1. This work was carried out under the auspices of the Boltzmann-Zuse Society (BZS) of Computational Molecular Engineering. The simulations were performed on the Cray XC40 (Hornet) at the High Performance Computing Center Stuttgart (HLRS) under the grant MMHBF2.

Appendix A. Supplementary data

Supplementary data related to this article can be found at http://dx.doi.org/10.1016/j.fluid.2015.09.047.

References

[1] P. Colonna, N.R. Nannan, A. Guardone, E.W. Lemmon, Fluid Phase Equilib. 244 (2006) 193–211.
[2] R. Abbas, Anwendung der Gruppenbeitragszustandsgleichung VTPR für die Analyse von reinen Stoffen und Mischungen als Arbeitsmittel in technischen Kreisprozessen (PhD thesis), Technische Universität Berlin, Germany, 2011.
[3] R. Lustig, G. Rutkai, J. Vrabec, Mol. Phys. 113 (2015) 910–931.
[4] G. Rutkai, M. Thol, R. Lustig, R. Span, J. Vrabec, J. Chem. Phys. 139 (2013) 041102.
[5] G. Rutkai, J. Vrabec, Empirical fundamental equation of state for phosgene based on molecular simulation data, J. Chem. Eng. Data, http://dx.doi.org/10.1021/acs.jced.5b00266
[6] M. Thol, G. Rutkai, A. Köster, M. Kortmann, R. Span, J. Vrabec, Chem. Eng. Sci. 121 (2015) 87–99, and 134, 887–890 (2015).
[7] M. Thol, G. Rutkai, R. Span, J. Vrabec, R. Lustig, Int. J. Thermophys. 36 (2015) 25–43.
[8] R. Span, Multiparameter Equations of State: An accurate Source of Thermodynamic Property Data, Springer Verlag, Berlin, 2000.
[9] P. Kortbeek, M. Muringer, N. Trappeniers, S. Biswas, Rev. Sci. Instrum. 56 (1985) 1269–1273.
[10] F.H. Dubberke, D.B. Rasche, E. Baumhögger, J. Vrabec, Rev. Sci. Instrum. 85 (2014) 084901.
[11] C. Lin, J. Trusler, J. Chem. Phys. 136 (2012) 094511.
[12] S. Ball, J. Trusler, Int. J. Thermophys. 22 (2001) 427–443.
[13] G. Benedetto, R. Gavioso, P.G. Albo, S. Lago, D.M. Ripa, R. Spagnolo, Int. J. Thermophys. 26 (2005) 1667–1680.
[14] F.H. Dubberke, E. Baumhögger, J. Vrabec, Rev. Sci. Instrum. 86 (2015) 054903.
[15] H. Gedanitz, M. Davila, E. Baumhögger, R. Span, J. Chem. Thermodyn. 42 (2010) 478–483.
[16] G.R. Harris, J. Acoust. Soc. Am. 70 (1981) 10–20.
[17] K. Meier, The Pulse-echo Method for High Precision Measurements of the Speed of Sound in Fluids (Habilitation thesis), Bundeswehruniversität, Hamburg, Germany, 2006.
[18] M.W. Schmidt, K.K. Baldridge, J.A. Boatz, S.T. Elbert, M.S. Gordon, J.H. Jensen, S. Koseki, N. Matsunaga, K.A. Nguyen, S. Su, T.L. Windus, M. Dupuis, J.A. Montgomery, J. Comput. Chem. 14 (1993) 1347–1363.
[19] R. Rowley, W. Wilding, J. Oscarson, Y. Yang, N. Zundel, T. Daubert, R. Danner, The DIPPR Data Compilation of Pure Compound Properties, Design Institute for Physical Properties, AIChE, New York, 2006.
[20] T. Schnabel, A. Srivastava, J. Vrabec, H. Hasse, J. Phys. Chem. B 111 (2007) 9871–9878.
[21] J. Vrabec, J. Stoll, H. Hasse, J. Phys. Chem. B 105 (2001) 12126–12133.
[22] J. Stoll, Molecular Models for the Prediction of Thermalphysical Properties of Pure Fluids and Mixtures, Fortschritt-berichte VDI, Reihe 3, vol. 836, VDI-Verlag, Düsseldorf, 2005.
[23] I.A. McLure, A.J. Pretty, P.A. Sadler, J. Chem. Eng. Data 22 (1977) 372–376.
[24] B. Eckl, J. Vrabec, H. Hasse, Mol. Phys. 106 (2008) 1039–1046.
[25] G. Guevara-Carrion, C. Nieto-Draghi, J. Vrabec, H. Hasse, J. Phys. Chem. B 112 (2008) 16664–16674.
[26] C.B. Hurd, J. Am. Chem. Soc. 68 (1946) 364–370.
[27] D.F. Wilcock, J. Am. Chem. Soc. 68 (1946) 691–696.
[28] R. Lustig, Mol. Sim. 37 (2011) 457–465.
[29] R. Lustig, Mol. Phys. 110 (2012) 3041–3052.
[30] S. Deublein, B. Eckl, J. Stoll, S.V. Lishchuk, G. Guevara-Carrion, C.W. Glass, T. Merker, M. Bernreuther, H. Hasse, J. Vrabec, Comp. Phys. Commun. 182 (2011) 2350–2367.
[31] C.W. Glass, S. Reiser, G. Rutkai, S. Deublein, A. Köster, G. Guevara-Carrion, A. Wafai, M. Horsch, M. Bernreuther, T. Windmann, H. Hasse, J. Vrabec, Comput. Phys. Commun. 185 (2014) 3302–3306.
[32] D. Frenkel, B. Smit, Understanding Molecular Simulation: from Algorithms to Applications, Academic Press, Elsevier, San Diego, 2002.
[33] J.A. Barker, R.O. Watts, Mol. Phys. 26 (1973) 789–792.
[34] B. Widom, J. Chem. Phys. 39 (1963) 2808–2812.
[35] A.M. Mosin, A.M. Mikhailov, Zh. Fiz. Khim 46 (1972) 537.
[36] D.W. Scott, J.F. Messerly, S.S. Todd, G.B. Guthrie, I.A. Hossenlopp, R.T. Moore, A. Osborn, W.T. Berg, J.P. McCullough, J. Phys. Chem. 65 (1961) 1320–1326.
[37] B.K. Harrison, W.H. Seaton, Ind. Eng. Chem. Res. 27 (1988) 1536–1540.
[38] B.E. Poling, J.M. Prausnitz, J.P. O'Connell, The Properties of Gases and Liquids, McGraw-Hill, New York, 2001.
[39] N.R. Nannan, P. Colonna, C.M. Tracy, R.L. Rowley, J.J. Hurly, Fluid Phase Equilib. 257 (2007) 102–113.
[40] L. Haar, J.S. Gallagher, G.S. Kell, J.V. Sengers (Eds.), Proc. 8th Symp. Thermophys. Prop, ASME, New York, 1982.
[41] U. Setzmann, W. Wagner, J. Phys. Chem. Ref. Data 20 (1991) 1061–1155.
[42] E.W. Lemmon, R.T. Jacobsen, J. Phys. Chem. Ref. Data 34 (2005) 69–108.
[43] E.W. Lemmon, M.O. McLinden, W. Wagner, J. Chem. Eng. Data 54 (2009) 3141–3180.
[44] E.W. Lemmon, W. Wagner (2015), to be published.
[45] I.A. McLure, E. Dickinson, J. Chem. Thermodyn. 8 (1976) 93–95.
[46] P.J. Mohr, B.N. Taylor, D.B. Newell, Rev. Mod. Phys. 84 (2012) 1527–1605.
[47] M.E. Wieser, M. Berglund, Pure Appl. Chem. 81 (2009) 2131–2156.
[48] E. Dickinson, I.A. McLure, B.H. Powell, J. Chem. Soc. Faraday Trans. 1 70 (1974) 2321–2327.
[49] I.A. McLure, J.F. Neville, J. Chem. Thermodyn. 9 (1977) 957–961.
[50] E.D. Nikitin, P.A. Pavlov, A.P. Popov, J. Chem. Thermodyn. 26 (1994) 1047–1050.
[51] C. Young, J. Chem. Thermodyn. 4 (1972) 65–75.
[52] C. Young, J. Chem. Soc. Faraday Trans. 2 (68) (1972) 452–459.
[53] M. Frenkel, R.D. Chirico, V. Diky, K. Kroenlein, C.D. Muzny, A.F. Kazakov, J.W. Magge, I.M. Abdulagatov, E.W. Lemmon, NIST Standard Reference Database 103b: NIST Thermo–data Engine – Pure Compounds, Binary Mixtures, Reactions, Version 8.0, National Institute of Standards and Technology, Standard Reference Data Program, Gaithersburg, 2013.
[54] R.A. Benkeser, H.R. Krysiak, J. Am. Chem. Soc. 76 (1954) 6353–6357.
[55] B.A. Bolotov, T.V. Orlova, N.P. Kharitonov, N.N. Shenberg, E.A. Batyaev, N.P. Usacheva, J. General Chem. (USSR) 40 (1970) 802–806.
[56] O.L. Flaningam, D.E. Williams, US-Patent, Pat. No. US 5,478,493 (1995) 1–6.
[57] O.L. Flaningam, J. Chem. Eng. Data 31 (1986) 266–272.
[58] J. Guzman, A.S. Teja, W.B. Kay, Fluid Phase Equilib. 7 (1981) 187–195.
[59] M.J. Hunter, E.L. Warrick, J.F. Hyde, C.C. Currie, J. Am. Chem. Soc. 68 (1946) 2284–2290.
[60] B. Kaczmarek, A. Radecki, Pol. J. Chem. 52 (1978) 431–434.
[61] B. Kaczmarek, A. Radecki, Pol. J. Chem. 61 (1987) 267–271.
[62] B. Kaczmarek, A. Radecki, J. Chem. Eng. Data 34 (1989) 195–197.
[63] B. Kaczmarek, Pol. J. Chem. 57 (1983) 617–619.
[64] B. Kaczmarek, J. Chem. Eng. Data 30 (1985) 249–251.
[65] B. Kaczmarek, Pol. J. Chem. 72 (1998) 1120–1123.
[66] C.A. Killgore, W.W. Chew, V. Orr, J. Chem. Eng. Data 11 (1966) 535–537.
[67] M.J. Pedersen, W.B. Kay, H.C. Hershey, J. Chem. Thermodyn. 7 (1975) 1107–1118.
[68] A. Radecki, B. Kaczmarek, J. Grzybowski, J. Chem. Eng. Data 20 (1975) 163–165.
[69] A. Radecki, B. Kaczmarek, J. Chem. Eng. Data 20 (1975) 378–381.
[70] A. Radecki, B. Kaczmarek, J. Chem. Eng. Data 22 (1977) 168–171.
[71] A. Radecki, B. Kaczmarek, J. Chem. Eng. Data 25 (1980) 230–232.
[72] H. Reuther, G. Reichel, Chem. Tech. 6 (1954) 479–480.
[73] R.O. Sauer, J. Am. Chem. Soc. 66 (1944) 1707–1710.
[74] J.L. Speier, J. Am. Chem. Soc. 70 (1948) 4142–4143.
[75] D.R. Stull, Ind. Eng. Chem. 39 (1947) 517–540.
[76] M.G. Voronkov, J. General Chem. (USSR) 29 (1959) 890–896.
[77] H.I. Waterman, W.V. Herwijen, H.W. Denhartog, J. Appl. Chem. 8 (1958) 625–631.
[78] W. Zhang, N. Meng, R. Sun, C. Li, J. Chem. Eng. Data 56 (2011) 5078–5080.
[79] A. Gubareva, Oniitekhim, Code 874 KHP – D83, 1983, pp. 1–6.
[80] A.P. Mills, C.A. MacKenzie, J. Am. Chem. Soc. 76 (1954) 2672–2673.
[81] G. Waddington, J.W. Knowlton, D.W. Scott, G.D. Oliver, S.S. Todd, W.N. Hubbard, C.J. Smith, H.M. Huffman, J. Am. Chem. Soc. 71 (1949) 797–808.
[82] D.R. Stull, Ind. Eng. Chem. Anal. Ed. 18 (1946) 234–242.

[83] E. Dickinson, I.A. McLure, J. Chem. Soc. Faraday Trans. 1 70 (1974) 2313–2320.
[84] Sigma–Aldrich Co. LLC (August 2015). [link]. URL https://www.sigmaaldrich.com.
[85] Merck Millipore Corporation (August 2015). [link]. URL http://www.merckmillipore.com.
[86] Alfa Aesar GmbH & Co KG (August 2015). [link]. URL http://www.alfa.com.
[87] E.W. Lemmon, R. Span, J. Chem. Eng. Data 51 (2006) 785–850.
[88] R. Anderson, B. Arkles, G.L. Larson, Silicon Compounds: Register and Review, Huls America Inc., Piscataway, 1991.
[89] E. Dickinson, J. Phys. Chem. 81 (1977) 2108–2113.
[90] H.W. Fox, P.W. Taylor, W.A. Zisman, Ind. Eng. Chem. 39 (1947) 1401–1409.
[91] G.L. Gaines Jr., J. Phys. Chem. 73 (1969) 3143–3150.
[92] O.Z. Golik, P.P. Cholpan, Ukr. Fiz. Zh. Ukr. Ed. 5 (1960) 242–251.
[93] W.D. Good, J.L. Lacina, B.L. DePrater, J.P. McCullough, J. Phys. Chem. 68 (1964) 579–586.
[94] B. Kaczmarek, Inz. Chem. Proces. 4 (1983) 497–502.
[95] D.H. Marcos, D.D. Lindley, K.S. Wilson, W.B. Kay, H.C. Hershey, J. Chem. Thermodyn. 15 (1983) 1003–1014.
[96] E. Matteoli, P. Gianni, L. Lepori, A. Spanedda, J. Chem. Eng. Data 56 (2011) 5019–5027.
[97] R.C. Weast, M.J. Astle, CRC Handbook of Data on Organic Compounds, CRC Press, Boca Raton, 1985.
[98] W. Wagner, A. Pruß, J. Phys. Chem. Ref. Data 31 (2002) 387–535.
[99] A. Schedemann, Aufbau und Inbetriebnahme einer Dichtemessanlage. Messung und Modellierung des PVT-Verhaltens bis zu Drücken von 1400 bar (PhD thesis), Universität Oldenburg, Germany, 2009.
[100] R.P. Singh, A.P. Kudchadker, J. Chem. Thermodyn. 11 (1979) 205–213.
[101] H.M. Huffman, Chem. Rev. 40 (1947) 1–14.
[102] H.J. Hoge, J. Res. Natl. Bur. Stand. (U.S.) 36 (1946) 111–118.
[103] R. Span, W. Wagner, Int. J. Thermophys. 18 (1997) 1415–1443.
[104] E.W. Lemmon, M.L. Huber, M.O. McLinden, REFPROP. Reference Fluid Thermodynamic and Transport Properties 9.1, National Institute of Standards and Technology, Boulder (USA), 2014.
[105] R. Span, T. Eckermann, S. Herrig, S. Hielscher, M. Thol, TREND. Thermodynamic Reference and Engineering Data 2.0, Lehrstuhl für Thermodynamik, Ruhr-Universität Bochum, Germany, 2015.

4.4 Thermodynamic properties of octamethylcyclotetrasiloxane

Monika Thol, Gabor Rutkai, Andreas Köster, Frithjof H. Dubberke, Thorsten Windmann, Roland Span, Jadran Vrabec,
Journal of Chemical & Engineering, Data 61, (2016) 2580-2595,
DOI: 10.1021/acs.jced.6b00261

Reprinted from the Journal of Chemical & Engineering data, (2016) with permission from ACS Publications.

The scientific work and discussion was coordinated and consolidated by Monika Thol under supervision of Roland Span and Jadran Vrabec.
The manuscript was prepared by Monika Thol and Andreas Köster.
Molecular modeling and simulation was carried out by Thorsten Windmann and Gabor Rutkai.
Speed of sound measurements and data evaluation were performed by Frithjof H. Dubberke.
The manuscript was revised by Roland Span and Jadran Vrabec.

This publication is in the context of the precise modelling of thermophysical properties research under supervision of Monika Thol at the chair of Thermodynamic of the University of Bochum headed by Prof. Dr.-Ing. habil. Roland Span and the chair of Thermodynamic and Energy Technology headed by Prof. Dr.-Ing. habil. Jadran Vrabec.

Journal of chemical & engineering data

Article

pubs.acs.org/jced

Thermodynamic Properties of Octamethylcyclotetrasiloxane

Monika Thol,[†] Gábor Rutkai,[‡] Andreas Köster,[‡] Frithjof H. Dubberke,[‡] Thorsten Windmann,[‡] Roland Span,[†] and Jadran Vrabec*[,‡]

[†]Thermodynamics, Ruhr-Universität Bochum, Universitätsstraße 150, 44801 Bochum, Germany

[‡]Thermodynamics and Energy Technology, Universität Paderborn, Warburger Straße 100, 33098 Paderborn, Germany

Ⓢ *Supporting Information*

ABSTRACT: An equation of state for octamethylcyclotetrasiloxane is presented. The available experimental data from the literature are supplemented by new measurements on the speed of sound. Furthermore, a new force field is proposed, allowing the generation of a comprehensive thermodynamic data set by means of molecular simulation. Both the experimental and molecular simulation data are applied to develop a fundamental equation of state in terms of the Helmholtz energy. On the basis of the experimental data, the equation of state is valid from the triple-point temperature to T = 590 K for pressures up to p = 180 MPa and can be used to calculate any thermodynamic equilibrium state property. Its accuracy is assessed by a comprehensive analysis of the underlying experimental data. Finally, the range of validity was extended to T_{max} = 1200 K and p_{max} = 520 MPa by means of molecular simulation data.

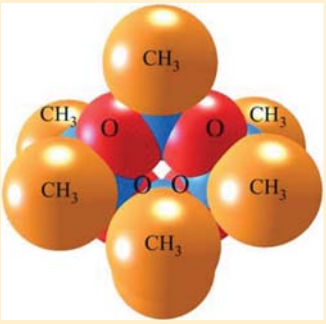

1. INTRODUCTION

Octamethylcyclotetrasiloxane (CAS no. 556-67-2, chemical formula $C_8H_{24}O_4Si_4$) is a cyclic siloxane that is a colorless, oily liquid under standard conditions. In the chemical industry, it is used as an adhesive and sealant, a finishing agent, or a solvent. Furthermore, it is an ingredient of paints, plastics, and rubber products.[1] In the field of energy technology, it is mainly employed as a working fluid in organic Rankine cycles (ORCs) because of some favorable properties, e.g., it is nontoxic, hardly flammable, and chemically stable up to high temperatures.[1] Over the last years, siloxanes were studied comprehensively with the aim to use them in ORC processes. For the design and optimization of such processes, it is essential to have an accurate knowledge of the thermodynamic properties of the fluids involved. The first fundamental equation of state in terms of the Helmholtz energy that provided this information was published in 2006 by Colonna et al.[2] Since the data situation was restricted in terms of quality and quantity at that time, it was challenging to develop a substance-specific equation of state for this fluid. Therefore, the generalized functional form for non- and weakly polar fluids of Span and Wagner[3] was applied, and only the coefficients of the equation of state were fitted to the available experimental database. Recent investigations showed that the available equation of state is disadvantageous with respect to the speed of sound and density in the homogeneous liquid phase as well as its extrapolation behavior.

In the last decades, several approaches have been proposed to overcome the problem of insufficient experimental data for the development of accurate fundamental equations of state, e.g., the construction of generalized functional forms for certain groups of fluids with analogous characteristics.[3−9] A new approach suggested by Rutkai et al.[10] comprises the implementation of molecular simulation data in the fitting procedure. Significant progress in computational technology and molecular modeling enables time-efficient and comprehensive simulations of thermodynamic properties. Here no restrictions due to challenging fluid characteristics (e.g., toxicity and corrosivity) or apparatus limitations with respect to temperature or pressure have to be taken into account. Therefore, these data provide a potential solution to fill gaps in the experimental database. This new approach was successfully applied to the development of fundamental equations of state for ethylene oxide[11] and hexamethyldisiloxane.[12] Following these lines, a potential model for octamethylcyclotetrasiloxane is presented in this work. The available experimental data are complemented by new measurements of the speed of sound in the liquid state. Both experimental and molecular simulation data sets were utilized for the development of the present equation of state.

2. SPEED OF SOUND MEASUREMENT AND MOLECULAR MODELING

The speed of sound of a given fluid can be determined by the time measurement of acoustic signal propagation through the fluid over some known distance. Here the applied measurement principle is based on estimating the time difference Δt between the detection of two distinct echoes of a signal emitted by a modulated high-frequency wave burst with a piezoelectric quartz crystal.[13,14] In the measurement cell, the crystal is placed

Received: March 22, 2016
Accepted: June 1, 2016
Published: June 10, 2016

DOI: 10.1021/acs.jced.6b00261
J. Chem. Eng. Data 2016, 61, 2580−2595

between two reflectors that are positioned at distances l_1 and l_2 from the crystal such that $l_1 < l_2$. The reflectors ensure that the echoes of the original signal are also detected with the crystal. The time shift between the detections, Δt, is caused by the different propagation path lengths l_1 and l_2. The speed of sound, w, is then given in terms of the ratio of the difference in the propagation distances l_1 and l_2 to Δt as

$$w = \frac{2(l_2 - l_1)}{\Delta t} \tag{1}$$

assuming that dispersion and diffraction effects can be neglected. The estimation of the time difference Δt was carried out here with the correlation method of Ball and Trusler[15] combined with signal enhancement by fast Fourier transformation. Details of the calculation method and the signal processing are given by Dubberke et al.[16]

The sample was obtained from Wacker with a given purity of ≥99%. Further details can be found in the Supporting Information. Before the measurement, the cell was filled with degassed octamethylcyclotetrasiloxane, and the fluid was compressed to about 20 MPa using a hand pump. A constant pressure level was reached after 1 h of equilibration. The pressure was measured with a transducer (Honeywell TJE with an operating range of up to 70 MPa), calibrated with a deadweight tester (Degranges and Hout, 5201-S), and protected by a blowout disc. The temperature was measured with a Pt100 thermometer (Rössel Messtechnik, RM-type), which was installed on the wall of the pressure cylinder next to the quartz crystal and was calibrated with a standardized 25 Ω platinum thermometer (Rosemount, 162 CE). The thermostat was constructed with three nested copper shields to allow for fine temperature adjustment of the cell over a wide temperature range. Each shield was equipped with its own independently adjustable heater; each was controlled with a combination of a proportional−integral−derivative (PID) controller and a proportional (P) controller. For the path length difference Δl, calibration measurements were carried out with water. Water at high purity and accurate speed of sound measurement data are available over a wide range of temperature and pressure. Details are described by Gedanitz et al.[17] The obtained speed of sound data were amended by the diffraction correction of Harris,[18] where significant dispersion effects are not expected for a resonance frequency of 8 MHz.[19] The reported uncertainties for the speed of sound were estimated according to the error propagation law, considering the uncertainty of the temperature and pressure measurements as well as the uncertainty of the referencing procedure. The measurements were carried out along six isotherms in the temperature range from 300 to 550 K at pressures of up to 26 MPa (54 data points in total). Numerical results are given in the Supporting Information.

In addition to the speed of sound measurements, molecular simulations were carried out to generate a data set of six Helmholtz energy derivatives at 87 state points, resulting in a set of 522 thermodynamically nonredundant entries. The calculations were performed with the molecular simulation tool ms2[20] through the use of the recently implemented formalism of Lustig.[21,22] This new feature enables the calculation of the residual part A^{r}_{nm} of the derivatives

$$\frac{\partial^{n+m} a(T,\rho)/(RT)}{\partial(1/T)^n \partial\rho^m}(1/T)^n \rho^m \equiv A_{nm} = A^{\circ}_{nm} + A^{\mathrm{r}}_{nm} \tag{2}$$

for any $n > 0$ or $m > 0$ per sampled state point, where a is the molar Helmholtz energy, T is the absolute temperature, ρ is the density, and R = 8.3144621 J·mol^{-1}·K^{-1} is the universal gas constant.[23] The ideal part $A^{\circ}_{00} = A^{\circ}_{00}(T) + \ln(\rho/\rho_{\mathrm{ref}})$, where ρ_{ref} is an arbitrary reference density,[24] corresponds to the value of $A_{00}(T,\rho)$ when no intermolecular interactions are present. Consequently, $A^{\circ}_{nm} = 0$ for $n > 0$ and $m > 0$, and $A^{\circ}_{nm} = (-1)^{1+m}$ for $n = 0$ and $m > 0$. $A^{\circ}_{nm}(T)$ has a nontrivial but exclusive temperature dependence and is a sum of contributions due to translational, rotational, and internal molecular degrees of freedom. Since $a/(RT)$ is a thermodynamic potential, every other equilibrium thermodynamic property can be obtained as a combination of A_{nm} derivatives. Examples are given later on (eqs 12 to 15). A more complete list is given by Span.[24]

The quality of molecular simulation results is predominantly dependent on the underlying molecular interaction model. The octamethylcyclotetrasiloxane model developed in this work consists of 16 Lennard-Jones (LJ) sites and eight point charges (cf. Figure 1). The geometry of the model was determined by quantum-chemical calculations applying the software package GAMESS(US)[25] with the Hartree−Fock method and the 6-31G basis set. The initial values of the LJ energy (ε) and size (σ) parameters as well as those of the point charges (q) were adopted from Thol et al.[12] In the initial phase, the magnitudes of the point charges were adjusted to fit experimental vapor−liquid equilibrium data, namely, saturated liquid density and vapor pressure data. In the last step, all of the model parameters, including the geometric structure, were fine-tuned with the reduced unit method.[26] The resulting model parameters are listed in Table 1. The model itself considers no internal degrees of freedom, which can be justified by the compact structure of the molecule. Therefore, the ideal part $A^{\circ}_{nm}(T)$ was taken from the current equation of state for the calculation of thermodynamic properties for which this contribution is necessary (cf. eqs 12, 14, and 15). Finally, the model was validated by comparing simulation results with experimental vapor−liquid equilibrium data as well as single-phase liquid density, speed of sound, second virial coefficient, and transport property data from the literature. The numerical simulation results and comparisons with the present equation of state are given in the Supporting Information. The molecular force field model by Matsubara et al.[27] is similar in terms of the united-atom approach and rigid-body approximation. Although

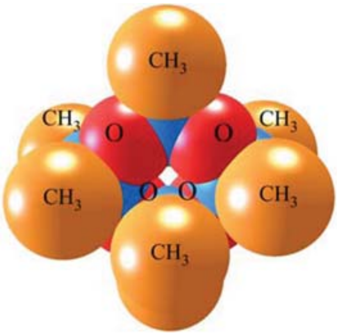

Figure 1. Present molecular interaction model for octamethylcyclotetrasiloxane. CH$_3$, methyl site; O, oxygen site; not labeled, silica site. The sphere diameters correspond to the Lennard-Jones size parameters, which are depicted according to the molecular geometry scale.

Table 1. Parameters of the Present Molecular Interaction Model for Octamethylcyclotetrasiloxane[a]

interaction site	x/Å	y/Å	z/Å	σ/Å	$\varepsilon \cdot k_B^{-1}$/K	q/e
CH_3	4.3198	−0.2718	1.3971	3.8181	122.4689	
CH_3	3.9847	−1.7562	−1.3286	3.8181	122.4689	
Si	3.1365	−0.7701	0.0267	3.5167	15.2895	0.3036
O	1.9213	−1.6816	0.7475	3.1248	44.0134	−0.3036
CH_3	1.6735	3.2187	−1.5120	3.8181	122.4689	
CH_3	1.4331	2.2420	1.4613	3.8181	122.4689	
Si	1.3378	1.7784	−0.3619	3.5167	15.2895	0.3036
O	2.4782	0.5925	−0.7067	3.1248	44.0134	−0.3036
CH_3	−2.2590	1.2815	1.3636	3.8181	122.4689	
CH_3	−2.6052	−0.1997	−1.3611	3.8181	122.4689	
Si	−1.4157	0.2953	0.0056	3.5167	15.2895	0.3036
O	−0.2012	1.2041	−0.7199	3.1248	44.0134	−0.3036
CH_3	0.2869	−2.6955	−1.4467	3.8181	122.4689	
CH_3	0.0459	−3.7042	1.5158	3.8181	122.4689	
Si	0.3828	−2.2517	0.3814	3.5167	15.2895	0.3036
O	−0.7576	−1.0687	0.7370	3.1248	44.0134	−0.3036

[a] Lennard-Jones sites are denoted by the modeled atoms or atomic groups. Electrostatic sites are denoted by point charge magnitudes q. Coordinates (x, y, z) are given with respect to the center of mass in a principal axes system. k_B is the Boltzmann constant.

it leads to excellent results for transport properties, the representation of the pressure−volume−temperature (pvT) relation is inferior. Recently, Xu and Leng[28] published a new model for octamethylcyclotetrasiloxane that is better suited for pvT data, considering the internal molecular degrees of freedom. The performance of the present molecular model for the speed of sound is shown in Figure 2. As can be seen, nearly all of the simulation results agree with the experimental values within their statistical uncertainties. Figure 3 shows the performance for the thermal conductivity and shear viscosity for liquid states. Simulation results were obtained by equilibrium molecular dynamics simulations and the Green−Kubo formalism (cf. Guevara-Carrion et al.[29]). The model slightly underpredicts the literature thermal conductivity data over the whole temperature range. For the shear viscosity, except for the value at 300 K, the simulation results agree with the literature data within their statistical uncertainties.

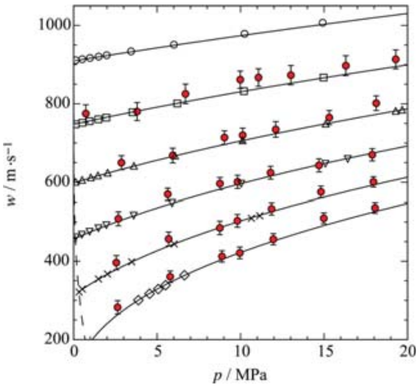

Figure 2. Speed of sound of octamethylcyclotetrasiloxane. Present experimental data: ○, 300 K; □, 350 K; △, 400 K; ▽, 450 K; ×, 500 K; ◇, 550 K. Red ●, present simulation data. Curves: —, present equation of state; − −, vapor pressure curve.

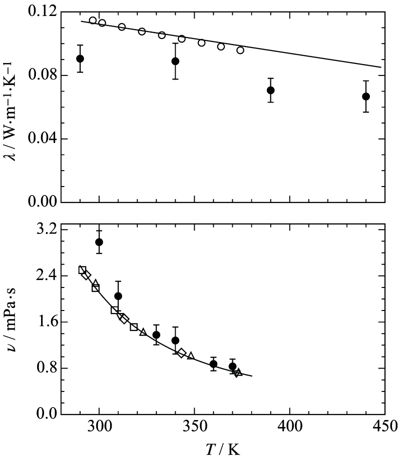

Figure 3. (top) Thermal conductivity and (bottom) shear viscosity of octamethylcyclotetrasiloxane at 0.1 MPa: ●, present simulation data; experimental data of ○, Abbas et al.;[30] □, Marsh;[31] ◇, Waterman et al.;[32] △, Reuther;[33] ▽, Wilcock;[34] —, correlation from the DIPPR database.[35]

3. EQUATION OF STATE

The equation of state presented here is expressed in terms of the molar Helmholtz energy a with the independent variables temperature T and density ρ. For a dimensionless description, the Helmholtz energy is reduced by the temperature and the universal gas constant R:

$$\alpha(\tau, \delta) = \frac{a(T, \rho)}{RT} \tag{3}$$

According to the theorem of corresponding states, the independent variables are reduced by the critical temperature T_c and critical density ρ_c. The reduced Helmholtz energy then reads as

$$\alpha(\tau, \delta) = \alpha^{\circ}(\tau, \delta) + \alpha^{r}(\tau, \delta) \tag{4}$$

DOI: 10.1021/acs.jced.6b00261
J. Chem. Eng. Data 2016, 61, 2580−2595

where $\tau = T_c/T$ and $\delta = \rho/\rho_c$. The ideal contribution (superscript "○") is derived from the following equation for the isobaric heat capacity:

$$\frac{c_p^\circ}{R} = (c_0 + 1) + \sum_{i=1}^{3} m_i \left(\frac{\theta_i}{T}\right)^2 \frac{\exp(\theta_i/T)}{(\exp(\theta_i/T) - 1)^2} \tag{5}$$

Polynomial terms were avoided to ensure correct extrapolation behavior. Since the present fundamental equation of state is expressed in terms of the reduced Helmholtz energy, eq 5 has to be integrated twice with respect to τ:

$$\alpha^\circ(\tau, \delta) = c^{\mathrm{II}} + c^{\mathrm{I}}\tau + c_0 \ln(\tau) + \sum_{i=1}^{3} m_i \ln(1 - \exp(-\theta_i/T_c\tau)) + \ln(\delta) \tag{6}$$

The integration constants c^{I} and c^{II} can be chosen arbitrarily. For fluids that are liquids under standard conditions, the most common reference state is the normal boiling point. At $p = 1$ atm, the saturation temperature T_0 and the saturated liquid density ρ_0' are determined. At this state point, the integration constants are chosen such that the enthalpy is $h_0(T_0, \rho_0') = 0$ J·mol^{-1} and the entropy is $s_0(T_0, \rho_0') = 0$ J·mol^{-1}·K^{-1}. The integration constants and the parameters for the Planck−Einstein terms are listed in Table 2.

Table 2. Parameters of the Ideal Part of the Present Equation of State (cf. eq 6)

m_1	0.292757
m_2	38.2456
m_3	58.975
θ_1/K	40
θ_2/K	200
θ_3/K	1800
c_0	3.0
c^{I}	−21.674365
c^{II}	71.163605

The residual part (superscript "r") comprises polynomial (Pol), exponential (Exp), and Gaussian bell-shaped (GBS) terms:

$$\alpha^{\mathrm{r}}(\tau, \delta) = \alpha^{\mathrm{r}}_{\mathrm{Pol}}(\tau, \delta) + \alpha^{\mathrm{r}}_{\mathrm{Exp}}(\tau, \delta) + \alpha^{\mathrm{r}}_{\mathrm{GBS}}(\tau, \delta) = \sum_{i=1}^{5} n_i \delta^{d_i} \tau^{t_i} + \sum_{i=6}^{10} n_i \delta^{d_i} \tau^{t_i} \exp(-\delta^{p_i}) + \sum_{i=11}^{15} n_i \delta^{d_i} \tau^{t_i} \exp[-\eta_i(\delta - \varepsilon_i)^2 - \beta_i(\tau - \gamma_i)^2] \tag{7}$$

The polynomial and exponential terms are in principle sufficient for the description of the whole fluid surface. The GBS terms, introduced by Haar et al.[36] and applied in a modified form to the fundamental equation of state for methane by Setzmann and Wagner,[37] allow for a more accurate representation of the critical region. Nowadays, these terms are used in all fluid regions, which leads to a reduction in the total number of terms. For a long time, equations with 20 to 50 terms were common practice,[24] whereas recent equations of state consist of 14 to 25 terms[38−41] because of this functional form. The present equation of state consists of five polynomial, five exponential, and five GBS terms. Its parameters are listed in Table 3.

The equation presented here was constrained to the critical temperature $T_c = 586.5$ K reported by Young.[42] The critical density $\rho_c = 1.043$ mol·dm^{-3} and the critical pressure $p_c = 1.347$ MPa were determined during the fit. The triple-point temperature $T_{\mathrm{tr}} = 290.25$ K reported by Mekhtiev and Karasharli[43] was applied as the lower temperature limit. The resulting triple-point density is $\rho_{\mathrm{tr}}' = 3.24$ mol·dm^{-3}. Additionally, the molecular weight $M = 296.61576$ g·mol^{-1} was adopted.[44]

The calculation of any thermodynamic equilibrium state property from the derivatives of the reduced Helmholtz energy with respect to its independent variables can be taken from Span.[24]

4. COMPARISON TO EXPERIMENTAL AND MOLECULAR SIMULATION DATA

In this section, the present equation of state is compared to experimental and molecular simulation data. An overview of the homogeneous data is given in Figure 4. The gray area indicates the region covered by experimental measurements. The triangles depict the state points where molecular simulation data were generated in this work. In addition to these

Table 3. Parameters of the Residual Part of the Present Equation of State (cf. eq 7)

i	n_i	t_i	d_i	p_i	η_i	β_i	γ_i	ε_i
1	$5.273743\cdot10^{-2}$	1.000	4					
2	$4.176401\cdot10^{+0}$	0.270	1					
3	$-4.737070\cdot10^{+0}$	0.510	1					
4	$-1.289588\cdot10^{+0}$	0.998	2					
5	$5.272749\cdot10^{-1}$	0.560	3					
6	$-2.558391\cdot10^{+0}$	1.750	1	2				
7	$-9.726737\cdot10^{-1}$	3.090	3	2				
8	$7.208209\cdot10^{-1}$	0.790	2	1				
9	$-4.789456\cdot10^{-1}$	2.710	2	2				
10	$-5.563239\cdot10^{-2}$	0.998	7	1				
11	$3.766589\cdot10^{+0}$	0.930	1		0.861	0.75	1.124	0.926
12	$8.786997\cdot10^{-2}$	3.170	1		1.114	0.55	1.388	1.300
13	$-1.267646\cdot10^{-1}$	1.080	3		1.010	1.00	1.148	1.114
14	$-1.004246\cdot10^{+0}$	1.410	2		1.110	0.47	1.197	0.996
15	$-1.641887\cdot10^{+0}$	0.890	2		1.032	1.36	0.817	0.483

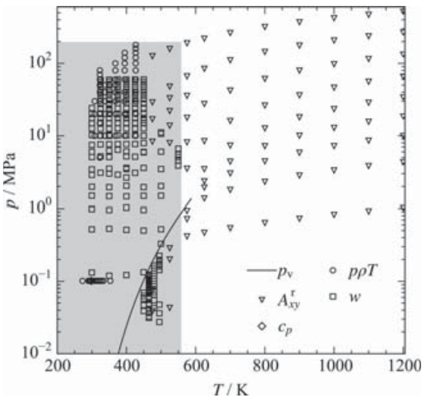

Figure 4. Available data for octamethylcyclotetrasiloxane in the homogeneous region. The gray area depicts the region where experimental data are available: $T < 590$ K and $p < 180$ MPa. The residual Helmholtz derivatives from molecular simulation extend this region up to $T_{\max} = 1200$ K and $p_{\max} = 520$ MPa.

properties, vapor−liquid equilibrium and ideal gas heat capacity data were available.

In the next sections, the data analysis is based on relative deviations ΔX, defined as

$$\Delta X = 100\frac{X_{\mathrm{DATA}} - X_{\mathrm{EOS}}}{X_{\mathrm{DATA}}} \tag{8}$$

Average absolute relative deviations (AADs) were calculated as follows:

$$\mathrm{AAD} = \frac{1}{N}\sum_{i=1}^{N} |\Delta X_i| \tag{9}$$

For the statistical analysis, vapor pressure, saturated liquid density, and saturated vapor density data are separated into three temperature ranges: low temperature (LT: $T/T_c \leq 0.6$), medium temperature (MT: $0.6 \leq T/T_c \leq 0.98$), and high temperature (HT: $T/T_c > 0.98$). All other properties are categorized as gas, liquid, critical region ($0.98 \leq T/T_c \leq 1.1$ and $0.7 \leq \rho/\rho_c \leq 1.4$), or supercritical region. The last of these is further divided into low density (LD: $\rho/\rho_c \leq 0.6$), medium density (MD: $0.6 \leq \rho/\rho_c \leq 1.5$), and high density (HD: $\rho/\rho_c > 1.5$). In the diagrams, the equation of Colonna et al.[2] and the correlation equations of the DIPPR[35] and TDE[45] databases are plotted for comparison.

4.1. Ideal Gas State.

In general, the ideal gas behavior of siloxanes has been only scarcely investigated. This challenge was discussed in detail by Thol et al.[12] and here will only be summarized briefly. When setting up the first set of Helmholtz equations, Colonna et al.[2] applied the Harrison−Seaton zeroth-order contribution method.[46] This was the only method providing information about Si−C bonds. However, the DIPPR database[35] reports a possible uncertainty of up to 25% for data from this method, which is not acceptable for accurate equations of state. Therefore, Nannan et al.[47] investigated the ideal gas behavior of several siloxanes more comprehensively. As a first approach, they measured speed of sound data for gaseous states, which they used to derive c_p° data. For small molecules, this is an accurate approach. However, with increasing complexity of the molecule, the uncertainty in this approach increases. A rough estimation can be made with the following relation:[24]

$$\left|\frac{\Delta c_p^\circ}{c_p^\circ}\right| = \left|2\left(\frac{c_p^\circ}{R} - 1\right)\frac{\Delta w^\circ}{w^\circ}\right| \tag{10}$$

Because of the large isobaric heat capacity of octamethylcyclotetrasiloxane, this results in an uncertainty of 3.9% with respect to c_p° data, although the speed of sound measurements are claimed to be accurate to within 0.02%.[47] Since the measurements were carried out over a restricted temperature range (450 to 495 K), these data are not sufficient to set up the ideal part for an equation of state covering the whole temperature range. Thus, Nannan et al.[47] determined c_p° data over a broad temperature range by means of ab initio calculations. They found similar results for two methods without giving any information on the accuracy of the data. Because the ab initio calculations were not done at the same temperatures as the measurements, the experiments cannot directly be used to assess the uncertainty of the calculations. The same calculations for hexamethyldisiloxane showed a deviation from the corresponding equation[12] of approximately 3%. Therefore, the c_p° data were used only as an approximate guide for the present fit. In Figure 5, the representation of the c_p° data of Nannan et al.[47] by the present equation of state is depicted. In the top panel, the reduced ideal gas heat capacity is illustrated as a function of temperature. For computational efficiency, Colonna et al.[2] applied a simple polynomial approach for their ideal gas equation of state, which does not extrapolate well. For $T \rightarrow 0$ K, only translational and rotational molecular degrees of freedom are excited,[12,24] which leads to $c_p^\circ/R = 4$. The polynomial approach of Colonna et al.[2] results in an incorrect value of $c_p^\circ/R \approx -2$.

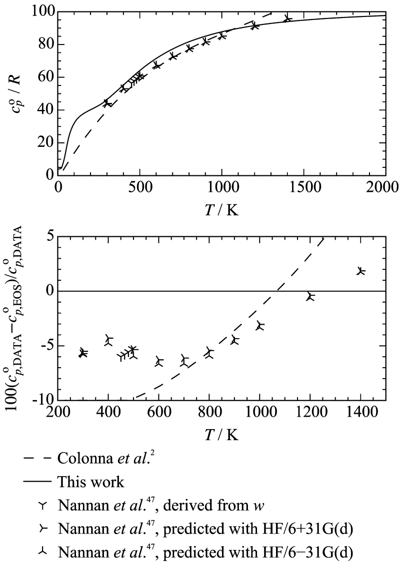

Figure 5. Representation of the isobaric heat capacity of the ideal octamethylcyclotetrasiloxane gas with the present equation of state.

For high temperatures, an asymptotic course with a limiting value based on the maximum number of molecular degrees of freedom has to be modeled. Because of the polynomial form, the ideal gas heat capacity of Colonna et al.[2] increases

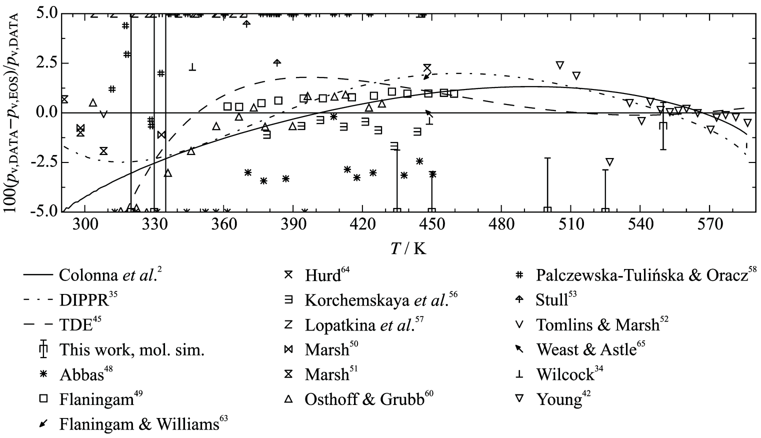

Figure 6. Relative deviations of the vapor pressure data from the present equation of state.

Table 4. Average Absolute Relative Deviations of Experimental Vapor Pressure Data and Saturated Liquid and Vapor Densities from the Present Equation of State[a]

			AAD/%			
authors	no. of data points	T range/K	LT[b]	MT[b]	HT[b]	overall
		Vapor pressure p_v				
Abbas et al.[48]	18	312−451	7.56	4.00	−	4.79
Flaningam[49]*	13	361−460	−	0.76	−	0.76
Flaningam and Williams[63]	1	448.15	−	1.87	−	1.87
Hurd[64]	1	447.99	−	2.26	−	2.26
Korchemskaya et al.[56]	10	378−446	−	2.44	−	2.44
Lopatkina et al.[57]	12	304−369	26.5	8.14	−	20.4
Marsh[50]	2	298−334	0.94	−	−	0.94
Marsh[51]	3	291−309	1.20	−	−	1.20
Osthoff and Grubb[60]	16	303−429	3.53	0.58	−	1.69
Palczewska-Tulińska and Oracz[58]	24	311−447	3.40	8.04	−	6.10
Stull[53]	10	294−445	12.5	5.97	−	8.60
Tomlins and Marsh[52]	1	308.14	0.063	−	−	0.063
Weast and Astle[65]	1	448.91	−	0.054	−	0.054
Wilcock[34]	2	346−449	2.32	0.40	−	1.36
Young[42]*	16	505−587	−	0.75	0.28	0.67
		Saturated liquid density ρ'				
Golik and Cholpan[66]	1	303.13	0.29	−	−	0.29
Hurd[64]	5	273−354	4.64	0.017	−	3.72
Korchemskaya et al.[56]	1	293.14	0.035	−	−	0.035
Levien[67]	1	298.14	0.024	−	−	0.024
Marsh[51]	3	291−309	0.044	−	−	0.044
McLure and Barbarin-Castillo[68]*	14	292−409	0.006	0.028	−	0.015
Palczewska-Tulińska and Oracz[58]	22	292−434	0.13	0.17	−	0.15
Patnode and Wilcock[55]	1	293.14	0.066	−	−	0.066
Shinoda and Hildebrand[69]	1	298.14	0.005	−	−	0.005
Tanaka[70]	1	293.14	0.066	−	−	0.066
Tomlins and Marsh[52]	1	308.14	0.043	−	−	0.043
Waterman et al.[32]	1	293.14	0.030	−	−	0.030
Young[42]*	7	503−577	−	0.24	0.44	0.26
		Saturated vapor density ρ''				
Korchemskaya et al.[56]	9	378−446	−	6.19	−	6.19
Young[42]	8	536−580	−	10.5	18.5	11.5

[a] All temperatures were adapted to the ITS-90 Scale; data sets that were applied to the fit are marked with an asterisk. [b] LT, $T/T_c \le 0.6$; MT, $0.6 \le T/T_c \le 0.98$; HT, $T/T_c > 0.98$.

monotonously, whereas the present functional form reaches a limiting value. In the bottom panel of Figure 5, the three different methods used by Nannan et al.[47] to predict c_p° data are compared with the present equation of state. For $T < 800$ K, the data systematically deviate by approximately 7%. At higher temperatures, the deviations decrease. The parameters of eq 5 were simultaneously adjusted to fit the c_p° data of Nannan et al.[47] and available data for the speed of sound and isobaric heat capacity (e.g., refs 47 and 48). During the fitting procedure, it turned out that it was not possible to represent the c_p° data in a more accurate way without compromising the other properties. Since the accuracy of the c_p° data is questionable, the speed of sound and isobaric heat capacity data were preferentially fitted and the comparably high deviations of the c_p° data have to be accepted here.

4.2. Vapor−Liquid Equilibrium. The available experimental vapor pressure data are summarized in Figure 6 and Table 4. Many authors report vapor pressure data in their publications to point out the purity of their samples. More comprehensive investigations were made by eight research groups, which are discussed in more detail here. As an indication of the quality of the data, the measurements on hexamethyldisiloxane, which were analyzed comprehensively by Thol et al.,[12] were considered where groups published data for both fluids. The lower-temperature region (T < 460 K) was investigated by several different authors, whereas the higher-temperature region was studied only by Young.[42] In the lower-temperature region, the present equation of state was fitted to the vapor pressure data of Flaningam[49] (AAD = 0.76%). He reported these measurements in the same publication as the results for hexamethyldisiloxane. Deviations of 0.5% with respect to the equation for hexamethyldisiloxane were assessed to be reasonable.[12] The experimental uncertainty in the octamethylcyclotetrasiloxane data is assumed to be higher than that in the case of hexamethyldisiloxane because of inferior sample purity (octamethylcyclotetrasiloxane, 99.49%; hexamethyldisiloxane, 99.9%), and the deviations of less than 1.1% with respect to the present equation of state seem to be realistic. In this way, the data of Marsh[50,51] and Tomlins and Marsh[52] scatter around the equation within 1.5% for T < 360 K. Since the vapor pressure of Tomlins and Marsh[52] was measured more recently than the data of Marsh,[50,51] this point was taken as a reference and was reproduced within 0.063% by the present equation of state. Fitting the data of Flaningam[49] in a more accurate way would cause higher deviations in the low-temperature regime. In the temperature region where Flaningam's data[49] are located, recent measurements by Abbas et al.[48] (AAD = 4.79%) are available. In analogy to the results for hexamethyldisiloxane, these data significantly differ from those obtained using the present equation and other literature data. Between 370 and 451 K, a systematic offset of approximately −2.7% can be observed. The deviations increase for lower temperatures, which is most probably caused by inappropriate handling of the apparatus (cf. Thol et al.[12]). The data of Stull[53] (AAD = 8.60%) are part of a comprehensive literature study summarizing vapor pressure data for more than 1200 organic substances. In that publication,[53] Hunter et al.,[54] Patnode and Wilcock,[55] and Wilcock[34] are cited to be the primary sources for octamethylcyclotetrasiloxane. In the original publications,[34,54,55] all of them investigated siloxane polymers, and they reported only the normal boiling points of the participating monomers. Since Stull's data[53] exhibit unreasonably high deviations of up to 20%, they were not considered any further. Korchemskaya et al.[56] (AAD = 2.44%) primarily investigated binary mixtures containing siloxanes and reported uncertainties only in terms of composition. No information is given for the uncertainty of the pure fluid data. Except for two state points at $T \geq 444$ K, the measured vapor pressures are systematically lower than values calculated from the present equation of state. However, they are still reproduced within 1.1%, which is the same accuracy as for the data of Flaningam.[49]

Lopatkina et al.[57] (AAD = 20.4%) measured the vapor pressure between 304 and 369 K by means of a static method with a quartz Bourdon gauge as a reference. The temperature was controlled with copper−constantan thermocouples. No information on the experimental uncertainties is given. The deviations with respect to the present equation of state increase from 5% to 38% with decreasing temperature. The measurements of Marsh,[50,51] which are located in the same temperature range, indicate that the data of Lopatkina et al.[57] are most likely not correct. Therefore, these data were not considered during the development of the present equation of state. Recent measurements by Palczewska-Tulińska and Oracz[58] were carried out with a comparative ebulliometer applying n-dodecane as the reference substance. The specified temperature uncertainty, ΔT = 0.005 K, and pressure uncertainty, Δp = 6.7 Pa, yield a combined expanded uncertainty of 0.03% to 3.8% (k = 2). The measurements of Palczewska-Tulińska et al.[59] on cyclohexane were made with the same technique and are reproduced by the equation of Zhou et al.[41] with an AAD of 0.13%. Nonetheless, the measurements on octamethylcyclotetrasiloxane exhibit deviations of up to 8.5% with respect to the present equation of state and other measurements in this region. Data at lower temperatures deviate significantly less than data at high temperatures. These findings agree with their own correlation results presented in ref 58. Similar behavior was found for hexamethylcyclotrisiloxane, and even worse deviations were observed for decamethylcyclopentasiloxane. Therefore, the data were not considered during the development of the present equation of state. Finally, measurements by Osthoff and Grubb[60] (AAD = 1.69%) are available over the same temperature range as the data sets discussed above. The sample purity was estimated to be 99.82% on the basis of a melting point measurement. For the vapor pressure measurements, a modified isoteniscope reported by Smith and Menzies,[61] which is categorized as a static method, was used. No information is given about the experimental uncertainties. For $T \geq 350$ K, deviations with respect to the present equation of state amount to 1%, which is in accordance with the data of Flaningam[49] and Korchemskaya et al.[56] For lower temperatures (T < 350 K), the percentage deviations increase. This is most likely related to the pressure measurement, which was carried out with a mercury manometer. Since the vapor pressure of octamethylcyclotetrasiloxane is low, only a small column of mercury was observed (1.49 mmHg at the lowest temperature). The percentage deviations from the equation yield systematic absolute deviations of approximately −0.3 mmHg. These differences can easily occur with visual detection of the meniscus. Furthermore, the vapor pressure at the lowest temperature agrees well with the data point of Tomlins and Marsh.[52] Thus, the increasing deviations of the data with respect to the present equation are assumed to be a problem in the data. In their publication, Osthoff and Grubb[60] introduced a correction for all of the vapor pressure data at $T \geq 353$ K by adding the vapor pressure of mercury. No further explanation for why they did not do the same correction for the low-temperature data was provided. The only experimental data set available for T > 460 K was published by Young[42] (AAD = 0.67%). A modified glass apparatus developed by Ambrose and Townsend[62] was used, and the specified uncertainty amounts to 0.5% to 2%. Except for two data points with deviations of

2.5%, all of their data scatter around the present equation of state within the given experimental uncertainty. On the basis of these results, the expected uncertainty in the vapor pressure data calculated with the present equation of state is 1.5% for $T \leq 460$ K and 2% for higher temperatures.

The representations of the saturated liquid and vapor densities are depicted in Figure 7, and the average absolute relative deviations are listed in Table 4. Similar to the vapor pressure, the lower-temperature region was measured by different authors, whereas the high-temperature region was investigated only by Young.[42] The most comprehensive data sets for $T < 440$ K were published by McLure and Barbarin-Castillo[68] (AAD = 0.015%) and Palczewska-Tulińska and Oracz[58] (AAD = 0.15%). Palczewska-Tulińska and Oracz[58] used an Anton Paar densimeter, and the specified uncertainties yield a combined expanded uncertainty of approximately 0.006% in density. Most probably, the stated uncertainty of the density measurement ($\Delta\rho = 0.01$ kg·m^{-3}) is too optimistic, so the real uncertainty is assumed to be higher. In comparison with the present equation of state and other literature data, the data of Palczewska-Tulińska and Oracz[58] differ by up to 0.4%. The deviations exhibit a parabolic shape, which is the same behavior as for their measurements of decamethylcyclopentasiloxane.[58] This leads to the assumption that either the apparatus or the measurement procedure was incorrect. Thus, the remaining data set of McLure and Barbarin-Castillo[68] was used to develop the present equation of state. The sample was purified up to 99.5%, and the measurements were carried out with a magnetically levitated Archimedian sinker.[68] The specified uncertainties result in a combined expanded uncertainty ($k = 2$) of 0.014%. For $T < 360$ K, the present equation of state reproduces the data within their experimental uncertainty. With increasing temperature, the deviations increase to 0.4%. This is caused by the high-temperature data of Young[42] (AAD = 0.26%), which scatter around the present equation of state within 0.45%. For each measurement, Young[42] filled a glass tube with liquid octamethylcyclotetrasiloxane, evacuated the tube while freezing the sample, and sealed the tube after degassing. Subsequently, each tube was heated slowly, and the temperature at which the tube was completely filled with liquid was detected. The mass of the sample was determined from the weight of the sealed tube including the sample and the weight of the opened tube that was purged of the sample. The volume was determined by measuring the weight of the full and cut tube in distilled water. These three steps involve several different sources of uncertainties, which are not discussed in the paper. However, Young[42] states an uncertainty of 0.1% to 0.3%. Since it is not completely clear how the experimental uncertainty was determined, the deviations of 0.45% with respect to the present equation of state seem to be acceptable.

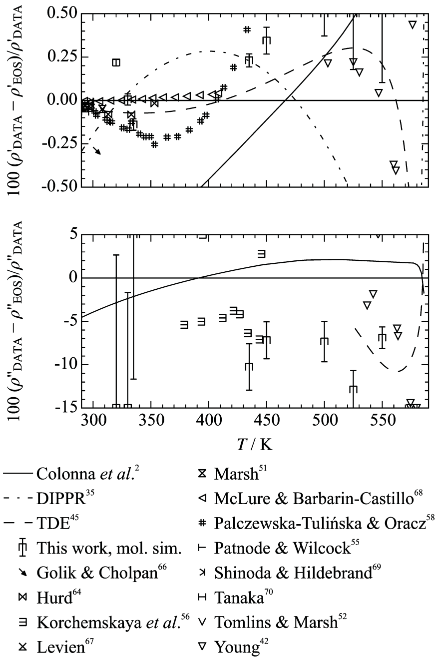

Figure 7. Relative deviations of the saturated density data from the present equation of state: (top), saturated liquid density; and (bottom), saturated vapor density.

Finally, data sets comprising only few state points were used to verify the representation of the saturated liquid density. The data of Korchemskaya et al.,[56] Levien,[67] Marsh,[51] Patnode and Wilcock,[55] Tanaka,[70] Tomlins and Marsh,[52] and Waterman et al.[32] are reproduced with an AAD < 0.07%. Therefore, the uncertainty in the saturated liquid density data calculated with the present equation of state is assessed to be 0.1% for $T < 360$ K and 0.5% for higher temperatures.

The saturated vapor density was investigated by Korchemskaya et al.[56] (AAD = 6.19%) and Young[42] (AAD = 11.5%). Korchemskaya et al.[56] focused on mixture measurements and did not provide information on the experimental uncertainties. Young[42] applied the same measuring procedure as for the saturated liquid density. The disappearance of the corresponding phases was detected visually, thus leading to higher uncertainties. For the liquid phase, a remaining gas bubble does not falsify the result too much, whereas a remaining liquid droplet in the gas phase has a large impact. Therefore, the deviations presented in Figure 7 are not surprising. For a reliable uncertainty statement, a more appropriate measuring technique has to be used to carry out new measurements.

4.3. Homogeneous Region.

Comparisons to homogeneous density data are shown in Figure 8 and summarized in Table 5. At the bottom of Figure 8, relative deviations of experimental data from the present equation of state at atmospheric pressure are illustrated. The temperature range is restricted to 290 to 355 K. Except for the data reported by Schuh and Fischer,[71] all of the data deviate by less than 0.1% from the present equation. The measurements of Marsh[50] (AAD = 0.058%) and Herring and Winnick[72] (AAD = 0.056%) agree perfectly with each other and are reproduced within 0.06%. An even better representation of the data was not possible without compromising the saturated liquid density.

Since the measured saturated liquid density data cover the entire vapor−liquid equilibrium temperature range and the homogeneous density measurements are restricted to a range of 65 K, the saturated liquid density data were primarily correlated. However, reproducing the homogeneous density data at atmospheric pressure in a more accurate way is most probably not required because the deviations can be explained by the claimed experimental uncertainty of the data. The correlation of the high-pressure data was more challenging because contradictory trends were observed (cf. Figure 8, top). Wappman et al.[78] utilized a sample with a purity of 99% for

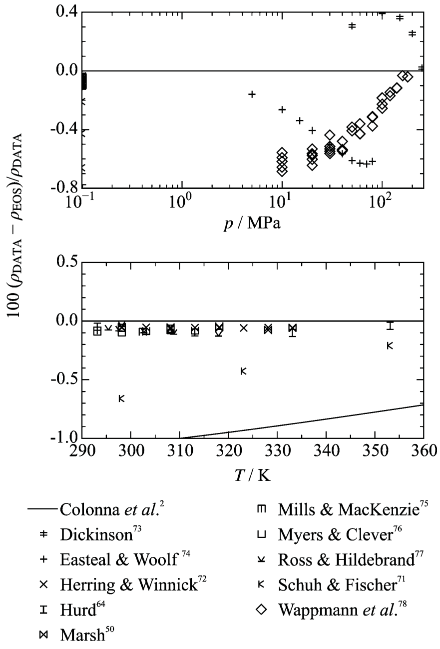

Figure 8. Representation of the homogeneous density of octamethylcyclotetrasiloxane. (top) Relative deviations of all available experimental homogeneous density data from the present equation of state. (bottom) Relative deviations of the homogeneous density data from the present equation of state at atmospheric pressure.

their measurements. The employed piston cylinder densimeter was described in detail by Wappmann et al.[82] The accuracy of the measurements was assessed with test measurements on methanol, which reproduced Goodwin's data[83] within 0.2%. Without any further explanation, Wappmann et al.[78] stated an experimental uncertainty of 0.4% for octamethylcyclotetrasiloxane. The second data set of Easteal and Woolf[74] shows an opposite trend with respect to the present equation of state. They investigated only one isotherm (323.15 K), which was not measured by Wappmann et al.[78] Therefore, it is not possible to compare these results directly with each other. Easteal and Woolf[74] measured their density data with an even lower sample purity than Wappmann et al.[78] (98%) in a bellows volumometer.[84] The specified uncertainties yield a combined expanded uncertainty of 0.06%, a value that is highly unrealistic considering the sample purity. It was not possible to represent any of the data within the claimed accuracy. Thus, test correlations were established to find out the cause of these problems. Fitting both data sets at the same time was not possible because of their contrary courses. Therefore, only one data set was correlated at a time, and it was still not possible to reach a satisfactory result. Hence, the interaction of different properties was investigated. Next to the homogeneous density data, the speed of sound measurements from this work and the isobaric heat capacity data of Abbas et al.[48] recently became available. Both data sets were considered in the fitting procedure. Since the heat capacity measurements by Abbas et al.[48] were reasonable for hexamethyldisiloxane,[12] it is unlikely that these data cause problems. As expected, no observable improvement of the density data could be reached when these data were deleted from the fit. Therefore, the present speed of

Table 5. Average Absolute Relative Deviations of the Experimental Data in the Homogeneous State from the Present Equation of State[a]

				AAD/%						
authors	no. of data points	T range/K	p range/MPa	gas	liq.	crit. reg.	LD	MD	HD	overall
			pvT Data							
Dickinson[73,b]	5	323.19	50.0−251	–	0.27	–	–	–	–	0.27
Easteal and Woolf[74]	10	323.19	5.0−81	–	0.47	–	–	–	–	0.47
Herring and Winnick[72]	8	298−334	0.101325	–	0.056	–	–	–	–	0.056
Hurd[64]	5	273−354	0.101325	–	3.74	–	–	–	–	3.74
Marsh[50]	5	293−334	0.101325	–	0.058	–	–	–	–	0.058
Mills and MacKenzie[75]	2	293−303	0.101325	–	0.087	–	–	–	–	0.087
Myers and Clever[76]	6	293−319	0.101325	–	0.078	–	–	–	–	0.078
Ross and Hildebrand[77]	6	295−318	0.101325	–	0.071	–	–	–	–	0.071
Wappmann et al.[78]*	36	308−427	10.0−181	–	0.42	–	–	–	–	0.42
Schuh and Fischer[71]	3	298−354	0.101325	–	0.43	–	–	–	–	0.43
			Speed of sound w							
this work*	54	299−550	0.1−27	–	0.12	–	–	–	0.15	0.14
Golik and Cholpan[79]	1	303.13	0.101325	–	0.15	–	–	–	–	0.15
Nannan et al.[47]*	53	450−496	0.0−1.0	0.17	–	–	–	–	–	0.17
Niepmann and Schmidt[80]	117	299−450	2.6−61	–	–	–	–	–	0.47	0.47
Waterman et al.[32]	1	293.14	0.101325	–	0.026	–	–	–	–	0.026
			Isobaric heat capacity c_p							
Abbas et al.[48]*	28	298−434	0.101325	–	0.18	–	–	–	–	0.18
Marsh and Tomlins[81]	1	298.14	0.101325	–	1.81	–	–	–	–	1.81
Mekhtiev and Karasharli[43]	1	298.14	0.101325	–	2.73	–	–	–	–	2.73
Palczewska-Tulińska and Oracz[58]	24	293−426	p_v	–	2.05	–	–	–	–	2.05

[a] All temperatures were adapted to the ITS-90 scale. Data sets that were applied to the fit are marked with an asterisk. For the pvT data in the critical region, pressure deviations are considered instead of density deviations. Critical region: $0.98 \leq T/T_c \leq 1.1$ and $0.7 \leq \rho/\rho_c \leq 1.4$. Supercritical region: LD, $\rho/\rho_c \leq 0.6$; MD, $0.6 \leq \rho/\rho_c \leq 1.5$; HD, $\rho/\rho_c > 1.5$. [b] Calculated.

sound measurements were tested. After these data were deleted from the fit, the requested result was achieved. The homogeneous density data of Wappmann et al.[78] could be fitted significantly better than before. Hence, the two data sets are not consistent with each other. This effect can be explained on the basis of the definition of the speed of sound:

$$w^2 = \frac{c_p}{c_v}\left(\frac{\partial p}{\partial \rho}\right)_T \tag{11}$$

One of the two data sets comprises a wrong course of the compressibility, so the other data set cannot be correlated within the required accuracy. Since no independent data set for the homogeneous density that could support the data of Wappmann et al.[78] is available, the present speed of sound measurements were chosen to be primarily fitted.

For the present speed of sound measurements, the same apparatus as for hexamethyldisiloxane,[12] ammonia,[14] oxygen,[85] and hydrogen chloride was utilized. In general, the data could be reproduced within 0.5% by the corresponding equations of state, so this accuracy was also the aim in the case of octamethylcyclotetrasiloxane. Figure 9 shows that the speed of sound data are represented by the present equation of state within the specified experimental uncertainties. Additional speed of sound data located in the liquid phase were published by Niepmann and Schmidt.[80] They employed an accurate pulse-echo method, which was also used in the present work. The reported uncertainty of 0.8 m·s^{-1} corresponds to a relative uncertainty of 0.1%. However, with the same apparatus they measured speed of sound data for benzene, which scatter around the corresponding equation of state of Thol et al.[40] within 0.4%. Therefore, relative deviations of approximately 0.5%, except for the isotherms at 350 and 375 K, are plausible. With these deviations in the liquid speed of sound data, a relative deviation of the density data of Wappmann et al.[78] from the present equation of 0.65% could be achieved. The data of Easteal and Woolf[74] deviate in the same range. Finally, the speed of sound data in the gaseous state of Nannan et al.,[47] which were already discussed in section 4.1, are shown in Figure 9. The relative deviation is 0.16% for $T \leq 465$ K and increases to 0.45% for higher temperatures. The large deviations occur close to the saturated vapor phase, whereas the deviations decrease in the limit of low pressure. This trend proves that the ideal gas contribution α° of the present equation of state is reasonable.

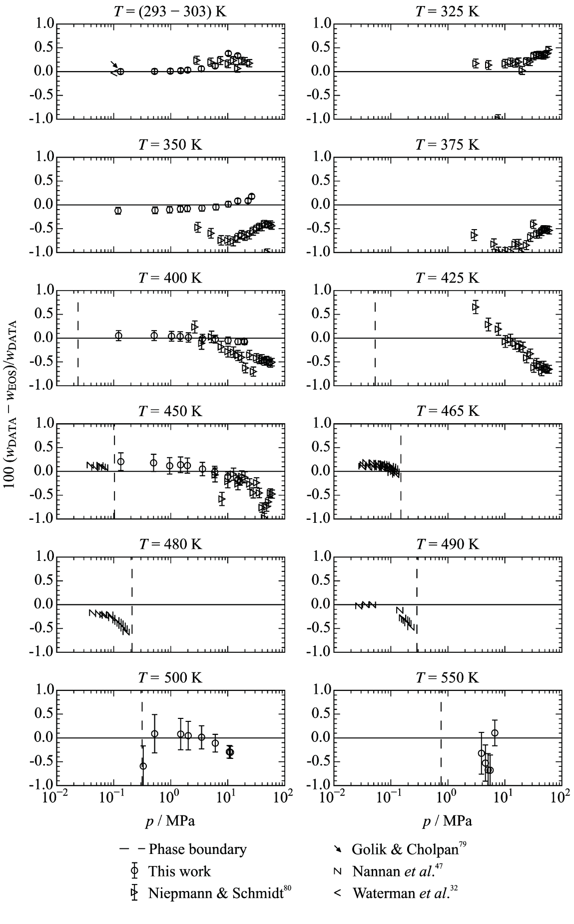

Figure 9. Relative deviations of experimental speed of sound data from the present equation of state.

To summarize the discussion above, the homogeneous density can be calculated from the present equation of state within 0.1% at atmospheric pressure and 0.7% for higher pressures. Vapor phase measurements are not available, so no statement on the accuracy of the present equation of state can be made. Speed of sound data in the liquid and vapor states can be calculated from the present equation with an expected uncertainty of 0.5%

In Figure 10, comparisons of available experimental isobaric heat capacity data with the present equation of state are depicted. The two main data sets were published by Abbas et al.[48] (AAD = 0.18%) and Palczewska-Tulińska and Oracz[58] (AAD = 2.05%) and exhibit a contrary course. In accordance with the previous discussion on vapor pressure and saturated liquid density, significant deviations of the heat capacity measurements in the saturated liquid state of all substances investigated in the publication of Palczewska-Tulińska and Oracz[58] with respect to other literature data can be observed. Therefore, these data were not considered during the development of the present equation of state. The isobaric heat capacity data for hexamethyldisiloxane measured at atmospheric pressure by Abbas et al.[48] showed good agreement with the corresponding equation and other literature data (cf. Thol et al.[12]). Therefore, the data for octamethylcyclotetrasiloxane were assumed to be reliable and were used in the fit. A

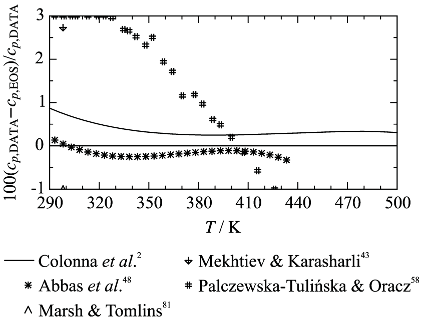

Figure 10. Relative deviations of experimental isobaric heat capacity data from the present equation of state.

relative deviation of 0.3% could be achieved, which is clearly within the experimental uncertainty of 1% as stated by the authors. Thus, the expected uncertainty in the heat capacity data in the saturated liquid state calculated with the present equation of state is 1% according to the experimental uncertainty of the data of Abbas et al.[48]

4.4. Representation of Molecular Simulation Data. After the present equation of state was fitted exclusively to experimental measurements, molecular simulation data up to 1200 K and 520 MPa were added to the data set used in the fit in order to extend the range of validity. Since the molecular structure of octamethylcyclotetrasiloxane is chemically not stable at such high temperatures and pressures, this extension of the validity range has to be perceived as an extrapolation beyond the stable region. The simulated vapor pressure data differ by up to 10% for $T \geq 435$ K. Lower temperatures are reproduced even worse. However, the simulated saturated liquid density data differ from the present equation of state within the stated accuracy of 1%, except for the highest temperature ($T = 550$ K). The accuracy of the molecular model in the homogeneous region was assessed by simulations of the density and speed of sound at selected state points (cf. Figure 11). The homogeneous density is represented within 0.7%, which is the expected uncertainty of the present equation of state. The simulated pvT data support the course of the density calculated from the equation of state, which resulted primarily from a fit to saturated liquid density and speed of sound data rather than from a fit to the available pvT data. The gaseous speed of sound data differ by 1.3% from the present equation of state, whereas the liquid state points deviate by up to 15%. The differences become evident from the following equation:

$$\frac{w^2}{RT} = 1 + 2A^{\mathrm{r}}_{01} + A^{\mathrm{r}}_{02} - \frac{(1 + A^{\mathrm{r}}_{01} - A^{\mathrm{r}}_{11})^2}{A^{\circ}_{20} + A^{\mathrm{r}}_{20}} \qquad (12)$$

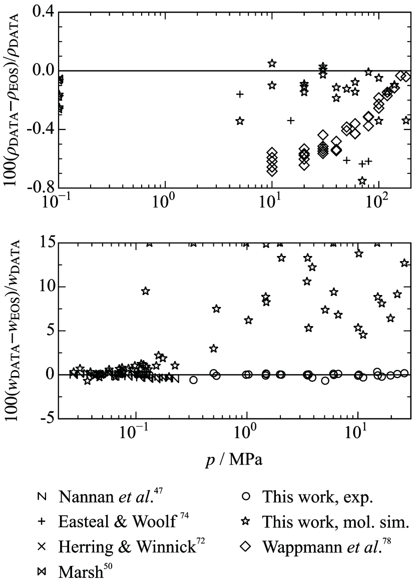

Figure 11. Relative deviations of selected (top) density and (bottom) speed of sound data from the present equation of state. At the same $p-T$ state points, molecular simulation data are presented to verify the accuracy of the present molecular model.

The speed of sound is composed of several residual Helmholtz energy derivatives and the ideal gas heat capacity, which is considered by A°_{20}. Because only the residual parts are simulated, the ideal gas part is taken from the present equation of state. In the gas phase, the ideal gas contribution is the dominant part, which compensates for uncertainties of the simulated residual Helmholtz energy derivatives. The liquid state is prevailed by the residual contribution, so the impact of the ideal gas contribution is smaller, which leads to higher deviations.

Comparisons of the simulated residual Helmholtz energy derivatives from the present equation of state along selected isotherms are shown in Figure 12. A comprehensive overview of all of the available simulation data is given in the Supporting Information. Deviations of the residual Helmholtz energy, A^{r}_{00}, and the first derivative with respect to the temperature, A^{r}_{10}, amount to 10%. Except for a few data points at the zero crossing or at very low densities, the same accuracy can be observed for the first derivative with respect to the density, A^{r}_{01}. The first mixed derivative with respect to the temperature and density, A^{r}_{11}, is reproduced by the present equation of state within 15%. The second derivative with respect to the temperature, A^{r}_{20}, and the second derivative with respect to the density, A^{r}_{02}, differ by approximately 30%. For a better

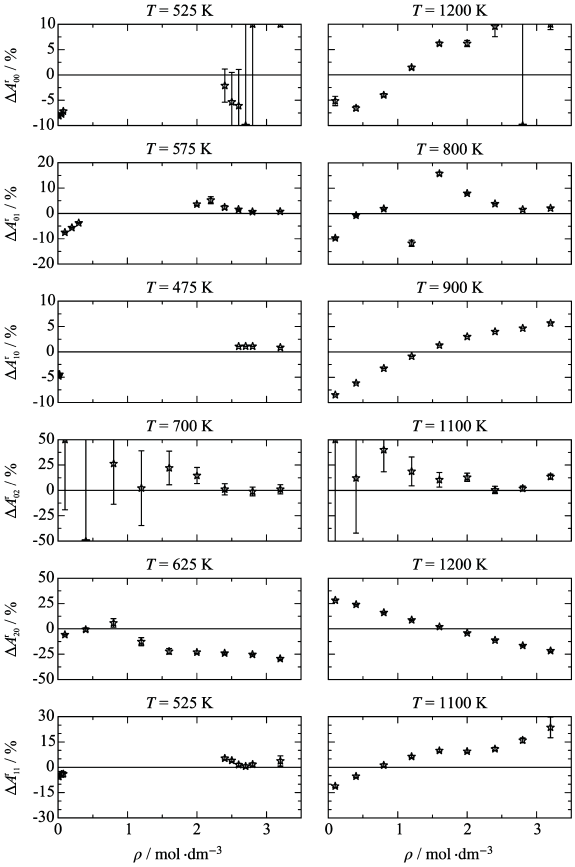

Figure 12. Relative deviations of simulated residual Helmholtz energy derivatives data from the present equation of state along selected isotherms. The relative deviations are calculated according to eq 8.

classification of these deviations, the Helmholtz energy derivatives were transferred to common thermodynamic properties (pressure, heat capacities, and speed of sound) according to eq 12 and the following equations:

$$\frac{p}{\rho RT} = 1 + A_{01}^{\mathrm{r}} \tag{13}$$

$$\frac{c_v}{R} = -(A_{20}^{\circ} + A_{20}^{\mathrm{r}}) \tag{14}$$

$$\frac{c_p}{R} = -(A_{20}^{\circ} + A_{20}^{\mathrm{r}}) + \frac{(1 + A_{01}^{\mathrm{r}} - A_{11}^{\mathrm{r}})^2}{1 + 2A_{01}^{\mathrm{r}} + A_{02}^{\mathrm{r}}} \tag{15}$$

For the calculation of caloric properties, the ideal contribution of the present equation of state was adopted.

Figure 13 depicts the relative deviations of common thermodynamic properties from the present equation of state.

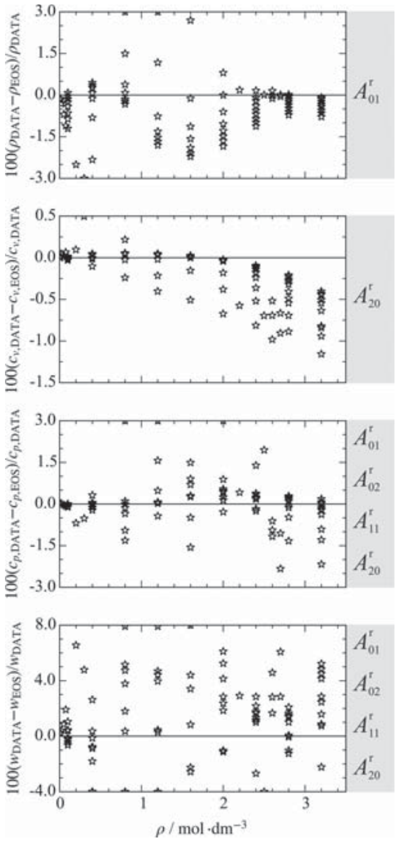

Figure 13. Comparison of the present equation of state with thermodynamic properties obtained from molecular simulation data generated in this work. The involved residual Helmholtz energy derivatives are indicated in the gray boxes.

The homogeneous density and the isobaric heat capacity are represented within 2%. The isochoric heat capacity differs from the present equation of state by 1% and for $\rho \leq 1.2$ mol·dm^{-3} the difference is even 0.5%. Finally, the speed of sound data are reproduced within 7%. Of course, for a reliable statement of the accuracy of the present equation of state, experimental measurements in this range are required.

5. PHYSICAL AND EXTRAPOLATION BEHAVIOR

In addition to the accurate representation of experimental and simulation data, the correct physical and extrapolation behavior in regions where no data are available is an essential aspect in the development of equations of state. Especially for the application to mixture models, a reasonable course of thermodynamic properties has to be ensured. Typical diagrams that are analyzed during fitting procedures are shown in Figure 14. On the top left, the vapor−liquid equilibrium is presented in a $T-\rho$ diagram. The isobars are smooth, and the rectilinear diameter is a straight line up to the critical point. The critical isobar exhibits a saddle point at the critical point. The hypothetical saturated liquid phase of the isochoric heat capacity (top right) increases with decreasing temperature, and the two saturated phases merge at a maximum at the critical point. This diagram is also an indication of the qualitatively correct behavior of the speed of sound, which was observed during the fit as well. In the center of Figure 14, the phase identification parameter[86] is presented as a function of density (left) and temperature (right). Both plots show a correct course as described by Thol et al.[87] and Lemmon et al.[88] No unreasonable changes in slope or curvature were observed. The virial coefficients B, C, and D are presented at the bottom left. No unreasonable features can be observed for the second virial coefficient. The third virial coefficient exhibits a slight shift of its maximum to lower temperatures than the critical one. It should most likely be located closer to the critical temperature, similar to that of hexamethyldisiloxane.[12] Since this is not a fully investigated phenomenon and it has not been experimentally proven that the maximum occurs approximately at the critical temperature, this slight shift was accepted here. The same holds for the fourth virial coefficient. The qualitative behavior is in very good agreement with the previously analyzed equations of state for Lennard-Jones fluids[87,89] and hexamethyldisiloxane.[12] However, the maximum is also not located at the critical temperature but shifted to a lower value. A noticeable feature can be observed in the further course of the fourth virial coefficient. For Lennard-Jones fluids,[87,89] a second maximum was predicted from the equations of state and statistical mechanics independently. The same effect is observed here for octamethylcyclotetrasiloxane. Without any information on experimental virial coefficients, the present equation of state exhibits this second maximum. Finally, characteristic ideal curves[90] are presented on the bottom right in Figure 14. No unreasonable courses can be observed, ensuring correct extrapolation behavior to very high temperatures, pressures, and densities.

6. CONCLUSION

The present equation of state for octamethylcyclotetrasiloxane is written in terms of the reduced Helmholtz energy, so any equilibrium thermodynamic property can be obtained from its derivatives with respect to temperature and density. The ideal contribution contains three Planck−Einstein terms, whereas the residual contribution consists of five polynomial, five exponential, and five Gaussian bell-shaped terms. The range of validity based on experimental data is for temperatures from the triple point to 590 K at pressures up to 180 MPa. The expected uncertainty in the vapor pressure data from the present equation of state is 1.5% for $T \leq 460$ K and 2% for higher temperatures. Saturated liquid density data are accurate within 0.1% for $T < 360$ K and 0.5% for higher temperatures.

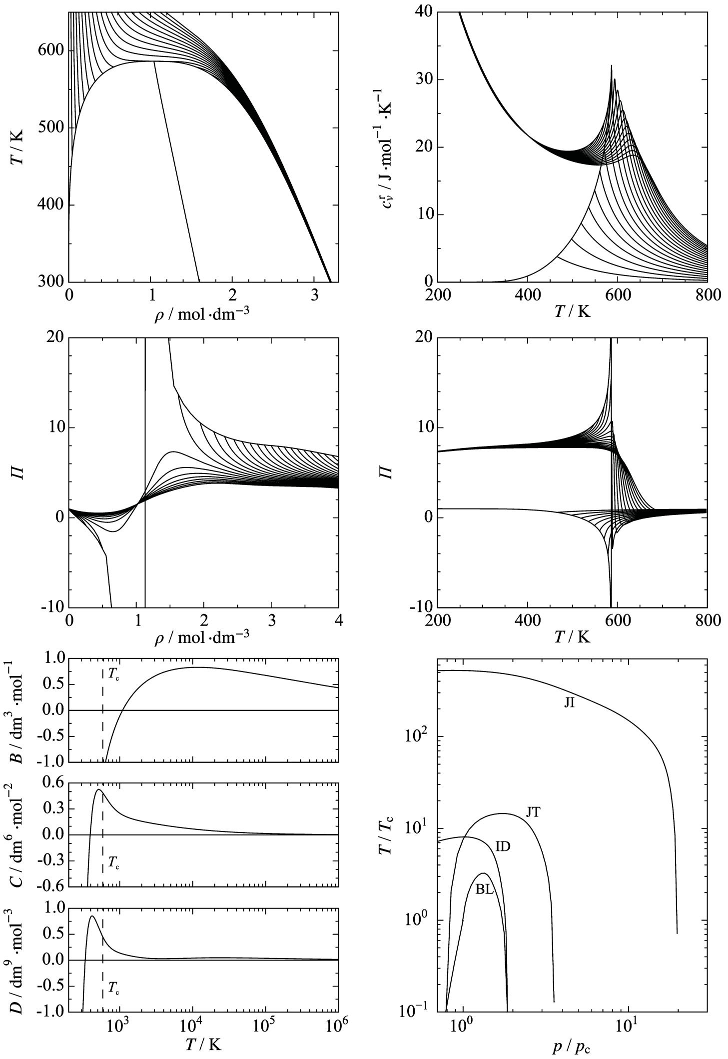

Figure 14. Plots of some thermodynamic properties of octamethylcyclotetrasiloxane: (top left) vapor−liquid equilibrium curves together with the rectilinear diameter; (top right) residual isochoric heat capacity; (center) phase identification parameter as a function of (left) temperature and (right) density; (bottom left) second, third, and fourth virial coefficients; (bottom right) characteristic ideal curves[90] (ID, ideal curve; BL, Boyle curve; JT, Joule−Thomson inversion curve; JI, Joule inversion curve).

The uncertainty in the homogeneous density at atmospheric pressure is assessed to be 0.1%. The available experimental data in the high-pressure region are not consistent with the present speed of sound measurements, so the equation is assumed to be accurate within only 0.7%. The expected uncertainty in the speed of sound data calculated with the present equation of state is 0.5%. Next to the analysis of experimental measurements, the extrapolation behavior was investigated comprehensively and found to be reasonable. Finally, the range of validity was extended to $T_{\max} = 1200$ K and $p_{\max} = 520$ MPa by means of molecular simulation data. Since no experimental measurements are available in this region, no uncertainty statements can be made, but indications based on the simulation data are given.

Reference values to verify computer implementation are given in the Supporting Information. Additionally, ancillary equations were developed for the vapor pressure as well as saturated liquid and vapor densities, which can be used for initial calculations of starting values of iterative phase calculations. The corresponding equations and parameters are also listed in the Supporting Information. Furthermore, a parameter file for the software packages TREND[91] and REFPROP[92] and a file containing C++ source code are provided.

■ ASSOCIATED CONTENT

Ⓢ Supporting Information

The Supporting Information is available free of charge on the ACS Publications website at DOI: 10.1021/acs.jced.6b00261.

Ancillary equations for vapor pressure, saturated liquid density, and saturated vapor density; simulation details; Tables S6−S9 and S11−S13; and Figures S15−S24 (PDF)

Table S10 (XLSX)

Parameter file for the software packages TREND[91] and REFPROP[92] (TXT)

C++ source code for the calculation of selected thermodynamic properties at homogeneous states (TXT)

Explanatory notes (TXT)

AUTHOR INFORMATION

Corresponding Author

*E-mail: jadran.vrabec@uni-paderborn.de.

Notes

The authors declare no competing financial interest.

REFERENCES

(1) EPA National Center for Biotechnology Information. PubChem Compound Database, CID = 11169. https://pubchem.ncbi.nlm.nih.gov/compound/11169 (accessed Nov 3, 2015).

(2) Colonna, P.; Nannan, N. R.; Guardone, A.; Lemmon, E. W. Multiparameter Equations of State for Selected Siloxanes. *Fluid Phase Equilib.* **2006**, *244*, 193−211.

(3) Span, R.; Wagner, W. Equations of State for Technical Applications. I. Simultaneously Optimized Functional Forms for Nonpolar and Polar Fluids. *Int. J. Thermophys.* **2003**, *24*, 1−39.

(4) Span, R.; Wagner, W. Equations of State for Technical Applications. II. Results for Nonpolar Fluids. *Int. J. Thermophys.* **2003**, *24*, 41−109.

(5) Span, R.; Wagner, W. Equations of State for Technical Applications. III. Results for Polar Fluids. *Int. J. Thermophys.* **2003**, *24*, 111−162.

(6) Thol, M.; Piazza, L.; Span, R. A New Functional Form for Equations of State for Some Weakly Associating Fluids. *Int. J. Thermophys.* **2014**, *35*, 783−811.

(7) Sun, L.; Ely, J. F. A Corresponding States Model for Generalized Engineering Equations of State. *Int. J. Thermophys.* **2005**, *26*, 705−728.

(8) Alexandrov, I.; Gerasimov, A.; Grigor'ev, B. Generalized Fundamental Equation of State for the Normal Alkanes (C5-C50). *Int. J. Thermophys.* **2013**, *34*, 1865−1905.

(9) Grigor'ev, B.; Alexandrov, I.; Gerasimov, A. Generalized Equation of State for the Cyclic Hydrocarbons over a Temperature Range from the Triple Point to 700 K with Pressures up to 100 MPa. *Fluid Phase Equilib.* **2016**, *418*, 15−36.

(10) Rutkai, G.; Thol, M.; Lustig, R.; Span, R.; Vrabec, J. Communication: Fundamental Equation of State Correlation with Hybrid Data Sets. *J. Chem. Phys.* **2013**, *139*, 041102.

(11) Thol, M.; Rutkai, G.; Köster, A.; Kortmann, M.; Span, R.; Vrabec, J. Fundamental Equation of State for Ethylene Oxide Based on a Hybrid Dataset. *Chem. Eng. Sci.* **2015**, *121*, 87−99; **2015**, *134*, 887−890.

(12) Thol, M.; Dubberke, F.; Rutkai, G.; Windmann, T.; Köster, A.; Span, R.; Vrabec, J. Fundamental Equation of State Correlation for Hexamethyldisiloxane Based on Experimental and Molecular Simulation Data. *Fluid Phase Equilib.* **2016**, *418*, 133−151.

(13) Lin, C.-W.; Trusler, J. P. M. The Speed of Sound and Derived Thermodynamic Properties of Pure Water at Temperatures Between (253 and 473) K and at Pressures up to 400 MPa. *J. Chem. Phys.* **2012**, *136*, 094511.

(14) Dubberke, F. H.; Rasche, D. B.; Baumhögger, E.; Vrabec, J. Apparatus for the Measurement of the Speed of Sound of Ammonia up to High Temperatures and Pressures. *Rev. Sci. Instrum.* **2014**, *85*, 084901.

(15) Ball, S. J.; Trusler, J. P. M. Speed of Sound of n-Hexane and n-Hexadecane at Temperatures Between 298 and 373 K and Pressures up to 100 MPa. *Int. J. Thermophys.* **2001**, *22*, 427−443.

(16) Dubberke, F. H.; Baumhögger, E.; Vrabec, J. Burst Design and Signal Processing for the Speed of Sound Measurement of Fluids with the Pulse-echo Technique. *Rev. Sci. Instrum.* **2015**, *86*, 054903.

(17) Gedanitz, H.; Davila, M. J.; Baumhögger, E.; Span, R. An Apparatus for the Determination of Speeds of Sound in Fluids. *J. Chem. Thermodyn.* **2010**, *42*, 478−483.

(18) Harris, G. R. Review of Transient Field Theory for a Baffled Planar Piston. *J. Acoust. Soc. Am.* **1981**, *70*, 10−20.

(19) Meier, K. The Pulse-Echo Method for High Precision Measurements of the Speed of Sound in Fluids. Habilitation Thesis, University of the Federal Armed Forces, Hamburg, Germany, 2006.

(20) Glass, C. W.; Reiser, S.; Rutkai, G.; Deublein, S.; Köster, A.; Guevara-Carrion, G.; Wafai, A.; Horsch, M.; Bernreuther, M.; Windmann, T.; Hasse, H.; Vrabec, J. ms2: A Molecular Simulation Tool for Thermodynamic Properties, New Version Release. *Comput. Phys. Commun.* **2014**, *185*, 3302−3306.

(21) Lustig, R. Direct Molecular NVT Simulation of the Isobaric Heat Capacity, Speed of Sound and Joule−Thomson Coefficient. *Mol. Simul.* **2011**, *37*, 457−465.

(22) Lustig, R. Statistical Analogues for Fundamental Equation of State Derivatives. *Mol. Phys.* **2012**, *110*, 3041−3052.

(23) Mohr, P. J.; Taylor, B. N.; Newell, D. B. CODATA Recommended Values of the Fundamental Physical Constants: 2010. *Rev. Mod. Phys.* **2012**, *84*, 1527−1605.

(24) Span, R. *Multiparameter Equations of State: An Accurate Source of Thermodynamic Property Data*; Springer: Berlin, 2000.

(25) Schmidt, M. W.; Baldridge, K. K.; Boatz, J. A.; Elbert, S. T.; Gordon, M. S.; Jensen, J. H.; Koseki, S.; Matsunaga, N.; Nguyen, K. A.; Su, S.; Windus, T. L.; Dupuis, M.; Montgomery, J. A. General Atomic and Molecular Electronic Structure System. *J. Comput. Chem.* **1993**, *14*, 1347−1363.

(26) Merker, T.; Vrabec, J.; Hasse, H. Engineering Molecular Models: Efficient Parameterization Procedure and Cyclohexanol as Case Study. *Soft Mater.* **2012**, *10*, 3−24.

(27) Matsubara, H.; Pichierri, F.; Kurihara, K. Design of a Versatile Force Field for the Large-Scale Molecular Simulation of Solid and Liquid OMCTS. *J. Chem. Theory Comput.* **2010**, *6*, 1334−1340.

(28) Xu, R.-G.; Leng, Y. Solvation Force Simulations in Atomic Force Microscopy. *J. Chem. Phys.* **2014**, *140*, 214702.

(29) Guevara-Carrion, G.; Nieto-Draghi, C.; Vrabec, J.; Hasse, H. Prediction of Transport Properties by Molecular Simulation: Methanol and Ethanol and their Mixture. *J. Phys. Chem. B* **2008**, *112*, 16664−16674.

(30) Abbas, R.; Ihmels, E. C.; Enders, S.; Gmehling, J. Measurement of Transport Properties for Selected Siloxanes and their Mixtures Used as Working Fluids for Organic Rankine Cycles. *Ind. Eng. Chem. Res.* **2011**, *50*, 8756−8763.

(31) Marsh, K. N. Mutual Diffusion in Octamethylcyclotetrasiloxane Mixtures. *Trans. Faraday Soc.* **1968**, *64*, 894.

(32) Waterman, H. I.; Van Herwijnen, W. E. R.; Den Hartog, H. W. Statistical-Graphical Survey of Series of Linear and Cyclic Dimethylsiloxanes. *J. Appl. Chem.* **1958**, *8*, 625−631.

(33) Reuther, H. Über Silikone XIV: Über das Viskosität-Temperatur-Verhalten von Silikonölen unter besonderer Berücksichtigung des Bereichs unter 0°C. *Chem. Technol.* **1953**, *5*, 268.

(34) Wilcock, D. F. Vapor Pressure-Viscosity Relations in Methylpolysiloxanes. *J. Am. Chem. Soc.* **1946**, *68*, 691−696.

(35) Rowley, R. L.; Wilding, W. V.; Oscarson, J.; Yang, Y.; Zuendel, N.; Daubert, T.; Danner, R. *DIPPR Data Compilation of Pure Chemical Properties*; Taylor & Francis: New York, 2004.

(36) Haar, L.; Gallagher, J. S.; Kell, G. S. The Anatomy of the Thermodynamic Surface of Water: The Formulation and Comparisons with Data. In *Proceedings of the 8th Symposium on Thermophysical Properties*; Sengers, J. V., Ed.; ASME, New York, 1982; pp 298−302.

(37) Setzmann, U.; Wagner, W. A New Equation of State and Tables of Thermodynamic Properties for Methane Covering the Range from the Melting Line to 625 K at Pressures up to 100 MPa. *J. Phys. Chem. Ref. Data* **1991**, *20*, 1061−1155.

(38) Lemmon, E. W.; Jacobsen, R. T. A New Functional Form and New Fitting Techniques for Equations of State with Application to Pentafluoroethane (HFC-125). *J. Phys. Chem. Ref. Data* **2005**, *34*, 69−108.

(39) Lemmon, E. W.; McLinden, M. O.; Wagner, W. Thermodynamic Properties of Propane. III. A Reference Equation of State for Temperatures from the Melting Line to 650 K and Pressures up to 1000 MPa. *J. Chem. Eng. Data* **2009**, *54*, 3141−3180.

(40) Thol, M.; Lemmon, E. W.; Span, R. Equation of State for Benzene for Temperatures from the Melting Line up to 725 K with Pressures up to 500 MPa. *High Temp. - High Press.* **2012**, *41*, 81−97.

(41) Zhou, Y.; Liu, J.; Penoncello, S. G.; Lemmon, E. W. An Equation of State for the Thermodynamic Properties of Cyclohexane. *J. Phys. Chem. Ref. Data* **2014**, *43*, 043105.

(42) Young, C. L. Equilibrium Properties of Octamethylcyclotetrasiloxane near its Critical Point and Applicability of the Principle of Corresponding States. *J. Chem. Thermodyn.* **1972**, *4*, 65−75.

(43) Mekhtiev, S. A.; Karasharli, K. A. Analysis of the Results of Thermodynamic Studies of a Series of Organosolicon Compounds. *Azerb. Khim. Zhur.* **1981**, *5*, 85−88.

(44) Wieser, M. E.; Berglund, M. Atomic Weights of the Elements 2007 (IUPAC Technical Report). *Pure Appl. Chem.* **2009**, *81*, 2131−2156.

(45) Frenkel, M.; Chirico, R. D.; Diky, V.; Kroenlein, K.; Muzny, C. D.; Kazakov, A. F.; Magge, J. W.; Abdulagatov, I. M.; Lemmon, E. W. *NIST Standard Reference Database 103b: NIST Thermo-Data-Engine—Pure Components, Binary Mixtures, Reactions*, version 8.0; Standard Reference Data Program; National Institute of Standards and Technology: Gaithersburg, MD, 2013.

(46) Harrison, B. K.; Seaton, W. H. Solution to Missing Group Problem for Estimation of Ideal Gas Heat Capacities. *Ind. Eng. Chem. Res.* **1988**, *27*, 1536−1540.

(47) Nannan, N. R.; Colonna, P.; Tracy, C. M.; Rowley, R. L.; Hurly, J. J. Ideal-Gas Heat Capacities of Dimethylsiloxanes from Speed-of-Sound Measurements and ab initio Calculations. *Fluid Phase Equilib.* **2007**, *257*, 102−113.

(48) Abbas, R.; Schedemann, A.; Ihmels, C.; Enders, S.; Gmehling, J. Measurement of Thermophysical Pure Component Properties for a Few Siloxanes Used as Working Fluids for Organic Rankine Cycles. *Ind. Eng. Chem. Res.* **2011**, *50*, 9748−9757.

(49) Flaningam, O. L. Vapor Pressures of Poly(dimethylsiloxane) Oligomers. *J. Chem. Eng. Data* **1986**, *31*, 266−272.

(50) Marsh, K. N. Thermodynamics of Octamethylcyclotetrasiloxane Mixtures. *Trans. Faraday Soc.* **1968**, *64*, 883−893.

(51) Marsh, K. N. Enthalpies of Mixing and Excess Gibbs Free Energies of Mixtures of Octamethylcyclotetrasiloxane+Cyclopentane at 291.15, 298.15, and 308.15 K. *J. Chem. Thermodyn.* **1970**, *2*, 359−365.

(52) Tomlins, R. P.; Marsh, K. N. A New Apparatus for Measuring the Vapour Pressure of Liquid Mixtures. Excess Gibbs Free Energy of Octamethylcyclotetrasiloxane + Cyclohexane at 308.15 K. *J. Chem. Thermodyn.* **1976**, *8*, 1185−1194.

(53) Stull, D. R. Vapor Pressure of Pure Substances: Organic Compounds. *Ind. Eng. Chem.* **1947**, *39*, 517−540.

(54) Hunter, M. J.; Hyde, J. F.; Warrick, E. L.; Fletcher, H. J. Organo-Silicon Polymers. The Cyclic Dimethyl Siloxanes. *J. Am. Chem. Soc.* **1946**, *68*, 667−672.

(55) Patnode, W.; Wilcock, D. F. Methylpolysiloxanes. *J. Am. Chem. Soc.* **1946**, *68*, 358−363.

(56) Korchemskaya, K. M.; Shakhparonov, M. I.; Lelchuk, S. L.; Korablina, T. P.; Baburina, I. I.; Voronina, R. D. Pressure and Density of the Vapors of Binary Solutions of Clorosilanes: IV. Silane. *Izv. Vyssh. Uchebn. Zaved., Khim. Khim. Tekhnol.* **1962**, *5*, 65−69.

(57) Lopatkina, I. L.; Kucherskaya, L. A.; Kuznetsova, A. G.; Shaulov, Y. K. Vapour Pressure of Cyclosiloxanes. *Russ. J. Phys. Chem.* **1973**, *47*, 1626−1627.

(58) Palczewska-Tulińska, M.; Oracz, P. Selected Physicochemical Properties of Hexamethylcyclotrisiloxane, Octamethylcyclotetrasiloxane, and Decamethylcyclopentasiloxane. *J. Chem. Eng. Data* **2005**, *50*, 1711−1719.

(59) Palczewska-Tulińska, M.; Choliński, J.; Szafrański, A.; Wyrzykowska-Stankiewicz, D. Maximum-Likelihood Evaluation of Antoine Equation Constants for Vapor Pressures of Morpholine, n-Heptane, Cyclohexane and Methylcyclohexane. *Fluid Phase Equilib.* **1983**, *11*, 233−243.

(60) Osthoff, R. C.; Grubb, W. T. Physical Properties of Organosilicon Compounds: III. Thermodynamic Properties of Octamethylcyclotetrasiloxane. *J. Am. Chem. Soc.* **1954**, *76*, 399−401.

(61) Smith, A.; Menzies, A. W. C. Studies in Vapor Pressure. III. A Static Method for Determining the Vapor Pressures of Solids and Liquids. *J. Am. Chem. Soc.* **1910**, *32*, 1412−1434.

(62) Ambrose, D.; Townsend, R. 681. Thermodynamic Properties of Organic Oxygen Compounds. Part IX. The Critical Properties and Vapour Pressures, above Five Atmospheres, of Six Aliphatic Alcohols. *J. Chem. Soc.* **1963**, *37*, 3614−3625.

(63) Flaningam, O. L.; Williams, D. E. Octamethylcyclotetrasiloxane Azeotropes. U.S. Patent 5,492,647, May 8, 1995.

(64) Hurd, C. B. Studies on Siloxanes: I. The Specific Volume and Viscosity in Relation to Temperature and Constitution. *J. Am. Chem. Soc.* **1946**, *68*, 364−370.

(65) Weast, R. C.; Astle, M. J. *CRC Handbook of Data on Organic Compounds*; CRC Press: Boca Raton, FL, 1985.

(66) Golik, O. Z.; Cholpan, P. P. *Ukr. Fiz. Zh.* **1960**, *5*, 242−251.

(67) Levien, B. J. Excess Volumes of Mixtures of Globular Molecules. II. *J. Chem. Thermodyn.* **1973**, *5*, 679−687.

(68) McLure, I. A.; Barbarin-Castillo, J. M. Orthobaric Liquid Densities for Octamethylcyclotetrasiloxane, Decamethylcyclopentasiloxane, Dimethicone 20, and a Cyclic Poly(dimethylsiloxane). *J. Chem. Eng. Data* **1994**, *39*, 12−13.

(69) Shinoda, K.; Hildebrand, J. H. Compressibilities and Iochores of $(C_3F_7COOCH_2)_4C$, c-$Si_4O_4(CH_3)_8$, n-C_5H_{12}, n-C_8H_{18}, 2,2,4-$C_5H_9(CH_3)_3$, c-C_5H_{10}, c-C_6H_{12}, c-$C_6H_{11}CH_3$, $C_6H_5CH_3$, p-$C_6H_4(CH_3)_2$, s-$C_6H_3(CH_3)_3$, CH_2Cl_2. *J. Phys. Chem.* **1961**, *65*, 183.

(70) Tanaka, T. Heats of Formation of Lower Members of Dimethyl- and Methylisopropoxy-cyclopolysiloxanes. *Bull. Chem. Soc. Jpn.* **1960**, *33*, 282−286.

(71) Schuh, H.-H.; Fischer, H. The Kinetics of the Bimolecular Sel-Reaction of t-Butyl Radicals in Solution: I. Termination Rates. *Helv. Chim. Acta* **1978**, *61*, 2130−2164.

(72) Herring, W.; Winnick, J. Excess Volumes of Octamethylcyclotetrasiloxane + Carbon Tetrachloride. *J. Chem. Thermodyn.* **1974**, *6*, 957−964.

(73) Dickinson, E. Pressure Dependence of Shear Viscosity in n-Alkane + Dimethylsiloxane Mixtures. *J. Phys. Chem.* **1977**, *81*, 2108−2113.

(74) Easteal, A. J.; Woolf, L. A. Self-diffusion and Volumetric Measurements for Octamethylcyclotetrasiloxane under Pressure at 323 K. *J. Chem. Soc., Faraday Trans. 1* **1984**, *80*, 549−551.

(75) Mills, A. P.; MacKenzie, C. A. The Application of Bond Parachors to Organosilicon Chemistry. *J. Am. Chem. Soc.* **1954**, *76*, 2672−2673.

(76) Myers, R. S.; Clever, H. L. Surface Tension of Octamethylcyclotetrasiloxane and Hexamethyldisilazane and their Solutions with Carbon Tetrachloride and n-Hexadecane. *J. Chem. Eng. Data* **1969**, *14*, 161−164.

(77) Ross, M.; Hildebrand, J. H. Energy Volume Relations of Octamethylcyclotetrasiloxane and its Mixtures with Carbon Tetrachloride. *J. Phys. Chem.* **1963**, *67*, 1301−1303.

(78) Wappmann, S. J.; Tarassov, I. N.; Lüdemann, H.-D. Densities of Octamethylcyclotetrasiloxane + Methane and 2,2-Dimethylpropane + Methane from 10 to 200 MPa and from 294 to 433 K. *J. Chem. Eng. Data* **1996**, *41*, 84−88.

(79) Golik, A.; Cholpan, P. F. Investigation of Speed of Sound for Some Polysiloxanes. *Akust. Zh.* **1961**, *7*, 33−39.

(80) Niepmann, R.; Schmidt, U. Speeds of Sound in Liquid Octamethylcyclotetrasiloxane. *J. Chem. Thermodyn.* **1980**, *12*, 1133−1137.

(81) Marsh, K. N.; Tomlins, R. P. Excess Enthalpies of Octamethylcyclotetrasiloxane Mixtures. *Trans. Faraday Soc.* **1970**, *66*, 783−790.

(82) Wappmann, S. J.; Karger, N.; Lüdemann, H.-D. pVT Data of Liquid 1-, 2- and 3-Pentanol from 10 to 200 MPa and from 233 to 433 K. *J. Chem. Eng. Data* **1995**, *40*, 233−236.

(83) Goodwin, R. D. Methanol Thermodynamic Properties from 176 to 673 K at Pressures to 700 bar. *J. Phys. Chem. Ref. Data* **1987**, *16*, 799−892.

(84) Back, P. J.; Easteal, A. J.; Hurle, R. L.; Woolf, L. A. High-precision Measurements with a Bellows Volumometer. *J. Phys. E: Sci. Instrum.* **1982**, *15*, 360−363.

(85) Dubberke, F. H.; Riepold, M.; Baumhögger, E.; Vrabec, J. Speed of Sound of Oxygen in Supercritical States up to 500 K and 100 MPa. *J. Chem. Eng. Data* **2016**, *61*, 1632−1636.

(86) Venkatarathnam, G.; Oellrich, L. Identification of the Phase of a Fluid Using Partial Derivatives of Pressure, Volume, and Temperature without Reference to Saturation Properties: Applications in Phase Equilibria Calculations. *Fluid Phase Equilib.* **2011**, *301*, 225−233.

(87) Thol, M.; Rutkai, G.; Köster, A.; Span, R.; Vrabec, J.; Lustig, R. Equation of State for the Lennard-Jones Fluid. *J. Phys. Chem. Ref. Data* **2016**, *45*, 023101.

(88) Lemmon, E. W.; Overhoff, U.; McLinden, M. O.; Wagner, W. Equation of State for Propylene. *J. Phys. Chem. Ref. Data* **2016**, to be published.

(89) Thol, M.; Rutkai, G.; Span, R.; Vrabec, J.; Lustig, R. Equation of State for the Lennard-Jones Truncated and Shifted Model Fluid. *Int. J. Thermophys.* **2015**, *36*, 25−43.

(90) Span, R.; Wagner, W. On the Extrapolation Behavior of Empirical Equations of State. *Int. J. Thermophys.* **1997**, *18*, 1415−1443.

(91) Span, R.; Eckermann, T.; Herrig, S.; Hielscher, S.; Thol, M. *TREND: Thermodynamic Reference and Engineering Data*, version 2.0; Lehrstuhl für Thermodynamik, Ruhr-Universität Bochum: Bochum, Germany, 2015 (private communication).

(92) Lemmon, E. W.; Huber, M. L.; McLinden, M. O. *NIST Standard Reference Database 23: Reference Fluid Thermodynamic and Transport Properties—REFPROP*, version 9.1; National Institute of Standards and Technology: Gaithersburg, MD, 2013.

4.5 Speed of sound of oxygen in supercritical states up to 500 K and 100 MPa

Frithjof H. Dubberke, Markus Riepold, Elmar Baumhögger, and Jadran Vrabec,
Journal of Chemical & Engineering Data 61, (2016) 1632-1636,
DOI: 10.1021/acs.jced.5b01007

Reprinted from the Journal of Chemical & Engineering Data, (2016) with permission from ACS Publications.

The scientific work and discussion was coordinated and consolidated by Frithjof H. Dubberke under supervision of Jadran Vrabec.
The manuscript was prepared by Frithjof H. Dubberke
Electrical design and wiring was carried out by Elmar Baumhögger.
Speed of sound measurements and data evaluation were performed by Frithjof H. Dubberke, Markus Riepold and Elmar Baumhögger.
The manuscript was revised by Elmar Baumhögger and Jadran Vrabec.

This publication is in the context of the master thesis of Markus Riepold under supervision of Frithjof H. Dubberke at the chair of Thermodynamics and Energy Technology headed by Prof. Dr.-Ing. habil. Jadran Vrabec.

Journal of chemical & engineering data

Article

pubs.acs.org/jced

Speed of Sound of Oxygen in Supercritical States up to 500 K and 100 MPa

Frithjof H. Dubberke, Markus Riepold, Elmar Baumhögger, and Jadran Vrabec*

Thermodynamics and Energy Technology, University of Paderborn, Warburger Str. 100, 33098 Paderborn, Germany

ABSTRACT: Oxygen is the second-most abundant element in the earth's atmosphere and plays an important role in various engineering applications. The precise knowledge of its thermophysical properties is thus important. As a fully fledged thermodynamic property, the speed of sound substantially contributes to the development and parametrization of equations of state. This work presents experimental speed of sound data for oxygen measured with an apparatus that is based on the pulse-echo technique with a double path-length. When working with pure oxygen at high temperatures and pressures, tight safety requirements have to be met, limiting the present measurements to 500 K and 100 MPa.

INTRODUCTION

For optimizing industrial processes and for scientific applications the precise knowledge of thermodynamic properties is crucial. Oxygen, which is behind nitrogen the second-most abundant element in the earth's atmosphere, plays a major role in many industrial applications. The most accurate equation of state (EOS) for oxygen was established in the year 1985 by Schmidt and Wagner.[1] Highly accurate thermodynamic property data from experimental measurements are the basis for developing fundamental EOS[2] and speed of sound data are well suited for this purpose. However, there is a lack of speed of sound data in the supercritical region at elevated temperatures and moderate pressures, as illustrated in Figure 1.

Experiments with oxygen have been carried out by numerous authors and date back to the early 1900s, when Cook[3] used Kundt's tube[20] for speed of sound measurements of oxygen and air. First ultrasonic measurements were accomplished in the 1930s, primarily in low pressure regions. Van Itterbeek and co-workers[4,6−8,11,14,15] established an acoustic interferometer, enabling for measurements with uncertainties of about 0.1%. In 1938, Liepmann[9] determined data for liquid oxygen using a light diffraction method for measurements at low temperatures. In the middle of that century, Galt,[10] Boyer,[12] and Verhaegen[13] contributed further data for low temperature and pressure regions. In 1962, van Itterbeek and van Dael[14] used the pulse-echo method in the liquid region between 64 and 91 K and pressures of up to 92 MPa. Baidakov and Kaverin[18] determined data with an uncertainty of 0.17% for superheated liquid oxygen for the first time in 1989, employing the pulse-echo technique by using an acoustic cell made out of glass. In 1999, Abramson at al.[19] reached extremely high pressures of up to 12.6 GPa with a diamond-anvil cell, attaining an overall uncertainty of 2% in their measurements. An extensive study on the speed of sound of compressed liquid oxygen was presented by Straty and Younglove[17] in 1973, employing the pulse-echo technique. An overview of these data is given in Figure 1. The present work follows up on these measurements in a poorly sampled region, i.e. for temperatures between 300 and 500 K and pressures between 40 and 100 MPa. This region intentionally overlaps for

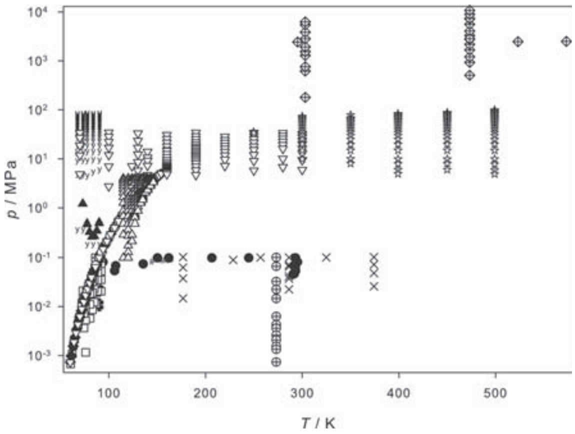

Figure 1. Experimental speed of sound data for oxygen: ●, Cook;[3] #, Keesom et al.;[4] ▼, Bär;[5] bold +, van Itterbeek and Mariëns;[6] ×, van Itterbeek and Mariëns;[7] □, van Itterbeek and van Paemel;[8] ■, Liepmann;[9] ◇, Galt;[10] ▲, van Itterbeek and de Bock;[11] ⊕, Boyer;[12] ⊞, Verhaegen;[13] y, van Itterbeek and van Dael;[14] ◆, van Dael et al.;[15] ○, Blagoi et al.;[16] ▽, Straty and Younglove;[17] △, Baidakov and Kaverin;[18] ◇ with cross, Abramson et al.;[19] ☆, this work.

Received: November 25, 2015
Accepted: February 28, 2016
Published: March 9, 2016

DOI: 10.1021/acs.jced.5b01007
J. Chem. Eng. Data 2016, 61, 1632−1636

one state point at 250 K and 34 MPa and for the 300 K isotherm over a pressure range from 10 to 32 MPa with data by Straty and Younglove,[17] cf. Figure 2.

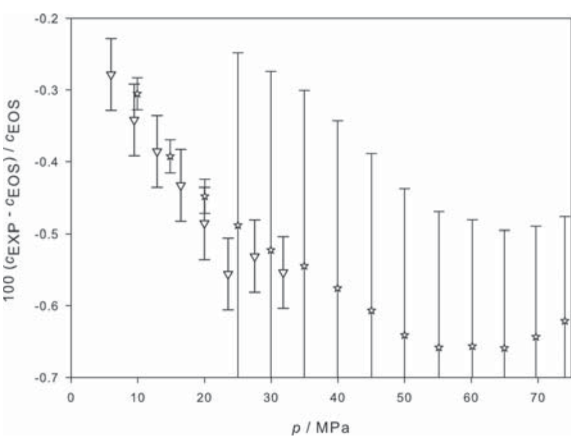

Figure 2. Comparison of speed of sound data for oxygen at 300 K measured by Straty and Younglove[17] (▽) and in the present work (☆) with the equation of state (EOS) by Schmidt and Wagner.[1]

Speed of sound measurements of compressed oxygen in the supercritical state over a temperature range from 300 to 500 K and a pressure of up to 100 MPa were carried out with the pulse-echo technique.[21] The measurement principle was based on a sample cell that has two known propagation path lengths l_1 and l_2, where $l_2 > l_1$.[22] By emitting a modulated high frequency wave burst with a piezoelectric quartz crystal with a resonance frequency of 8 MHz, which was positioned between two reflectors in the fluid, the speed of sound c was determined by the time measurement of the wave propagation through the fluid. Applying a Fourier transformation based digital filter on the sampled acoustic wave signals increased their signal-to-noise ratio and enhanced their time and amplitude resolutions, improving the overall measurement accuracy.[23] In addition, burst design led to technical advantages for determining the propagation time due to the associated conditioning of the echo. A complete description of the method, apparatus and discussion of uncertainties has been published in preceding work.[24,25]

■ SAFETY REQUIREMENTS FOR HANDLING OXYGEN

When working with pure oxygen, especially at high temperatures and pressures, tight safety requirements have to be met because it supports combustion and corrosion. Being highly oxidizing, it reacts vigorously with combustible materials and enhances fire or explosion, liberating large amounts of energy in a short time. A chemical reaction in an oxygen environment takes place, if the activation energy (i.e., ignition temperature) of a material is exceeded. To prevent temperature peaks by adiabatic pressure surges, high fluid velocities through valves etc. of the apparatus should be avoided. Therefore, charging and discharging the measuring cell with oxygen through the piping system was done here very gently. Furthermore, the apparatus had to be free of welding beads and swarfs due to their sensitivity to pressure surges.[26−28]

The technical norm DIN EN 1797 introduces a method for testing the behavior of materials exposed to pressure surges, which can be caused by adiabatic compression or high gas velocities in pipes or components.[29,30] According to the recommendation BGR 500,[26] which demands an appropriate steel alloy with an accumulated mass fraction of chrome and nickel above 22%, the measurement cell was made out of highly corrosion resistant stainless steel (1.4571) and the cylindrical pressure vessel (sealed with a copper gasket) out of highly tensile steel (1.4462) that are both suitable for applications with pure oxygen.[29,31−34]

Pure copper has an ignition temperature of 1338 K in pure oxygen at 70 MPa.[35] It is even harder to ignite than stainless steel[36] and is recommended in the literature as ”particularly useful for resisting ignition by particle impact and therefore can be used in high-velocity gas applications for which burn-resistant alloys are required”.[28]

The piezoelectric quartz crystal was connected by circular gold electrodes that do not hold any risks. The Teflon coated cables were mechanically connected to the gold electrodes and on the other end soldered, without using any flux, to the electrical feed through.[24] Upon combustion even small amounts of material may liberate large quantities of energy, resulting into an increasing temperature. This may lead to a chain reaction if the ignition temperature of other materials is attained. Thus, the lowest ignition temperature of all materials in the apparatus must not be exceeded.[29] Before use, the apparatus was very carefully cleaned and freed from impurities, especially of oily and greasy contaminants, which can induce a high risk due to their low ignition temperature.[26,28]

Before assembling all internal surfaces of the piping system including valves, both pressure sensors and the pressure cylinder were cleaned with acetone. After assembling, the system was evacuated and then flushed about five times with argon, at a temperature of 400 K. After a final evacuation, the system was flushed with oxygen for about 1 h to minimize contamination by argon.

■ RESULTS AND DISCUSSION

The measuring cell was filled at low temperatures of around 250 K, closed, and then heated up to each studied isotherm. This isochoric pressurizing has a low risk of an increase of temperature through adiabatic compression by a feed pump or by a pressure surge in the piping system. Measurements were carried out from high to low pressure by releasing fluid to the ambient through a valve. Below a pressure of 5 MPa, measurements were not feasible due to the usual limitations of the pulse-echo technique, such as acoustic impedance and attenuation. These effects predominantly play a role in low density fluids, i.e., gases up to the critical region and other highly attenuating liquids, and impede the readability of the echoes due to their distortion, temporal extension and low amplitude.[25]

The first measurement was performed for a data point at 250 K and 34 MPa and showed a good agreement in a range of 0.07% with the data by Straty and Younglove,[17] which is within the stated uncertainty. The overall uncertainty of the temperature measurement with a Pt 100 thermometer (Rössel Messtechnik RM-type) was less than $u_{c,\Delta T}$ = 30 mK. The

Table 1. Sample Table

chemical name	source	impurity	purification method
argon	Air Liquide	≤10 ppm	none
oxygen	Air Liquide	≤15 ppm	none

DOI: 10.1021/acs.jced.5b01007

Table 2. Experimental Data for the Speed of Sound of Oxygen[a]

T (K)	p (MPa)	c (m/s)	$\pm u_c$ (m/s)	T (K)	p (MPa)	c (m/s)	$\pm u_c$ (m/s)
299.997	74.03	645.07	0.93	399.090	7.95	393.26	0.08
299.966	69.69	624.95	0.95	399.091	6.02	389.77	0.08
299.966	64.96	602.28	0.98	399.092	4.96	388.03	0.08
299.968	60.16	578.47	1.01				
299.966	55.14	552.86	1.04	449.950	88.05	662.01	0.67
299.966	50.01	525.82	1.06	449.794	87.52	660.32	0.68
299.967	45.03	498.92	1.08	449.883	85.02	652.33	0.68
299.969	39.96	471.20	1.09	449.867	80.01	636.12	0.68
299.972	34.96	443.87	1.08	449.877	75.27	620.61	0.69
299.971	29.96	417.33	1.03	449.887	70.12	603.58	0.69
299.970	25.03	392.82	0.94	449.888	65.18	587.16	0.69
299.969	20.05	370.99	0.09	449.896	60.07	570.12	0.69
299.965	14.86	352.65	0.08	449.896	55.09	553.54	0.68
299.967	9.92	340.22	0.08	449.939	49.91	536.52	0.67
				449.940	45.09	520.58	0.66
349.976	78.85	641.85	0.82	449.934	40.05	504.35	0.65
349.987	68.69	600.07	0.85	449.934	35.03	488.60	0.62
350.030	64.93	584.11	0.86	449.935	30.00	473.40	0.59
349.988	59.91	562.59	0.88	449.938	24.94	458.85	0.56
349.985	55.11	541.66	0.88	449.943	20.01	445.60	0.09
349.983	49.90	518.73	0.89	449.944	15.00	433.26	0.09
349.986	45.02	497.15	0.88	449.936	9.97	422.01	0.09
350.033	40.05	475.39	0.87	449.948	8.01	418.16	0.09
349.987	35.08	454.09	0.84	449.941	6.01	414.33	0.09
349.977	29.99	433.29	0.79				
349.988	24.98	414.20	0.72	498.908	100.06	699.53	0.62
349.988	19.64	396.03	0.09	498.901	95.00	684.96	0.62
349.990	14.98	382.53	0.08	498.906	90.00	670.28	0.63
349.988	10.07	370.90	0.08	498.925	84.89	655.27	0.63
349.978	8.03	367.01	0.08	498.918	79.99	640.74	0.63
				498.908	74.96	625.69	0.63
399.051	83.18	648.15	0.74	498.833	69.94	610.55	0.63
399.066	79.99	636.78	0.75	498.895	65.00	595.63	0.63
399.072	74.59	617.20	0.76	498.888	60.01	580.54	0.63
399.083	70.10	600.65	0.76	499.030	54.81	564.89	0.62
399.082	64.90	581.28	0.77	499.026	49.93	550.29	0.61
399.077	60.07	563.14	0.77	499.004	44.90	535.41	0.60
399.080	54.97	543.88	0.77	498.990	40.01	521.13	0.59
399.086	50.09	525.43	0.76	499.000	34.73	506.11	0.57
399.083	44.98	506.29	0.75	498.999	29.91	492.81	0.54
399.081	39.97	487.82	0.73	499.014	24.90	479.52	0.52
399.084	34.89	469.60	0.71	499.037	20.07	467.39	0.10
399.089	29.90	452.47	0.67	499.016	14.94	455.31	0.09
399.092	25.01	436.72	0.62	498.943	10.00	444.64	0.09
399.064	19.90	421.58	0.09	499.026	7.82	440.23	0.09
399.095	15.01	408.72	0.09	499.031	5.91	436.52	0.09
399.109	9.98	397.34	0.08	499.027	4.92	434.71	0.09

[a] Standard uncertainties u are $u(T) = 0.03$ K, $u(p) = 0.2$ MPa for $p \geq 20$ MPa, and $u(p) = 0.01$ MPa for $p \leq 20$ MPa where $u(p)$ contributed around 95% above 20 MPa and around 40% below 20 MPa to the combined uncertainty u_c.

pressure was measured with two transducers (Honeywell TJE), one with a measuring range from 0 to 20 MPa and the second one with a measuring range up to 200 MPa. The first one had an uncertainty of ±0.05% and the second one of ±0.1% with respect to their full scale and therefore had a maximum absolute uncertainty of ±0.2 MPa above 20 MPa, which had the largest impact at low temperatures. This is a consequence of the pressure uncertainty, combined with the high isothermal compressibility of the fluid at such thermodynamic states. The propagation path lengths were referenced at the two isotherms 300 and 350 K up to a pressure of 40 MPa with pure argon (cf. Table 1) using values calculated from the EOS by Tegeler et al.[37] with an uncertainty $u_{\mathrm{EOS}} = 0.02\%$. Here, the temperature was measured with the same Pt 100 thermometer which was used during the present oxygen measurements, and the pressure was measured with a dead weight tester (DH-Budenberg 580 EHX) with an overall absolute uncertainty $u_{c,\Delta p,\mathrm{REF}} = 0.02\%$.

According to the error propagation law, the combined speed of sound measurement uncertainty u_c is composed of the relevant contributions due to uncertainties of temperature (in this case twice, i.e., for referencing and measuring) and pressure measurements, as well as the uncertainties of the referencing procedure

$$u_c = \sqrt{2(u_{c,\Delta T})^2 + (u_{c,\Delta p})^2 + (u_{\mathrm{EOS}})^2 + (u_{c,\Delta p,\mathrm{REF}})^2} \quad (1)$$

The uncertainty of the operation procedure was limited by the internal time reference of the function generator and was thus neglected. Likewise the uncertainty of the very low impurity of oxygen (cf. Table 1) was not considered. Numerical experimental data together with their uncertainties are listed in Table 2.

■ CONCLUSION

The speed of sound of oxygen was measured in the supercritical region along five isotherms from 300 to 500 K and from somewhat above 5 MPa up to 100 MPa. The measured speed of sound data for oxygen were compared with the EOS by Schmidt and Wagner.[1] The uncertainties of the EOS which is valid in the temperature range from the triple point to 300 K and a pressure of up to 80 MPa were stated as 1% for the speed of sound, except for the critical region. The present measurements confirm this uncertainty and show that for temperatures above 400 K the maximum deviation increases to about 1.6%, cf. Figure 3.

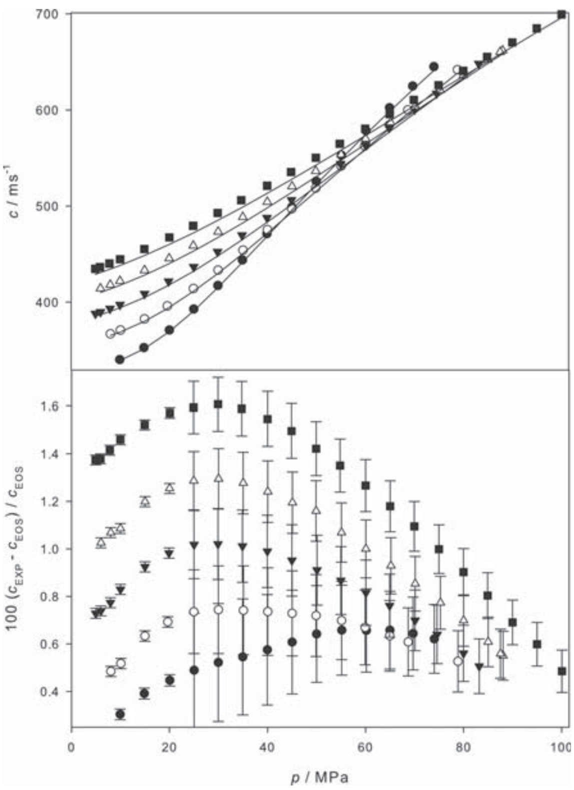

Figure 3. Absolute values (top) and deviations (bottom) of present experimental speed of sound data from the equation of state (EOS) for oxygen by Schmidt and Wagner[1] at ●, 300 K; ○, 350 K; ▼, 400 K; △, 450 K and ■, 500 K.

Steeper slopes of the isotherms at lower temperatures for the speed of sound as a function of pressure in the supercritical region can also be observed for other diatomic fluids like nitrogen (measurements by Costa Gomez et al.[38]) or hydrogen (equation of state by Leachman et al.[39]) at comparable states (cf. Figure 3 (top)). Due to the large contribution of the pressure uncertainty (for measurements above 20 MPa around 95% and below 20 MPa around 40%) to the overall uncertainty, u_c has its maximum of almost 0.25% for the data point at 300 K and 30 MPa, cf. Figure 3 (bottom).

This work covered a wide range of temperature and pressure in the supercritical state for which no experimental data were available for oxygen. The present results show that the pulse-echo technique is a reliable and accurate method for the measurement of the speed of sound of supercritical oxygen.

■ AUTHOR INFORMATION

Corresponding Author

*E-mail: jadran.vrabec@uni-paderborn.de. Phone: +49-5251/60-2421. Fax: +49-5251/60-3522.

Notes

The authors declare no competing financial interest.

■ ACKNOWLEDGMENTS

The authors thank Christian Binder, Thomas Kasch, and Siegfried Lehné of the Bundesamt für Materialforschung (BAM) in Berlin for consultancy about safety issues with respect to pure oxygen.

■ REFERENCES

(1) Schmidt, R.; Wagner, W. A New Form of the Equation of State for Pure Substances and its Application to Oxygen. *Fluid Phase Equilib.* **1985**, *19*, 175−200.

(2) Span, R. *Multiparameter Equations of State: An accurate Source of Thermodynamic Property Data*; Springer: Berlin, 2000.

(3) Cook, S. R. On the velocity of sound in gases, and the ratio of the specific heats, at the temperature of liquid air. *Phys. Rev. (Series I)* **1906**, *23*, 212−237.

(4) Keesom, W. H.; van Itterbeek, A.; Lammeren, J. A. Measurements about the velocity of sound in oxygen gas. *Commun. Phys. Lab. Leiden* **1931**, *216*, 996−1003.

(5) Bär, R. Velocity of sound in liquid oxygen. *Nature* **1935**, *135*, 153.

(6) van Itterbeek, A.; Mariëns, P. Measurement with ultra-sonics on the velocity and absorption of sound at ordinary and at low temperatures. *Physica* **1937**, *4*, 207−215.

(7) van Itterbeek, A.; Mariëns, P. Measurements on the velocity and absorption of sound in various gases between + 100°C and − 100°C - Influence of pressure on the absorption. *Physica* **1937**, *4*, 609−616.

(8) van Itterbeek, A.; van Paemel, O. Measurements on the velocity of sound as a function of pressure in oxygen gas at liquid oxygen temperatures. Calculation of the second virial coefficient and the specific heats. *Physica* **1938**, *5*, 593−604.

(9) Liepmann, H. W. Die Schallgeschwindigkeit in flüssigem Sauerstoff als Funktion der Siedetemperatur bei Frequenzen von 7.5 und 1,5 × 10^6 Hz. *Helv. Phys. Acta* **1938**, *11*, 381−396.

(10) Galt, J. K. Sound absorption and velocity in liquefied argon, oxygen, nitrogen, and hydrogen. *Technical report, Massachusetts Institute of Technology* 1947, *46*.

(11) van Itterbeek, A.; de Bock, A. Velocity of sound in liquid oxygen. *Physica* **1948**, *14*, 542−544.

(12) Boyer, R. Velocity of sound in liquid oxygen. *J. Acoust. Soc. Am.* **1951**, *23*, 176−178.

(13) Verhaegen, L. Metingen over de voortplantingssnelheid van het geluid in enkele vloeibaar gemaakte gassen. *Verhandelingen van de KVAB voor Wetenschappen* **1952**, *38*, 1−65.

DOI: 10.1021/acs.jced.5b01007

(14) van Itterbeek, A.; van Dael, W. Velocity of sound in liquid oxygen and liquid nitrogen as a function of temperature and pressure. *Physica* **1962**, *28*, 861−870.

(15) van Dael, W.; van Itterbeek, A.; Cops, A.; Thoen, J. Sound velocity measurements in liquid argon, oxygen and nitrogen. *Physica* **1966**, *32*, 611−620.

(16) Blagoi, Y. P.; Butko, A. E.; Mikhailenko, S. A.; Yakuba, V. V. Sound velocity in liquid nitrogen, oxygen and argon in the region above normal boiling temperature. *Akusticheskij Zhurnal* **1966**, *12*, 405−410.

(17) Straty, G. C.; Younglove, B. A. Velocity of sound in saturated and compressed fluid oxygen. *J. Chem. Thermodyn.* **1973**, *5*, 305−312.

(18) Baidakov, V. G.; Kaverin, A. M. Ultrasonic speed in superheated liquid oxygen. *J. Chem. Thermodyn.* **1989**, *21*, 1159−1167.

(19) Abramson, E. H.; Slutsky, L. J.; Harrell, M. D.; Brown, J. M. Speed of sound and equation of state for fluid oxygen to 10 GPa. *J. Chem. Phys.* **1999**, *110*, 10493−10497.

(20) Kundt, A. Ueber eine neue Art akustischer Staubfiguren und über die Anwendung derselben zur Bestimmung der Schallgeschwindigkeit in festen Körpern und Gasen. *Ann. Phys.* **1866**, *203*, 497−523.

(21) Kortbeek, P.; Muringer, M.; Trappeniers, N.; Biswas, S. Apparatus for sound velocity measurements in gases up to 10 kbar: Experimental data for argon. *Rev. Sci. Instrum.* **1985**, *56*, 1269−1273.

(22) Lin, C.-W.; Trusler, J. P. M. The speed of sound and derived thermodynamic properties of pure water at temperatures between (253 and 473) K and at pressures up to 400 MPa. *J. Chem. Phys.* **2012**, *136*, 094511.

(23) Benedetto, G.; Gavioso, R.; Albo, P. G.; Lago, S.; Ripa, D. M.; Spagnolo, R. Speed of sound in pure water at temperatures between 274 and 394 K and at pressures up to 90 MPa. *Int. J. Thermophys.* **2005**, *26*, 1667−1680.

(24) Dubberke, F. H.; Rasche, D. B.; Baumhögger, E.; Vrabec, J. Apparatus for the measurement of the speed of sound of ammonia up to high temperatures and pressures. *Rev. Sci. Instrum.* **2014**, *85*, 084901.

(25) Dubberke, F. H.; Baumhögger, E.; Vrabec, J. Burst design and signal processing for the speed of sound measurement of fluids with the pulse-echo technique. *Rev. Sci. Instrum.* **2015**, *86*, 054903.

(26) Deutsche Gesetzliche Unfallversicherung, BGR 500. *Betreiben von Arbeitsmitteln* 2008, *500*.

(27) Grunewald, T.; Finke, R.; Grätz, R. Untersuchungen zur Zündwahrscheinlichkeit und Datenanalyse zur Erfassung der Einflussgrößen mechanisch erzeugter Stahl-Schlagfunken in explosionsfähigen Brenngas/Luft-Gemischen. *Forschungsbericht* **2010**, *292*.

(28) Beesom, H. D.; Smith, S. R.; Stewart, W. F. *Safe Use of Oxygen and Oxygen Systems: Handbook for Design, Operation, and Maintenance*; ASTM International, 2007.

(29) European Industrial Gases Association AISBL. *Safety Principles of High Pressure Oxygen Systems*; Eiga Safety Information, 2008.

(30) DIN EN 1797, *Cryogenic vessels - Gas/material compatibility*; Deutsches Institut für Normung e.V., 2002.

(31) Datenblatt X5CrNi18-10, *Nichtrostender austenitischer Stahl 1.4301*; Deutsche Edelstahlwerke, 2008.

(32) Datenblatt X6CrNiMoTi17-12-2, *Nichtrostender austenitischer Stahl 1.4571*; Deutsche Edelstahlwerke, 2008.

(33) Datenblatt X2CrNiMoN22-5-3, *Nichtrostender austenitischer-ferritischer Stahl 1.4462*; Deutsche Edelstahlwerke, 2008.

(34) Berufsgenossenschaft Rohstoffe und chemische Industrie, M 034-1, *Liste der nichtmetallischen Materialien zu Merkblatt M 034 Sauerstoff*; Jedermann Verlag, 2013.

(35) Bolobov, V. I.; Berezin, A. Y. Conditions for Ignition of Copper and Copper Alloys in Oxygen. *Combustion, Explosion, and Shock Waves* **1998**, *34*, 47−50.

(36) Emerson Process Management, Material Guidelines for Gaseous Oxygen Service. *Product Bulletin* 2006, *59:045*.

(37) Tegeler, C.; Span, R.; Wagner, W. A New Equation of State for Argon Covering the Fluid Region for Temperatures From the Melting Line to 700 K at Pressures up to 1000 MPa. *J. Phys. Chem. Ref. Data* **1999**, *28*, 779−850.

(38) Costa Gomes, M.; Trusler, J. The speed of sound in nitrogen at temperatures between T = 250 K and T = 350 K and at pressures up to 30 MPa. *J. Chem. Thermodyn.* **1998**, *30*, 527−534.

(39) Leachman, J.; Jacobsen, R.; Penoncello, S.; Lemmon, E. Fundamental Equations of State for Parahydrogen, Normal Hydrogen, and Orthohydrogen. *J. Phys. Chem. Ref. Data* **2009**, *38*, 721−748.

4.6 Thermodynamic properties of octamethyltrisiloxane and decamethyltetrasiloxane

Monika Thol, Frithjof H. Dubberke, Elmar Baumhögger, Roland Span, Jadran Vrabec, J. Chem. Eng. Data 62, (2017), 2633-2648; DOI: 10.1021/acs.jced.7b00092

Reprinted from the Journal of Chemical & Engineering data, (2017) with permission from ACS Publications.

The scientific work and discussion was coordinated and consolidated by Monika Thol under supervision of Roland Span and Jadran Vrabec.
The manuscript was prepared by Monika Thol.
Speed of Sound measurements and data evaluation were performed by Frithjof H. Dubberke and Elmar Baumhögger.
The manuscript was revised by Roland Span and Jadran Vrabec.

This publication is in context of the Precise Modelling of Thermophysical Properties research under supervision of Monika Thol at the chair of Thermodynamic of the University of Bochum of Prof. Dr.-Ing. habil. Roland Span and the chair of Thermodynamic and Energy Technology of Prof. Dr.-Ing. habil. Jadran Vrabec.

Journal of chemical & engineering data

Article

pubs.acs.org/jced

Speed of Sound Measurements and Fundamental Equations of State for Octamethyltrisiloxane and Decamethyltetrasiloxane

Monika Thol,*[†] Frithjof H. Dubberke,[‡] Elmar Baumhögger,[‡] Jadran Vrabec,[‡] and Roland Span[†]

[†]Thermodynamics, Ruhr-Universität Bochum, Universitätsstraße 150, 44801 Bochum, Germany

[‡]Thermodynamics and Energy Technology, Universität Paderborn, Warburger Straße 100, 33098 Paderborn, Germany

Supporting Information

ABSTRACT: Equations of state in terms of the Helmholtz energy are presented for octamethyltrisiloxane and decamethyltetrasiloxane. The restricted databases in the literature are augmented by speed of sound measurements, which are carried out by a pulse-echo method. The equations of state are valid in the fluid region up to approximately 600 K and 130 MPa and can be used to calculate all thermodynamic properties by combining the Helmholtz energy and its derivatives with respect to the natural variables. The accuracy of the equation is validated by comparison to experimental data and correct extrapolation behavior is ensured.

1. INTRODUCTION

The accurate description of thermodynamic properties of fluids is an important discipline in energy, process, and chemical engineering. For many applications in research and industry, these properties are mandatory for process simulation and the energetically but also economically efficient construction of plants. Nowadays, such information is provided by fundamental equations of state, the parameters of which are adjusted to experimental data. Therefore, it is evident that the quality of the corresponding mathematical models is primarily dependent on the availability and the accuracy of experimental data. For the development of a reliable equation of state, at least homogeneous density data and information on the vapor−liquid equilibrium are required. Well established calculation of caloric properties requires fits to either isobaric heat capacity or speed of sound data, where the latter can usually be measured more precisely. Previous studies on siloxanes already showed that these fluids were barely investigated experimentally and, therefore, the development of equations of state is challenging.[1−4]

In recent years, siloxanes experienced growing interest as working fluids in organic Rankine cycle (ORC) processes, which are viable approaches for converting waste heat to mechanical work. In addition to the technical development of efficient hardware, the design and performance of ORC processes rely on the selection of a suitable working fluid. Thus, for technically well-advanced ORC plants, reliable and accurate thermophysical property data on working fluids are a necessity.

Siloxanes belong to the wider class of organosilicone compounds and are classical examples of fluids that reveal a positive slope of the saturated vapor line. In particular, linear siloxanes, such as hexamethyldisiloxane (MM), octamethyltrisiloxane (MDM), or decamethyltetrasiloxane (MD_2M) as well as their mixtures, appear to be good candidates for becoming widely used working fluids in high-temperature ORC processes.[5] However, the current lack of accurate thermophysical data of siloxanes may lead to suboptimally designed cycles. During the design and construction of ORC plants, accurate thermophysical property data are directly relevant for a variety of cycle components, such as expansion devices, heat exchangers, condensers, and pumps, whereas data uncertainty may decrease the performance of those devices tremendously.

Colonna and co-workers[3,4,6] developed equations of state in terms of the Helmholtz energy for various linear and cyclic siloxanes in 2006 and 2008. Owing to limited experimental data sets, they applied a generalized functional form for the residual contribution to the Helmholtz energy, which was originally developed for the description of nonpolar and weakly polar fluids, such as hydrocarbons or fluorinated hydrocarbons.[7,8] Investigations of Thol et al.[1,2] showed that these equations are not well suited for accurate predictions of caloric properties, such as speed of sound or isobaric heat capacity. Furthermore, Abbas et al.[9] measured in 2011 density data in the homogeneous liquid phase for pressures of up to 130 MPa, which identified issues of the available models in the high-pressure region. Therefore, new equations of state for MDM and MD_2M are presented here, which are correlated to all available experimental data. For the appropriate description of caloric properties, additional speed of sound measurements were carried out by means of the pulse-echo technique.

Special Issue: Memorial Issue in Honor of Ken Marsh

Received: January 27, 2017
Accepted: June 23, 2017
Published: July 18, 2017

DOI: 10.1021/acs.jced.7b00092
J. Chem. Eng. Data 2017, 62, 2633−2648

Finally, the suitability of the siloxanes for the application in ORC processes is analyzed in terms of their possible affiliation to the class of Bethe-Zel'dovich-Thompson fluids as proposed by Colonna et al.[10]

2. SPEED OF SOUND MEASUREMENT

Octamethyltrisiloxane was purchased from Sigma-Aldrich (CAS No. 107-51-7) with a given purity of more than 99.9 vol %, and decamethyltetrasiloxane was obtained from Merck (CAS No. 141-62-8) with a purity better than 99.8 vol %. Aside from degassing with a vacuum pump, no further purification steps were applied to both fluids (see Table 1).

Table 1. Description of the Samples Used for the Speed of Sound Measurements of MDM and MD$_2$M

chemical name	source	initial mole fraction purity	purification method
MDM	Sigma-Aldrich	0.999	none
MD$_2$M	Merck	0.998	none

Speed of sound measurements were performed with the pulse-echo technique by determining the propagation time difference Δt of an acoustical wave burst, which propagates over known distances between two reflectors in the fluid sample, cf. Dubberke et al.[11] The experimental speed of sound is given by the ratio of propagation length and time, where diffraction and dispersion effects are taken into account.[12] The path length was calibrated to water for temperatures of 300 to 400 K with pressures of 10 to 120 MPa. Test measurements for water were accurate to within 0.05%. During the present experimental work, we further developed our speed of sound apparatus so that the two fluids were sampled with different measurement approaches and measurement instrumentation.

MDM. Speed of sound measurements were performed for MDM in the liquid state along six isotherms over a temperature range from 300 to 550 K and for pressures up to 30 MPa (Figure 1, top).

For this fluid, the measurement of the propagation time difference Δt was based on the correlation method, which was also used by Ball and Trusler,[13] combined with signal enhancement by applying Fast Fourier Transformation (FFT) to the sampled echo signals.[14] The two echoes were identified and selected by an oscilloscope and uploaded to a computer. Noise suppression was applied to the echo signals by a FFT filter before the propagation time difference Δt was determined with a correlation function.[1] The pressure sensor was a Honeywell TJE with an operating range of up to 70 MPa and an absolute measurement uncertainty of 0.05% with respect to the full scale. The temperature was measured with a Pt100 thermometer (Rössel Messtechnik, RM-type) with a given uncertainty of 20 mK.

The resulting experimental data together with the uncertainties based on the experimental setup are listed in Table 2.

MD$_2$M. Speed of sound measurements were performed for MD$_2$M in the liquid state along seven isotherms over a temperature range from 219 to 500 K and for pressures of up to 120 MPa (Figure 1, bottom).

In this case, Δt was determined by direct time difference measurement with a single burst approach in combination with burst design and signal processing, based on the peak-to-peak method (PPM). PPM relies on the fact that the maximum amplitudes occur at the equivalent time interval in both echoes and, therefore, Δt can be derived directly from the timing of those maxima, cf. Dubberke et al.[15] Here, burst design helped to shape a distinct echo signal and FFT processing supported the readability of the echo signal by boosting its time resolution and suppressing noise with a bandpass filter. This procedure was necessary for measurements at high temperature and low pressure because the signal-to-noise ratio was decreasing while approaching the critical point. Pressure measurement was done by three pressure sensors, i.e. two type Keller PAA 33X 10 μPa and 100 MPa and one type TJE 200 MPa. The combination of those three pressure sensors was applied as a cascaded serial connection with an operating range of up to 200 MPa and an absolute maximum measurement uncertainty of 0.05% with respect to the full scale (Figure 2). Here, the measurements were limited to 120 MPa due to the sealing of the pressure vessel. The pressure sensor type Keller 10 MPa was calibrated with a pneumatic dead weight tester (DH-Budenberg, D&H 5200) with nitrogen. Calibration of the sensor type Keller 100 MPa was done against a hydraulic dead weight tester (DH-Budenberg, 580 EHX). Since the zero drift of sensor type TJE 200 MPa had the largest uncertainty impact, it was continuously calibrated against the 100 MPa sensor.

The temperature was measured with a standardized 25 Ω platinum thermometer (Rosemount 162 CE, calibrated by PTB) together with a MKT 25 measuring bridge with a given overall uncertainty of 2.7 mK (regularly checked against the triple point of water). With respect to possible temperature differences between fluid and sensor position, the uncertainty of temperature measurement was estimated to be 0.02 K.

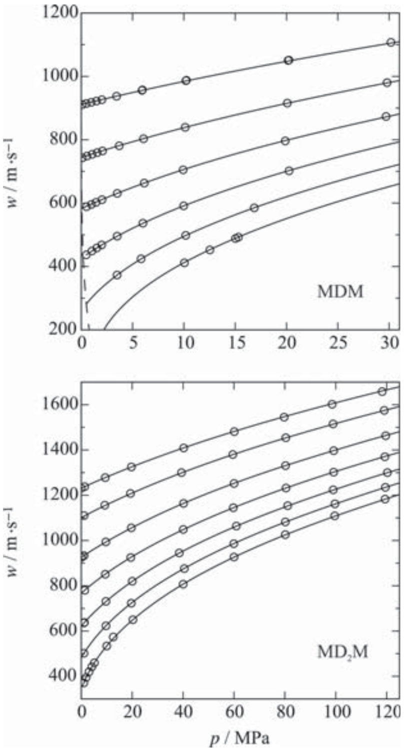

Figure 1. Speed of sound measurements of MDM and MD$_2$M. Present experimental data are depicted as circles, whereas the present equations of state are illustrated as solid curves. The dashed line, only visible for MDM, shows the speed of sound of the saturated liquid.

Table 2. Experimental Results for the Speed of Sound w of MDM

T	p	w	Δ_w
K	MPa	$m \cdot s^{-1}$	$m \cdot s^{-1}$[a]
299.619	0.101	911.32	0.92
299.627	0.502	914.41	0.92
299.636	0.984	918.29	0.92
299.644	1.480	922.14	0.92
299.647	2.012	926.38	0.92
299.664	3.441	937.36	0.92
299.692	5.923	955.80	0.91
299.612	10.196	986.47	0.91
299.676	20.155	1050.26	0.92
299.709	30.179	1107.31	0.93
349.908	0.111	742.97	0.97
349.686	0.558	748.58	0.96
349.647	1.075	754.20	0.96
349.598	1.556	759.34	0.95
349.589	2.066	764.64	0.94
349.576	3.704	781.00	0.93
349.606	6.067	803.25	0.91
349.592	10.127	839.26	0.88
349.605	20.075	915.62	0.86
349.638	29.800	980.01	0.87
399.965	0.508	588.68	1.15
399.965	0.993	595.83	1.13
399.958	1.439	602.33	1.11
399.946	2.018	610.77	1.09
399.957	3.510	630.80	1.04
400.020	9.928	704.99	0.92
400.150	19.875	796.17	0.84
399.420	29.701	873.39	0.82
449.990	0.492	436.70	1.60
449.960	1.045	448.89	1.53
449.980	1.523	458.69	1.47
450.010	1.994	468.09	1.42
450.050	3.497	495.73	1.30
450.090	6.009	536.60	1.15
450.140	9.983	591.45	1.01
450.220	20.246	701.94	0.85
449.440	23.518	734.50	0.82
499.040	1.000	292.60	2.48
499.020	1.521	313.47	2.25
498.960	1.989	328.83	2.08
498.940	3.487	373.05	1.73
499.000	5.834	424.21	1.41
499.020	10.178	498.23	1.12
499.050	16.859	585.07	0.92
549.790	4.484	279.71	2.10
549.740	6.653	340.31	1.61
549.800	10.050	411.61	1.26
549.840	12.528	452.26	1.12
549.670	15.312	492.60	1.01

[a] Δ_w denotes the combined expanded uncertainty ($k = 2$). The uncertainty contribution caused by the impurity of the fluid could not be estimated and was therefore not considered. However, impurities have a significant contribution to the experimental uncertainty, which may be higher than the uncertainties of the experimental setup. Uncertainties ($k = 2$): temperature: 0.1 K; time difference: 0.004 μs; propagation length: 14 μm; pressure: 0.07 MPa.

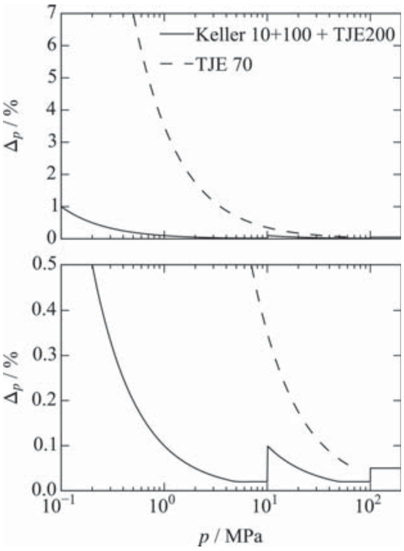

Figure 2. Uncertainty of pressure measurement Δ_p for the cascaded serial connection (CSC) of three sensors (solid line) over a pressure range from 0.1 to 200 MPa and for the TJE in a pressure range from 0.1 to 70 MPa. Below 10 MPa, the CSC presents a significantly lower pressure uncertainty compared to the single TJE sensor. The bottom plot shows a magnified view on the top plot.

The measurement range was limited for MDM (MD_2M) down to a pressure of about 4 MPa (1 MPa) along the 550 K (500 K) isotherm due to the limitation of the pulse-echo method for near critical states as a result of absorption and attenuation effects.[11]

Including the uncertainties from referencing the propagation lengths and the measurement procedure according to the error propagation law, the maximum uncertainty was about 0.8% for MDM and 0.08% for MD_2M ($k = 2$) with respect to the speed of sound. The uncertainty contribution caused by the impurity of the fluids could not be estimated and was therefore not considered. However, the impurities have a significant contribution to the experimental uncertainty, which is higher than the uncertainties of the experimental setup. The resulting experimental data together with the uncertainties based on the experimental setup are listed in Table 3.

3. EQUATIONS OF STATE

The present equations of state are expressed in terms of the Helmholtz energy a, which is reduced by the universal gas constant (R = 8.3144598 $J \cdot mol^{-1} \cdot K^{-1}$ according to the 2014 CODATA recommendations[16]) and the temperature T

$$\alpha(\tau, \delta) = \frac{a(T, \rho)}{RT} \qquad (1)$$

Furthermore, the reduced Helmholtz energy α is separated into an ideal (superscript $^{\circ}$) and a residual contribution (superscript ^{r}). The ideal part describes the effects of density independent intramolecular energy of the hypothetical ideal gas state, whereas the residual part considers the intermolecular interactions and

$$\alpha(\tau, \delta) = \alpha^{\circ}(\tau, \delta) + \alpha^{r}(\tau, \delta) \qquad (2)$$

Table 3. Experimental results for the speed of sound w of MD_2M

T	p	w	Δ_p	Δ_w
K	MPa	$m \cdot s^{-1}$	MPa	$m \cdot s^{-1}$[a]
217.814	0.002	1231.95	0.002	0.93
217.806	1.324	1238.80	0.002	0.94
217.848	9.419	1278.37	0.004	0.97
217.899	19.699	1325.19	0.020	1.01
217.992	40.255	1409.21	0.020	1.08
218.013	60.115	1481.33	0.024	1.14
218.085	79.712	1545.87	0.032	1.20
218.165	98.572	1602.99	0.039	1.25
218.238	118.233	1658.39	0.118	1.34
249.842	1.077	1110.11	0.002	0.83
249.843	9.240	1156.24	0.004	0.87
249.804	19.343	1208.71	0.020	0.91
249.800	39.384	1300.35	0.020	0.99
249.737	59.554	1380.75	0.024	1.05
249.647	80.370	1454.87	0.032	1.12
249.534	98.950	1515.20	0.040	1.17
249.424	119.047	1575.46	0.119	1.27
299.902	0.016	925.67	0.002	0.68
299.935	0.121	926.31	0.002	0.69
299.960	0.958	932.76	0.002	0.69
299.915	1.080	933.63	0.002	0.69
299.983	9.659	994.25	0.004	0.74
299.995	19.671	1056.26	0.020	0.79
300.006	40.202	1164.31	0.020	0.87
300.002	60.024	1252.37	0.024	0.94
300.005	80.266	1331.24	0.032	1.01
300.004	99.198	1397.65	0.040	1.07
300.035	119.626	1463.06	0.120	1.18
349.925	1.369	780.56	0.002	0.57
349.890	9.447	851.51	0.004	0.62
349.899	19.447	925.37	0.020	0.69
349.928	40.092	1049.16	0.020	0.78
349.867	59.744	1145.45	0.024	0.86
349.918	80.462	1232.54	0.032	0.93
349.895	99.170	1302.54	0.040	0.99
349.892	119.296	1370.82	0.119	1.11
399.597	1.077	636.31	0.002	0.47
399.665	1.234	638.18	0.002	0.47
399.596	9.691	731.33	0.004	0.53
399.669	20.055	820.52	0.020	0.62
399.685	38.533	945.04	0.020	0.70
399.695	60.934	1064.32	0.024	0.79
399.696	81.120	1154.26	0.032	0.86
399.696	99.014	1224.64	0.040	0.92
399.553	120.290	1300.12	0.120	1.06
450.052	1.060	502.02	0.002	0.37
449.895	9.702	623.33	0.004	0.45
449.920	19.667	723.35	0.020	0.55
449.959	40.506	876.94	0.020	0.65
449.990	59.941	986.94	0.024	0.73
450.013	80.184	1082.55	0.032	0.81
450.029	99.670	1162.66	0.040	0.87
450.039	119.488	1235.39	0.119	1.01
499.757	1.001	371.60	0.002	0.29
499.824	1.926	395.00	0.002	0.30
499.777	3.058	420.07	0.002	0.31
499.717	4.164	442.17	0.002	0.32
499.749	5.168	460.32	0.002	0.34
499.608	9.979	534.61	0.004	0.39
499.669	20.291	650.54	0.020	0.50
499.695	40.057	807.98	0.020	0.60
499.722	60.022	927.39	0.024	0.68
499.751	80.169	1026.54	0.032	0.76
499.802	99.589	1109.02	0.040	0.83
499.886	119.374	1183.60	0.119	0.98

[a] Δ_w denotes the combined expanded uncertainty ($k = 2$). The uncertainty contribution caused by the impurity of the fluid could not be estimated and was therefore not considered. However, impurities have a significant contribution to the experimental uncertainty, which may be higher than the uncertainties of the experimental setup. Expanded uncertainties ($k = 2$): temperature: 0.04 K, time difference: 0.004 μs, propagation length: 14 μm.

Because of practical reasons, the natural variables temperature and density are reduced by the critical parameters of the investigated fluid

$$\tau = \frac{T_c}{T} \quad \text{and} \quad \delta = \frac{\rho}{\rho_c} \tag{3}$$

For the isobaric heat capacity of the ideal gas, a simplified rigid rotator, harmonic oscillator approach according to Span[17] was applied

$$\frac{c_p^o}{R} = (c_0 + 1) + \sum_{i=1}^{I_{Pol}} n_i^* T^{t_i^*} + \sum_{k=1}^{K_{PE}} m_k \left(\frac{\theta_k}{T}\right)^2 \frac{\exp(\theta_k/T)}{(\exp(\theta_k/T) - 1)^2} \tag{4}$$

Because of the relation between the reduced Helmholtz energy and the isochoric heat capacity

$$\left(\frac{\partial^2 \alpha^o}{\partial \tau^2}\right)_\delta = -\frac{c_v^o}{R\tau^2}, \quad \text{with} \quad c_v^o = c_p^o - R \tag{5}$$

A two-fold integration yields the ideal gas contribution to the residual Helmholtz energy

$$\alpha^o(\tau, \delta) = c^{II} + c^I \tau + c_0 \ln(\tau) + \sum_{i=1}^{I_{Pol}} c_i \tau^{t_i} + \sum_{k=1}^{K_{PE}} m_k \ln[1 - \exp(-\theta_k/T_c \tau)] + \ln(\delta) \tag{6}$$

where $c_i = -n_i^*/(t_i^*(t_i^* + 1))T_c^{t_i^*}$ and $t_i = -t_i^*$.

In this work, only Planck−Einstein terms were used ($I_{pd} = 0$). The corresponding parameters are listed in Table 4.

The integration constants c^I and c^{II} can be chosen arbitrarily. Here, the normal boiling point reference state was applied, which is common practice in the literature for many fluids. Thus, the constants are calculated such that enthalpy and entropy are zero at the boiling temperature $T_B(p = 0.101325 \text{ MPa})$ and the corresponding saturated liquid density $\rho'(p = 0.101325 \text{ MPa})$.

The residual contribution to the reduced Helmholtz energy consists of three empirical term types

Table 4. Parameters of the Ideal Part of the Present Equations of State (eq 6)[a]

i	1	2	3	c_0	c^{I}	c^{II}
			MDM			
m_i	28.817	46.951	31.054	3	−19.6600754	117.994606
θ_i/K	20	1570	4700			
			MD_2M			
m_i	28.59	56.42	50.12	3	−26.3839138	131.089725
θ_i/K	20	1180	4240			

[a] Note that $I_{\mathrm{Pol}} = 0$.

$$\begin{aligned}\alpha^{\mathrm{r}}(\tau,\delta) &= \alpha^{\mathrm{r}}_{\mathrm{Pol}}(\tau,\delta) + \alpha^{\mathrm{r}}_{\mathrm{Exp}}(\tau,\delta) + \alpha^{\mathrm{r}}_{\mathrm{GBS}}(\tau,\delta) \\ &= \sum_{i=1}^{I_{\mathrm{Pol}}} n_i \delta^{d_i}\tau^{t_i} + \sum_{i=I_{\mathrm{Pol}}+1}^{I_{\mathrm{Pol}}+I_{\mathrm{Exp}}} n_i \delta^{d_i}\tau^{t_i}\exp(-\delta^{p_i}) \\ &\quad + \sum_{i=I_{\mathrm{Pol}}+I_{\mathrm{Exp}}+1}^{I_{\mathrm{Pol}}+I_{\mathrm{Exp}}+I_{\mathrm{GBS}}} n_i \delta^{d_i}\tau^{t_i}\exp(-\eta_i(\delta-\varepsilon_i)^2 - \beta_i(\tau-\gamma_i)^2)\end{aligned} \tag{7}$$

In principle, polynomial ($_{\mathrm{Pol}}$) and exponential ($_{\mathrm{Exp}}$) terms are sufficient for an accurate description of thermodynamic properties in the entire fluid region. However, the introduction of modified Gaussian bell-shaped terms ($_{\mathrm{GBS}}$) by Setzmann and Wagner[18] enables a better representation of the critical region. Nowadays, these terms are also used in other regions with moderate parameters, which results in a smaller overall number of terms.

In this work, a nonlinear fitting algorithm provided by the National Institute of Standards and Technology[19] was applied to determine the fluid-specific parameters. The basic features of the fitting algorithm were described by Lemmon and Jacobsen.[20] Since a nonlinear fitting technique requires adequate initial parameter values, it is beneficial to start the fitting procedure with a functional form of another fluid, which is known to yield physically reasonable results and exhibits correct extrapolation behavior. Here, the equation of state for chlorine[21] was applied. From this starting point, all parameters were optimized, including coefficients, temperature and density exponents, Gaussian bell-shaped parameters, and the number of terms. The resulting parameters for MDM and MD_2M are given in Tables 5 and 6. For both fluids, five polynomial, five exponential, and five Gaussian bell-shaped terms were chosen.

From this equation, all thermodynamic properties in the homogeneous state region can be calculated by means of the reduced Helmholtz energy and its derivatives with respect to the natural variables (see Span[17] or Lemmon et al.[22]). For the calculation of vapor pressure and saturated densities, an iterative procedure taking into account the thermal, mechanical, and chemical equilibrium has to be applied. For computer calculations, it is helpful to use ancillary equations to generate initial values for these iterations. Therefore, ancillary equations for vapor pressure, saturated liquid density, and saturated vapor density were developed, see eqs 8 to 10. The parameters are given in Table 7. These ancillary equations are not reference equations so that the fundamental equations of state must be used to calculate accurate saturation properties.

Vapor pressure

$$\ln\left(\frac{p_v}{p_c}\right) = \left(\frac{T_c}{T}\right)\sum_{i=1}^{5} n_i\left(1-\frac{T}{T_c}\right)^{t_i} \tag{8}$$

Saturated liquid density

$$\frac{\rho'}{\rho_c} = 1 + \sum_{i=1}^{5} n_i\left(1-\frac{T}{T_c}\right)^{t_i} \tag{9}$$

Saturated vapor density

$$\ln\left(\frac{\rho''}{\rho_c}\right) = \sum_{i=1}^{6} n_i\left(1-\frac{T}{T_c}\right)^{t_i} \tag{10}$$

4. COMPARISON TO EXPERIMENTAL DATA

In this section, the present equations of state are compared to experimental data. Figure 3 shows all experimental data in the homogeneous state. The red symbols depict data, which were available for the development of the equations of state of Colonna et al.[4] in 2008. For MDM at that time, there were only density data in the gaseous region and in the liquid state at atmospheric pressure available. Only a few state points in the liquid state at atmospheric pressure could be considered for the speed of sound. In the case of MD_2M in 2008, there were not even measurements in the gaseous state available. Therefore, it is not surprising that the equations of Colonna et al.[4] show disadvantages in the representation of homogeneous density data at elevated pressure and in the representation of caloric properties.

Table 5. Parameters of the Residual Part of the Present Equation of State for MDM (eq 7)

i	n_i	t_i	d_i	p_i	η_i	β_i	γ_i	ε_i
1	5.039724×10^{-2}	1.000	4					
2	$1.189992 \times 10^{+0}$	0.188	1					
3	$-2.468723 \times 10^{+0}$	1.030	1					
4	-7.438560×10^{-1}	0.700	2					
5	4.434056×10^{-1}	0.464	3					
6	$-1.371359 \times 10^{+0}$	2.105	1	2				
7	$-1.529621 \times 10^{+0}$	1.376	3	2				
8	4.445898×10^{-1}	0.800	2	1				
9	$-1.009921 \times 10^{+0}$	1.800	2	2				
10	-5.903694×10^{-2}	1.005	7	1				
11	$3.515188 \times 10^{+0}$	0.700	1		0.986	0.966	1.250	0.928
12	8.367608×10^{-2}	0.660	1		1.715	0.237	1.438	2.081
13	$1.646856 \times 10^{+0}$	1.138	3		0.837	0.954	0.894	0.282
14	-2.851917×10^{-1}	1.560	2		1.312	0.861	0.900	1.496
15	$-2.457571 \times 10^{+0}$	1.310	2		1.191	0.909	0.899	0.805

DOI: 10.1021/acs.jced.7b00092
J. Chem. Eng. Data 2017, 62, 2633−2648

Table 6. Parameters of the Residual Part of the Present Equation of State for MD_2M (eq 7)

i	n_i	t_i	d_i	p_i	η_i	β_i	γ_i	ε_i
1	1.458333×10^{-2}	1.000	4					
2	$3.227554 \times 10^{+0}$	0.319	1					
3	$-3.503565 \times 10^{+0}$	0.829	1					
4	$-2.017391 \times 10^{+0}$	0.780	2					
5	8.606129×10^{-1}	0.687	3					
6	$-2.196015 \times 10^{+0}$	1.290	1	2				
7	-9.289014×10^{-1}	3.910	3	2				
8	$2.027740 \times 10^{+0}$	0.770	2	1				
9	-9.168439×10^{-1}	3.055	2	2				
10	-6.383507×10^{-2}	1.013	7	1				
11	$2.674255 \times 10^{+0}$	1.070	1		0.982	0.7323	1.0420	0.874
12	4.662529×10^{-2}	1.890	1		2.700	0.5430	1.1000	1.430
13	-3.835361×10^{-1}	1.133	3		1.347	1.2600	1.1460	0.855
14	-4.273462×10^{-1}	0.826	2		0.864	0.8780	1.0850	0.815
15	$-1.148009 \times 10^{+0}$	0.830	2		1.149	2.2200	0.6844	0.491

Table 7. Parameters for the Ancillary Equations for MDM and MD_2M

	p_v: eq (8)		ρ': eq (9)		ρ'': eq (10)	
i	n_i	t_i	n_i	t_i	n_i	t_i
			MDM			
1	−8.8192	1.00	7.016	0.54	−5.3686	0.515
2	4.0952	1.50	−13.924	0.90	−11.85	4.580
3	−4.062	1.90	20.84	1.30	−16.64	2.060
4	−6.208	3.71	−16.64	1.73	−52.26	5.250
5	−3.212	14.6	5.906	2.20	−125.6	11.30
6					−235.7	21.60
			MD_2M			
1	−10.174	1.00	8.215	0.498	−4.5483	0.428
2	9.607	1.50	−24.65	0.855	−101.989	2.320
3	−10.08	1.83	47.23	1.220	224.06	2.800
4	−7.242	4.15	−42.44	1.600	−182.79	3.300
5	−30.56	17.8	15.18	2.040	−110.45	8.500
6					−330.87	17.50

In 2011, Abbas et al.[9] published comprehensive density measurements, which were considered for the development of the present equations of state. Furthermore, the present speed of sound data as described in section 2 were applied. On the basis of these data, the new equation for MDM is valid from the triple point temperature T_{tr} = 187.2 K to T_{max} = 570 K and a maximum pressure of 130 MPa. The equation for MD_2M is valid from the triple point temperature T_{tr} = 205.2 K according to Rowley et al.[23] to T_{max} = 600 K and a maximum pressure of 130 MPa. Other fluid-specific properties are given in Table 8.

In the following, percentage deviations between the equations of state and experimental data were calculated according to

$$\Delta X = 100\frac{X_{\mathrm{DATA}} - X_{\mathrm{EOS}}}{X_{\mathrm{DATA}}} \tag{11}$$

To quantify the representation of the experimental data, the average absolute relative deviation was evaluated for each author according to

$$\mathrm{AAD} = \frac{1}{N}\sum_{i=1}^{N}|\Delta X_i| \tag{12}$$

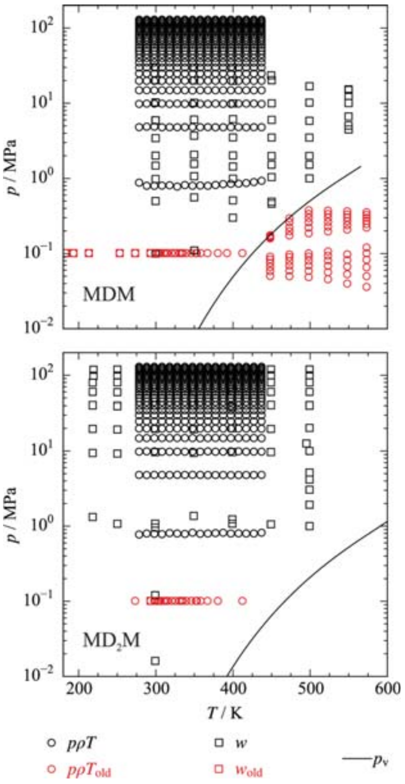

Figure 3. Available experimental data for MDM and MD_2M in the homogeneous region. The red symbols depict data that were available in 2008 for the development of the equations of state of Colonna et al.[4]

Data are shown in Tables 9, 10, 11, and 12. Vapor−liquid equilibrium data are classified in three different temperature ranges in relation to the critical temperature.

4.1. Ideal Gas State. The ideal contribution to the reduced Helmholtz energy was calculated by means of a two-fold integration of the isobaric heat capacity of the ideal gas with respect to the temperature (see section 3). For simplification, it was assumed that translation and rotation are always excited and molecules behave like rigid rotators and harmonic oscillators, cf. Span.[17] Hence, for complex molecules, such as siloxanes, c_p^o/R = 4 for

Table 8. Fluid-Specific Properties of MDM and MD_2M. If No Reference Is Given, the Property Was Calculated in This Work

	MDM	ref	MD_2M	ref
T_c/K	565.3609	24	599.4	24
ρ_c/mol·dm^{-3}	1.134	25	0.864	26
p_c/MPa	1.4375		1.144	
T_B/K	425.63		467.59	
T_{tr}/K	187.2	23	205.2	23
$\rho_{tr,liq.}$/mol·dm^{-3}	3.907		3.032	
M/g·mol^{-1}	236.5315	27	310.6854	27

Table 9. Average Absolute Relative Deviations of Experimental Vapor Pressure, Saturated Liquid, and Saturated Vapor Density Data from the Present Equation of State for MDM. Temperatures Were Adapted to the ITS-90 Scale

			AAD/%[a]			
author	no. of points	temp range/K	LT	MT	HT	overall
		Vapor Pressure				
Abbas et al.[9]	23	292–426	3.29	3.87		3.64
Flaningam[26]	12	346–437		0.075		0.075
Lindley and Hershey[25]	74	322–565	2.80	0.42	0.27	0.45
Patnode and Wilcock[28]	1	426.14		1.33		1.33
Reuther and Reichel[29]	7	273–344	5.21	0.98		4.60
Thompson[30]	1	426.14		0.50		0.50
Wilcock[31]	10	280–424	11.2	5.74		7.96
		Saturated Liquid Density				
Lindley and Hershey[25]	34	273–564	0.13	0.27	1.02	0.40
		Saturated Vapor Density				
Lindley and Hershey[25]	18	460–565		0.45	1.22	0.75

[a]LT: $T/T_c < 0.6$; MT: $0.6 \leq T/T_c \leq 0.98$; HT: $T/T_c > 0.98$.

Table 10. Average Absolute Relative Deviations of the Experimental Data of Homogeneous States from the Present Equation of State for MDM. Temperatures Were Adapted to the ITS-90 scale

author	no. of points	temp range/K	pressure range/MPa	AAD/%
		Isobaric Heat Capacity of the Ideal Gas		
Nannan and Colonna[32]	10	298–1201	$p \to 0$	0.17
Density				
Abbas et al.[9]	459	278–438	0.8–130	0.044
Golik and Cholpan[33]	1	303.13	0.101325	0.23
Hurd[34]	5	273–354	0.101325	0.089
Marcos et al.[35]	70	448–574	<0.1–1	0.51
McLure et al.[36]	17	299–413	0.101325	0.065
Sperkach and Cholpan[37]	6	183–304	0.101325	0.17
		Speed of Sound		
This work	48	299–550	0.1–31	0.10
Golik and Cholpan[33]	1	303.13	0.101325	0.11
Sperkach and Choplan[37]	6	183–304	0.101325	1.91
Waterman et al.[38]	1	293.14	0.101325	2.63
Weissler[39]	2	303–324	0.101325	0.17
		Isobaric Heat Capacity		
Abbas et al.[9]	38	213–394	p_v	0.21
McLure and Neville[40]	2	303–324	p_v	1.95
		Heat of Vaporization		
Wabiszczewicz[41]	33	294–401	p_v	2.08
Second Thermal Virial Coefficient (AAD in cm^3·mol^{-1})				
Marcos et al.[35]	6	448–574	$p \to 0$	32.4

Table 11. Average Absolute Relative Deviations of Experimental Vapor Pressure Data from the Present Equation of State for MD_2M. Temperatures Were Adapted to the ITS-90 Scale

			AAD/%[a]			
author	no. of points	temp range/K	LT	MT	HT	overall
Abbas et al.[9]	23	320–468	4.56	3.74		3.95
Flaningam[26]	15	366–480		0.066		0.066
Hurd[34]	1	467.00		1.42		1.42
Waterman et al.[38]	1	467.65		0.15		0.15
Wilcock[31]	2	361–468		0.96		0.96

[a]LT: $T/T_c < 0.6$; MT: $0.6 \leq T/T_c \leq 0.98$; HT: $T/T_c > 0.98$.

$T \to 0$ K holds. Furthermore, m_i and θ_i of eqs 4 and 6 were treated as adjustable parameters.[17] For both siloxanes, three temperature-dependent terms were sufficient to represent the available data with a reasonable accuracy.

For the adjustment of these parameters, there was only one data set of Nannan and Colonna[32] available. These data were predicted by means of *ab initio* calculations and an uncertainty of 6% was reported. Figure 4 shows the representation of these data with the present equations of state. For MDM, the data can be reproduced within 0.5%, whereas the equation for MD_2M shows deviations of up to 3.2%. Although both deviations are clearly within the specified uncertainty, the significant quality difference between both equations was further investigated. The publication of Nannan and Colonna[32] contains data for six linear and six cyclic siloxanes. c_p^o data are not available for comparison with none of the others, except for MM. The representation of the MM data is illustrated in Figure 5. Accurate measurements were presented up to 500 K and calculated for higher temperatures by Scott et al.[46] Their uncertainty was claimed to be 0.1%, which could be confirmed with a recent equation of state.[1] However, the data of Nannan and Colonna[32] deviate from the data of Scott et al.[46] and the equation of state by up to 3%. Especially in the low-temperature region, deviations increase. This is in line with the representation of the c_p^o data of MD_2M. Similar to MM, deviations increase with decreasing temperature and reach up to approximately 3%. A better representation of these data could not be achieved without compromising the speed of sound and isobaric heat capacity data from experiments. Therefore, it is assumed that the representation of the MD_2M data is reasonable.

4.2. Thermal Properties. Figure 6 shows the representation of the vapor pressure data for both fluids. For MDM, there are measurements available between 273 and 565 K. Some of these data were already available for MM and octamethylcyclotetrasiloxane (D_4) as investigated in detail by Thol et al.[1,2] Similar to MM and D_4, the vapor pressure data of Abbas et al.[9] exhibit a systematic negative offset of approximately 4% and increasing relative deviations for decreasing temperatures. As discussed before,[1] this behavior is most likely caused by an erroneous handling of the comparative ebulliometer. Therefore, these data were not considered for the development of the present

Table 12. Average Absolute Relative Deviations of the Experimental Data of Homogeneous States from the Present Equation of State for MD_2M. Temperatures Were Adapted to the ITS-90 Scale

author	no. of points	temp range/K	pressure range/MPa	AAD/%
Isobaric Heat Capacity of the Ideal Gas				
Nannan and Colonna[32]	11	298−1401	$p \rightarrow 0$	1.55
Density				
Abbas et al.[9]	459	278−438	0.8−130	0.05
Fox et al.[42]	1	293.14	0.101325	0.25
Golik and Cholpan[33]	1	303.13	0.101325	0.058
Hunter et al.[43]	1	298.14	0.101325	0.33
Hurd[34]	5	273−354	0.101325	0.034
Matteoli et al.[44]	1	303.15	0.101325	0.53
McLure et al.[36]	16	299−413	0.101325	0.12
Povey et al.[45]	1	293.15	0.101325	0.03
Waterman et al.[38]	1	293.14	0.101458	0.05
Speed of Sound				
this work	66	218−500	0.0−121	0.057
Golik and Cholpan[33]	1	303.13	0.101325	0.55
Povey et al.[45]	1	293.15	0.101325	0.61
Waterman et al.[38]	1	293.14	0.101325	0.40
Isobaric Heat Capacity				
Abbas et al.[9]	45	228−439	p_v	0.40
Heat of Vaporization				
Hurd[34]	1	467.00	p_v	0.85
Matteoli et al.[44]	1	298.15	p_v	5.25
Wilcock[31]	1	467.51	p_v	16.2

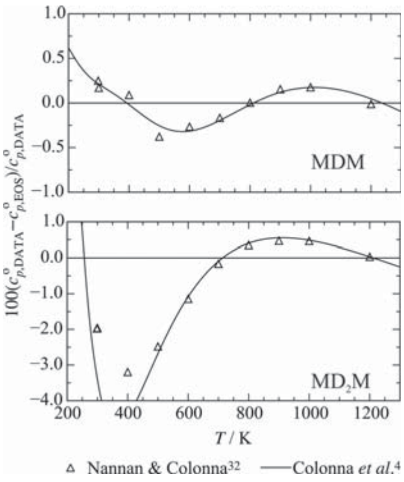

Figure 4. Representation of the isobaric heat capacity of the ideal gas of MDM and MD_2M with the present equations of state.

equations of state. The data of Flaningam[26] are represented within 0.15%. In this publication,[26] the author does not give any information about experimental uncertainties. However, when comparing to the equation of state and other experimental measurements for MM and D_4, an uncertainty of approximately 0.5% can be assumed. For temperatures $T > 437$ K, only one data set published by Lindley and Hershey[25] is available. During their measurements,[25] they applied two different measurement devices. In the temperature range from 322 to 426 K, a Swietoslawski ebulliometer was utilized. They state their temperature measurement to be accurate within 0.1 K and their pressure measurements within 3.4 to 7 kPa. When considering the lower value of 3.4 kPa, the uncertainty of the vapor pressure measurements is already above 3% in the best case. However, except for some outliers, the data scatter around the present equation of state and the data of Flaningam within 0.5%.[26] Therefore, the specified uncertainties seem to be too large and the data were used for the fit.

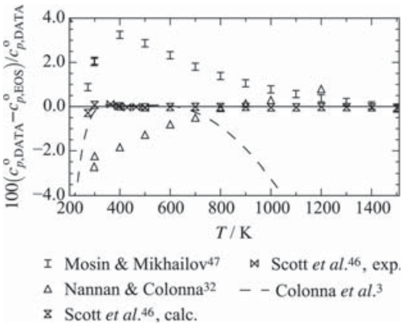

Figure 5. Representation of the isobaric heat capacity data of the ideal gas for MM with the equation of state of Thol et al.[1]

The high temperature range ($T > 426$ K) was investigated by means of a Kay type $p\rho T$ apparatus.[48,49] Since it was originally designed to determine saturated vapor and liquid densities, the accuracy of the vapor pressure measurements is slightly lower than what can be achieved with an ebulliometer. However, these data can be reproduced within the same accuracy as the low temperature data. On the basis of the data of Flaningam[26] and Lindley and Hershey,[25] the accuracy of vapor pressure data calculated with the present equation of state for MDM is estimated to be 0.5%.

For MD_2M, only the two data sets of Flaningam[26] and Abbas et al.[9] containing more than two data points are available. As stated above, the data of Abbas et al.[9] were not considered here. Since the data of Flaningam[26] only cover a restricted temperature range (366 to 480 K), a reliable estimation of the accuracy of vapor pressure data calculated with the present equation of state is not possible. However, the data are reproduced similarly to the data of MDM. Therefore, at least in this temperature range an uncertainty of 0.5% can be assumed.

In Figure 7, relative deviations of density data in homogeneous states from the present equations of state are shown. In addition to the present speed of sound measurements, density data in the liquid state published by Abbas et al.[9] are the most comprehensive and reliable data sets for both siloxanes. Moreover, they are the only density data at elevated pressures. For their measurement, Abbas et al.[9] used an Anton Paar vibrating tube densimeter, which was calibrated with water and heptane. Test measurements agreed with the corresponding equations of state[50,51] within 0.04% and 0.08%. The sample purity is reported to be better than 99.8% with a maximum water content below 100 ppm. Individual uncertainties are not clearly defined in the publication.[9] Only a temperature reproducibility (0.01 K) and an uncertainty value for the density measurement ($0.1\ \mathrm{mg \cdot cm^{-3}}$) are reported. Therefore, the works of Abbas[52] and Schedemann[53] as well as results for MM[1] were considered here for an assessment. On the basis of these results and the sample purity, an uncertainty of 0.1% to 0.15% is assumed for both fluids. Figure 7 shows that the new equations of state reproduce these data within the assumed uncertainty. For MDM, only five data points out of 459 exhibit a deviation above 0.1% (maximum deviation: 0.11%)

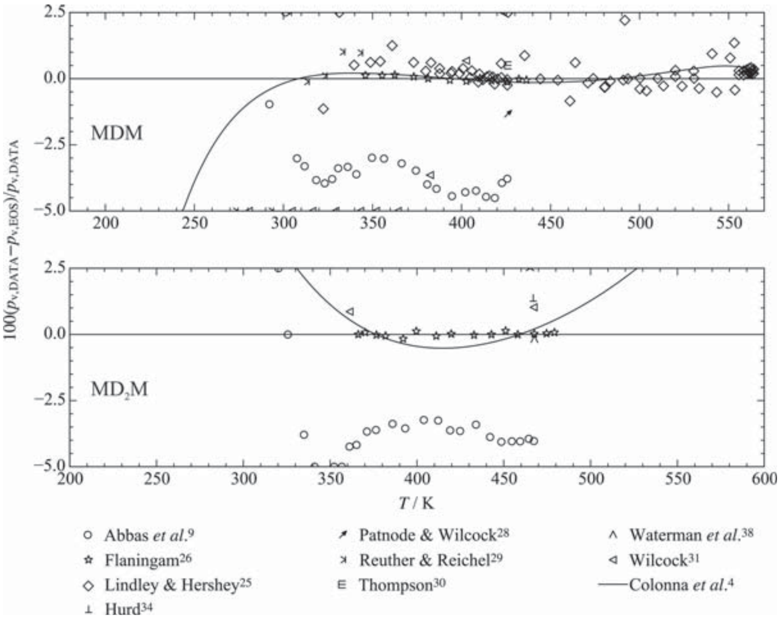

Figure 6. Relative deviations of the vapor pressure data for MDM and MD_2M from the present equations of state.

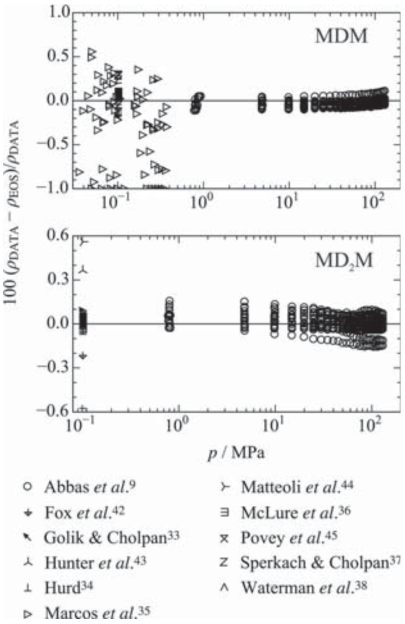

Figure 7. Relative deviations of the homogeneous density data for MDM and MD_2M from the present equations of state.

from the present equation of state. For MD_2M, the highest isotherm (T = 437 K) is represented with deviations between 0.1% and 0.15%. Among the remaining 432 state points, only 23 data points deviate by more than 0.1% (maximum deviation: 0.15%). Therefore, the uncertainty of density of the homogeneous liquid state calculated with the present equations of state is estimated to be within 0.15%.

Moreover, these data are not only important for the correct behavior of the equations of state at elevated pressures. Because of the restricted data situation, they were also applied to adjust the saturated liquid density.

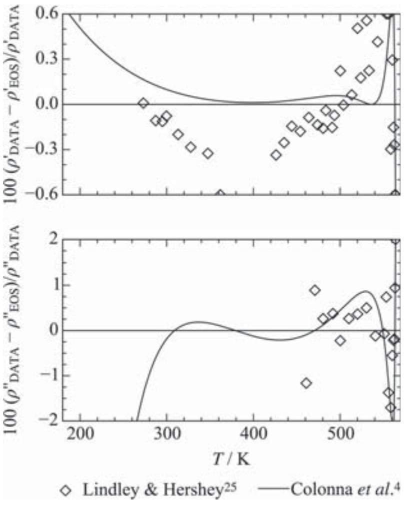

Figure 8. Relative deviations of the saturated liquid (top) and vapor (bottom) density data from the present equation of state for MDM.

In Figure 8, relative deviations of the saturated liquid and vapor density data from the present equation of state for MDM are illustrated. The measurements of Lindley and Hershey[25] are the only data available in the literature and cover a restricted temperature range. Since the homogeneous density data of Abbas et al.[9] are located sufficiently close to the saturated liquid line, the vapor−liquid equilibrium was mainly controlled by these data and the vapor pressure data. To ensure low uncertainties of the saturation densities over the entire temperature range, a linear rectilinear diameter according to $\rho_{RD} = (\rho' + \rho'')/2$ was applied as a constraint to the fit, which ends at the critical point given in Table 8. In this way, not only the saturated liquid but also

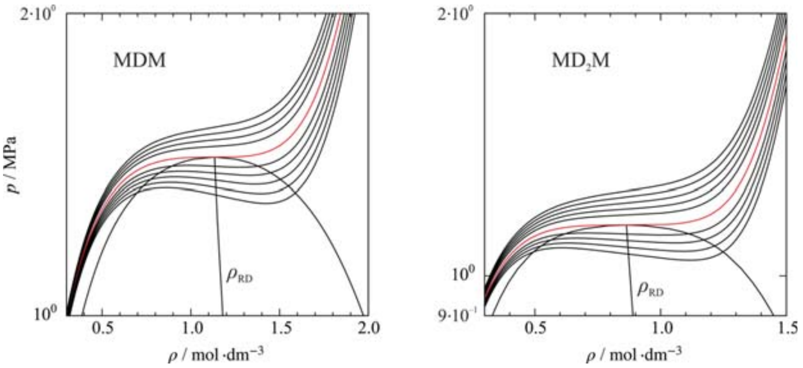

Figure 9. Pressure as a function of density along selected isotherms. The critical isotherm is marked in red. Note that the vertical axis is presented on a logarithmic scale.

the saturated vapor line could be modeled at least qualitatively correctly. In the case of MDM, the saturated densities of Lindley and Hershey[25] were employed to verify this approach, which was already successfully adopted for the development of the equation of state for MM.[1] The information on the uncertainties given in the publication of Lindley and Hershey[25] is not sufficient to estimate a combined uncertainty of their density measurements; thus no statement on the accuracy of the present equation with respect to the saturated densities can be made. However, the saturated liquid density data are reproduced within 0.5%, whereas the saturated vapor density data are represented within 1.5%. Considering the measurement technique and the sample purity of 99%, these deviations are reasonable. For the saturated densities of MD_2M, no experimental data are available in the literature to verify the phase boundaries.

Because of the limited database, a straight rectilinear diameter was applied in the critical region, and the critical point reported in Table 8 was applied to the fit. A correct behavior of the isotherms in this region was controlled by modeling a saddle point of the critical isotherm at the critical point for both fluids (cf. Figure 9)

$$\left(\frac{\partial p}{\partial \rho}\right)_{T_c} = 0 \quad \text{and} \quad \left(\frac{\partial^2 p}{\partial \rho^2}\right)_{T_c} = 0 \tag{13}$$

In this way, the critical temperature and density calculated from the equation of state differ from the values given in Table 8 by less than 0.001%.

Relative deviations of experimental density data at atmospheric pressure from the equation of state are depicted in Figure 10. For MDM, the equation of Colonna et al.[4] agrees better with the course of the data of McLure et al.[36] than the present equation of state, and deviations between both equations increase for decreasing temperature. During the development of the equation in this work, it was not possible to fit to these data more accurately without deteriorating the representation of the homogeneous density data of Abbas et al.[9] For MD_2M, the representation of the data is similar with both equations. The data of McLure et al.[36] and Hurd[34] agree much better with each other than in case of MDM. This might be an indication that the data of MD_2M are more accurate than those for MDM. This assumption is also supported by the representation of the data with the present equations of state. However, for both fluids, deviations do not exceed 0.14%. Moreover, since Abbas et al.[9] measured down to $p_{\min} = 0.77$ MPa, the uncertainty statement of 0.15% is also assumed to be valid for atmospheric pressure.

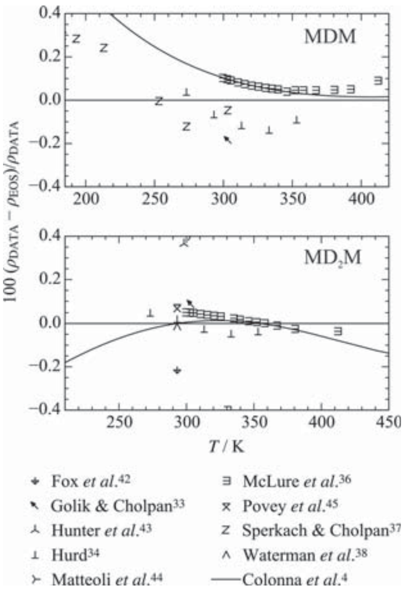

Figure 10. Relative deviations of the homogeneous density data at atmospheric pressure for MDM and MD_2M from the present equations of state.

Finally, there are some density measurements in the homogeneous gas state for MDM available. Figure 7 shows that these data scatter around the present equation of state within approximately 1.5%. The uncertainty of the data was analyzed in detail for MM by Thol et al.[1] and was assessed to be at least 1%. Except for the highest isotherm (T = 573 K), the data are represented within this uncertainty.

Since the data were measured at very low density, it is possible to extrapolate the isotherms down to vanishing pressure to determine the second thermal virial coefficient B. According to the virial expansion, the compressibility factor can be expressed as

$$Z = \frac{p}{\rho RT} = 1 + B\rho + C\rho^2 + \ldots \tag{14}$$

On the basis of this approach, the second thermal virial coefficient can be extrapolated as shown in Figure 11. This figure depicts that the isotherms are self-consistent for $\rho > 0.04$ mol·dm^{-3} only.

DOI: 10.1021/acs.jced.7b00092
J. Chem. Eng. Data 2017, 62, 2633−2648

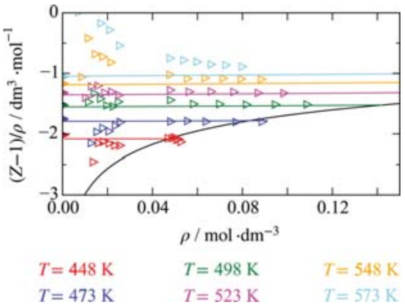

Figure 11. $(Z\text{-}1)/\rho$ as a function of density along six isotherms. Open triangles represent experimental density data of Marcos et al.,[35] solid triangles mark the extrapolated second thermal virial coefficient data of Marcos et al.,[35] and the solid lines depict the present equation of state for MDM.

The low-density data should thus not be considered in such a procedure. Nevertheless, it is not completely clear how the second thermal virial coefficient data of Marcos et al.[35] were determined. Especially for 548 and 573 K, a significant offset persists between the extension of the experimental data and the provided virial coefficients.[35] Despite this discrepancy, the present equation of state matches with the virial coefficient data better than with the density data. Therefore, deviations of up to 1.5% for the low-density data were accepted, whereas the second thermal virial coefficient data are represented within 70 cm^3·mol^{-1} (3%).

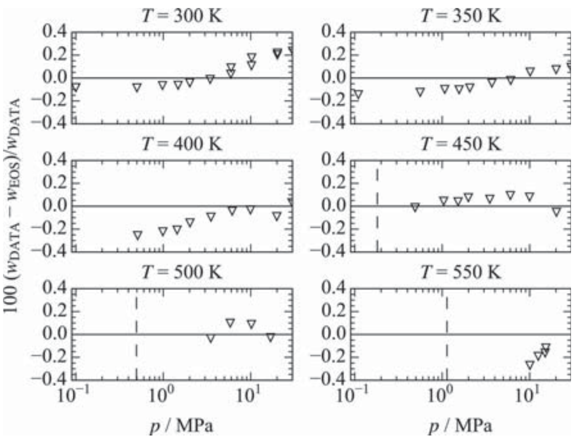

Figure 12. Relative deviations of experimental speed of sound data measured in this work from the present equation of state for MDM.

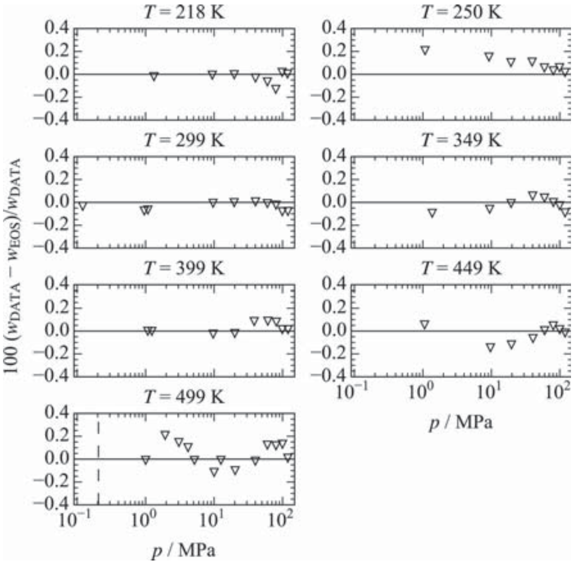

Figure 13. Relative deviations of experimental speed of sound data measured in this work from the present equation of state for MD_2M.

4.3. Caloric Properties.

In Figures 12 and 13, relative deviations of the speed of sound data measured in this work from the present equations of state are shown. In combination with the density data of Abbas et al.,[9] these data formed the basis for the development of the present equations of state. For MDM, a temperature range from 300 to 550 K with a maximum pressure of p = 30 MPa was covered. The data are reproduced within 0.3%, which is well within the uncertainty of the data. The equation of Colonna et al.[4] deviates by more than 15% because no density or speed of sound data at elevated pressures were available when that equation was developed. Only three data points of Waterman et al.[38] and Weissler[39] at atmospheric pressure were available. However, they were still missed by about 10% because they were not included in the fitting procedure.[4] With the present equation of state they are reproduced within 3%, whereby the two data points of Weissler[39] agree well with the data measured in this work. Moreover, they are supported by the data point of Golik and Cholpan.[33] Measurements of Sperkach and Cholpan[37] show positive deviations up to 3%, whereas the data point of Waterman et al.[38] deviates by −2.6%. For both data sets, no information on the uncertainty is available so that the main focus was given to the correct description of the data measured in this work.

As explained in section 2, another pressure sensor enabled the measurement of data at higher pressures for the measurements of MD_2M. Here, a temperature range of 218 to 500 K with a maximum pressure of $p_{\max}$ = 120 MPa was considered. These data are represented within 0.2%. Considering the accuracy of the apparatus and the sample purity, this is most likely within the measurement uncertainties. For the same reason as in the case of MDM, the equation of Colonna et al.[4] again exhibits large deviations of up to 16%. The available data of Waterman et al.[38] and Weissler[39] were not considered by Colonna et al.[4] so that deviations of up to 14.5% can be observed. These deviations were reduced to approximately 0.5% in the present work.

Figure 14 shows isobaric heat capacity data along the saturated liquid line for both fluids. The experimental uncertainties of the data of Abbas et al.[9] are 1% according to the authors. Therefore, deviations of 0.6% with respect to the present equations of state are well within these uncertainties. The equations of Colonna et al.[4] deviate by up to 5%. The main reason can be attributed to the inappropriate description of the ideal gas contribution and the speed of sound. A better description of both properties entailed a much better characterization of the isobaric heat capacity.

5. PHYSICAL AND EXTRAPOLATION BEHAVIOR

The correct description of the physical and extrapolation behavior is a crucial task during the development of equations of state. Many applications require the knowledge of thermodynamic properties not only outside the range of validity

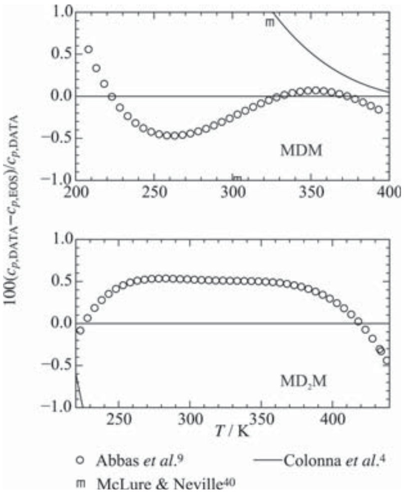

Figure 14. Relative deviations of experimental isobaric heat capacity data of MDM and $\mathrm{MD_2M}$ from the present equations of state. Deviations from the equation of Colonna et al.[4] are out of range for almost all calculated states for $\mathrm{MD_2M}$.

(e.g., in mixture models) but also of thermodynamic properties that were not investigated experimentally. Since all thermodynamic properties can be calculated from combinations of the Helmholtz energy and its derivatives with respect to the natural variables, it is possible to predict properties at least qualitatively. Therefore, appropriate behavior was a major aspect in this work. The equation was carefully analyzed by means of characteristic properties, which are well-known to be an indication for good extrapolation behavior. Detailed information can be found in the literature.[20,22,54,55] This includes the isobaric and isochoric heat capacity, speed of sound, phase identification parameter,[56] Grüneisen parameter,[57] characteristic ideal curves,[54] thermal virial coefficients, thermal behavior ($p\rho T$) at extreme conditions, etc. All of these properties exhibit reasonable behavior, which is representatively shown for the speed of sound and the characteristic ideal curves in Figure 15.

6. BETHE−ZEL'DOVICH−THOMPSON FLUIDS

Because of their special characteristics, siloxanes are considered as working fluids for ORC processes. In this context, the possible affiliation of siloxanes to the class of so-called Bethe−Zel'dovich−Thompson (BZT) fluids is discussed in the literature.[10] This phenomenon is based on theoretical observations of Bethe[58] and Zel'dovich[59] in the 1940s and was applied to ORC working fluids by Thompson[60] in 1971. In ORC processes, turbines are often operated at transonic conditions. This causes huge losses due to distinct pressure gradients evoked by compression waves and the available energy cannot fully be exploited.[61] The basic idea of BZT fluids is that these losses can be reduced with the use of working fluids with unusual behavior in the gaseous regime near the critical point. Numerous studies were conducted to identify such fluids in the literature.[61−64]

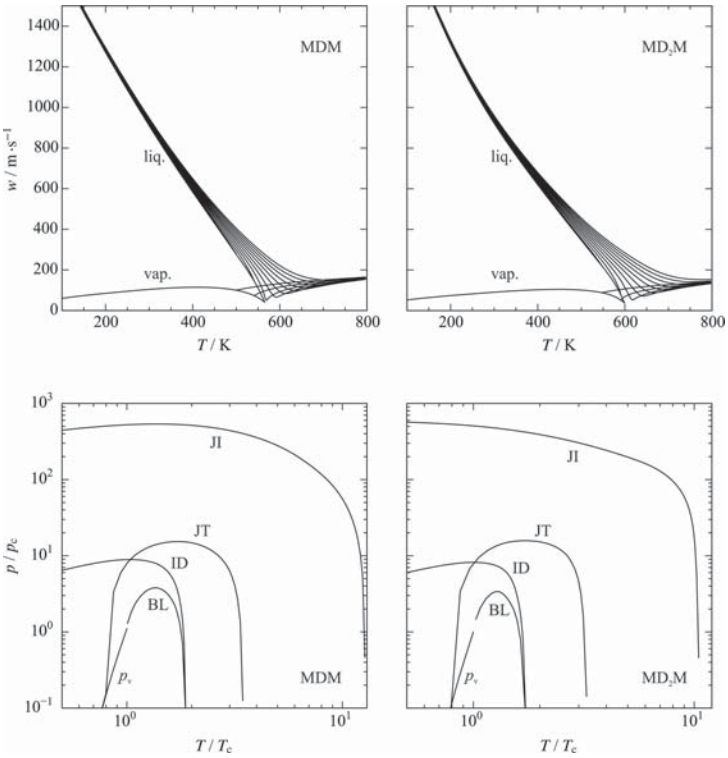

Figure 15. Speed of sound as a function of temperature (top) and characteristic ideal curves[54] (bottom) of MDM and $\mathrm{MD_2M}$. ID: ideal curve; BL: Boyle curve; JT: Joule−Thomson inversion curve; JI: Joule inversion curve.

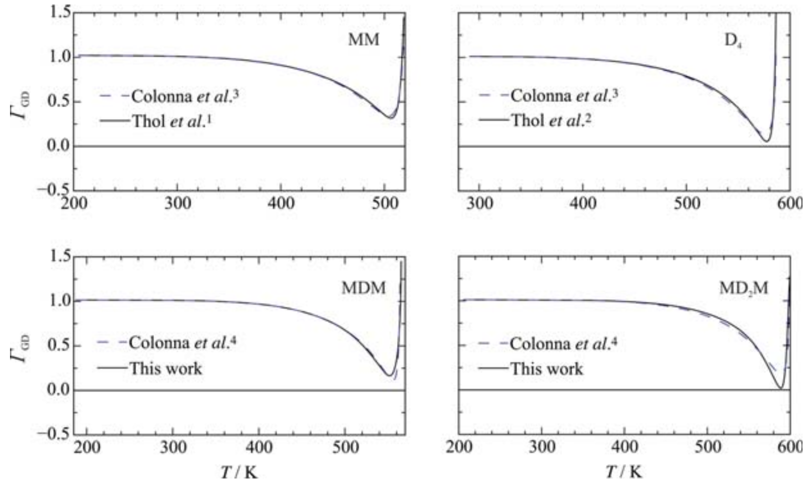

Figure 16. Fundamental derivative of gas dynamics as a function of temperature along the saturated vapor line for MM, MDM, D_4, and MD_2M.

The decisive criterion for the unusual behavior is the fundamental derivative of gas dynamics introduced by Hayes[65]

$$\Gamma_{GD} = 1 + \frac{\rho}{w}\left(\frac{\partial w}{\partial \rho}\right)_s = \frac{v^3}{2w^2M}\left(\frac{\partial^2 p}{\partial v^2}\right)_s \tag{15}$$

If a fluid exhibits a negative fundamental derivative of gas dynamics along the saturated vapor line, it is considered to be a BZT fluid, which is desired for a particularly effective operation of ORC processes.

On the basis of their equations of state, Colonna et al.[10] suggested siloxanes as possible BZT fluid candidates. However, eq 15 shows that this property is highly dependent on the correct description of density and speed of sound. As shown by Thol et al.,[1,2] Colonna et al.,[3,4] and in this work, the experimental databases were very limited when Colonna et al.[3,4] developed their equations of state. With the recent accurate and comprehensive density and speed of sound measurements, the description of these properties by means of the recent equations of state is much more reliable. Thus, the question whether the siloxanes may be BZT fluids is reinvestigated here. Figure 16 shows that the first three linear siloxanes (MM, MDM, MD_2M) and the first cyclic siloxane (D_4) do *not* exhibit a negative fundamental derivative of gas dynamics. The equations of Colonna et al.[3,4] already showed this behavior, which is confirmed by the equations presented in Thol et al.[1,2] and in this work. In Figure 17, the same property is depicted for four siloxanes of higher order (MD_3M, MD_4M, D_5, and D_6). Except for D_5, according to the equations of Colonna et al.,[3,4] all of them *do* show a negative fundamental derivative of gas dynamics, which may lead to the conclusion that those are BZT fluids. However, the underlying equations of state are based on such a weak experimental database that new measurements and equations of state are required for a reliable statement. This task is planned for future work.

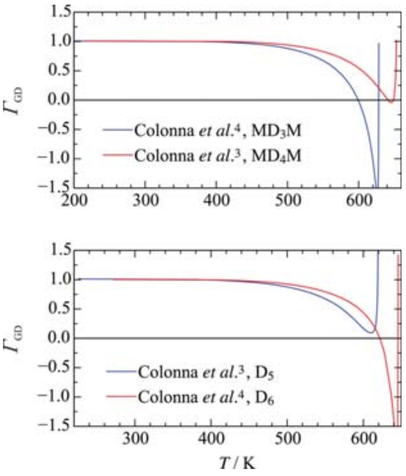

Figure 17. Fundamental derivative of gas dynamics as a function of temperature along the saturated vapor line for MD_3M, MD_4M, D_5, and D_6.

7. CONCLUSION

Equations of state for octamethyltrisiloxane and decamethyltetrasiloxane are presented. Because the experimental database was rather limited, speed of sound measurements were carried out in the compressed liquid as well as in the supercritical region by means of the pulse-echo technique.

The equations are expressed in terms of the Helmholtz energy and can be used to calculate all thermodynamic properties. For both fluids, the ideal contribution contains three Planck−Einstein terms, whereas the residual contribution comprises five polynomial, five exponential, and five Gaussian bell-shaped terms. They are valid from the triple point temperature up to a maximum temperature of $T_{\mathrm{max,MDM}}$ = 570 K and $T_{\mathrm{max,MD2M}}$ = 600 K with a maximum pressure of p_{max} = 130 MPa. On the basis of recent density and speed of sound measurements, the representation of these properties could significantly be improved when compared to the equations of Colonna et al.[4] The uncertainty of density data calculated with the new equations of state is expected to be 0.15%. The speed of sound can be reproduced with an uncertainty of 0.3% (MDM) and 0.2% (MD_2M). Calculated vapor pressure data are expected to be accurate to within 0.5%.

Reference values to verify computer implementation are given in the Appendix. Furthermore, parameter files for the application

Table 13. Test Values for Computer Implementation

T	ρ	p	c_p	w	h	s	a
K	$mol \cdot dm^{-3}$	MPa	$J \cdot mol^{-1} \cdot K^{-1}$	$m \cdot s^{-1}$	$J \cdot mol^{-1}$	$J \cdot mol^{-1} \cdot K^{-1}$	$J \cdot mol^{-1}$
				MDM			
320	0.0001	2.659237×10^{-4}	$3.434178 \times 10^{+2}$	$1.073143 \times 10^{+2}$	$-2.908074 \times 10^{+3}$	$2.842609 \times 10^{+1}$	$-1.466366 \times 10^{+4}$
320	3.5	$2.548165 \times 10^{+1}$	$4.276187 \times 10^{+2}$	$1.025009 \times 10^{+3}$	$-4.446580 \times 10^{+4}$	$-1.407280 \times 10^{+2}$	$-6.713301 \times 10^{+3}$
500	0.05	1.919677×10^{-1}	$4.641575 \times 10^{+2}$	$1.237605 \times 10^{+2}$	$6.824950 \times 10^{+4}$	$1.494223 \times 10^{+2}$	$-1.030103 \times 10^{+4}$
500	3	$3.498485 \times 10^{+1}$	$5.164433 \times 10^{+2}$	$7.526067 \times 10^{+2}$	$4.256670 \times 10^{+4}$	$6.633294 \times 10^{+1}$	$-2.261391 \times 10^{+3}$
575	2	$3.511622 \times 10^{+0}$	$5.972631 \times 10^{+2}$	$2.044220 \times 10^{+2}$	$8.116803 \times 10^{+4}$	$1.600291 \times 10^{+2}$	$-1.260453 \times 10^{+4}$
				MD_2M			
350	0.0001	2.908572×10^{-4}	$4.676281 \times 10^{+2}$	$9.760521 \times 10^{+1}$	$-1.931507 \times 10^{+4}$	$-1.227574 \times 10^{+1}$	$-1.792715 \times 10^{+4}$
350	2.9	$9.764338 \times 10^{+1}$	$5.681542 \times 10^{+2}$	$1.295433 \times 10^{+3}$	$-4.764493 \times 10^{+4}$	$-2.080510 \times 10^{+2}$	$-8.497211 \times 10^{+3}$
500	0.05	1.848863×10^{-1}	$5.872108 \times 10^{+2}$	$1.034085 \times 10^{+2}$	$5.810375 \times 10^{+4}$	$1.184514 \times 10^{+2}$	$-4.819665 \times 10^{+3}$
500	2.7	$1.157619 \times 10^{+2}$	$6.494756 \times 10^{+2}$	$1.168896 \times 10^{+3}$	$4.895828 \times 10^{+4}$	$5.385695 \times 10^{+0}$	$3.390654 \times 10^{+3}$
590	2.5	$8.978835 \times 10^{+1}$	$6.856283 \times 10^{+2}$	$9.877431 \times 10^{+2}$	$1.019224 \times 10^{+5}$	$1.210574 \times 10^{+2}$	$-5.416819 \times 10^{+3}$

in the software packages TREND[66] and REFPROP[67] are provided in the Supporting Information.

Since siloxanes are considered for the application in ORC processes, the affiliation of these fluids to the so-called Bethe–Zel'dovich–Thompson (BZT) class was analyzed. The results show that MM, MDM, MD_2M, and D_4 exhibit a positive fundamental derivative of gas dynamics along the entire saturated vapor line. Therefore, they are not categorized as BZT fluids.

■ APPENDIX

Reference values to verify computer implementation are shown in Table 13.

■ ASSOCIATED CONTENT

Ⓢ Supporting Information

The Supporting Information is available free of charge on the ACS Publications website at DOI: 10.1021/acs.jced.7b00092.

Parameters of the equations for MDM. (For the use in TREND or REFPROP, rename the file MDM.FLD) (TXT)

Parameters of the equations for MD_2M (For the use in TREND or REFPROP, rename the file MD2M.FLD) (TXT)

■ AUTHOR INFORMATION

Corresponding Author

*E-mail: m.thol@thermo.rub.de. Fax: +49 234 32 14163.

ORCID

Monika Thol: 0000-0002-3250-0515

Jadran Vrabec: 0000-0002-7947-4051

Notes

The authors declare no competing financial interest.

■ ACKNOWLEDGMENTS

We thank M. Körber and G. T. Toris for their assistance during the development of the equations of state.

■ REFERENCES

(1) Thol, M.; Dubberke, F. H.; Rutkai, G.; Windmann, T.; Köster, A.; Span, R.; Vrabec, J. Fundamental Equation of State Correlation for Hexamethyldisiloxane Based on Experimental and Molecular Simulation Data. *Fluid Phase Equilib.* **2016**, *418*, 133−151.

(2) Thol, M.; Rutkai, G.; Köster, A.; Dubberke, F. H.; Windmann, T.; Span, R.; Vrabec, J. Thermodynamic Properties for Octamethylcyclotetrasiloxane. *J. Chem. Eng. Data* **2016**, *61*, 2580−2595.

(3) Colonna, P.; Nannan, N. R.; Guardone, A.; Lemmon, E. W. Multiparameter Equations of State for Selected Siloxanes. *Fluid Phase Equilib.* **2006**, *244*, 193−211.

(4) Colonna, P.; Nannan, N. R.; Guardone, A. Multiparameter Equations of State for Siloxanes: $[(CH_3)_3\text{-Si-}O_{1/2}]_2\text{-}[O\text{-Si-}(CH_3)_2]_{i=1,...,3}$, and $[O\text{-Si-}(CH3)_2]_6$. *Fluid Phase Equilib.* **2008**, *263*, 115−130.

(5) Preißinger, M.; Brüggemann, D. Thermal Stability of Hexamethyldisiloxane (MM) for High-Temperature Organic Rankine Cycle (ORC). *Energies* **2016**, *9*, 183.

(6) Nannan, N. R.; Colonna, P.; Tracy, C. M.; Rowley, R. L.; Hurly, J. J. Ideal-Gas Heat Capacities of Dimethylsiloxanes from Speed-of-Sound Measurements and ab initio Calculations. *Fluid Phase Equilib.* **2007**, *257*, 102−113.

(7) Span, R.; Wagner, W. Equations of State for Technical Applications. I. Simultaneously Optimized Functional Forms for Nonpolar and Polar Fluids. *Int. J. Thermophys.* **2003**, *24*, 1−39.

(8) Span, R.; Wagner, W. Equations of State for Technical Applications. II. Results for Nonpolar Fluids. *Int. J. Thermophys.* **2003**, *24*, 41−109.

(9) Abbas, R.; Schedemann, A.; Ihmels, C. E.; Enders, S.; Gmehling, J. Measurement of Thermophysical Pure Component Properties for a Few Siloxanes Used as Working Fluids for Organic Rankine Cycles. *Ind. Eng. Chem. Res.* **2011**, *50*, 9748−9757.

(10) Colonna, P.; Guardone, A.; Nannan, N. R. Siloxanes: A New Class of Candidate Bethe-Zel'dovich-Thompson Fluids. *Phys. Fluids* **2007**, *19*, 086102.

(11) Dubberke, F. H.; Rasche, D. B.; Baumhögger, E.; Vrabec, J. Apparatus for the Measurement of the Speed of Sound of Ammonia up to High Temperatures and Pressures. *Rev. Sci. Instrum.* **2014**, *85*, 084901.

(12) Meier, K., The Pulse-echo Method for High Precision Measurements of the Speed of Sound in Fluids. Habilitation thesis, University of the Federal Armed Forces, Hamburg (Germany), 2006.

(13) Ball, S. J.; Trusler, J. P. M. Speed of Sound of n-Hexane and n-Hexadecane at Temperatures between 298 and 373 K and Pressures up to 100 MPa. *Int. J. Thermophys.* **2001**, *22*, 427−443.

(14) Benedetto, G.; Gavioso, R. M.; Albo, P. A. G.; Lago, S.; Ripa, D. M.; Spagnolo, R. A Microwave−Ultrasonic Cell for Sound-Speed Measurements in Liquids. *Int. J. Thermophys.* **2005**, *26*, 1651−1665.

(15) Dubberke, F. H.; Baumhögger, E.; Vrabec, J. Burst Design and Signal Processing for the Speed of Sound Measurement of Fluids with the Pulse-echo Technique. *Rev. Sci. Instrum.* **2015**, *86*, 054903.

(16) Mohr, P. J.; Newell, D. B.; Taylor, B. N. CODATA Recommended Values of the Fundamental Physical Constants: 2014. *J. Phys. Chem. Ref. Data* **2016**, *45*, 043102.

(17) Span, R. *Multiparameter Equations of State: An Accurate Source of Thermodynamic Property Data*; Springer: Berlin, 2000.

(18) Setzmann, U.; Wagner, W. A New Equation of State and Tables of Thermodynamic Properties for Methane Covering the Range from the

Melting Line to 625 K at Pressures up to 100 MPa. *J. Phys. Chem. Ref. Data* **1991**, *20*, 1061−1155.

(19) Lemmon, Eric W. *Numerical Fitting Algorithm for the Development of Equations of State*. personal communication, 2016.

(20) Lemmon, E. W.; Jacobsen, R. T. A New Functional Form and New Fitting Techniques for Equations of State with Application to Pentafluoroethane (HFC-125). *J. Phys. Chem. Ref. Data* **2005**, *34*, 69−108.

(21) Herrig, S.; Thol, M.; Span, R. *A Fundamental Equation of State for Chlorine*. Unpublished.

(22) Lemmon, E. W.; McLinden, M. O.; Wagner, W. Thermodynamic Properties of Propane. III. A Reference Equation of State for Temperatures from the Melting Line to 650 K and Pressures up to 1000 MPa. *J. Chem. Eng. Data* **2009**, *54*, 3141−3180.

(23) Rowley, R. L.; Wilding, W. V.; Oscarson, J.; Yang, Y.; Zuendel, N.; Daubert, T.; Danner, R. *DIPPR Data Compilation of Pure Chemical Properties*; Taylor & Francis Publishing Company: New York, 2004.

(24) Dickinson, E.; McLure, I. A. Thermodynamics of n-Alkane + Dimethylsiloxane Mixtures: Part 1.-Gas-Liquid Critical Temperatures and Pressures. *J. Chem. Soc., Faraday Trans. 1* **1974**, *70*, 2313−2320.

(25) Lindley, D. D.; Hershey, H. C. The Orthobaric Region of Octamethyltrisiloxane. *Fluid Phase Equilib.* **1990**, *55*, 109−124.

(26) Flaningam, O. L. Vapor Pressures of Poly(dimethylsiloxane) Oligomers. *J. Chem. Eng. Data* **1986**, *31*, 266−272.

(27) Wieser, M. E.; Berglund, M. Atomic Weights of the Elements 2007 (IUPAC Technical Report). *Pure Appl. Chem.* **2009**, *81*, 2131−2156.

(28) Patnode, W.; Wilcock, D. F. Methylpolysiloxanes. *J. Am. Chem. Soc.* **1946**, *68*, 358−363.

(29) Reuther, H.; Reichel, G. Über Silikone XXVI: Über den Dampfdruck und die Verdampfungswärme einiger definierter siliziumorganischer Verbindungen. *Chem. Technol.* **1954**, *6*, 479−480.

(30) Thompson, R. 392. Heats of Combustion and Formation of Some Linear Polydimethylsiloxanes; the Si−C and Si−O Bond-Energy Terms. *J. Chem. Soc.* **1953**, *0*, 1908−1914.

(31) Wilcock, D. F. Vapor Pressure-Viscosity Relations in Methylpolysiloxanes. *J. Am. Chem. Soc.* **1946**, *68*, 691−696.

(32) Nannan, N. R.; Colonna, P. Improvement on Multiparameter Equations of State for Dimethylsiloxanes by Adopting More Accurate Ideal-Gas Isobaric Heat Capacities: Supplementary to P. Colonna, N.R. Nannan, A. Guardone, E.W. Lemmon, Fluid Phase Equilib. 244, 193 (2006). *Fluid Phase Equilib.* **2009**, *280*, 151−152.

(33) Golik, O. Z.; Cholpan, P. P. Molecular Structure, Compressibility, Surface Tension and Viscosity of Some Polysiloxanes. *Ukr. Fiz. Zh.* **1960**, *5*, 242−251.

(34) Hurd, C. B. Studies on Siloxanes: I. The Specific Volume and Viscosity in Relation to Temperature and Constitution. *J. Am. Chem. Soc.* **1946**, *68*, 364−370.

(35) Marcos, D. H.; Lindley, D. D.; Wilson, K. S.; Kay, W. B.; Hershey, H. C. A (p, V, T) Study of Tetramethylsilane, Hexamethyldisiloxane, Octamethyltrisiloxane, and Toluene from 423 to 573 K in the Vapor Phase. *J. Chem. Thermodyn.* **1983**, *15*, 1003−1014.

(36) McLure, I. A.; Pretty, A. J.; Sadler, P. A. Specific Volumes, Thermal Pressure Coefficients, and Derived Quantities of Five Dimethylsiloxane Oligomers from 25 to 140 °C. *J. Chem. Eng. Data* **1977**, *22*, 372−376.

(37) Sperkach, V.; Choplan, F. Study of Acoustic Scattering in Some Siloxanes. *Fiz. Zhidk. Sostoyaniya* **1979**, 104−109.

(38) Waterman, H. I.; van Herwijnen, W. E. R.; Den Hartog, H. W. Statistical-Graphical Survey of Series of Linear and Cyclic Dimethylsiloxanes. *J. Appl. Chem.* **1958**, *8*, 625−631.

(39) Weissler, A. Ultrasonic Investigation of Molecular Properties of Liquids. III. 1 Linear Polymethylsiloxanes 2. *J. Am. Chem. Soc.* **1949**, *71*, 93−95.

(40) McLure, I. A.; Neville, J. F. An Analysis of the Gas-Liquid Critical Properties of the Dimethylsiloxanes Establishing Tetramethylsilane as the Forerunner of the Series. *J. Chem. Thermodyn.* **1977**, *9*, 957−961.

(41) Wabiszczewicz, M., Vermessung und Auswertung der Verdampfungsenthalpie der Siloxane Decamethylcyclopentasiloxan (D5), Octamethyltrisiloxan (MDM) und Hexamethyldisiloxan (MM) unter Verwendung eines Differenzkalorimeters (Measurement and evaluation of the vaporization enthalpy of the siloxanes decamethylcyclopentasiloxane (D5), octamethyltrisiloxane (MDM) and hexamethyldisiloxane (MM) using a differential calorimeter). Bachelor Thesis, Universität Paderborn, Paderborn, 2014.

(42) Fox, H.; Taylor, P.; Zisman, W. Polyorganosiloxanes⋯: Surface Active Properties. *Ind. Eng. Chem.* **1947**, *39*, 1401−1409.

(43) Hunter, M. J.; Warrick, E. L.; Hyde, J. F.; Currie, C. C. Organosilicon Polymers: II. The Open Chain Dimethylsiloxanes with Trimethylsiloxy End Groups. *J. Am. Chem. Soc.* **1946**, *68*, 2284−2290.

(44) Matteoli, E.; Gianni, P.; Lepori, L.; Spanedda, A. Thermodynamic Study of Heptane + Silicone Mixtures. Excess Volumes and Enthalpies at 298.15 K. *J. Chem. Eng. Data* **2011**, *56*, 5019−5027.

(45) Povey, M. J. W.; Hindle, S. A.; Kennedy, J. D.; Stec, Z.; Taylor, R. G. The Molecular Basis for Sound Velocity in n-Alkanes, 1-Alcohols and Dimethylsiloxanes. *Phys. Chem. Chem. Phys.* **2003**, *5*, 73−78.

(46) Scott, D. W.; Messerly, J. F.; Todd, S. S.; Guthrie, G. B.; Hossenlopp, I. A.; Moore, R. T.; Osborn, A.; Berg, W. T.; McCullough, J. P. Hexamethyldisiloxane: Chemical Thermodynamic Properties and Internal Rotation about the Siloxane Linkage. *J. Phys. Chem.* **1961**, *65*, 1320−1326.

(47) Mosin, A. M.; Mikhailov, A. M. Thermodynamic Functions of Hexamethyldisiloxane. *Zh. Fiz. Khim.* **1972**, *46*, 537.

(48) Kay, W. B. The Vapor Pressures and Saturated Liquid and Vapor Densities of the Isomeric Hexane. *J. Am. Chem. Soc.* **1946**, *68*, 1336−1339.

(49) Kay, W. B.; Donham, W. E. Liquid-Vapor Equilibria in the Iso-Butanol-n-Butanol, Methanol-n-Butanol and Diethylether-n-Butanol Systems. *Chem. Eng. Sci.* **1955**, *4*, 1−16.

(50) Wagner, W.; Pruss, A. The IAPWS Formulation 1995 for the Thermodynamic Properties of Ordinary Water Substance for General and Scientific Use. *J. Phys. Chem. Ref. Data* **2002**, *31*, 387−535.

(51) Lemmon, E. W.; Span, R. Short Fundamental Equations of State for 20 Industrial Fluids. *J. Chem. Eng. Data* **2006**, *51*, 785−850.

(52) Abbas, R., Anwendung der Gruppenbeitragszustandsgleichung VTPR für die Analyse von reinen Stoffen und Mischungen als Arbeitsmittel in technischen Kreisprozessen (Application of the group contribution state equation VTPR for the analysis of pure substances and mixtures working in technical circles). Ph.D. Thesis, Technische Universität Berlin, Berlin, 2011.

(53) Schedemann, A., Aufbau und Inbetriebnahme einer Dichtemessanlage. Messung und Modellierung des PVT-Verhaltens bis zu Drücken von 1400 bar (Construction and commissioning of a sealing system. Measurement and modeling of PVT behavior up to pressures of 1400 bar). Diploma thesis, Universität Oldenburg, Oldenburg, 2009.

(54) Span, R.; Wagner, W. On the Extrapolation Behavior of Empirical Equations of State. *Int. J. Thermophys.* **1997**, *18*, 1415−1443.

(55) Thol, M.; Rutkai, G.; Köster, A.; Span, R.; Vrabec, J.; Lustig, R. Equation of State for the Lennard-Jones Fluid. *J. Phys. Chem. Ref. Data* **2016**, *45*, 023101.

(56) Venkatarathnam, G.; Oellrich, L. R. Identification of the Phase of a Fluid Using Partial Derivatives of Pressure, Volume, and Temperature without Reference to Saturation Properties: Applications in Phase Equilibria Calculations. *Fluid Phase Equilib.* **2011**, *301*, 225−233.

(57) Arp, V.; Persichetti, J. M.; Chen, G.-b. The Grüneisen Parameter in Fluids. *J. Fluids Eng.* **1984**, *106*, 193−201.

(58) Bethe, H. A., On the Theory of Shock Waves for an Arbitrary Equation of State. In *Classic Papers in Shock Compression Science*; Johnson, J. N., Chéret, R., Eds.; High-Pressure Shock Compression of Condensed Matter; Springer: New York, NY, 1998; pp 421−495.

(59) Zel'dovich, Y. B. *Theory of Shock Waves and Introduction to Gas Dynamics*; Izdatel'stvo Akademii Nauk SSSR: Moscow, 1946.

(60) Thompson, P. A. A Fundamental Derivative in Gasdynamics. *Phys. Fluids* **1971**, *14*, 1843−1849.

(61) Brown, B. P.; Argrow, B. M. Application of Bethe-Zel'dovich-Thompson Fluids in Organic Rankine Cycle Engines. *J. Propul. Power* **2000**, *16*, 1118−1124.

(62) Schnerr, G. H.; Leidner, P. Diabatic Supersonic Flows of Dense Gases. *Phys. Fluids A* **1991**, *3*, 2445−2458.
(63) Cramer, M. S., Nonclassical Dynamics of Classical Gases. In *Nonlinear Waves in Real Fluids*; Kluwick, A., Ed.; Springer: Vienna, 1991.
(64) Fergason, S.; Guardone, A.; Argrow, B. Construction and Validation of a Dense Gas Shock Tube. *J. Thermophys. Heat Transfer* **2003**, *17*, 326−333.
(65) Hayes, W. D., The Basic Theory of Gasdynamic Discontinuities. In *Fundamentals of Gas Dynamics. High Speed Aerodynamics and Jet Propulsion*, 1st ed.; Emmons, H. W., Ed.; Princeton University Press: Princeton, 1958; Vol. *III*.
(66) Span, R.; Eckermann, T.; Herrig, S.; Hielscher, S.; Jäger, A.; Thol, M. *TREND. Thermodynamic Reference and Engineering Data 3.0*; Lehrstuhl für Thermodynamik, Ruhr-Universität Bochum: Bochum, Germany, 2016.
(67) Lemmon, E. W.; Bell, I. H.; Huber, M. L.; McLinden, M. O. *NIST Standard Reference Database 23: Reference Fluid Thermodynamic and Transport Properties-REFPROP, Version 9.1.1*; National Institute of Standards and Technology: Gaithersburg, USA, 2014.

4.7 Experimental setup of a cascaded two-stage organic Rankine cycle

Frithjof H. Dubberke, Matthias Linnemann, Wameedh Khider Abbas, Elmar Baumhögger, Klaus-Peter Priebe, Maximilian Roedder, Matthias Neef, and Jadran Vrabec, Appl. Therm. Eng., 131, (2018), 958-964; DOI: 10.1016/j.applthermaleng.2017.11.137

The scientific work and discussion was coordinated and consolidated by Frithjof H. Dubberke under supervision of Jadran Vrabec.
The manuscript was prepared by Frithjof H. Dubberke.
Layout and design of cycle was done by Klaus-Peter Priebe and Frithjof H. Dubberke.
Layout and design of expansion device was done by Klaus-Peter Priebe, André Heim and the set up was supported by Stefan Rode.
Construction and set up was coordinated by Frithjof H. Dubberke and supported by Rüdiger Pflock, Alex Reimann and Norbert Temborius. Electrical design and wiring was carried out by Martin Mader, Steffen Greve and Elmar Baumhögger.
Measurements and data evaluation were performed by Frithjof H. Dubberke, Wameedh Abbas and Matthias Linnemann.
The manuscript was revised by Jadran Vrabec.

This publication is in context of several bachelor and master thesis under supervision of Frithjof H. Dubberke at the chair of Thermodynamics and Energy Technology headed by Prof. Dr.-Ing. habil. Jadran Vrabec.

Applied Thermal Engineering 131 (2018) 958–964

Contents lists available at ScienceDirect

Applied Thermal Engineering

journal homepage: www.elsevier.com/locate/apthermeng

Research Paper

Experimental setup of a cascaded two-stage organic Rankine cycle

Frithjof H. Dubberke [a], Matthias Linnemann [a], Wameedh Khider Abbas [a], Elmar Baumhögger [a], Klaus-Peter Priebe [a], Maximilian Roedder [b], Matthias Neef [b], Jadran Vrabec [a,*]

[a] *Thermodynamik und Energietechnik, Universität Paderborn, Warburger Straße 100, 33098 Paderborn, Germany*
[b] *Zentrum für innovative Energiesysteme, Hochschule Düsseldorf, Münsterstraße 156, 40476 Düsseldorf, Germany*

ARTICLE INFO

Article history:
Received 22 August 2017
Revised 24 October 2017
Accepted 27 November 2017
Available online 27 November 2017

Keywords:
Organic Rankine cycle
Cascade
Multicomponent working fluid
Temperature-glide
Pinch point
Exergetic efficiency

ABSTRACT

In combination with a bottoming cycle, operated with a pure fluid in transcritical mode, the usage of a zeotropic mixture as a working fluid appears to be exergetically favorable for power cycle efficiency in cascaded two-stage organic Rankine cycles (CORC). A CORC is set up and initially tested with cyclopentane and propane as working fluids in its high temperature and low temperature cycle, respectively. A thermal oil cycle serves as the heat source and is powered electrically with a maximum heat flow of 158 kW. The design of this experimental setup allows for a rapid replacement of individual components and for a wide range of conditions in terms of fluids and thermodynamic states. The components of all cycles and the measurement and control technology are described in detail. A testing procedure is presented, followed by a discussion of the measurement results, where it is shown that the intended concept of two cascaded organic Rankine cycles is operational and that the measured data are consistent.

1. Introduction

Many types of organic Rankine cycles (ORC) for the recovery of waste heat have been described in the literature [1–5]. Different cycle layouts and components, combined with a variety of organic working fluids, lead to a wide range of power cycle efficiency values mainly due to the characteristics of the heat source. Lampe et al. [6] proposed a design tool to maximize process performance by optimizing both process parameters and varying the working fluid. Taking the economic situation of an individual project into account, cycle construction can be realized in a sophisticated way to reach higher power efficiency [7].

To maximize performance of ORC processes, the usage of mixtures as working fluids appears to be beneficial due to an exergetically favorable heat transfer caused by the temperature glide during evaporation [8,9]. Having a more constant temperature difference ΔT while transferring heat from the heat source due to the temperature glide of zeotropic mixtures may minimize exergetic losses [10]. On the other hand, the temperature glide is exergetically unfavorable during condensation and may neutralize the exergetic advantage during evaporation. Therefore, a second low temperature (LT) cycle was coupled in this work as a cascade to utilize the residual exergy that is discharged by the condenser of the high temperature (HT) cycle [11–13]. Thus, a cascaded two-staged ORC, where the HT cycle is operated with a zeotropic mixture and the LT cycle is operated with a pure fluid in transcritical mode [14], may facilitate both heat uptake from the source as well as heat discharge to the environment in a favorable way.

As a test rig for two-stage cycle innovations, an electrically heated cascaded ORC (CORC) was designed and commissioned in Paderborn. To achieve a high efficiency, the design strongly depends on the temperature level of the heat source. The integration of four electrical heating rods as a primary heat source for the HT cycle enabled for the specification of different temperature levels and the LT cycle was supplied with the residual thermal energy discharged by the HT cycle. After successful commissioning of the two-stage CORC, experimental results were used to evaluate component and cycle performance in comparison to the intended design. Fig. 1 (left) shows the non-isothermal heat flow $\dot{Q}$, formally separated into the exergy flow $\dot{E}$ and anergy flow $\dot{A}$, which is determined by the ambient temperature T_a in a temperature-entropy diagram [15]. For a non-isothermal heat source, $\dot{E}$ ranges from the inlet temperature T_{in} down to T_a. Fig. 1 (right) illustrates a combination of two pure fluids that exemplify heat integration between the HT and LT cycles and their exergetic utilization of a given heat source. State points 2 to 3 outline the exergy uptake of the HT cycle and state points B to C outline the exergy uptake of the LT cycle. The pinch point characterizes the minimum temperature difference ΔT^{pp} during the heat transfer to the HT and LT cycle.

---

[*] Corresponding author.
E-mail address: jadran.vrabec@upb.de (J. Vrabec).

https://doi.org/10.1016/j.applthermaleng.2017.11.137
1359-4311/

Nomenclature

AI/AO	analog input/ output [–]
CC	cooling cycle [–]
CORC	cascaded two-stage organic Rankine cycle [–]
DI/DO	digital input/ output [–]
EOS	equation of state [–]
GUI	graphical user interface [–]
HC	heating cycle [–]
HT	high temperature cycle [–]
LT	low temperature cycle [–]
M	motor or feed pump [–]
ORC	organic Rankine cycle [–]
PCH	power contactor controlled heating rod [–]
PLC	programmable logic controller [–]
pp	pinch point [–]
TCH	thyrister controlled heating rod [–]
VFD	variable-frequency driver [–]
h_i	specific enthalpy at state i [J g^{-1}]
$\dot{m}$	mass flow [g s^{-1}]
$\dot{Q}$	heat flow [J s^{-1}]
s	specific entropy [J g^{-1} K^{-1}]
S	entropy [J K^{-1}]
T	temperature [K]

A feature of the present CORC test rig is that individual components, such as heat exchangers, pumps, condensers, turbines as well as working fluids, can be varied rapidly at comparably low cost. The long-term goal of the present project is to put a two-stage CORC system into practice, exploiting waste heat sources at temperature levels above 600 K, particularly from biogas engines. An additional target is to identify combinations of working fluids (pure fluids and mixtures) that may exploit a maximum of the incoming exergy from waste heat sources, cf. Fig. 1 (right).

Instead of a zeotropic mixture, cyclopentane was chosen in this work as the working fluid for the HT cycle for testing reasons, following a recommendation by Lai et al. [17], and propane was chosen as the working fluid for the LT cycle. Propane was proposed by Schilling et al. [18] for low temperature applications. With a critical temperature of $T_c = 369.8$ K it is suitable for transcritical operation at a comparably low temperature. Fig. 2 shows potential thermodynamic state points in a temperature-entropy diagram for the present working fluid selection of the CORC, where the HT cycle was operated with cyclopentane and the LT cycle with propane.

The use of an internal heat exchanger was not considered in this work because it does not affect the exergetic efficiency. It impacts the thermal efficiency which is governed by the temperature level of the heat transfer and is not suitable for rating the performance of a cycle exploiting a non-isothermal heat source [19].

2. CORC apparatus setup

Due to safety reasons, e.g. because flammable working fluids may be employed, the CORC was placed outside of the laboratory in a separate container, cf. Fig. 3. Both the HT and LT cycle were designed according to AD 2000-Regelwerk B7 (HT/ LT in PN 100/ PN 60). All flanges were sealed with meshed metal (chrome-nickel-molybdenum alloy, Material-Nr. 1.4404) strengthened graphite gaskets novaphit SSTCTA-L provided by Frenzelit [20], limiting the leakage rate to a tolerable amount which was assessed by pressure tests.

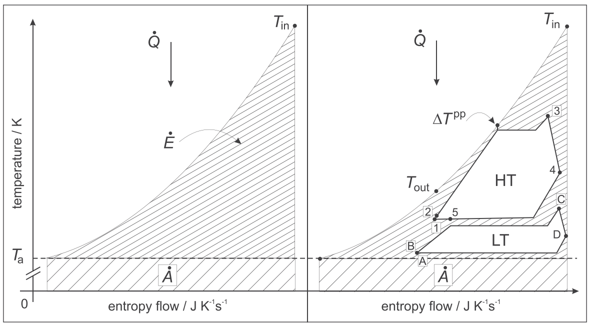

Fig. 1. (left) Exergy flow ($\dot{E}$) and anergy flow ($\dot{A}$) of a non-isothermal heat source for ambient temperature T_a. (right) Potential arrangement of high temperature (HT) and low temperature (LT) cycles of the CORC to maximize the utilization of the exergy flow $\dot{E}$, cf. Baehr [16].

To ensure that the maximum working temperature of 353 K of the pressure sensors (6.4 MPa) was not exceeded, a flexible metal tube was used as an extension which was connected with a tube fitting to the piping system and sealed with a copper gasket and PTFE sealing.

2.1. Heating cycle

The heating cycle (HC) mass flow was driven by a pump (Allweiler NTWH 25 200/01; 0.3 kW), which was capable of a feeding mass flow of up to 700 g/s of Therminol 66 [21]. Heat was supplied by four electrical heating rods with a combined power of 158 kW, three with 50 kW and one with 8 kW. One 50 kW heating rod was thyristor-controlled (TCH) and fully adjustable, the three remaining ones were controlled by power contactors (PCH). Consequently, the combination of all four heating rods enabled for a variable heating power from 0 to 158 kW, where switching of the PCH was necessary. Fig. 5 (top) illustrates the heating concept by depicting total power, which results from the sum of the TCH and the three PCH, over increasing or decreasing heating power. The switching points were chosen differently, depending on

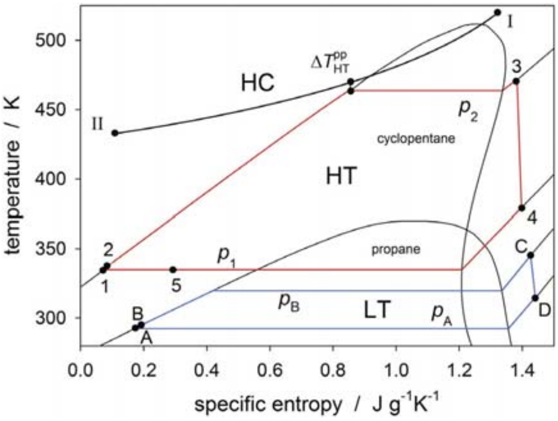

Fig. 2. CORC process in a temperature-entropy diagram: the high temperature (HT) cycle operated with cyclopentane was driven by the heating cycle (HC); the low temperature (LT) cycle operated with propane and was connected to the HT cycle by a heat exchanger acting as a condenser for the HT cycle and an evaporator for the LT cycle. The pinch point characterizes the minimum temperature difference ΔT^{pp}_{HT} between the HC and the HT cycle during heat transfer, cf. DiPippo [9].

Fig. 3. CORC setup in a container that was placed outside of the laboratory due to safety reasons. Heat exchangers and piping system were thermally insulated with mineral wool.

increasing or decreasing heating power, which led to a switching offset of 8 kW. This strategy supported a more rapid attainment of stationary operation, in particular a stable inlet temperature T_{in} at the evaporator.

2.2. High and low temperature cycles

The main difference between the two cycles was that the HT cycle had a turbine, while a variable throttle was used as an expansion device in the LT cycle. This was done for practical reasons, since at this stage of the experiment the thermodynamic conditions, which are essential for the design of a turbine, were not constrained for the LT. The HT cycle was filled with about 40 kg of cyclopentane and the LT cycle with about 20 kg of propane. Both cycles were pressure tested up to a pressure of 4 MPa (HT) or 6 MPa (LT).

2.3. Feed pumps

Progressive cavity pumps (NETZSCH NEMO® [22]) were applied as feed pumps (M1, M2), which worked with a helical rotor inside a helical stator. This type of pump is capable to deal with two-phase fluids, is not susceptible to cavitation and works up to high pressure. The emerging cavities between rotor and stator move along the axis and transport the fluid. These cavities do not change in their size and are sealed among each other's so that volume flow is controlled by rotational speed. Disadvantages of this type of pump are that they may not run dry and that the pumped fluid must be harmonized with the material of the stator. Typically, this material selection is preceded by chemical compatibility and moisture expansion tests [23]. Modification of the stator geometry, such as expansion due to temperature or chemical non-compatibility, may lead to a decrease of pump efficiency or even to failure. For pumping propane in the LT cycle, glycerin was used as a friction modifier, as described by Hadfield et al. [24] and Granryd [25]. Approximately 100 g of glycerin was placed directly in the inlet of the stator on the suction side.

2.4. Heat exchanger

Plate and shell heat exchangers from Vahterus [26] were applied as HE1 and HE2 with a total volume of 13 l and 25 l. Their operation pressure range of up to 6 MPa for HE1 and up to 10 MPa for HE2 was large. In combination with the maximum design temperature of 523 K, they allow for the study of a wide range of thermodynamic states. In both cases, evaporation of the working fluids took place in the plate of the heat exchanger due to higher flow velocity of the steam which led to a higher heat transfer coefficient. To ensure a proper steam quality, a demister was connected downstream to HE1 in the HT cycle. It reversed the flow direction of the steam twice within a tube geometry. At high flow velocities (here about 13 m/s) liquid droplets, which may be carried by the superheated steam, centrifuge to the outer edges of the tube and evaporate at the tube surface, cf. Fig. 6.

2.5. Cooling cycle

The overall waste heat was discharged via an air-blown cooler (type H.T.E.) outside of the container by a cooling cycle, which was connected to the condensers C1 and C2 (plate heat exchangers type GEA WTT PL 150) of the HT and LT cycles. It operated on the basis of a binary ethylene-glycol/water (1 : 1.125) mixture driven by pump M5 (Grundfos TP 50-120/2) with a volume flow of about 17.6 m^3/h. M5 circulated the cooling liquid through C1 and C2, where residual heat was taken after the turbine from the HT cycle and after the throttle from the LT cycle, cf. Fig. 4 (top).

2.6. Turbine and generator

The design of the CORC turbine was based on an axially fed centrifugal pump that expanded the superheated vapor through its curved laval nozzles that were embedded in a blade wheel (1.4305/ X8CrNiS) outwards to the radial expansion tube in the turbine casing (1.4006 + QT/ X12Cr13), cf. Fig. 7. Due to the impulse principle, the torque was mainly generated by the acceleration of the high velocity flow in the blades, as described e.g. by Fister [27]. The connection between turbine and generator, which was a six pole synchronous servomotor operating at 50 Hz (type SK-190-1-30-560 T1), was maintained by non-contacting magnetic coupling. The synchronous machine switches from motor to generator operation as soon as the force of the steam exceeds the break loose torque of the driving shaft. To minimize gap losses in the CORC turbine, the gap was designed as a labyrinth seal with 12 steps with a width of 0.25 mm and a rotary shaft seal. Two angular ball bearings in O arrangement and one deep groove ball bearing formed the fixed shaft bearing at the turbine side, which lead to a minimum slackness of the blade wheel. For cooling and lubrication of the ball bearings, the casing was flodded with hydraulic oil (Mobil DTE 10 EXCEL 15). The construction of the wheel blade enabled for a quick and easy adaption to different thermodynamic states for varying working fluids at low cost. The focus of this turbine lied on its applicability for testing a large variety of working fluids over a wide range of thermodynamic states and therefore the efficiency was subordinate at this point in time. A variable throttle in the LT cycle allowed adjusting a suitable expansion ratio, according to mass flow and fluid properties.

2.7. Controllers and sensors

The CORC software framework was based on two systems: a graphical user interface (GUI), which was programmed in Agilent VEE, and a C program providing functions for the GUI to access the programmable logic controller (PLC). The PLC allowed for

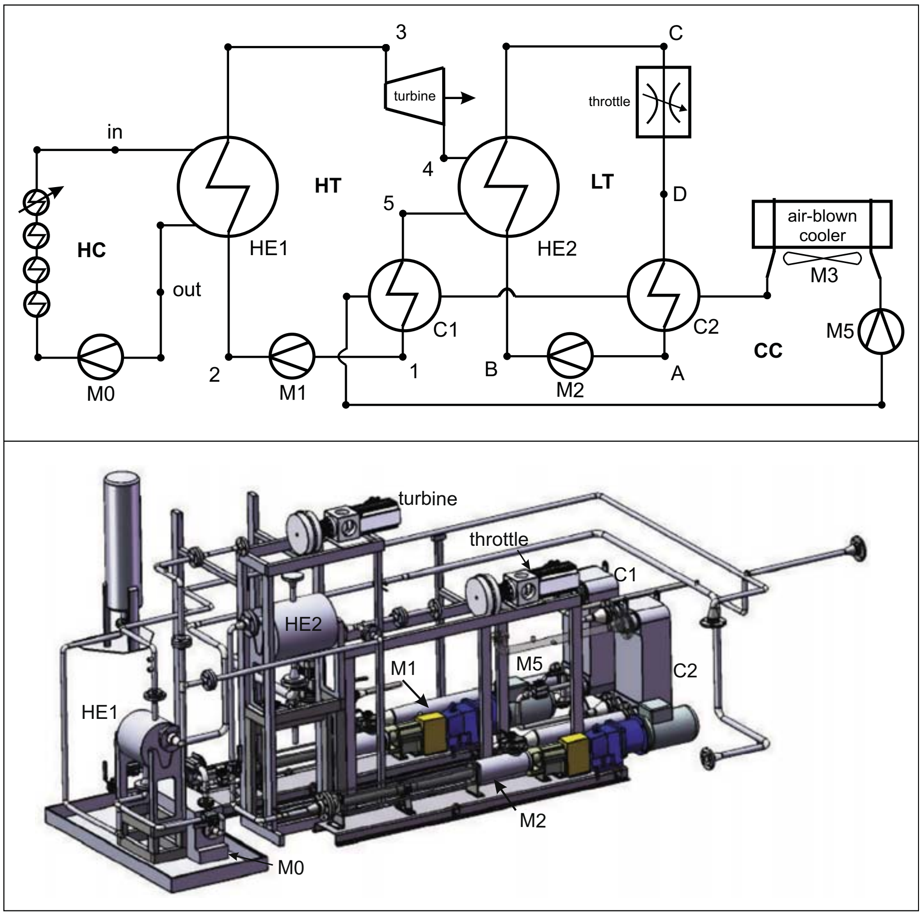

Fig. 4. (top) Design of the experimental CORC setup: a high temperature (HT) and a low temperature (LT) cycle were coupled to a cascade (CORC) by a heat exchanger (HE2) to maximize exergetic utilization. The heating cycle (HC) was realized by four electrical heating rods and a pump (M0). Heat was discharged from the HT and LT cycles to the ambient by an air-blown cooler (M3) using an ethylene-glycol/water mixture, which was pumped (M5) through the cooling cycle (CC) via condensers (C1, C2) in the HT and LT cycles. (bottom) CORC construction layout: HT heat exchanger (HE1) and feed pumps (M1, M2) of the HT and LT cycles, respectively. For the present testing reasons, the LT cycle had a variable throttle as an expansion device instead of a turbine.

digital in- and output (DI/DO) and analog in- and output (AI/AO), which expect either a voltage from 0 to 10 V, a current from 4 to 20 mA or a resistance from temperature (Pt1000) and pressure sensors. The AO connectors were used for setting the motor speed of the pumps by sending a signal from 0 to 10 V to these devices. The DI could only detect an activated (24 V) or deactivated voltage (0 V) and was used for receiving error status from the devices. With the DO, variable-frequency drivers (VFD) or non-controllable actors were turned on and off by sending a current to them or their dedicated contactors. All in- and output streams were monitored and accessed by the GUI, cf. Fig. 8. An alternative to the PLC was a hard-wired programmed logic controller (HPC), which was used for safety functions. A VFD, that is often applied in electromechanical systems as a frequency converter, was used to control the pumps and the generator. The mass flow measurement in the HT and LT cycles worked with a differential pressure aperture according to DIN EN ISO 5167.

2.8. Safety precautions

Working with the CORC mandated dedicated safety requirements because flammable and potentially hazardous fluids were employed at high temperatures and pressures. The experimental setup was therefore placed in a container outside of the laboratory. A gas leakage monitoring system with an infrared gas transmitter sensor (Dräger Polytron IR type 334) [28] calibrated for hydrocarbons was linked to an electric autonomous ventilation system as explosion prevention to avoid a flammable atmosphere in the container. In addition, any gas detection would have triggered an emergency shutdown and switched all electric parts to dead voltage, preventing igniting sparks. Redundant temperature and pressure sensors were hard-wired programmed for the feed pumps M1 to a maximum pressure of 3.5 MPa and M2 to a maximum pressure of 2.5 MPa as well as for the HC to a maximum temperature of 573 K. A manual emergency valve was implemented in the LT cycle for releasing its working fluid (here propane) outside of the container.

3. Experimental setup and initial operation

The initial operation aimed at the evaluation of the components of the experimental setup and the basic function of the apparatus, namely exploiting a heat source by two cascaded cycles. At this stage, the focus lied on the heat exchangers, especially HE2 coupling the two cycles as the central element of the cascade. Before start up, a variety of technical preparations was required. Before and during the filling of the HT cycle with cyclopentane, inert gas was removed by a vacuum pump in combination with a cooling trap. The LT cycle was evacuated before its filling. To enhance the

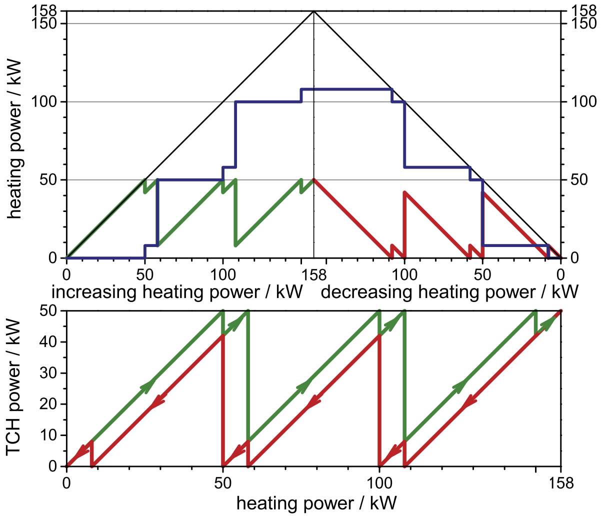

Fig. 5. (top) Heating concept: combination of three power contactor heating rods (PHC, blue) and one thyristor controlled heating rod (THC) with a different switching strategy for increasing (green) and decreasing (red) total heating power output (black) to avoid excessive switching due to a small hysteresis. (bottom) THC power over total heating power in case of increasing (green) or decreasing (red) total heating power output. (For interpretation of the references to colour in this figure legend, the reader is referred to the web version of this article.)

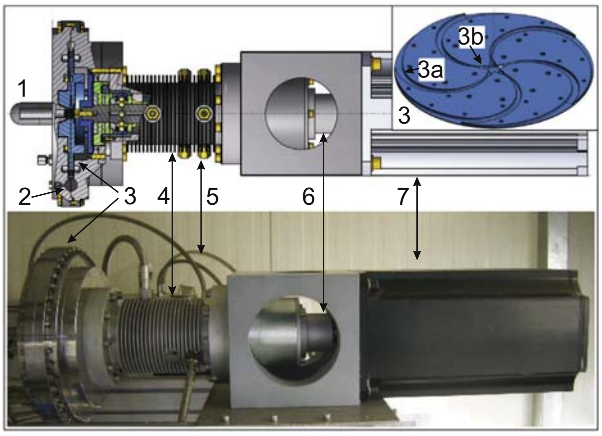

Fig. 7. Centrifugal radial turbine with two angular ball bearings and a magnetic coupling to the generator: (1) axial steam inlet; (2) steam outlet; (3) blade wheel; (3a) blade channel; (3b) laval nozzle; (4) shaft bearing; (5) cooling and lubrication cycle; (6) magnetic coupling; (7) generator.

filling process, the pressure difference between the propane gas bottle and the LT cycle was increased. Therefore, the temperature of the propane gas bottle, which was hung upside down to force the liquid phase into the hose, was raised by about 15 K above ambient temperature. Because of the flammability of cyclopentane and propane, as a mandatory safety procedure, the ventilation system of the container (open doors) was activated and access to the laboratory was prohibited. The positioning of all valves was checked. First, the heating cycle was warmed up along a temperature ramp and the cooling cycle was activated at the same time. Before the mass flow of M1 in the HT cycle was gradually increased and the turbine was set to 50 Hz rotation, lubrication and the cooling cycle of the turbine ball bearing started. Subsequently, the mass flow of the HT cycle $\dot{m}_{HT}$ was raised by feed pump M1 until a heat flow of about $\dot{Q}_{HT}$ = 70 kW was transferred from the HC to the HT cycle at constant quality of evaporation (dry steam) behind the demister.

4. Performance of heat transfer

Because the CORC was based on two cascaded cycles, HE2 played a major role as the central element transferring heat from the HT cycle to the LT cycle. The dimensioning and layout design of HE2 determined the overall cycle performance. Therefore, at this stage of the experimental setup it was important to learn about the characteristics of HE 2 due to its process parameters, such as mass flow and temperature, as a function of the thermophysical properties of the working fluids. To simplify this complex interrelationship, the inlet temperature T_{in} of the HC was controlled at 493 K for a constant mass flow of about 0.5 kg/s of Therminol 66®, whereas the mass flows of the working fluids driven by the feed pumps M1 and M2 were variable parameters. All subordinate parameters were derived from this setting. This knowledge enables for an optimization of future cycle design and operation. For a proper validation of all heat exchangers, the balancing calculations were done on the basis of a steady state flow process.

A constant heat flow $\dot{Q}_{HC} = 70$ kW from the HC led to an enthalpy flow $\Delta\dot{H}$ into the HT cycle, where isobaric conditions were assumed in the heat exchanger. Feed pump M1 pressurized a mass flow of about $\dot{m}_{HT} = 0.110$ kg/s of cyclopentane to a pressure of 1.6 MPa. It was preheated from state point 2 at a temperature of $T_2 = 297$ K and an enthalpy of h_2 = −46.32 kJ/kg, evaporated and superheated to a temperature of $T_3 = 452$ K at state point 3. In addition to the measured temperature and pressure data, other thermodynamic properties were derived with REFPROP [29], based on accurate equations of state (EOS) from Gedanitz et al. [30] for cyclopentane and from Lemmon et al. [31] for propane.

The pinch point temperature difference ΔT_{HT}^{pp} between the HC and HT cycle in HE1 was determined by equating the heat flow from state points 2 to s_{HT} (saturated liquid) in the HT cycle and state points II to pp of the HC, cf. Fig. 9.

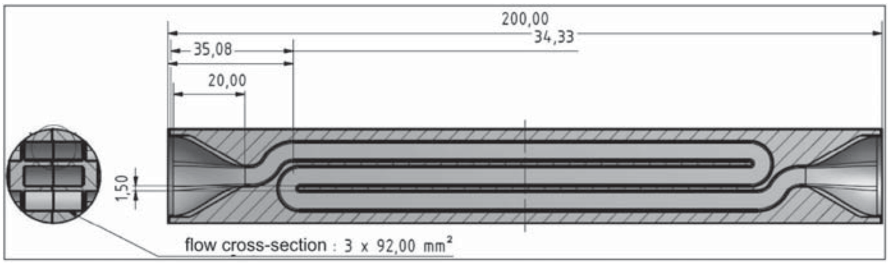

Fig. 6. Cut through the demister, which reversed the flow direction of the steam twice within a tube geometry. At high flow velocities, liquid droplets, which may be carried by the superheated steam, centrifuge to the outer edges of the tube and evaporate. All lengths are given in millimeter.

$$-\dot{Q}_{\mathrm{II,pp}} = \dot{Q}_{2,s_{\mathrm{HT}}}. \tag{1}$$

The heat flow in this section of the HT cycle was

$$\dot{Q}_{2,s_{\mathrm{HT}}} = \dot{m}_{\mathrm{HT}} \cdot \left(h^{s}_{\mathrm{HT}} - h_2\right) = 0.11\,\frac{\mathrm{kg}}{\mathrm{s}} \cdot (273.67 - (-46.32))\,\frac{\mathrm{kJ}}{\mathrm{kg}} = 35.2\ \mathrm{kW}, \tag{2}$$

where the saturated liquid state point s_{HT} of the HT cycle with its temperature T^{s}_{HT} (1.6 MPa) = 441.15 K and has an enthalpy h^{s}_{HT} (1.6 MPa) = 273.67 kJ/kg. With an average isobaric heat capacity of $\bar{c}_{\mathrm{p,T}} = 2.19$ kJ/(kg K) of Therminol, the heat flow in this section of the HC was

$$\dot{Q}_{\mathrm{II,pp}} = \dot{m}_{\mathrm{HC}} \cdot \bar{c}_{\mathrm{p,T}} \cdot \left(T_{\mathrm{II}} - T^{\mathrm{pp}}_{\mathrm{HC}}\right). \tag{3}$$

With the knowledge of the pinch point temperature of Therminol

$$T^{\mathrm{pp}}_{\mathrm{HC}} = \frac{\dot{Q}_{\mathrm{II,pp}}}{\dot{m}_{\mathrm{HC}} \cdot \bar{c}_{\mathrm{p,T}}} + T_{\mathrm{II}} = \frac{-35.2\ \mathrm{kW}}{0.54\ \mathrm{kg\,s^{-1}} \cdot 2.19\ \mathrm{kJ\,kg^{-1}\,K^{-1}}} + 434.15\ \mathrm{K} = 463.91\ \mathrm{K}, \tag{4}$$

the pinch point temperature difference was given

$$\Delta T^{\mathrm{pp}}_{\mathrm{HT}} = T^{s}_{\mathrm{HT}} - T^{\mathrm{pp}}_{\mathrm{HC}} = (463.91 - 441.15)\ \mathrm{K} = 22.7\ \mathrm{K}. \tag{5}$$

In this work, the design of the turbine in the HT cycle was not optimized for cyclopentane. Therefore, a nearly isoenthalpic expansion in the radial turbine to a pressure $p_1 = 0.23$ MPa led to an inlet temperature to the HE2 of $T_4 = 426.84$ K at state point 4. Between state points 4 and 5 cyclopentane was cooled in its gas state down to a temperature $T_5 = 362$ K.

The mass flow of propane in the LT cycle $\dot{m}_{\mathrm{LT}}$ was gradually raised by feed pump M2 until the temperature difference between inlet temperature T_4 and outlet temperature T_{C} of HE2 was reduced down to $\Delta T_{4,\mathrm{C}} = 74.4$ K. At the same time, the adjustable throttle was continuously controlled manually so that pressure p_2 reached about 2.58 MPa, which led to a mass flow of $\dot{m}_{\mathrm{LT}} = 0.03$ kg/s. Here, the heat flow

$$\dot{Q}_{\mathrm{B,C}} = \dot{m}_{\mathrm{LT}} \cdot (h_{\mathrm{C}} - h_{\mathrm{B}}) = 0.03\,\frac{\mathrm{kg}}{\mathrm{s}} \cdot (659.02 - 248.35)\,\frac{\mathrm{kJ}}{\mathrm{kg}} = 12.32\ \mathrm{kW}, \tag{6}$$

was transferred via HE2 from the HT to the LT cycle. The pinch point temperature difference $\Delta T^{\mathrm{pp}}_{\mathrm{LT}}$ in the LT cycle was determined from the equality of the heat flows

$$-\dot{Q}_{\mathrm{pp},4} = \dot{Q}_{s_{\mathrm{LT}},\mathrm{C}}, \tag{7}$$

with

$$\dot{Q}_{s_{\mathrm{LT}},\mathrm{C}} = \dot{m}_{\mathrm{LT}} \cdot \left(h_{\mathrm{C}} - h^{s}_{\mathrm{LT}}\right) = 0.03\,\frac{\mathrm{kg}}{\mathrm{s}} \cdot (659.02 - 401.91)\,\frac{\mathrm{kJ}}{\mathrm{kg}} = 7.71\ \mathrm{kW}. \tag{8}$$

The saturated liquid state point s_{LT} of propane in the LT cycle had a temperature T^{s}_{LT}(2.58 MPa) = 343.01 K and enthalpy h^{s}_{LT}(2.58 MPa) = 401.91 kJ/kg. With the knowledge that heat was transferred only from superheated steam between state points 4 and 5 from the HT to the LT cycle, the heat flow was given by

$$\dot{Q}_{\mathrm{pp},4} = \dot{m}_{\mathrm{HT}} \cdot \bar{c}_{\mathrm{p,C}} \cdot \left(T_4 - T^{\mathrm{pp}}_{\mathrm{LT}}\right). \tag{9}$$

Here, an average isobaric heat capacity of cyclopentane

$$\bar{c}_{\mathrm{p,C}}(406.92\ \mathrm{K}, 0.23\ \mathrm{MPa}) = 1.758\,\frac{\mathrm{kJ}}{\mathrm{kg} \cdot \mathrm{K}}, \tag{10}$$

was assumed. With the knowledge of the pinch point temperature derived from Eq. (9),

$$T^{\mathrm{pp}}_{\mathrm{HT}} = \frac{\dot{Q}_{\mathrm{pp},4}}{\dot{m}_{\mathrm{HT}} \cdot \bar{c}_{\mathrm{p,C}}} + T_{\mathrm{C}} = -\frac{-7.71\ \mathrm{kW}}{0.11\ \mathrm{kg\,s^{-1}} \cdot 1.758\ \mathrm{kJ\,kg^{-1}\,K^{-1}}} + 426.8\ \mathrm{K} = 386.96\ \mathrm{K}, \tag{11}$$

the pinch point temperature difference was determined

$$\Delta T^{\mathrm{pp}}_{\mathrm{LT}} = T^{\mathrm{pp}}_{\mathrm{HT}} - T^{s}_{\mathrm{LT}} = (386.9 - 343)\ \mathrm{K} = 43.9\ \mathrm{K}. \tag{12}$$

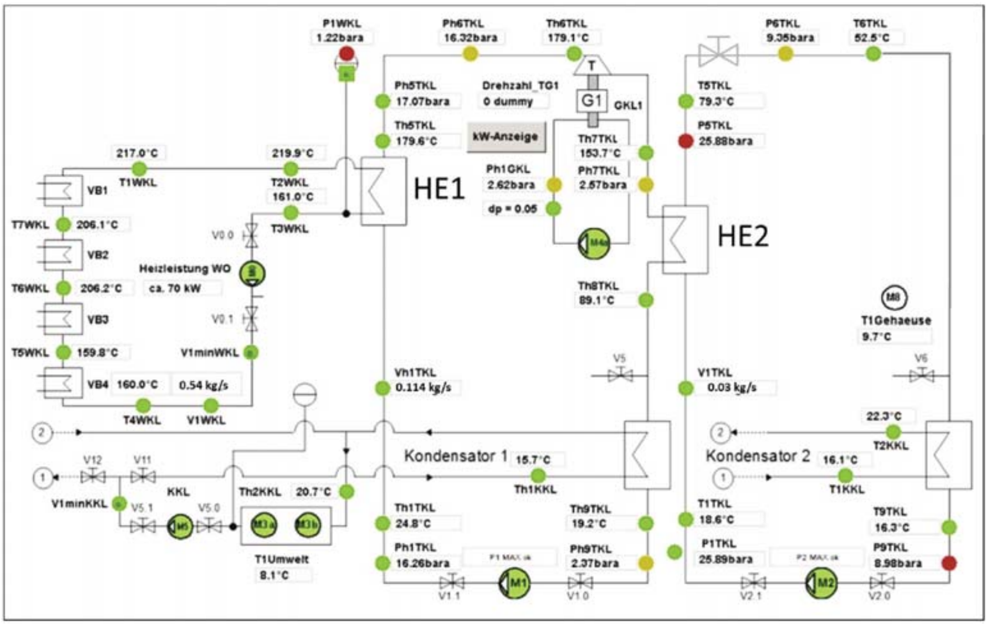

Fig. 8. CORC master display visualizing the hydraulic schematic with essential operation parameters, such as temperatures and pressures of the HC, the HT and LT cycles as well as the CC. It enabled for an operation of the actors and allowed to set different thermodynamic states within the cycles.

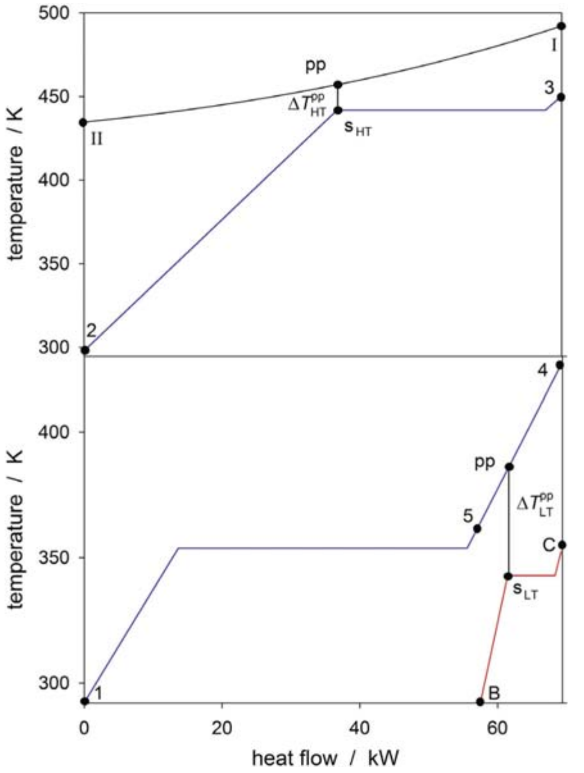

Fig. 9. (top) Heat transfer in HE1: Therminol 66® (black) from the HC supplied a heat flow of 70 kW to the HT cycle, where a mass flow of cyclopentane (red) was heated, evaporated and superheated from state point 2 to state point 3 at a pressure of $p_2 = 1.6$ MPa. (bottom) Heat transfer in HE2: the LT cycle absorbed a heat flow of 12.32 kW from the HT cycle (red) to heat, evaporate and superheat a mass flow of propane (blue) from state point B to state point C at a pressure of $p_B = 2.56$ MPa. Residual heat from the HT and LT cycles was discharged via condensers C1 and C2. The pinch point temperature difference in HE2 $\Delta T^{pp}_{LT} = 43.9$ K was about twice as large as the one in HE1 $\Delta T^{pp}_{HT} = 22.7$ K. (For interpretation of the references to colour in this figure legend, the reader is referred to the web version of this article.)

Since the turbine of the HT cycle did not yield any significant power output and a throttle was applied in the LT cycle, the overall heat flow of about 70 kW was dissipated by the air blown cooler to the ambient with the condensers C1 between state points 5 and 1 in the HT cycle and with C2 between state points D and A in the LT cycle. Because the dimensioning of C1, C2 and the air-blown cooler were excessively large, the dissipation of the waste heat from HT and LT cycles was done at a small temperature difference of $\Delta T < 8$ K.

5. Conclusion

The combination of zeotropic mixtures and pure working fluids in two-staged ORC applications may be exergetically favorable due to small temperature differences during heat exchange. The CORC process was constructed by coupling a HT and a LT cycle as a cascade that allows for different test modes. In the present experiment, the overall functionality and of all equipment parts was tested with the pure fluids cyclopentane and propane operating in the HT cycle and the LT cycle, respectively. The focus of the experiment was on the heat transfer between the two cycles. It was shown that the setup enables to partially use the waste heat from the HT to evaporate the LT working fluid. However, the majority of the waste heat from the HT, particularly most of the heat from condensation, was not transferred to the LT. In the future, more suitable fluid pairs, including zeotropic mixtures, have to be identified that allow larger mass flows and with this a better thermal integration. To clarify the advantages of a two-staged ORC, the temperature of the heating cycle should be increased. Moreover, the design of the turbine in the HT cycle needs to be adapted to the thermodynamic state of its operation condition and the throttle needs to be replaced by a turbine in the LT cycle.

Acknowlegdements

The authors gratefully acknowledge fruitful discussions with Johann Fischer, Universität für Bodenkultur Wien, and Deutsche Forschungsgemeinschaft (DFG) for funding the experimental CORC setup.

References

[1] S. Lecomptea, H. Huisseune, Renew. Sustain. Energy Rev. 47 (2015) 448.
[2] S. Amicabilea, J. Lee, Appl. Therm. Eng. 87 (2015) 574.
[3] J. Song, C. Gu, Energy Convers. Manage. 105 (2015) 995.
[4] A. Schuster, S. Karellas, R. Aumann, Energy 35 (2010) 1033.
[5] H. Chen, D.Y. Goswami, M.M. Rahman, E.K. Stefanakos, Energy 36 (2011) 549.
[6] M. Lampe, M. Stavrou, H.M. Bücker, J. Gross, A. Bardow, Ind. Eng. Chem. Res. 53 (2014) 8821.
[7] L. Tocci, T. Pal, I. Pesmazoglou, B. Franchetti, Energies 10 (2017) 1.
[8] G. Angelino, P. Colonna, Energy 23 (1998) 449.
[9] R. DiPippo, Geothermics 33 (2004) 565.
[10] N. Eğrican, S. Uygur, Energy Convers. Manage. 32 (1991) 375.
[11] B. Liu, P. Rivière, C. Coquelet, R. Gicquel, F. David, Appl. Energy 100 (1985) 285.
[12] G. Shu, L. Liu, H. Tian, H. Wei, Y. Liang, Energy Convers. Manage. 76 (2013) 234.
[13] M. Mehrpooya, M. Ashouri, A. Mohammadi, Energy 126 (2017) 899.
[14] Z. Shengjun, W. Huaixin, G. Tao, Appl. Energy 88 (2011) 2740.
[15] Z. Rant, Forsch. Ing. Wes. 22 (1956) 36.
[16] H.D. Baehr, Thermodynamik: Eine Einführung in die Grundlagen und ihre technischen Anwendungen; mit 80 Beispielen, fourth ed., Springer, Berlin, 1978.
[17] N.A. Lai, M. Wendland, J. Fischer, Energy 36 (2011) 199.
[18] J. Schilling, M. Lampe, J. Gross, A. Bardow, Chem. Eng. Sci. 159 (2017) 217.
[19] M. Yari, Renew. Energy 35 (2010) 112.
[20] Frenzelit, novaphit® SSTC Technical Datasheet (Frenzelit Werke).
[21] FRAGOL, Therminol 66® Produktinformation (FRAGOL SCHMIERSTOFF).
[22] NETZSCH Pumpen und Systeme, NEMO® Progressing Cavity Pumps (NETZSCH Pumpen und Systeme, 2015).
[23] NETZSCH Incorporated, NEMO-NM MINI: Operating and Maintenance Instruction (NETZSCH NEMO® Pump, 1999).
[24] N.P. Garland, M. Hadfield, Mater. Des. 26 (2005) 578.
[25] E. Granryd, Int. J. Refrig. 24 (2001) 15.
[26] VAHTERUS, Plate & Shell® Heat Exchanger VAHTERUS, Finland, 2014.
[27] W. Fister, Fluidenergiemaschinen, Springer Verlag, Berlin, Heidelberg, 1984.
[28] Dräger Safety, Dräger Polytron IR type 334 and type 340, Dräger Safety, eighth edition, 2008.
[29] E. Lemmon, M. Huber, M. McLinden, Reference Fluid Thermodynamic and Transport Properties REFPROP, Version 9.1, 2013, National Institute of Standards and Technology, Standard Reference Data Program, Gaithersburg, 2013, 2013.
[30] H. Gedanitz, M.J. Davila, E.W. Lemmon, J. Chem. Eng. Data 60 (2015) 1331.
[31] E.W. Lemmon, M.O. McLinden, W. Wagner, J. Chem. Eng. Data 54 (2009) 3141.

5 Speed of sound measurements in additional fluids

Additional speed of sound measurements were performed that are not yet published. Before discussing their results in this section, experiences and construction aspects are described.

(I) Sulfur hexafluoride

Sulfur hexafluoride (SF_6) is an almost nonpolar substance and due to its electrical and chemical stability it is applied in the electrical industry as an isolation gas or as a tracer in chemistry [66]. Since its thermophysical properties are well known and an accurate EOS of Guder and Wagner [66] is available, SF_6 was chosen for test reasons. It was filled from a gas cylinder into the speed of sound apparatus through condensation into the measurement cell that was cooled down to a temperature of 240 K. At this temperature, the expected saturation pressure of 0.44 MPa was found of that saturated liquid state point, where the speed of sound is 474.67 m/s according to the EOS by Guder and Wagner. However, there was no signal received from the 8 MHz quartz crystal, even pressurizing SF_6 up to 30 MPa with a hand pump. Since speed of sound measurements before and after this experiment with argon as a reference gas were successful, it is expected that this fluid shows very strong absorbtion effects due to relaxation phenomena, as described by O'Connor [67].

(II) Nitrogen

Another interesting question was how the measurement cell, especially the quartz crystal, reacts to cryogenic temperatures, thereby testing the capability of the apparatus for measurements at low temperatures. Initially, a piece of crystal was quenched into liquid nitrogen to test whether it would crack by the rapid cooling to approximately 77 K at ambient pressure. Since the crystal was not damaged, the measurement cell, together with the 8 MHz quartz crystal, was cooled down slowly in supercritical liquid nitrogen at ambient pressure in a dewar-vessel. Even though the electrical signal emitted from the quartz crystal was very weak despite the inductive adjustment of the electrical system, speed of sound measurements could be performed.

(III) Ionic liquids

Ionic liquids (IL) belong to the group of electrolytes, but unlike ionic solutions, they are only composed out of ions and therefore contain no solvent. Beside numerous potential chemical applications, the use of IL might also be interesting in the field of energy technology due to their unique properties, like negligible volatility, wide liquidus range, non-flammability, high thermal conductivity, chemical and physical stability and high potential for recycling [68]. Here, speed of sound measurements may help to characterize thermophysical properties. Since the IL have a high electric conductibility due to the presence of anions and cations, the electrical signal input (erection of the quartz crystal) and output (resulting from the received mechanical echo of the quartz quartz crystal) was short-circuited and the echo signals amplitude was damped to zero. Therefore, the quartz crystal needs to be nonconducting with respect to its surrounding fluid. A promising attempt to isolate the gold electrode of the quartz crystal by a surface coating was to use polyamide-imides (PAI), which are high performance thermoplastic polymers. Their properties, such as high heat capability, broad chemical resistance and the possibility of very thin layering to ensure the minimization of acoustic effects to the quartz crystal make these compounds attractive. Referencing measurement tests with coated quartz crystals in deionized water showed no negative influence on the acoustic properties, only a weak amplitude damping of the echo. However, measurements of 1-ethyl-3-methylimidazolium ethylsulfate as an IL test fluid were not successful. Even for various PAI layer thicknesses no isolation of the gold electrodes could be accomplished, cf. LaRubia [69].

A different approach to isolate the electrical bonding to the piezoelectric transducer was made by Esperança et al. [70] by contacting on one side directly to one of the reflectors and on the other to a copper ring insulated by a Teflon ring from the main cell. Azevedo et al. [71] presenting a novel non-intrusive measuring cell, were the transmitter and receiver is placed outside the pressure vessel. This measurement principle is based on the single time of flight measurement of one propagation length.

5.1 Refrigerant mixture of 1,1,1,3,3-pentafluorobutane and perfluoropolyether

The azeotropic refrigerant mixture of 1,1,1,3,3-pentafluorobutane (R365mfc) and of perfluoropolyether (Galden® HT 55) [72] with a 65/35 mass ratio is also known as SES 36 and is a potential candidate for low temperature ORC applications. A compre-

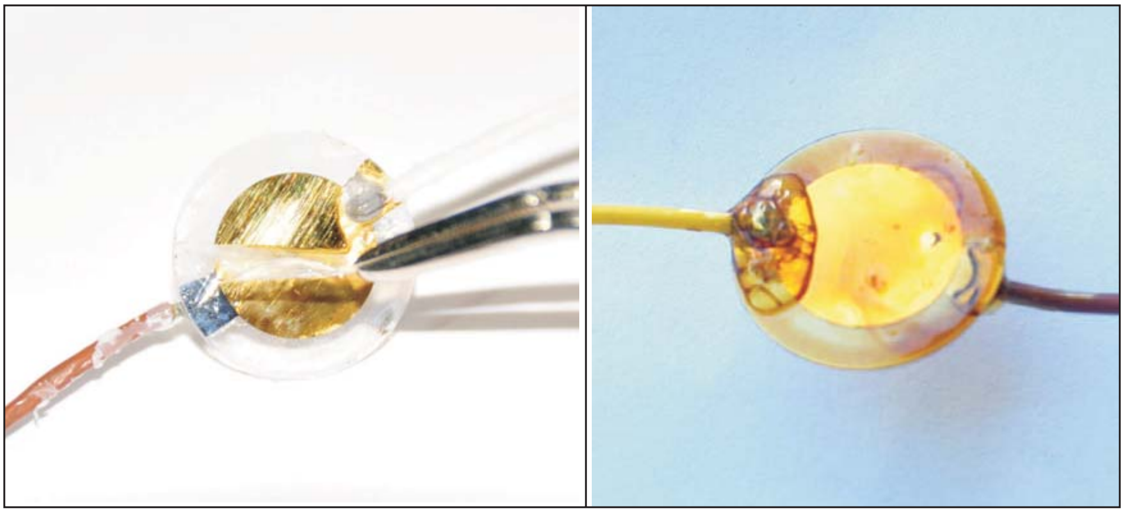

Figure 5.1: (Left) A Coating on the basis of isophorone diisocyanate (IPDI) for isolation shows good acoustic behavior in deionized water, but is dissolving in the ionic liquid (IL) 1-ethyl-3-methylimidazolium ethylsulfate. (Right) Polyamide-imides (PAI) coating shows a good acoustic behavior in deionized water and good surface condition in IL but leads to strong damping in case for this IL.

hensive experimental study of various thermophysical properties, amongst others the speed of sound in a temperature range of 293 K up to 523 K and a pressure of up to 2.5 MPa based on the light scattering technique, was published by Fröba et al. [51] in 2007. Fig. 5.2 illustrates the measured speed of sound data points and the vapor pressure curve according to the EOS by Thol et al. [73] in a pressure-temperature diagram.

Fröba et al. measured nine isotherms in the vapor phase and several others under saturated conditions in the liquid and vapor phase. In the present work, speed of sound measurements were performed along four isotherms in the liquid and supercritical liquid region in a temperature range of 313 K to 450 K and up to a pressure of 81 MPa. The state points are illustrated in Fig. 5.2. In addition, it can be seen that the region around the critical point was covered much closer by the measurements by Fröba et al. than with the present work. For the critical temperature $T_c = 450.7$ K measurements were performed from the gaseous region up to a pressure of around 2.5 MPa, i.e. close to $p_c = 2.84$ MPa according to Fröba et al., whereas present measurements below 14.1 MPa in the supercritical liquid region could not be made. Obviously, the light scattering technique was not influenced as strongly by fluid behavior at the critical point as the pulse-echo method.

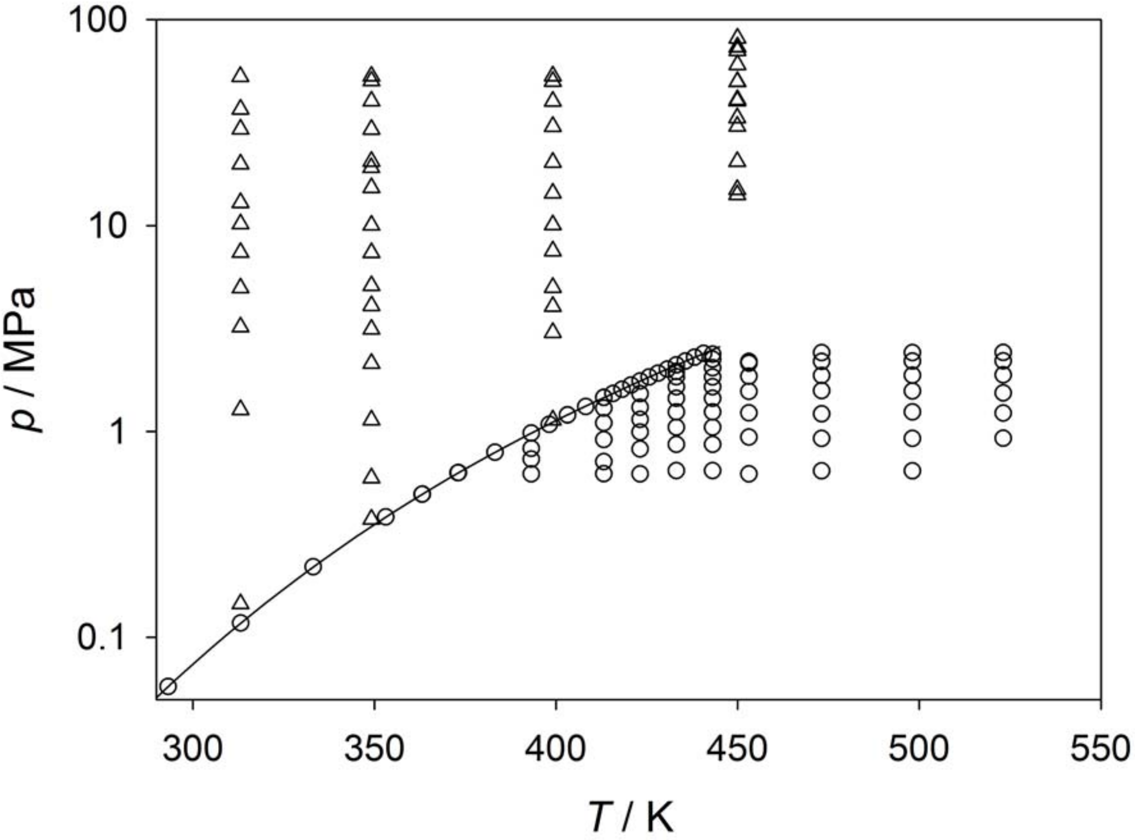

Figure 5.2: Overview of speed of sound measurements for SES 36. The vapor pressure curve is shown according to the EOS by Thol et al. [73] and speed of sound measurements by Fröba et al. [51] (○) and the present work (△) are indicated.

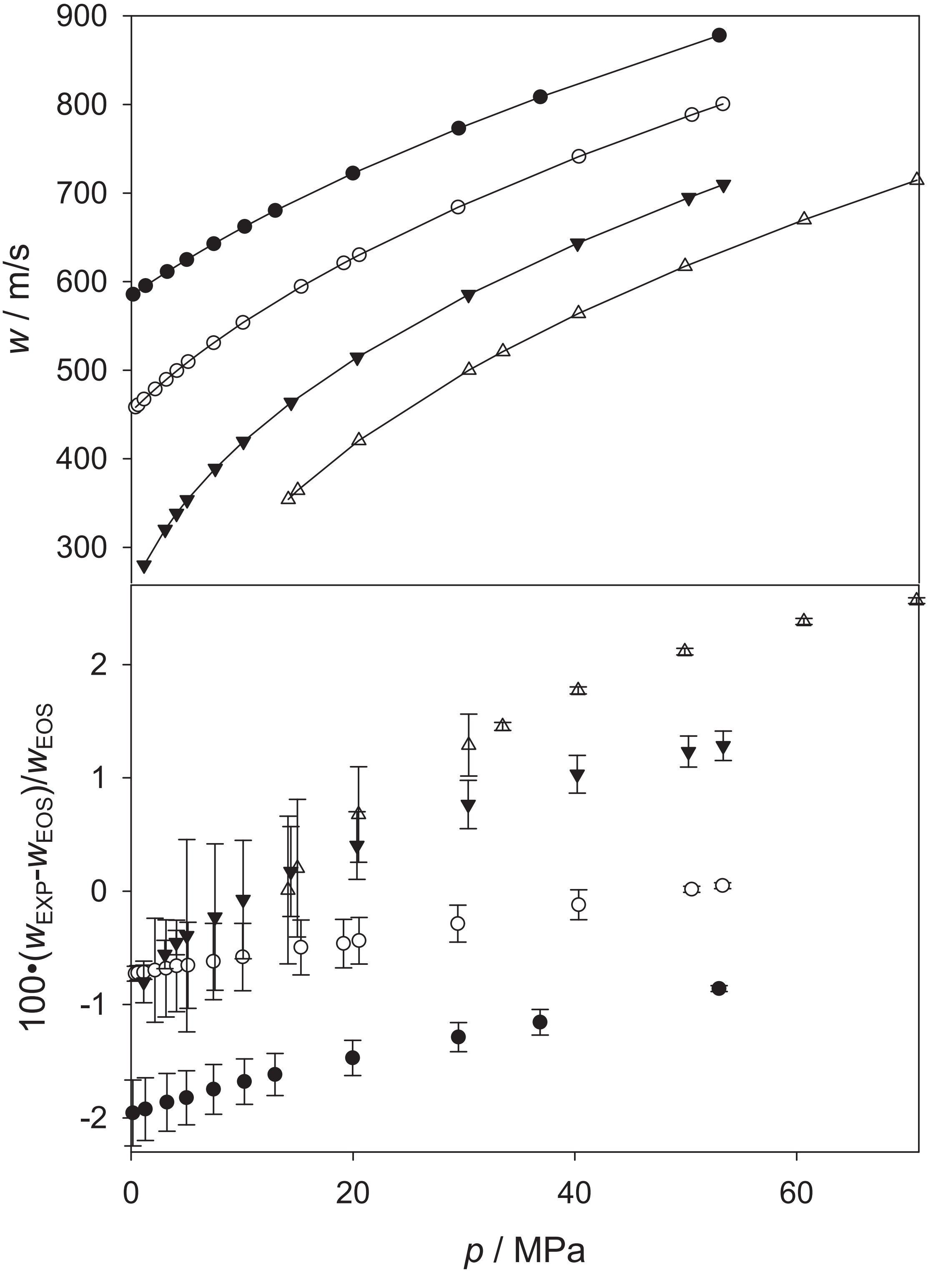

Figure 5.3: Absolute values (top) and deviations (bottom) of present experimental speed of sound data from the equation of state (EOS) for SES 36 by Thol et al. [73] at (•) 313 K, (○) 350 K, (▼) 400 K and (△) 450 K.

At 313 K the speed of sound w of liquid SES 36 increases from 585 m/s at a pressure of 0.15 MPa to almost 900 m/s at a pressure of about 53 MPa, whereas with an increase of the temperature, the speed of sound continuously decreases to around 616 m/s at 450 K at a comparable pressure of about 50 MPa, cf. Fig. 5.3 (left). The deviation from the EOS by Thol et al. is within -2% and 3% and increases with temperature and pressure, cf. Fig. 5.3 (right). The overall measurement uncertainty results from the sum of uncertainties during the measurement process and was extensively discussed in previous works, [6, 74].

While filling the measuring cell with SES 36 using a hand pump, an unusually large amount of volume had to be displaced before a significant pressure increase was achieved. Unlike for water, using the hand pump for liquid SES 36, the fluid was considerably more compressible, nearly like compressing a gaseous fluid under supercritical conditions. This might be due to the strong repulsion of the negative fluorine atoms in the molecules, causing a strongly pronounced mean free path.

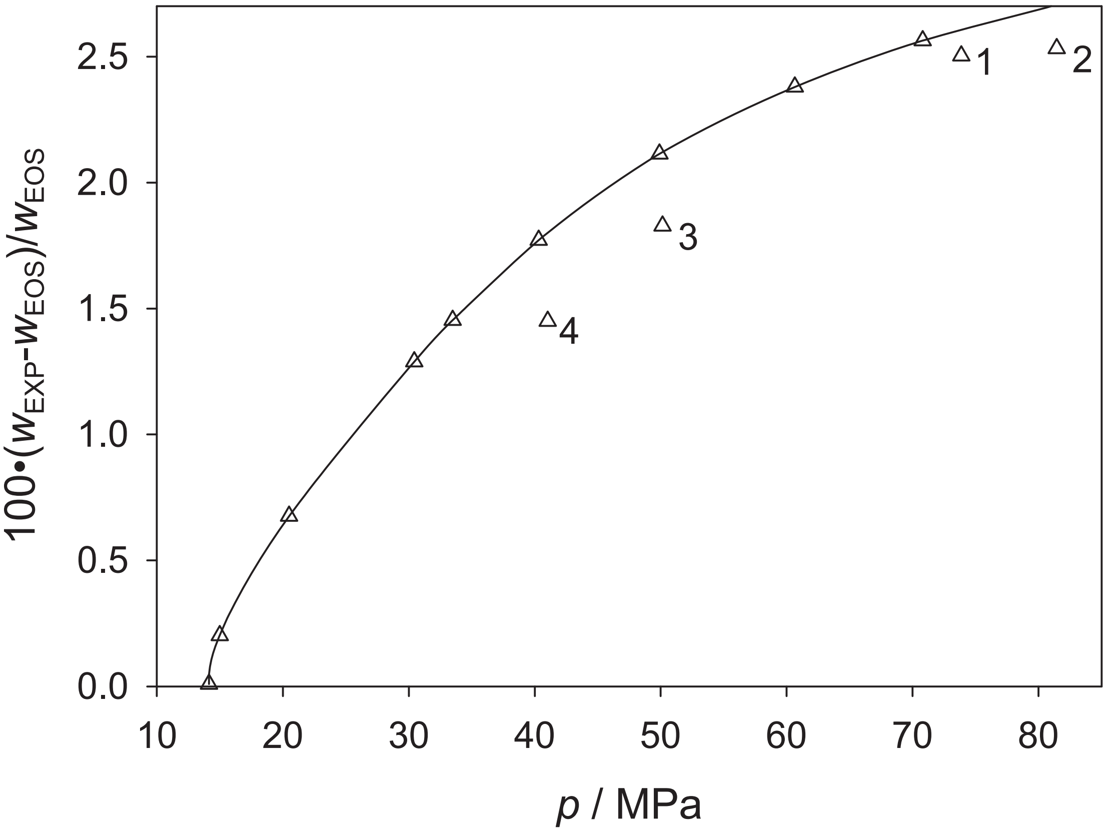

Figure 5.4: Deviations of the speed of sound measurements to the equation of state (EOS) by Thol et al. [73] for SES 36 at 450 K (△). Measurements were performed along the correlation function (——) from low to high pressures. The final measuring points 1 and 2 show a deviation to the correlation function. To verify the results measurements were done towards lower pressures for the same isotherm (state points 2-4). It is shown that they were not in line with previous results due to a fluid decomposition activity caused by thermal stressing.

An usual behavior occurred during measurements of the 450 K isotherm. They were carried out from low pressure to high pressure, where for each state point, system equilibration lasted for about 1 h. At pressures of 73.6 MPa and 81.4 MPa (cf. state points 1 and 2 in Fig. 5.4) the deviation to the EOS by Thol et al. [73] was not in line with other deviations at lower pressures, cf. Fig. 5.4. By lowering the pressure for comparing measurements to previous results for the same isotherm, the deviations to the EOS even increased, cf. state points 3 and 4 in Fig. 5.4. Beyond state point 3, no measurement was possible because the quartz crystal echo signal faded out and finally disappeared. A fluid sample from the measuring cell revealed a change of the properties of SES 36 in terms of odor and optical appearance. The fluid's color changed from colorless to darkish grey and the odor from ether-like to acid-like. Dismantling the measurement cell showed a severe damage to the quartz crystal, where the contacts of the gold electrodes peeled off the quartz crystals surface, cf. Fig. 5.5. Moreover, the surface of the stainless steel cell was intensively oxidized and corroded.

Apparently the fluid was cracked into aggressive products, presumably to gaseous hydrogen fluoride, fluorophosgene and others, as described by the safety data sheet SOLKATHERM® SES 36 [72]. Since the decomposition occurred at the highest measuring temperature of 450 K and a time delay between the measurement of the state points 1 and 2, 3, 4 of at least 15 h (overnight), this occurred most likely due to thermal stress. However, it should be noted that Fröba et al. [51] performed measurements at even higher temperatures of up to 523 K and did not report any decomposition activity.

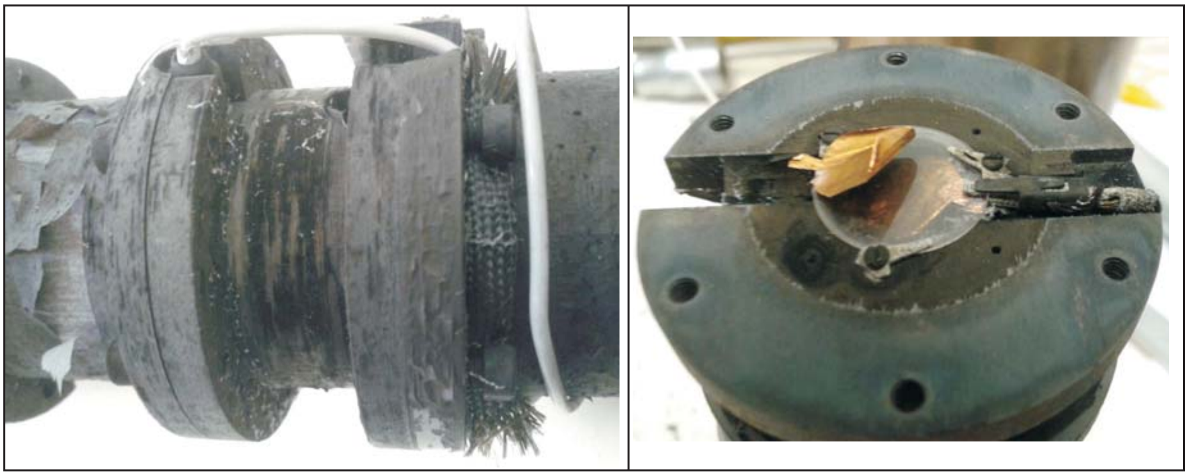

Figure 5.5: Severe damage of measuring cell (left) and quartz crystal (right) by corrosion due to the chemical decomposition of SES 36 by thermal stress.

5.2 Hydrogen chloride

Speed of sound measurements were performed for hydrogen chloride (HCl, CAS-Nr. 7647-01-0) which was purchased at Air Liquide with a given purity of $\geq$ 99.8 Vol.% and a content of inert gases of $<$ 2000 ppm [75]. It was delivered in a gas cylinder (6 kg) at a vapor pressure of about 4.25 MPa at 293.15 K. HCl is a colorless gas with a strong penetrative odor and develops in contact with air white smoke due to its intense hygroscopicity [76]. For filling the measuring cell with that fluid, the HCl gas cylinder was mounted upside down to take advantage of the liquid phase. In addition, the measuring cell was cooled down to a temperature of 218 K to support the flow into the measurement cell due to the difference in lower vapor pressure. Due to special safety precautions the hand pump was not used. Unlike the measurements of other fluids that were carried out along isotherms, isochoric measurements were performed here to avoid gas filling and release processes as much as possible. Therefore, the measuring cell was only filled once at 218 K and then during the isochoric measurements heated up until a pressure of 40 MPa was reached, which was the maximum chosen pressure due to safety considerations. After each isochor, HCl was released through a valve and fed through a tube with a connected glass frit on the end into a washing bottle, where the HCl gas was neutralized in sodium hydroxide solution, cf. Fig 5.6. As safety indicator, phenolphthalein was used, signalizing chemical equilibrium and therefore the necessity to renew the alkaline solution. After that, the temperature was decreased until the vapor pressure was reached and in this way measurements were iterated up to a temperature of 479 K. Speed of sound measurements were performed along nine isochors in a temperature range of 218 K to 479 K and a pressure range from somewhat above the vapor pressure up to 40 MPa, cf. Fig. 5.7. At the time of the measurements, the author was not aware of other available speed of sound data.

Fig. 5.8 (top) depicts the absolute speed of sound over the pressure along nine isochors. The speed of sound increases with pressure p and density ρ. Fig. 5.8 (bottom) shows the deviations to the EOS by Thol et al. [77] over pressure and their measurement uncertainty u_w. It can be seen that u_w increases towards lower pressures. Because the applied pressure transducer (Honeywell TJE), with a measuring range of up to 200 MPa and an uncertainty of ±0.1 % with respect to its full scale, had a maximum absolute uncertainty of ±0.2 MPa, its usage, especially at low pressure, was not adequate[1]. Appendix A provides the present data together with their uncertainties.

---

[1] The pressure uncertainty $u(p)$ has the largest impact at low temperatures. This is a consequence of the pressure uncertainty, combined with the high isothermal compressibility of the fluid at such thermodynamic states.

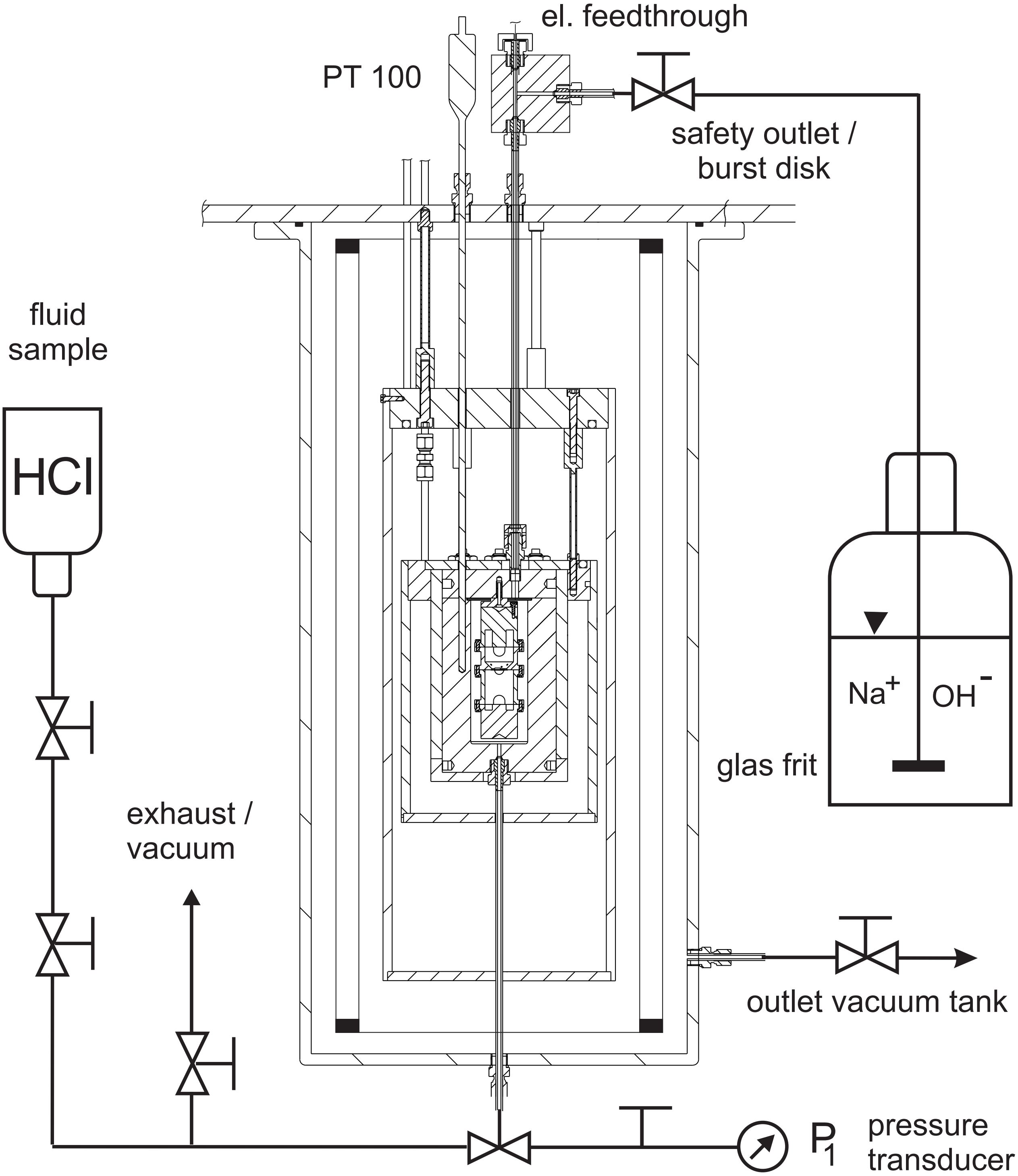

Figure 5.6: Hydraulic set up of the speed of sound measurement apparatus. The measuring cell was filled by hydrogen chloride (HCl) through condensation at a temperature of 218 K. Outgoing fluid disposal was neutralized through a glass frit into sodium hydroxide solution.

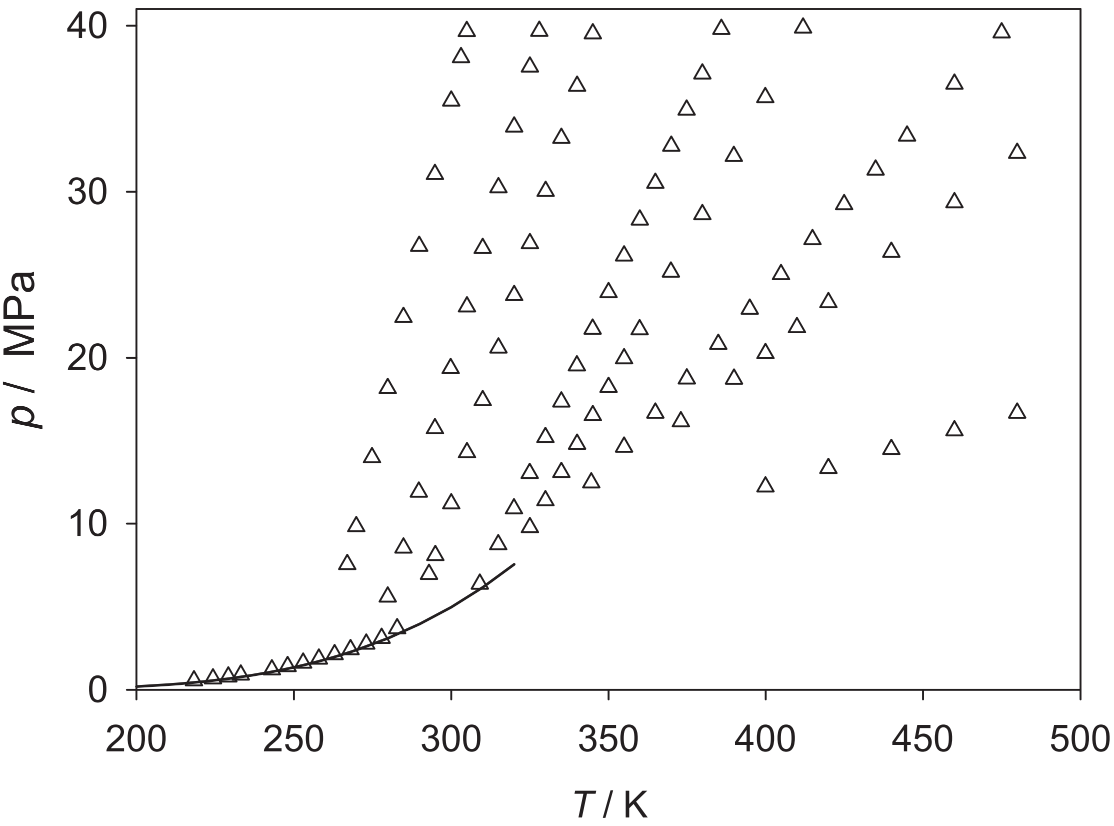

Figure 5.7: Overview of speed of sound measurements carried out in the present work for hydrogen chloride (△). The vapor pressure (—) curve is shown according to the EOS by Thol et al. [77].

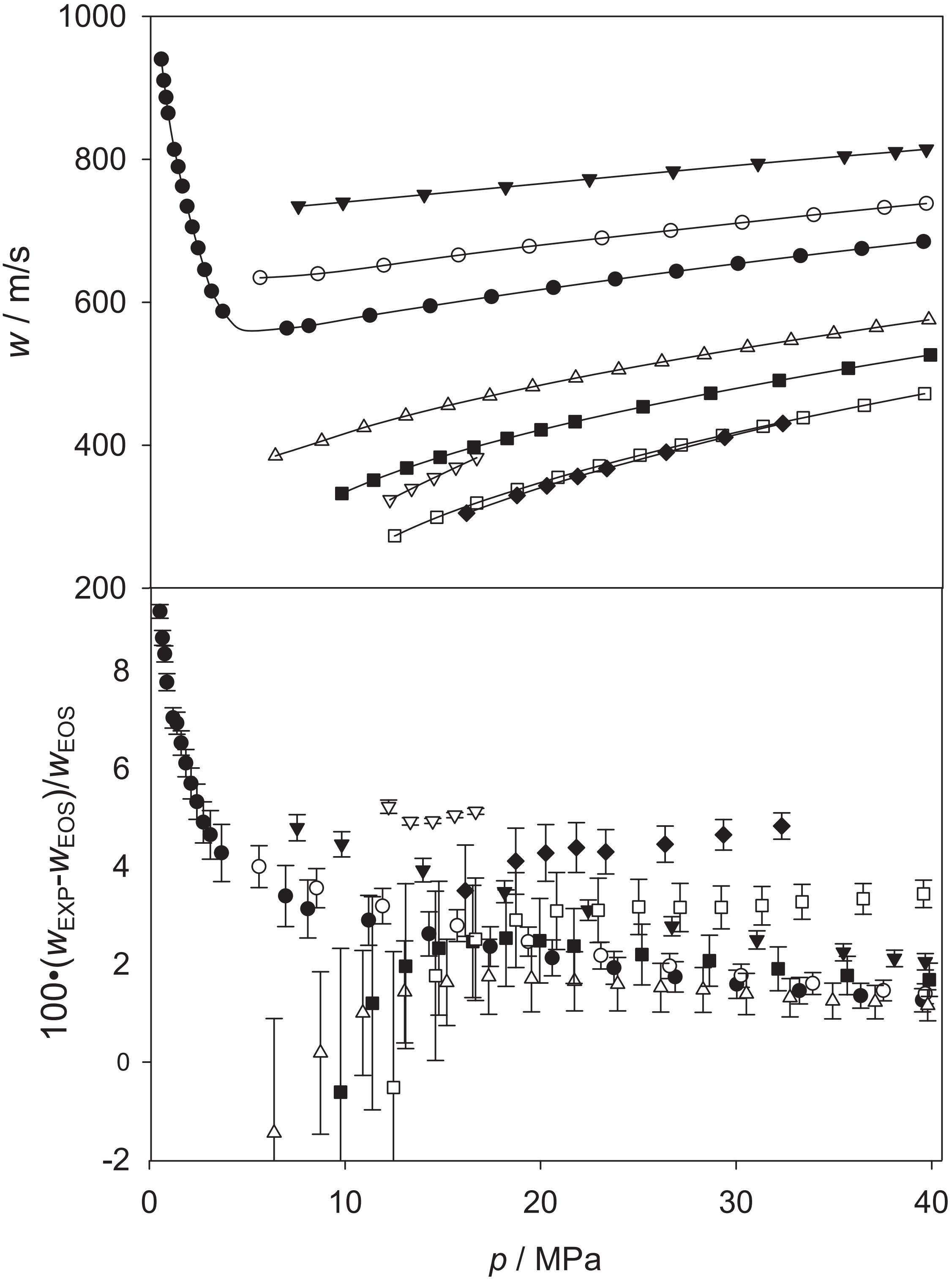

Figure 5.8: (Top) Absolute speed of sound depicted over the pressure along nine isochors for hydrogen chloride (HCl) at (•) 930 kg/m^3, (▼) 670 kg/m^3, (○) 610 kg/m^3, (△) 486 kg/m^3, (■) 420 kg/m^3, (□) 370 kg/m^3, (◆) 350 kg/m^3 and (▽) 336 kg/m^3. (Bottom) Deviations to the EOS by Thol et al. [77].

5.3 Dodecamethylpentasiloxane

Dodecamethylpentasiloxane (MD_3M) belongs to the class of linear siloxanes and is a potential working fluid candidate for high temperature ORC applications. The fluid (CAS-Nr.:141-63-9) was purchased at Sigma Aldrich with a given purity of $\geq$ 97 Vol.%.

Speed of sound measurements were performed for dodecamethylpentasiloxane (MD_3M) in the saturated liquid and supercritical states over a temperature range from 300 to 550 K and up to a pressure of 30 MPa. The measurement range was limited down to a pressure of about 1 MPa for the 550 K isotherm due to the limitations of the pulse-echo method for near-critical states as a result of absorption and attenuation effects, cf. Fig 5.9. Fig. 5.10 shows the absolute values (top) and the corresponding deviations

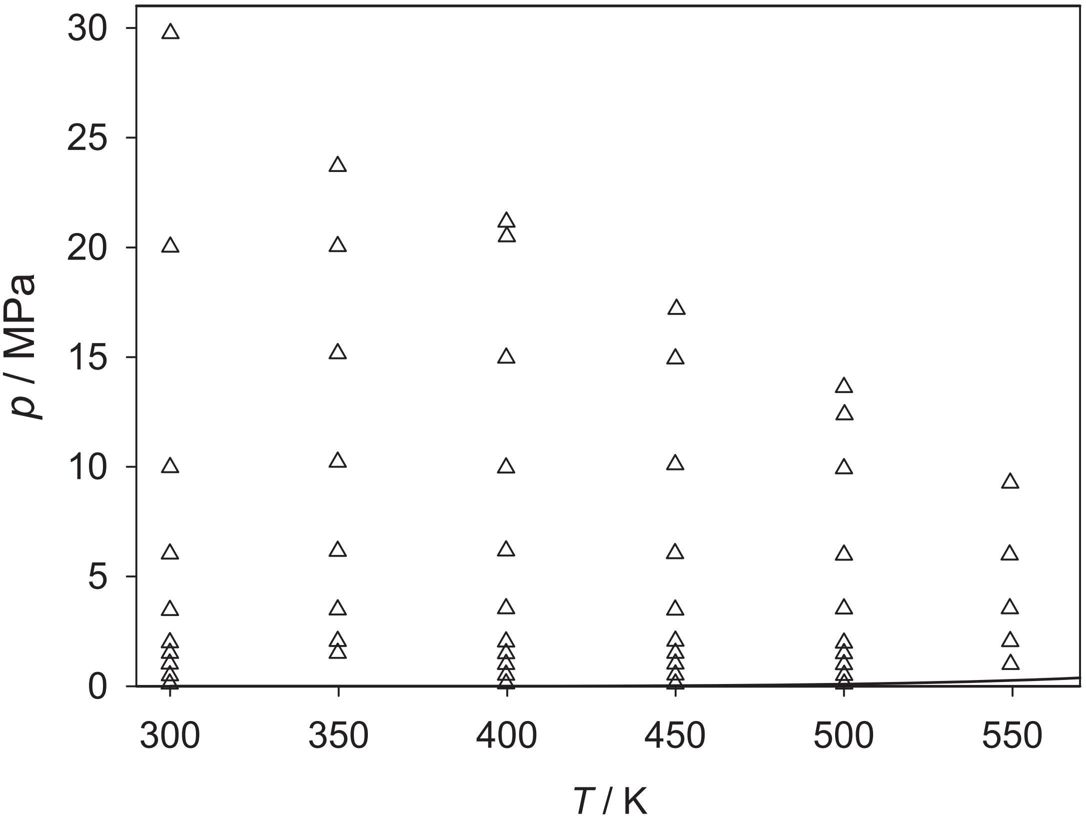

Figure 5.9: Overview of speed of sound measurements carried out in the present work for dodecamethylpentasiloxane (MD_3M) (△). The vapor pressure curve (—) is shown according to the EOS by Colonna et al. [45].

to the EOS by Colonna et al. [45] along six isotherms (bottom). The speed of sound increases towards lower temperatures and higher pressures to about 1120 m/s at 300 K and 30 MPa and has the lowest value of the present measurements of around 295 m/s at 550 K at 1 MPa.

However, the total uncertainty increased up to 2% for measurements at 550 K below 1 MPa. This increase is due to the fact that the relative uncertainty of the pressure measurement was significantly higher at low pressures, combined with the high isothermal compressibility of the fluid at such thermodynamic states. For the remaining state points, the total uncertainty varied between 0.06% and 0.4%. Appendix A provides the present data together with their uncertainties in numerical form.

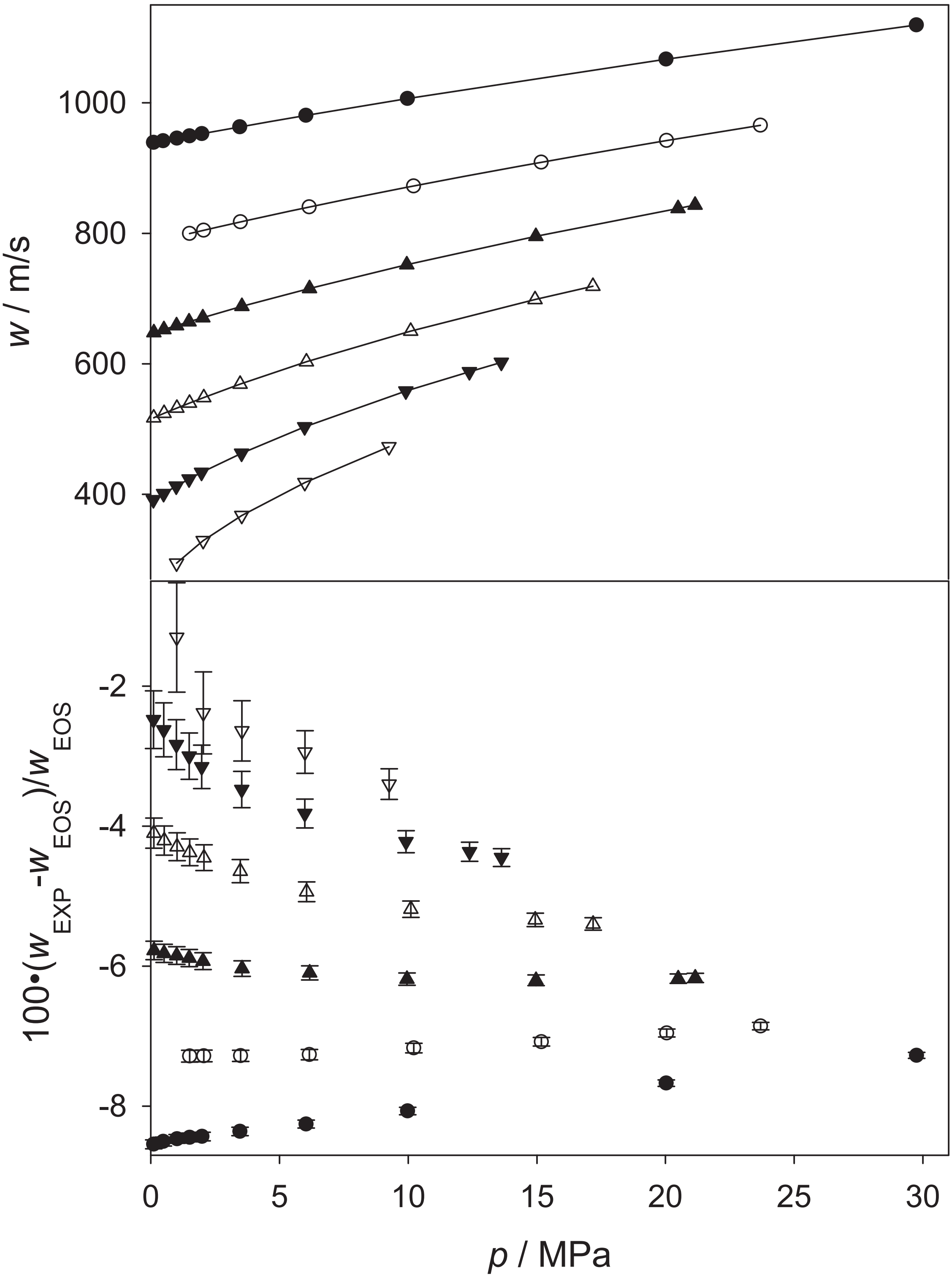

Figure 5.10: (Top) Absolute speed of sound over pressure of dodecamethylpentasiloxane (MD$_3$M) along six isotherms at (•) 300 K, (∘) 350 K, (△) 400 K, (△) 450 K, (▼) 500 K and (▽) 550 K. (Bottom) Deviations to the EOS by Colonna et al. [45].

6 Summary and conclusions

The present work is divided into two parts, the determination of the speed of sound of fluids and the construction of an ORC test-rig. Although these topics may appear to have a quite different nature, it is shown that technical applications, such as ORC processes, crucially depend on thermodynamic properties.

The first section deals with the fluid selection for ORC applications. Within this scope, an ORC test-rig was designed and constructed which coupled two cycles in a cascade via an internal heat exchanger so that the second cycle (C2) is driven by the residual heat from the first cycle (C1). On the basis of this setup, upcoming measurements for fluids and combination of pure fluids or fluid mixtures are planned. First test runs showed that both cycles may operate independent of each other and that heat was successfully transferred from C1 to C2. In the next steps, fluid selection and modification of the cycle has to be done. In this context, the consideration of trilateral cycles with the utilization of a flash turbine, which could be configurated with this test-rig, should be investigated because theoretical research predicts significant benefits over traditional cycles. Overall, it became obvious that the thermodynamic design and the technical layout of an ORC, yielding an optimized cycle efficiency, is not possible without reliable thermodynamic property data. Here, precise EOS are crucial as a working basis. Since reliable property data and their associated EOS are limited to a few common fluids, the need for new property data allowing for a wider fluid selection has to be satisfied. This was especially true for siloxanes, which are presumed to be promising working fluid candidates for ORC processes, but exhibit a lack of thermophysical properties which impede the development of accurate EOS.

Hence, the second section describes the determination of the speed of sound as a thermodynamic property and using these data as a basis, in addition to other experimental and simulation data, for the development of EOS. The measurement results of the present work may be of general interest, nevertheless, the emphasis lies in the application of the speed of sound in the field of thermodynamic property research, to support the development of EOS and therefore to improve the availability and quality for ORC working fluid models. An apparatus for the measurement of the speed of sound of liquids on the basis of the pulse-echo technique was designed according to existing devices, such as by Gedanitz et al. [8] or Meier [58]. For controlling the cell with a high accuracy over a wide range of temperature between 220 K and 550 K, the thermostat was constructed with three copper shields. Each was monitored with respect to the temperature and equipped with one independently adjustable heater. To quickly specify a constant temperature at the quartz without overshooting, a combination of a PID controller and an additional proportional (P) controller was used. The pressure cylinder was designed for pressures of up to 180 MPa. After installation, the measuring cell was referenced and validated with water by comparing the results with a very accurate EOS for water and recently published experimental data by Lin and Trusler [78]. The propagation time difference Δt was determined by the correlation method, downloading both echoes resulting from a one burst signal via an oscilloscope to a computer. For time extended echoes and echoes with a low amplitude, the measurement uncertainty increased, especially in the near-critical region and towards lower pressures. In this context, the speed of sound of ammonia was measured and compared with the EOS by Tillner-Roth et al. [79], cf. Dubberke et al. [6]. Moreover, speed of sound data for MM and D4 as well as for MDM and MD_2M were used for the development of new EOS to supersede the EOS by Colonna et al. [44], cf. Thol et al. [42] and [80]. For an additional linear siloxane (MD_3M) and for SES 36, which both are potential ORC working fluid candidates too, speed of sound measurements were performed.

The next step was the improvement of the propagation time measurement, which was basically done by computational signal design and echo analysis. It was shown that the direct time difference measurement approach, either based on peak-to-peak measurement or on the Hilbert transform, has numerous advantages over the traditional correlation methods. This was also true for the double burst methods with burst design and signal processing for fluids in gaseous and supercritical states. As an example for the new procedure, extending the measurement range of the pulse-echo technique in supercritical fluids, measurements were performed for argon and nitrogen down to pressures of 5 MPa at ambient temperature [14]. Moreover, the new procedure offers a fast and nearly fully automatized measurement routine. Within this framework, speed of sound measurements for oxygen and hydrogen chloride were done, covering a wide range in temperature and pressure, cf. Dubberke et al. [74]. The main uncertainty contribution for all speed of sound measurements was due to the uncertainty of the pressure measurement and contributed up to 95 %. Because measurements were performed over a wide pressure range, the pressure was measured with a transducer Honeywell TJE with a measuring range from 0 to 200 MPa and an accuracy of $\pm 0.1\%$ with respect to its full scale. Even though for measurements for oxygen, where a second pressure sensor with a measuring range of up to 20 MPa was used for the lower pressure range and the pressure uncertainty contribution decreased to about 40 %, the overall measurement uncertainty was still large and unsatisfying. A new system with three capacitive pressure sensors in a cascade configuration should be implemented, increasing the overall measurement accuracy by one order of magnitude for the same measurement range. Efforts have been done to prepare the measuring cell for electrically conductive fluids, such as ionic liquids. Several attempts to isolate the electrodes of the quartz crystal by coatings were unsuccessful. A reliable quartz isolation for a wide range of temperature and pressure (without any negative acoustical effects) would be attractive because this ability would enlarge the applicability of the operation range with respect to a variety of numerous other fluids.

Bibliography

[1] A. Schuster, S. Karellas, E. Kakaras, H. Spliethoff, Energetic and economic investigation of Organic Rankine Cycle applications., Appl. Therm. Eng. 29 (2009) 1809–1817.

[2] A. W. Adam, Organic Rankine Cycles, Vol. 4, John Wiley & Sons, New York, 1995.

[3] H. Chen, D. Y. Goswami, E. K. Stefanakos, A review of thermodynamic cycles and working fluids for the conversion of low-grade heat, Renewable and Sustainable Energy Reviews 14 (2010) 3059–3067.

[4] S. Gupta, J. D. Olson, Industrial needs in physical properties, Ind. Eng. Chem. Res. 42 (2003) 6359–6374.

[5] R. Span, Multiparameter Equations of State: An accurate source of thermodynamic property data, Springer, Berlin, New York, 2000.

[6] F. H. Dubberke, D. B. Rasche, E. Baumhögger, J. Vrabec, Apparatus for the measurement of the speed of sound of ammonia up to high temperatures and pressures, Rev. Sci. Instrum. 85 (2014) 084901.

[7] P. J. Kortbeek, M. J. P. Muringer, N. J. Trappeniers, S. N. Biswas, Apparatus for sound velocity measurements in gases up to 10 kbar: Experimental data for argon, Rev. Sci. Instrum. 56 (1985) 1269–1273.

[8] H. Gedanitz, M. Davila, E. Baumhögger and R. Span, An apparatus for the determination of speeds of sound in fluids, J. Chem. Thermodyn. 42 (2010) 478–483.

[9] S. Ye, J. Alliez, B. Lagourette, H. Saint-Guirons, J. Arman, P. Xans, Réalisation d'un dispositif de mesure de la vitesse et de l'atténuation d'ondes ultrasonores dans des liquides sous pression, Rev. Phys. Appl. 25 (1990) 555–565.

[10] Z. Wang, A. Nur, Ultrasonic velocities in pure hydrocarbons and mixtures, J. Acoust. Soc. Am. 89 (1991) 2725–2730.

[11] A. Zak, M. Dzida, M. Zorebski, A. Ernst, A high pressure device for measurements of the speed of sound in liquids, Rev. Sci. Instrum. 71 (2000) 1756–1765.

[12] G. Benedetto, R. M. Gavioso, P. A. G. Albo, S. Lago, D. M. Ripa, R. Spagnolo, A microwave–ultrasonic cell for sound-speed measurements in liquids, Int. J. Thermophys. 26 (2005) 1651–1665.

[13] K. Meier, S. Kabelac, Speed of sound instrument for fluids with pressures up to 100 MPa, Rev. Sci. Instrum. 77 (2006) 123903.

[14] F. H. Dubberke, E. Baumhögger, J. Vrabec, Burst design and signal processing for the speed of sound measurement of fluids with the pulse-echo technique, Rev. Sci. Instrum. 86 (2015) 054903.

[15] R. DiPippo, Second law assessment of binary plants generating power from low-temperature geothermal fluids, Geothermics 33 (2004) 565–586.

[16] F. S. Johnson, The solar constant, J. Meteorology 11 (1954) 431–439.

[17] C. Invernizzi, P. Iora, P. Silva, Bottoming micro-Rankine cycles for micro-gas turbines, Appl. Therm. Eng. 27 (2007) 100–110.

[18] U. Drescher, D. Brüggemann, Fluid selection for the Organic Rankine Cycle (ORC) in biomass power and heat plants, Appl. Therm. Eng. 27 (2007) 223–228.

[19] P. Bombarda, C. M. Invernizzi, C. Pietra, Heat recovery from diesel engines: A thermodynamic comparison between Kalina and ORC cycles, Appl. Therm. Eng. 30 (2010) 212–219.

[20] J. Larjola, Electricity from industrial waste heat using high-speed organic rankine cycle (orc), Int. J. Production Economics 41 (1995) 227–235.

[21] S. Karellas, A. Schuster, Supercritical fluid parameters in Organic Rankine cycle applications, Int. J. Thermodyn. 11 (2008) 101–108.

[22] A. Schuster, S. Karellas, R. Aumann, Efficiency optimization potential in supercritical Organic Rankine Cycles, Energy 35 (2010) 1033–1039.

[23] H. Chen, D. Y. Goswami, M. M. Rahman, E. K. Stefanakos, A supercritical Rankine cycle using zeotropic mixture working fluids for the conversion of low-grade heat into power, Energy 36 (2011) 549–555.

[24] H. Yamaguchi, X. R. Zhang, K. Fujima, M. Enomoto, N. Sawada, Solar energy powered Rankine cycle using supercritical CO2, Appl. Therm. Eng. 26 (2006) 2345–2354.

[25] M. Kanoglu, Exergy analysis of a dual-level binary geothermal power plant, Geothermics 31 (2002) 709–724.

[26] B. Liu, P. Rivière, C. Coquelet, R. Gicquel, F. David, Investigation of a two stage Rankine cycle for electric power plants, Appl. Energy 100 (2012) 285–294.

[27] N. A. Lai, J. Fischer, Efficiencies of power flash cycles, Energy 44 (2012) 1–11.

[28] T. Ho, S. S. Mao, R. Greif, Comparison of the Organic Flash Cycle (OFC) to other advanced vapor cycles for intermediate and high temperature waste heat reclamation and solar thermal energy, Energy 42 (2012) 213–223.

[29] M. K. Löffler, Flash Evaporation in Cyclones, Chem. Eng. Technol. 31 (2008) 1062–1065.

[30] I. K. Smith, R. P. M. da Silva, Development of the trilateral flash cycle system part 2: Increasing power output with working fluid mixtures, Proc. Inst. Mech. Eng., Part A: J. Power Energy 208 (1994) 135–144.

[31] Z. Rant, Exergie, ein neues Wort für 'Technische Arbeitsfähigkeit', Forsch. Ing. Wes. 22 (1956) 36–37.

[32] H. D. Baehr, Thermodynamik, 10. Auflage, Springer-Verlag, Berlin, 2000.

[33] F. Bošnjaković, Technische Thermodynamik (II. Teil), 5. Auflage, Verlag Theodor Steinkopff, Dresden, 1971, p. 461–479.

[34] A. Bejan, Second law analysis in heat transfer, Energy 5 (1980) 721–732.

[35] T. C. Hung, Waste heat recovery of Organic Rankine Cycle using dry fluids, Energy Convers. Manage. 42 (2001) 539–553.

[36] P. J. Mago, L. M. Chamra, K. Srinivasan, C. Somayaji, An examination of regenerative Organic Rankine Cycles using dry fluids, Appl. Therm. Eng. 28 (2008) 998–1007.

[37] B. Liu, K. Chien, C. Wang, Effect of working fluids on Organic Rankine Cycle for waste heat recovery, Energy 29 (2004) 1207–1217.

[38] B. Saleh, G. Koglbauer, M. Wendland, J. Fischer, Working fluids for low-temperature organic rankine cycles, Energy 32 (2007) 1210–1221.

[39] A. Borsukiewicz-Gozdur, W. Nowak, Comparative analysis of natural and synthetic refrigerants in application to low temperature Clausius - Rankine cycle, Energy 32 (2007) 344–352.

[40] N. A. Lai, M. Wendland, J. Fischer, Working fluids for high-temperature organic rankine cycles, Energy 36 (2011) 199–211.

[41] C. Rücker, K. Kümmerer, Environmental Chemistry of Organosiloxanes, Chem. Rev. 115 (2015) 466–524.

[42] M. Thol, F. H. Dubberke, G. Rutkai, T. Windmann, A. Köster, R. Span, J. Vrabec, Fundamental equation of state correlation for hexamethyldisiloxane based on experimental and molecular simulation data, Fluid Phase Equilib. 418 (2016) 133–151.

[43] M. Thol, G. Rutkai, A. Köster, F. H. Dubberke, T. Windmann, R. Span, J. Vrabec, Thermodynamic properties of octamethylcyclotetrasiloxane, J. Chem. Eng. Data 61 (2016) 2580–2595.

[44] P. Colonna, N. Nannana, A. Guardone, E. W. Lemmon, Multiparameter equations of state for selected siloxanes, Fluid Phase Equilib. 244 (2006) 193–211.

[45] P. Colonna, N. Nannana, A. Guardone, Multiparameter equations of state for siloxanes, Fluid Phase Equilib. 263 (2008) 115–130.

[46] A. Uusitalo, T. Turunen-Saaresti, J. Honkatukia, P. Colonna, J. Larjola, Siloxanes as working fluids for mini-orc systems based on high-speed turbogenerator technology, J. Eng. Gas Turbines Power 135 (2013) 042305.

[47] B. Kaczmarek, Ternary liquid - liquid equilibria: Hexamethyldisiloxane – Dimethyl Sulfoxide Methyl Ethyl Ketone (Diethyl Ketone), Polish J. Chem. 74 (2000) 885–887.

[48] N. R. Nannana, P. Colonna, C. M. Tracy, R. L. Rowley, J. J. Hurly, Ideal-gas heat capacities of dimethylsiloxanes from speed-of-sound measurements and ab initio calculations, Fluid Phase Equilib. 257 (2007) 102–113.

[49] N. A. Lai, M. Wendland, J. Fischer, Description of linear siloxanes with PC-SAFT equation, Fluid Phase Equilib. 283 (2009) 22–30.

[50] M. Preißinger, D. Brüggemann, Thermal stability of hexamethyldisiloxane (MM) for high-temperature Organic Rankine Cycle (ORC), Energies 9 (2016) 1–11.

[51] A. P. Fröba, H. Kremer, A. Leipertz, F. Flohr, C. Meurer, Thermophysical Properties of a Refrigerant Mixture of R365mfc (1,1,1,3,3-Pentafluorobutane) and Galden® HT 55 (Perfluoropolyether), Int. J. Thermophys. 28 (2007) 449–480.

[52] R. E. Tapscott, E. W. Heinonen, J. D. Mather, Identification and proof testing of new total flooding angents: Toxicity and global environmental assessment New Mexico Engineering Research Institute, NMERI 97/29/33010, (1998) Albuquerque, New Mexico.

[53] Frenzelit, novaphit® SSTC Technical Datasheet, Frenzelit Werke GmbH.

[54] FRAGOL, Therminol 66® Product information, FRAGOL SCHMIERSTOFF GMBH + CO. KG.

[55] Dortmund Data Bank, http://www.dbbst.com.

[56] R. Rowley, W. Wilding, J. Oscarson, Y. Yang, N. Zundel, T. Daubert, R. Danner, DIPPR Data Compilation of Pure Compound Properties, Design Institute for Physical Properties, AIChE, New York, 2003.

[57] E. Lemmon, M. Huber, M. McLinden, Reference Fluid Thermodynamic and Transport Properties REFPROP, Version 9.1, 2013.

[58] K. Meier, The Pulse-Echo Method for High Precision Measurements of the Speed of Sound in Fluids, Habilitation Thesis, University of the Federal Armed Forces, Hamburg, 2006.

[59] M. J. P. Muringer, N. J. Trappeniers, S. N. Biswas, The effect of pressure on the sound velocity and density of toluene and n-heptane up to 2600 bar, Phys. Chem. Liq. 14 (1985) 273–296.

[60] S. J. Ball, J. P. M. Trusler, Speed of sound of n-hexane and n-hexadecane at temperatures between 298 and 373 K and pressures up to 100 MPa, Int. J. Thermophys. 22 (2001) 427–443.

[61] H. Gedanitz, M. Davila, E. Baumhögger, R. Span, An apparatus for the determination of speeds of sound in fluids, J. Chem. Thermodyn. 42 (2010) 478–483.

[62] K. Meier, S. Kabelac, Speed of sound instrument for fluids with pressure up to 100 MPa, Rev. Sci. Instrum. 77 (2006) 123903.

[63] G. Benedetto, R. M. Gavioso, P. A. G. Albo, S. Lago, D. M. Ripa, R. Spagnolo, Speed of sound in pure water at temperatures between 274 and 394 K and at pressures up to 90 MPa, Int. J. Thermophys. 26 (2005) 1667–1680.

[64] Refrigerants - Requirements and Symbols - Ref. Nr. DIN 8960: 1998-11, Normenausschuss Kältetechnik (FNKä).

[65] R. Wegge, M. Richter, R. Span, Speed of sound measurements in ethanol and benzene over the temperature range from (253.2 to 353.2) K at pressures up to 30 MPa, J. Chem. Eng. Data. 60 (2015) 1345–1353.

[66] C. Guder, W. Wagner, A Reference Equation of State for the Thermodynamic Properties of Sulfur Hexafluoride (SF6) for Temperatures from the Melting Line to 625 k and Pressures up to 150 MPa, J. Phys. Chem. Ref. Data 38 (2009) 33–94.

[67] C. L. O'Connor, Thermal relaxation of vibrational states in sulfur hexafluoride, J. Acoust. Soc. Am. 26 (1954) 361–364.

[68] R. Gardas, J. Coutinho, Estimation of speed of sound of ionic liquids using surface tensions and densities: A volume based approach, Fluid Phase Equilib. 267 (2008) 188–192.

[69] C. G. la Rubia García, Speed of Sound Measurements in Ammonia and Ionic Liquids, Master Thesis, Chair of Thermodynamics and Energy Technology, University of Paderborn, 2012.

[70] J. M. S. S. Esperança, Z. P. Visak, N. V. Plechkova, K. R. Seddon, H. J. R. Guedes, L. P. N. Rebelo, Density, Speed of Sound, and Derived Thermodynamic Properties of Ionic Liquids over an Extended Pressure Range. 4. [C3mim][NTf2] and [C5mim][NTf2], J. Chem. Eng. Data 51 (2006) 2009–2015.

[71] R. G. de Azevedo, J. Szydlowski, P. F. Pires, J. M. S. S. Esperança, H. J. R. Guedes, L. P. N. Rebelo, A novel non-intrusive microcell for sound-speed measurements in liquids. Speed of sound and thermodynamic properties of 2-propanone at pressures up to 160 MPa, J. Chem. Thermodyn. 36 (2004) 211–222.

[72] Solvay product stewardship, safety data sheet SOLKATHERM ® SES 36, SOLVAY FLUORIDES, LLC 1.02 / CA (Z8) (P00000019486).

[73] M. Thol, E. W. Lemmon, R. Span, Equation of State for a Refrigerant Mixture of r365mfc (1,1,1,3,3-Pentafluorobutane) and Galden® HT 55 (Perfluoropolyether), Research report, Ruhr-Universität Bochum, 2009.

[74] F. H. Dubberke, M. Riepold, E. Baumhögger, J. Vrabec, Speed of Sound of Oxygen in Supercritical States up to 500 K and 100 MPa, J. Chem. Eng. Data 61 (2016) 1632–1636.

[75] AIR LIQUIDE, CHLORWASSERSTOFF N28, Air Liquide's Gas Encyclopedia (2009) 771–778.

[76] AIR LIQUIDE, Sicherheitsdatenblatt gemäß RL 1907/2006/EG (REACH), AIR LIQUIDE Deutschland GmbH (Versions-Nr.: 2 - 01).

[77] M. Thol, L. Piazza, R. Span, A new functional form for equations of state for some polar and weakly associating fluids, Int. J. Thermophys. 35 (2014) 783–811.

[78] C.-W. Lin, J. P. M. Trusler, The speed of sound and derived thermodynamic properties of pure water at temperatures between (253 and 473) K and at pressures up to 400 MPa, J. Chem. Phys. 136 (2012) 094511.

[79] R. Tillner-Roth, F. Harms-Watzenberg, H. D. Baehr, Eine neue Fundamentalgleichung für Ammoniak, DKV-Tagungsbericht 20 (1993) 167–181.

[80] M. Thol, F. H. Dubberke, E. Baumhögger, J. Vrabec, R. Span, Speed of sound measurements and fundamental equations of state for octamethyltrisiloxane and decamethyltetrasiloxane, J. Chem. Eng. Data.

A Appendix

A.1 Tabulated speed of sound measurement data

Table 1: Experimental results for the refrigerant mixture 1,1,1,3,3-pentafluorobutane and perfluoropolyether.

T [K]	p [MPa]	c [m/s]	$\pm\ u_c$ [m/s]	T [K]	p [MPa]	c [m/s]	$\pm\ u_c$ [m/s]
313.101	0.15	585.66	0.27	349.124	50.53	788.49	0.88
313.100	1.28	595.31	0.26	349.125	53.32	800.57	0.86
313.101	3.23	611.18	0.26				
313.101	4.99	624.79	0.25	399.053	1.14	280.02	0.52
313.100	7.42	642.74	0.24	399.067	3.04	320.18	0.40
313.099	10.21	662.12	0.24	399.071	4.06	338.31	0.36
313.100	12.96	680.18	0.23	399.067	5.02	353.63	0.34
313.102	19.96	722.33	0.23	399.071	7.55	389.00	0.29
313.100	29.50	773.17	1.00	399.068	10.09	419.56	0.26
313.101	36.87	808.58	0.93	399.073	14.39	463.66	0.23
313.039	53.01	878.09	0.80	399.076	20.35	514.68	1.53
				399.077	30.38	585.40	1.24
349.127	0.38	458.18	0.30	399.070	40.21	643.34	1.06
349.128	0.60	460.84	0.30	399.066	50.24	694.83	0.94
349.124	1.14	467.25	0.30	399.070	53.38	709.70	0.92
349.122	2.15	478.72	0.28				
349.126	3.14	489.50	0.28	449.923	14.14	354.15	0.26
349.127	4.09	499.36	0.27	449.921	14.98	364.42	0.25
349.124	5.12	509.56	0.26	449.922	20.50	420.72	1.76
349.127	7.41	530.94	0.25	449.929	30.42	500.12	1.35
349.125	10.06	553.81	0.24	449.925	33.47	521.12	1.27
349.127	15.30	594.44	0.22	449.928	40.31	564.14	1.13
349.103	19.14	621.04	0.22	449.929	49.91	617.44	0.99
349.124	20.54	630.24	1.30	449.948	60.65	669.89	0.89
349.124	29.44	684.06	1.12	449.951	70.80	714.51	0.81
349.126	40.35	741.26	0.98				

Standard uncertainties u are $u(T) = 0.03$ K, $u(p) = 0.2$ MPa for $p \geq 20$ MPa and $u(p) = 0.01$ MPa for $p \leq 20$ MPa, where $u(p)$ contributed around 95 % above 20 MPa and around 40 % below 20 MPa to the combined uncertainty u_c. The uncertainty contribution of the measurement procedure was $u(m) = 500$ ppm.

Table 2: Experimental data for the speed of sound of hydrogen chloride.

T [K]	p [MPa]	c [m/s]	± u_c [m/s]	T [K]	p [MPa]	c [m/s]	± u_c [m/s]
218.29	0.55	940.18	1.32	299.82	19.37	678.26	2.02
224.26	0.67	910.37	1.39	304.99	23.08	689.99	1.89
229.18	0.79	886.70	1.46	309.99	26.60	700.39	1.79
233.12	0.89	864.75	1.52	314.98	30.26	711.60	1.70
243.01	1.21	813.78	1.68	319.98	33.91	722.37	1.62
248.00	1.40	789.56	1.78	324.98	37.53	732.54	1.55
252.95	1.62	762.36	1.90	327.98	39.67	738.39	1.51
257.96	1.86	734.25	2.04				
262.97	2.12	705.36	2.22	267.00	7.55	734.60	1.96
267.98	2.42	676.01	2.44	269.85	9.83	739.93	1.90
272.99	2.75	645.54	2.71	274.84	13.98	750.68	1.80
277.91	3.11	615.57	3.06	279.81	18.15	761.40	1.71
282.80	3.68	587.37	3.43	284.81	22.44	772.62	1.62
292.94	6.96	563.84	3.52	289.81	26.72	783.42	1.54
294.95	8.09	567.18	3.37	294.81	31.06	794.27	1.47
300.00	11.21	581.74	2.98	299.99	35.48	804.70	1.41
304.98	14.29	594.91	2.69	303.14	38.09	810.52	1.37
309.98	17.43	607.88	2.46	304.98	39.66	814.17	1.36
314.98	20.60	620.52	2.27				
319.98	23.76	632.37	2.12	309.09	6.37	385.22	9.03
324.99	26.88	643.33	2.00	314.96	8.75	405.89	6.74
329.99	30.04	654.24	1.89	319.97	10.90	424.84	5.43
334.98	33.23	665.08	1.80	324.97	13.04	441.00	4.60
339.98	36.37	675.09	1.71	329.97	15.20	455.81	4.02
344.98	39.52	684.97	1.64	334.97	17.34	468.97	3.60
				339.97	19.53	481.92	3.26
279.84	5.60	634.36	2.72	344.97	21.73	494.11	2.99
284.83	8.55	639.91	2.56	349.98	23.94	505.66	2.76
289.69	11.92	651.65	2.36	354.97	26.14	516.61	2.57
294.80	15.73	665.97	2.17	359.97	28.31	526.72	2.41

Table 3: Continued

T [K]	p [MPa]	c [m/s]	$\pm\ u_c$ [m/s]	T [K]	p [MPa]	c [m/s]	$\pm\ u_c$ [m/s]
364.97	30.52	536.85	2.27	384.90	20.83	355.19	2.80
369.97	32.75	546.72	2.14	394.90	22.94	371.24	2.45
374.88	34.93	555.93	2.03	404.88	25.02	386.13	2.18
379.88	37.11	564.79	1.94	414.89	27.13	400.31	1.98
385.89	39.79	575.49	1.83	424.92	29.24	413.74	1.81
				434.93	31.32	426.43	1.68
324.98	9.77	332.55	9.77	444.94	33.37	438.53	1.57
329.97	11.40	351.23	7.66	459.95	36.49	455.90	1.43
334.98	13.09	368.31	6.22	474.95	39.58	472.23	1.32
339.98	14.80	383.39	5.25				
344.99	16.52	397.38	4.56	373.03	16.15	305.04	2.85
349.98	18.22	409.75	4.05	389.92	18.73	329.93	2.23
354.98	19.96	421.76	3.64	399.92	20.26	343.40	2.00
359.95	21.71	433.15	3.31	409.93	21.83	356.47	1.82
369.89	25.18	453.98	2.82	419.93	23.33	367.66	1.66
379.89	28.64	472.83	2.47	439.94	26.37	390.30	1.44
389.88	32.15	490.75	2.20	459.95	29.36	411.14	1.28
399.86	35.68	507.75	1.99	479.91	32.33	430.51	1.16
411.88	39.88	526.56	1.79				
				399.93	12.22	323.86	0.44
344.54	12.47	273.22	7.60	419.93	13.33	339.37	0.25
354.99	14.62	299.23	5.18	439.95	14.48	354.55	0.18
364.93	16.67	319.30	4.00	459.97	15.60	369.14	0.20
374.90	18.74	338.05	3.28	479.94	16.67	382.65	0.24

Standard uncertainties u are $u(T) = 0.05$ K, $u(p) = 0.2$ MPa and the uncertainty of the measurement procedure $u(m) = 500$ ppm, where $u(p)$ contributed up to around 95 % to the combined uncertainty u_c.

Table 4: Experimental data for the speed of sound of dodecamethylpentasiloxane ($MD3M$).

T [K]	p [MPa]	c [m/s]	$\pm u_c$ [m/s]
299.890	0.11	939.34	0.54
299.901	0.48	941.85	0.54
299.899	1.02	945.63	0.54
299.905	1.51	949.22	0.54
299.914	1.99	952.70	0.53
299.927	3.46	963.07	0.52
299.949	6.03	980.77	0.51
299.977	9.97	1006.47	0.49
300.031	20.03	1067.02	0.45
300.082	29.76	1119.26	0.43
349.743	1.51	799.74	0.63
349.734	2.05	804.71	0.62
349.721	3.49	817.57	0.60
349.717	6.16	840.42	0.58
349.718	10.22	872.52	0.54
349.726	15.17	909.03	0.51
349.722	20.05	942.17	0.49
349.726	23.70	965.52	0.47
399.695	0.12	647.85	0.80
399.687	0.51	652.73	0.79
399.674	1.00	658.70	0.78
399.666	1.49	664.50	0.77
399.651	2.03	670.87	0.75
399.647	3.54	688.10	0.72
399.666	6.17	715.53	0.67
399.674	9.95	752.00	0.62
399.710	14.97	795.40	0.57
399.904	20.49	838.27	0.53
399.782	21.16	843.36	0.52
449.984	0.11	517.36	1.07
449.985	0.52	524.18	1.04
449.991	1.02	532.20	1.01
449.979	1.51	539.94	0.99
449.966	2.06	548.28	0.96
449.887	3.48	568.93	0.90
449.833	6.05	603.15	0.81
449.890	10.10	650.02	0.71
449.968	14.94	698.60	0.64
450.328	17.19	718.84	0.61
500.015	0.11	391.53	1.57
500.019	0.50	400.96	1.50
499.992	0.99	412.44	1.43
499.981	1.49	423.28	1.36
499.963	1.98	433.51	1.30
499.960	3.53	462.97	1.16
499.963	5.98	503.34	1.00
499.959	9.91	558.18	0.84
500.177	12.38	587.70	0.77
499.959	13.62	602.21	0.74
549.424	1.01	294.42	2.27
549.294	2.04	329.09	1.88
549.224	3.54	367.40	1.54
549.152	5.99	417.99	1.23
549.325	9.26	472.81	1.00

Standard uncertainties u are $u(T) = 0.03$ K, $u(p) = 0.07$ MPa for $p \geq 70$ MPa, where $u(p)$ contributed between 80 and 99 % to the combined uncertainty u_c. The uncertainty contribution of the measurement procedure was $u(m) = 500$ ppm.

A.2 List of publications

Previous to this dissertation work:

- G.C. Lehmann, F. Dubberke, M. Horsch, Y.-L. Huang, S. Miroshnichenko, R. Pflock, G. Sonnenrein and Jadran Vrabec: Research on the behavior of liquid fluids atop superhydrophobic gas-bubble surfaces: Sixth International Conference on Computational Fluid Dynamics, p. 108-109, VVM Publishing Co., St. Petersburg, 2010

Publications related to this thesis:

- K. Hasselmann, F. Reinker, S. aus der Wiesche, E. J. Kenig, F. H. Dubberke, and J. Vrabec: Perfomance predictions of axial turbines for organic rankine cycles (ORC) applications based on measurements of the flow through two-dimensional cascades of blades, Proceedings of the ASME 2014 Power Conference POWER2014 (32098), July 28-31, 2014, Baltimore, Maryland, USA
- F. H. Dubberke, D. B. Rasche, E. Baumhögger, and J. Vrabec: Apparatus for the measurement of the speed of sound of ammonia up to high temperatures and pressures, Rev. Sci. Instrum. 85, 084901 (2014); doi: 0.1063/1.4891795
- F. H. Dubberke, E. Baumhögger, and J. Vrabec: Burst design and signal processing for the speed of sound measurement with the pulse-echo technique, Rev. Sci. Instrum. 86, 054903 (2015); doi: 10.1063/1.4921478
- F. H. Dubberke, M. Riepold, E. Baumhögger, and J. Vrabec: Speed of Sound of Oxygen in Supercritical States up to 500 K and 100 MPa, J. Chem. Eng. Data 2016, 61, 1632-1636, DOI: 10.1021/acs.jced.5b01007
- M. Thol, F. H. Dubberke, G. Rutkai, T. Windmann, A. Köster, R. Span and J. Vrabec: Fundamental equation of state correlation for hexamethyldisiloxane based on experimental and molecular simulation data; Fluid Phase Equilibr., Volume 418, 25 June 2016, Pages 133-151, dx.doi.org/10.1016/j.fluid.2015.09.047
- M. Thol, G. Rutkai, A. Köster, F. H. Dubberke, T. Windmann, R. Span and J. Vrabec: Thermodynamic Properties of Octamethylcyclotetrasiloxane; J. Chem. Eng. Data, Volume 61, 2016, Pages 2580-2595; DOI: 10.1021/acs.jced.6b00261
- M. Thol, F. H. Dubberke, E. Baumhögger, J. Vrabec and R. Span: Speed of Sound Measurements and Fundamental Equations of State for Octamethyltrisiloxane and Decamethyltetrasiloxane; J. Chem. Eng. Data 62, (2017), 2633-2648; DOI: 10.1021/acs.jced.7b00092

- F. H. Dubberke, M. Linnemann, W. Khider Abbas, E. Baumhögger, K.-P. Priebe, M. Roedder, M. Neef, and J. Vrabec: Experimental setup of a cascaded two-stage organic Rankine cycle; Appl. Therm. Eng., 131, (2018), 958-964; DOI: 10.1016/j.applthermaleng.2017.11.137

Scientific talks:

- F. H. Dubberke, J. Vrabec: Speed of sounds of silxoxanes as working fluids for organic rankine cycles, First International seminar on ORC-Power Cycles, Delft, September 2011
- F. H. Dubberke, S. Schönborn, E. Baumhögger, J. Vrabec: Schallgeschwindigkeitsmessungen bei hohen Temperaturen und Drücken, Piezoforum, Paderborn, April 2012
- F. H. Dubberke, T. Windmann, G. Rutkai, J. Vrabec: Speed of Sound of Siloxanes from Experiment and Molecular Simulation, Eighteenth Symposium on Thermophysical Properties, Boulder, June 2012
- F. H. Dubberke, E. Baumhögger, J. Vrabec: Optimierung der Puls-Echo-Methode zur Messung der Schallgeschwindigkeit durch Signalaufbereitung und Pulsdesign, Thermodynamik Kolloquium, Hamburg, Juni 2013
- F. H. Dubberke, E. Baumhögger, J. Vrabec: Method for enlarging the measuring range of the pulse-echo technique for supercritical states, Nineteenth Symposium on Thermophysical Properties, Boulder, June 2015

Poster presentations:

- M. Gerber, F. H. Dubberke, R. Span: Temperaturverteilung in einer Biogasanlage, Fachverband für Biogas 2008, Nürnberg
- F. H. Dubberke, J. Vrabec: Test-rig ORC, Advanced Waste Heat Valorisation Technologies 2012, Kortrijk, Belgium
- F. H. Dubberke, J. Vrabec: Speed of sound in Siloxanes, ESAT 2012, Potsdam

Student theses

The following student theses were prepared under the supervision of the author of the present doctoral thesis in the frame of his research:

- **Andreas Kochbeck**, An apparatus for measuring the speed of sound of siloxanes at high temperature and pressure, BA, 2011

- **Ewald Japs**, Untersuchung der Wärmeübertragungsmechanismen an dachintegrierten kristallinen Photovoltaikmodulen, DA, 2011
- **Hanke Bohlen**, Auslegung und Entwurf von Wärmeübertragerkonzepten zur Direktverdampfung und Überhitzung von Mehrfluidsystemen für den ORC Kaskadenprozeß, DA, 2011
- **Ning Kuang**, Wirkungsgradoptimierung durch Anpassung von Arbeitsmedien am Beispiel eines ORC-Kraftwerkes, BA, 2011
- **Simon T. Schönborn**, Speeds of sound measurement in hexamethyldisiloxane at high temperature and pressure, DA, 2011
- **Sven Indermark**, Ausarbeitung einer Gefährdungsbeurteilung für eine ORC-Anlage, StdA, 2011
- **Andreas Sennekamp**, Datensammlung und Korrelation der Zustandsgrößen von Hexamethyldisiloxan und Verbesserung der Zustandsgleichung mit Daten aus der Simulation, SA, 2013
- **Can Kosocou**, Speisepumpen in ORC-Anlagen, SA, 2013
- **Carlos Guillermo la Rubia García**, Speed of sound measurements in ammonia and ionic liquids, MA, 2012
- **Patrick Dubjella**, Speeds of sound measurement in siloxanes at high temperature and pressure, BA, 2012
- **Philip Kiene**, Mechanical design and construction of a piping system for the CORC test-rig, BA, 2012
- **Stefan Rode**, Radial expansion turbine for high pressure and temperature for the CORC, SA, 2012
- **Stefan Rode**, Development of radial centrifugal flash turbine for power flash cycle, MA, 2013
- **Steffen Greve**, Programming, installation and documentation of the CORC master display, SA, 2012
- **Tobija Stemmer**, Speed of sound in ammonia, BA, 2013
- **Yuelon Zong**, Schallgeschwindigkeitsmessung in Wasser bei hohen Drücken und Temperaturen im Vergleich zur IAPWS-95, BA, 2012

- **Frederik Ikemeyer**, An improved cross-correlation method for the pulse-echo approach, BA, 2013
- **Markus Riepold**, Dispersion effects in speed of sound measurements in gases, BA, 2013
- **Vitali Boldt**, Preparation and operation of the high temperature cycle of the CORC, SA, 2013
- **Lasse Tigges**, Ertragsanalyse eines Windparks mittels Vergleich zu Ertragsgutachten und anderen Windparks, BA, 2014